# Doors to Darkness: Phenomenology of Dark Matter Portal Interactions

Von der Fakultät für Mathematik, Informatik und Naturwissenschaften der RWTH Aachen University zur Erlangung des akademischen Grades einer Doktorin der Naturwissenschaften genehmigte Dissertation

*vorgelegt von*

Saniya HEEBA, M.Sc.

*aus*

Roorkee, Indien

Berichter: Jun.-Prof. Dr. Felix Kahlhöfer
Univ.-Prof. Dr. Michael Krämer

Tag der mündlichen Prüfung: 10 September 2021

DOCTORAL THESIS

# Doors to Darkness: Phenomenology of Dark Matter Portal Interactions

*by*

Saniya HEEBA

*Supervisor*

Jun. -Prof. Dr. Felix KAHLHÖFER

*This thesis was realised at the*

INSTITUTE FOR THEORETICAL PARTICLE PHYSICS AND COSMOLOGY,

RWTH AACHEN UNIVERSITY

Aachen, September 2021

# *Abstract*

## Doors to Darkness: Phenomenology of Dark Matter Portal Interactions

by Saniya HEEBA

The Dark Matter (DM) question has taken centre-stage in modern-day particle physics and cosmology, with the microphysical nature of DM remaining stubbornly elusive. In this thesis, we explore different classes of particle DM models based on the interactions of DM with the Standard Model (SM). Our interests lie in obtaining accurate relic density estimates with the inclusion of finite temperature corrections and other in-medium effects, as well as in detailing the detection prospects of these models using direct detection experiments and accelerator searches. We will focus on the so-called portal models, in which a single type of interaction connects the DM particle to the SM. We will distinguish between the case where this portal interaction arises from the exchange of a scalar, *the Higgs Portal*, and from a vector particle, *the vector portal*.

For the Higgs portal, we consider a scalar singlet DM model where the relic abundance is set by the leakage of energy from the SM thermal bath (the so-called *freeze-in mechanism*), and where the dominant contribution does not arise from Higgs boson decays. The latter can be achieved if such decays are kinematically forbidden or if the reheating temperature is much smaller than the Higgs boson mass.

For the vector portal, we consider two dark photon models. One, with a kinetically mixed dark photon where the relic abundance is set by resonantly enhanced annihilations during or after *freeze-out*, i.e., when DM decouples from the thermal bath. And the second, where both the SM and DM are gauged under an additional $U(1)'$, and the relic abundance is set by freeze-in.

Further, mediators in both scalar and vector portal models may also give rise to long-range DM-DM interactions, potentially alleviating the tensions between astrophysical observations and predictions from collisionless cold DM. To discuss these effects, we provide a new quantum-mechanical treatment of such self-interactions and derive analytic results for the momentum transfer and viscosity cross-section for the case of interactions arising from a Yukawa potential.

Through these representative models, we make the following observations: i) Thermal corrections, in-medium effects and a proper treatment of the electroweak and QCD phase transition are highly relevant for relic density calculations especially for the case of freeze-in, and ii) some of the simplest models with light and/or feebly coupled DM can be probed in a complementary fashion at ongoing and upcoming direct detection and accelerator experiments, spelling exciting times for the future of DM research.

# *Zusammenfassung*

## Pforten zur Finsternis: Phänomenologie von Portal-Wechselwirkungen dunkler Materie

von Saniya HEEBA

Die Thematik um die dunkle Materie (DM) steht im Mittelpunkt der modernen Teilchenphysik und Kosmologie, wobei sich uns bislang die mikrophysikalische Natur der DM hartnäckig entzieht. In dieser Dissertation werden unterschiedliche Modelle von DM-Teilchen und ihren Wechselwirkungen mit dem Standardmodell (SM) eingehend untersucht. Der Fokus liegt hierbei einerseits darauf, korrekte Abschätzungen der Reliktdichte zu bestimmen, wofür die Berücksichtigung von temperaturabhängigen Korrekturen sowie weiteren In-Medium-Effekten notwendig ist. Andererseits wird die Überprüfbarkeit dieser Modelle durch Beschleuniger und direkte Detektionsexperimente detailliert diskutiert. Konkret werden sogenannte Portalmodelle diskutiert, in denen eine einzige Art von Wechselwirkung das DM-Teilchen an das SM koppelt. Dabei werden zwei Fälle betrachtet: eine Wechselwirkung über ein skalares Austauschteilchen (das *Higgs-Portal*) und über ein Vektorteilchen (das *Vektorportal*).

Für den Fall des Higgs-Portals wird ein skalares Singlet-DM-Modell betrachtet. Die Reliktdichte wird hierbei durch das Austreten von Energie aus dem SM-Wärmebad generiert (der sogenannte *Freeze-In-Mechanismus*), wobei Zerfälle des Higgs-Bosons nicht den dominanten Beitrag ausmachen. Letzteres kann entweder dadurch realisiert werden, dass der Zerfall kinematisch nicht erlaubt ist oder dass die Temperatur beim Wiederaufheizen des Universums kleiner ist als die Masse des Higgs-Bosons. Für den Fall eines Vektorportals werden zwei konkrete Dunkle-Photon-Modelle betrachtet. Im ersten Szenario wird ein dunkles Photon im Kontext kinetischer Mischung diskutiert, wobei die Reliktdichte über resonant verstärkte Annihilationen während oder nach dem Freeze-out, d.h. dem Entkoppeln von DM aus dem Wärmebad, erzeugt wird In dem zweiten Modell sind hingegen sowohl das SM als auch die DM unter einer zusätzlichen $U(1)'$-Symmetrie geladen und die Reliktdichte wird über Freeze-in erzeugt. Des Weiteren können Austauschteilchen in Skalar- und Vektorportal-Modellen zu langreichweitigen DM-DM-Wechselwirkungen führen. Dies ermöglicht es insbesondere viele der Diskrepanzen zwischen astrophysikalischen Observationen und Vorhersagen für kalte DM zu mildern. Um diese Effekte zu diskutieren, wird für den Fall einer Wechselwirkung über ein Yukawa-Potential ein neuer quantenmechanischer Ansatz für solche Selbstwechselwirkungen vorgestellt sowie analytische Ergebnisse für den Impulsübertrags- und Viskositätswirkungsquerschnitt hergeleitet. Mit Hilfe dieser repräsentativen Modelle können folgende Schlussfolgerungen gezogen werden: i) Temperaturabhängige Korrekturen, In-Medium-Effekte und eine richtige Behandlung des elektroschwachen und QCD-Phasenübergangs sind hochrelevant für die Berechnungen der Reliktdichte, insbesondere für Freeze-In-Szenarien. ii) Einige der einfachsten Modelle mit leichter und/oder gänzlich schwach wechselwirkender DM können auf eine komplementäre Weise mit aktuellen sowie zukünftigen Experimenten

an Beschleunigern und mit solchen zum direkten Nachweis von DM getestet werden, sodass der DM-Forschung eine aufregende Zukunft bevorsteht.

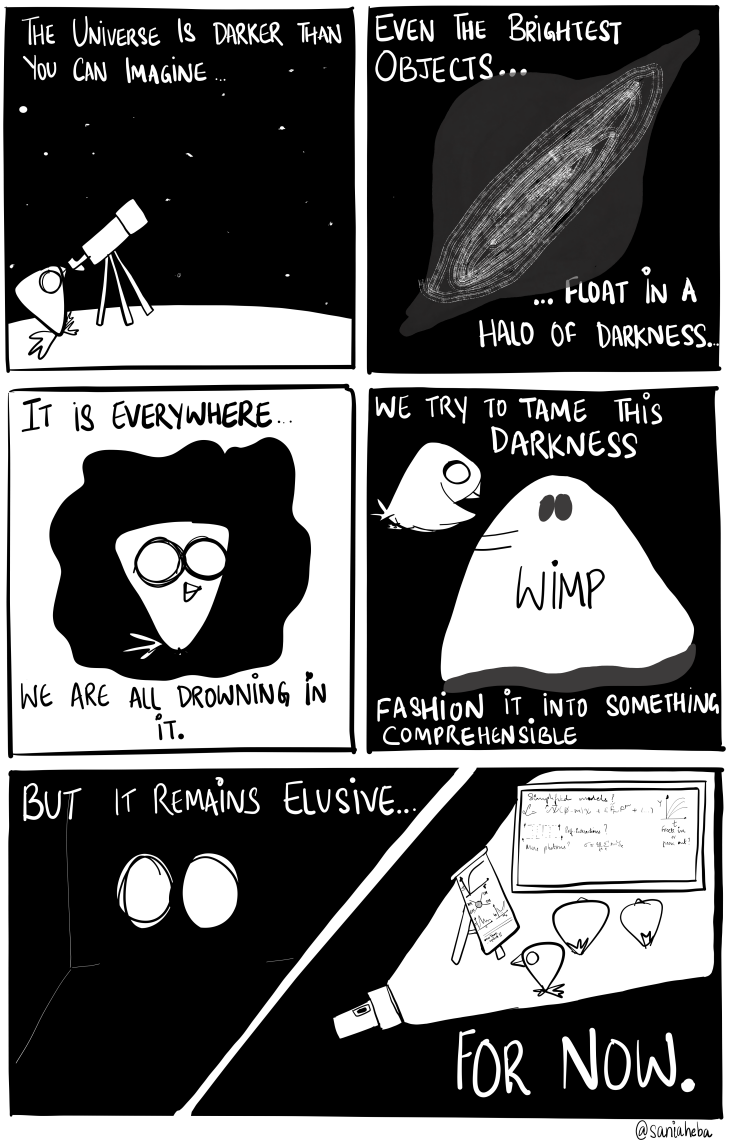
THE UNIVERSE IS DARKER THAN YOU CAN IMAGINE...
EVEN THE BRIGHTEST OBJECTS...
... FLOAT IN A HALO OF DARKNESS..
IT IS EVERYWHERE...
WE ARE ALL DROWNING IN IT.
WE TRY TO TAME THIS DARKNESS
WIMP
FASHION IT INTO SOMETHING COMPREHENSIBLE
BUT IT REMAINS ELUSIVE...
FOR NOW.
@saniaheba

# *Acknowledgements*

*Given that the second half of my PhD was carried out during Very Strange Times, it goes without saying that all acknowledgments listed here fall woefully short. But here they are anyway.*

First, I would like to thank Felix Kahlhoefer for being an incredible supervisor and mentor and an all-round stellar human being, who has been consistent and generous with his support and guidance. I have learned so much from Felix in the last four years both academically and otherwise, and our discussions have significantly shaped my perspective on physics. I am also extremely grateful to him (and Inés and Martin!) for celebrating Eid with me while I was stranded here last year.

I would also like to thank Michael Kraemer for being the second reviewer for this thesis and also for his support and encouragement ever since I came to RWTH for my Master's.

I would be remiss to not mention my amazing collaborators in the last three years, Brian Colquhoun, Elias Bernreuther, Kristian Vangsnes, Katelin Schutz, Laura Sagunski, Sean Tulin, Torsten Bringmann and Tongyan Lin who have ensured that all of our projects have been enlightening and fun. A special thanks to Torsten and Kristian for providing lots of help with DARKSUSY, to Sean and Laura for providing the SIDM data we used in our project, to Elias for coding up the accelerator constraints in DARKCAST for our resonant DM project, and to Felix for implementing our light dark photon model in DDCALC.

I am sure that my stay in Germany (especially given The Year Of The Long Inside) would have been significantly worse (possibly unbearable) without the members of the TTK institute. A special thanks to all my officemates for the last four years: Carlo, Eike, Fatih, Patrick, Jonas, Juliana, Stephan, Sven, Tim (and Elias who might as well be an officemate given the amount of time he spent there in the Before Times). Coming to work never felt like a chore with all of you around and learning physics with you has been an absolute blast.

Just a huge, huge thanks to my proofreaders– Carlo, Dania, Deanna, Fatih, Jesús and Shashwat, who did not even hesitate when I asked them to read/edit tens of pages at the literal last minute. This thesis would have been poorer without your input. I'm also especially grateful to Fatih for providing the German translation of the abstract[1] (and also for helping me navigate thesis-related bureaucracy and putting up with my billion questions), and to Elias and Carlo for translating the title in five hundred different ways before agreeing on the "goth" version which, just to be clear, does not maintain the alliteration because "*in German, we actually do know how to pronounce a 'p' at the beginning of a word before a consonant*".

My deepest thanks to the following people for being so ridiculously kind and generous with their friendship despite the absolute, dreadful chaos of last year. Deanna, the cat pictures and murder threads and academia rants and checkins were life-savers. Shalaka, you have been so amazing and so inspiring and it is always so fulfilling to talk to you. Shashwat, our ice-cream appointments have always been uniquely fun.

And of course, an incredible, unquantifiable amount of love and gratitude to my family, to whom I owe everything, who have always been the beginning and the end; my parents,

[1] I modified it a bit afterwards and therefore any mistakes there are most definitely a result of my schlechtes deutsch.

for always being so sure of me even (especially) when I was not sure of myself, for teaching me everything I know about integrity, and compassion, and for the privilege and gift of me being capable to do any of this in the first place; my brothers, Saad and Sarim, for keeping me company through many solitary pandemic *iftars* despite the time difference, for having my back like no one else ever can, and just for their unquestionably irreplaceable presence in my life; my sister, Dania, for being my closest friend through and through, for her delightfully morbid sense of humour somehow always in line with my own, and for her many (weirdly specific, sometimes pedantic) opinions on the "art" that appears in this thesis; my nani, the happiest, strongest, woman I ever knew, who had so much *zindagi*, and who is never far from my thoughts, and my nana, dada and dadi, who have always had such profound trust and faith and hope in me, and to whom I can finally say, *hogayi khatam thesis akhir. Ban gayi apki beti doctor.*

# Declaration of Authorship

I, *Saniya Heeba*, declare that this thesis and the work presented in it are my own and have been generated by me as the result of my own original research. I do solemnly swear that to the best of my knowledge:

1. This work was done wholly or mainly while in candidature for the doctoral degree at this faculty and university;
2. No part of this thesis has previously been submitted for a degree or any other qualification at this university or any other institution;
3. Where I have consulted the published work of others or myself, this is always clearly attributed;
4. Where I have quoted from the work of others or myself, the source is always given. This thesis is entirely my own work, with the exception of such quotations;
5. I have acknowledged all major sources of assistance;
6. Where the thesis is based on work done by myself jointly with others, I have made clear exactly what was done by others and what I have contributed myself;
7. The research carried out during this thesis and described in this work has led to several scientific publications, listed on the following page.

Date Signature

# List of Publications

This thesis is based on the research I carried out during my doctoral studies at the Institute for Theoretical Particle Physics and Cosmology at the RWTH Aachen University, culminating in the following publications,

1. Saniya Heeba and Felix Kahlhoefer, *"Probing the freeze-in mechanism in dark matter models with $U(1)'$ gauge extensions"*, published in **Phys. Rev. D 101.3 (2020)** [1].

2. Brian Colquhoun, Saniya Heeba, Felix Kahlhoefer, Laura Sagunski, and Sean Tulin, *"Semiclassical regime for dark matter self-interactions"*, published in **Phys. Rev. D 103.3 (2021)** [2].

3. Elias Bernreuther, Saniya Heeba, and Felix Kahlhoefer, *"Resonant sub-GeV Dirac dark matter"*, published in **JCAP 03 (2021)** [3].

4. Torsten Bringmann, Saniya Heeba, Felix Kahlhoefer, and Kristian Vangsnes, *"How to freeze-in scalar singlets: A closer look"*, **in prep (2021)** [4].

# Contents

**Abstract** iii

**Zusammenfassung** v

**Acknowledgements** ix

**Declaration of Authorship** xi

**List of Publications** xii

**Contents** xiii

**Prelude** 1

**I The Beginning** 3

**1 Touched By Light: The Past We Can See** 5
1.1 Standard Model in a Nutshell . . . 5
1.1.1 Phase Transitions in the SM . . . 8
1.2 The Standard Model at Finite Temperature . . . 11
1.2.1 Quantum Systems in Thermal Equilibrium: Imaginary Time Formalism 11
1.2.2 Masses at Finite Temperature . . . 14
1.2.3 Electroweak Phase Transition Revisited . . . 18
1.3 Particle Cosmology in a Nutshell . . . 24
1.3.1 Phase Space Distributions in Equilibrium . . . 27
1.3.2 Quantifying Interaction Rates . . . 30
1.4 From The Earliest Times Until Today . . . 31

**2 Whispers from the Dark: Hidden Sectors In The Early Universe** 35
2.1 Evidence and Properties of Dark Matter . . . 35
2.2 Production Mechanisms of Dark Matter . . . 39
2.2.1 The Boltzmann Equation . . . 39
2.2.2 Freeze-out: Conventions and Caveats . . . 41
2.2.3 Freeze-in: The Old And The New . . . 47
2.2.4 WIMPs, FIMPs, and Other Things . . . 52
2.3 Early Universe Probes of Dark Matter . . . 53
2.3.1 Big Bang Nucleosynthesis . . . 55
2.3.2 Cosmic Microwave Background . . . 56

**II The Middle** 59

**3 Mediators Galore** 61

**4 Higgs Portal** **63**
4.1 Scalar Singlet Dark Matter . . . 64
4.1.1 Off-shell Higgs Decays . . . 65
4.1.2 Cross-sections at Large Energies: Unitarity Considerations . . . 66
4.1.3 Cross-Sections at Small Energies: The Effects of Chiral Symmetry Breaking 68
4.2 Freeze-in Production . . . 70
4.2.1 High Reheating Temperature . . . 70
4.2.2 Low Reheating Temperature . . . 71
4.3 Conclusions . . . 73

**5 Dark Photon Portal** **75**
5.1 The Structure of a Dark Photon Lagrangian . . . 76
5.1.1 Kinetic Mixing . . . 76
5.1.2 Light Dark Photons In-Medium: Effects on Masses and Couplings . . . 77
5.2 Resonant Dark Photon Model . . . 80
5.2.1 Relic Abundance Calculation . . . 80
5.2.2 Cosmological Constraints . . . 84
5.3 $B - L$ Dark Photon Model . . . 85
5.3.1 Relic Abundance Calculation . . . 87
5.4 Conclusions . . . 91

**6 Semi-Classical Treatment of Mediators** **93**
6.1 Small Scale Problems . . . 93
6.2 Describing Non-Relativistic Interactions . . . 97
6.2.1 Classical Description . . . 97
6.2.2 Quantum-Mechanical Description . . . 98
6.3 Self-interactions in a Yukawa Potential . . . 100
6.3.1 Cross-sections in the Semi-Classical Regime . . . 104
6.3.2 Summary . . . 112
6.4 Velocity Averaging . . . 115
6.5 Phenomenological implications . . . 118
6.6 Conclusions . . . 120

**III The Now** **123**

**7 Detection Strategies** **125**
7.1 Direct Detection . . . 125
7.2 Accelerator Constraints . . . 132
7.3 Constraining Resonant Dark Photons . . . 134
7.3.1 Accelerator Constraints . . . 134
7.3.2 Direct Detection Constraints . . . 138
7.4 Constraining B-L Dark Photons . . . 140
7.4.1 Accelerator Constraints . . . 141
7.4.2 Direct Detection Constraints . . . 142
7.5 Conclusions . . . 144

**8 Conclusions** **147**

**A In-medium Cross-Section And Thermal Average** **151**

**B Derivation of phase shifts** **155**

**Bibliography** **157**

# Prelude

We do not know what eighty percent of the Universe is made of [5].

This is not an exaggeration. We have stared into the cosmos for millennia, reshaped the world we inhabit in irreversible ways, brought home carved-out pieces of other worlds as well, but we do not know what eighty percent of the Universe is made of. Here is another fact, commonly stated yet always surprising: there are more stars in the Universe than grains of sand on the Earth. And what I am telling you is when you add all of that up, all of those stars, all of those grains of sand, everything you can see, touch, manipulate, you can explain the constitution of only about twenty percent of what is actually out there. What I am telling you is that we are only at the surface of what there is to know, that while we've dug our heels and made ourselves comfortable in our little corner of the Universe, there still remains much room to leap.

We do not know what eighty percent of the Universe is made of but we are curious and passionate and determined. We call the missing eighty percent Dark Matter and we have spent the last several decades sketching out its shape [6]. We know it is stable. We know it interacts very weakly, if at all, with the kind of matter we are familiar with. The only interactions we are sure about are gravitational. We've buried experiments deep into the heart of the Earth and sent satellites into space in an effort to see *something*. But even though we *know* it is there, from the structure of our universe, from the movement of stars, from tiny fluctuations in ancient light, it eludes our experiments, its microphysical properties just slightly out of reach.

The last fifty years have seen a tremendous increase in both the theoretical and experimental sides of dark matter research: better, more precise experiments exploring a diversity of what-ifs proposed by solid theoretical modelling. From using gravitational waves [7]—literal ripples in space time—to exoplanets [8], we are exploring every avenue. But the absence of a clear, uncontested dark matter signal, and the range of possibilities have made it imperative that we rethink our approach toward dark matter modelling. Theoretical research into the question of dark matter has now become an exercise in balance: between the unique features offered by each model and the degeneracies in phenomenology and detection prospects it shares with others. The complementarity of search strategies demand a complementarity in model phenomenology and therefore in model-building.

In this thesis, I will approach the dark matter question from the perspective of its possible connections to visible matter. Non-gravitational interactions between the dark and the visible sectors, if present, are necessarily small. But these can result in observable signatures at scales

ranging from the very big (in the structure of the universe) to the very small (in properties of visible sector particles). The imprints that dark matter leaves on our Universe span our entire cosmological history, culminating in the experiments we build today that target a whole host of potential properties dark matter could have. Keeping in mind this range of scales as well as the myriad model possibilities that may map onto the same physical observables, the discussion of models in this thesis is structured along the axis of cosmological time.

In Part I, *The Beginning*, I describe the happenings in the Universe at the earliest timescales both in the visible and the dark sectors, specifying what is known, what is posited, and what is assumed. Chapter 1 provides an introduction to the Standard Model of Particle Physics, including a description of particle interactions at finite temperature, as well as a brief review of the cosmological history of the universe. Chapter 2 provides a more formal introduction to dark matter and establishes mechanisms of dark matter production and evolution. It also discusses how dark matter affects our cosmological history and therefore how observations of the early universe can be used to make statements about its particle nature.

In Part II, *The Middle*, we meet dark matter in the middle and discuss two different portals between the dark and the visible sectors. Chapter 3 serves as a brief introduction to what follows. Then, using the formalism developed in Part I, Chapters 4 and 5 describe scalar and vector portals respectively, and their early universe phenomenology. Particles that mediate the interactions between the two sectors can also result in self-interactions within the dark sector, affecting the structures of galaxies and galaxy clusters. Chapter 6 elaborates on these self-interactions and their phenomenological consequences.

Finally, in Part III, *The Now*, we discuss our attempts to look for dark matter with terrestrial experiments, focusing on the models discussed in Part II. Chapter 7 introduces three different search strategies for dark matter, discussing in detail two of them: direct detection and accelerator searches. The general conclusions are presented in Chapter 8 along with a brief outlook into what the future holds.

# Part I

# The Beginning

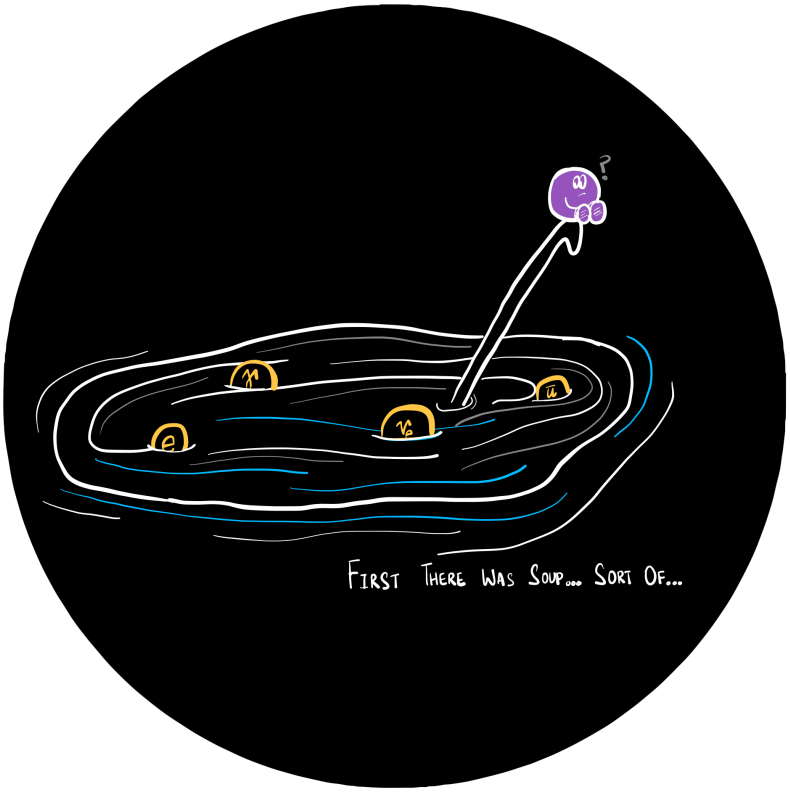

# Chapter 1

# Touched By Light: The Past We Can See

The cosmological history of the universe is usually presented in units of temperature— a measure of the energy contained in the Standard Model (SM) heat bath. Some of these temperatures are known to a high degree of accuracy from cosmological and astrophysical observations (such as the temperature at which the universe became transparent or at which light nuclei such as helium began to form), while some only have upper (or lower) bounds inferred from our current understanding of cosmology (such as the temperature of reheating).

To understand how the universe came to be, and to establish notational convention, we begin this chapter with a brief introduction to the SM of particle physics in Section 1.1. Since the SM particles and fields are generally described at zero-temperature (or in vacuum), which the early universe was decidedly not, we take a small detour in Section 1.2 to understand how the field theory machinery of SM is modified at finite-temperature. In doing so, we discuss phase-transitions in the SM and other in-medium effects for particles in a thermal bath. We then shift scales and provide a short overview to Particle Cosmology in Section 1.3, sketching out the kinds of calculations needed to quantify cosmological interaction rates. Finally, we put everything together in Section 1.4 and summarise the cosmological history of the universe.

The following sections are largely based off of the references [9–13]. Additional references, when used, are cited in-text.

## 1.1 Standard Model in a Nutshell

The Standard Model of particle physics, also called the Glashow-Weinberg-Salam model, provides a prescription for describing the fundamental particles in the universe and three of the four forces which connect them.[1] The particles in the SM can be classified into fermions and bosons on the bases of their spin. Elementary fermions and their bound states such as protons and neutrons comprise the entirety of the visible sector of our universe. Bosons act as mediators of the three different forces: the photon, $\gamma$, mediates the electromagnetic interaction, the $W$- and $Z$- bosons mediate the weak interaction, and the gluons, $g$, mediate the strong interaction. Lastly, the Higgs boson generates the mass of all particles except neutrinos which

[1] Gravity is yet to be included in the SM.

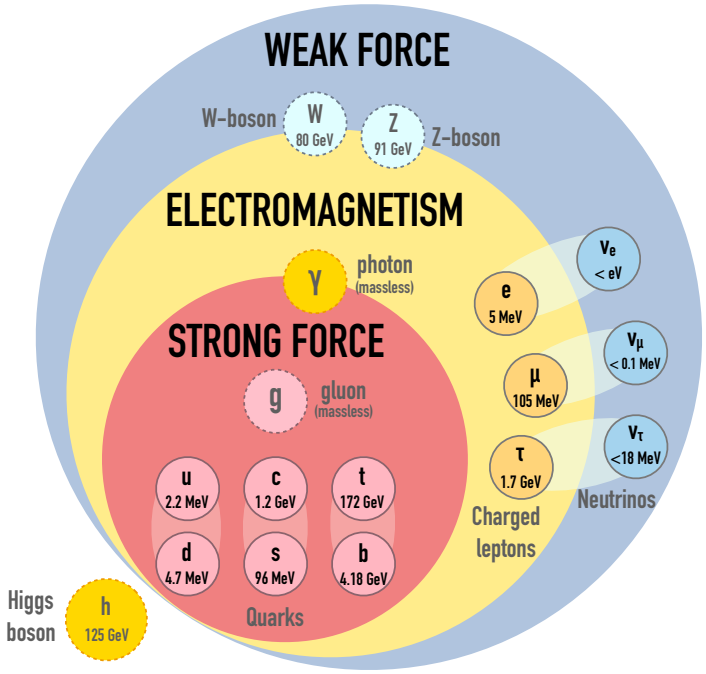


FIGURE 1.1: A sketch of the particles in present in the SM with their approximate masses. The shading between particles indicates fermion generations. (Sketch adapted from a talk by K. Schutz.)

in the current formulation of the SM remain massless. Taken together, these particles describe everything we can quite literally "see".

The mathematical construction of the SM is based in a relativistic quantum field theory (QFT) framework. Relativistic quantum fields realised in nature satisfy certain global symmetries, for example, invariance under translations, rotations and boosts in space and time. The translational and Lorentz invariance is grouped under the *Poincaré symmetry*. Additionally, fields in the SM satisfy certain internal or local symmetries which then determine the possible interactions (forces) between these fields or equivalently between the various SM particles. Mathematically, these local symmetries are represented by the non-abelian gauge group $SU(3)_C \times SU(2)_L \times U(1)_Y$. The generators of each group correspond to the mediators of the strong, weak and electromagnetic interactions respectively. The indices $C$, $L$, and $Y$ correspond to the particle properties of colour, chirality and hypercharge as detailed below.

Also known as the colour group, the $SU(3)_C$ gauge symmetry characterises the strong interactions in the SM called Quantum Chromodynamics (QCD). A fermion's charge under $SU(3)_C$ classifies it as a quark or a lepton. Quarks are triplets under $SU(3)_C$ meaning that each quark can have 3 possible "colours": red, blue and green.[2] This triplet representation also implies that quarks interact via the strong force. These interactions are mediated by the gluons, as mentioned previously, which are the generators of this gauge group. On the other hand, leptons are singlets under the colour group and thus do not have strong interactions.

[2]This has nothing to do with actual colour but instead should be thought about as an intrinsic property or an additional degree of freedom. Ref. [14] provides an insightful commentary on how certain terms in physics, like colored particles, are a stark reflection of the social context in which physics is done.

The electromagnetic and weak interactions are unified under the $SU(2)_L \times U(1)_Y$ symmetry. The SM is a *chiral* theory meaning that left- and right- handed particles have different interactions, represented by the different transformation properties of these particles under the electroweak gauge group. The left-handed leptons and quarks are arranged in weak isodoublets (i.e., charged under both $SU(2)_L$ and $U(1)_Y$),

$$L = \begin{pmatrix} \nu \\ e \end{pmatrix}_L ; Q = \begin{pmatrix} u \\ d \end{pmatrix}_L \tag{1.1}$$

while the right-handed ones are in weak isosinglets (charged only under $U(1)_Y$): $e_R$, $u_R$, $d_R$. Note that right-handed neutrinos do not exist in the current formulation of the SM, although they are often invoked as an explanation for neutrino masses [15]. Both quarks and leptons have 6 different flavours grouped into three generations or families. The second and third generations of leptons can be represented as $L_2 = (\nu_\mu, \mu)_L$, $e_{R_2} = \mu_R$ and $L_3 = (\nu_\tau, \tau)$, $e_{R_2} = \tau_R$ respectively. Similarly for the quarks we have $Q_2 = (c, s)$, $u_{R_2} = c_R$, $d_{R_2} = s_R$ and $Q_3 = (t, b)$, $u_{R_3} = t_R$, $d_{R_2} = b_R$

The SM particle content and interactions are summarised in Fig. 1.1. Once the various fields and their respective charges are defined, the SM Lagrangian is constructed by including all terms of mass dimension four or less that are allowed by the respective gauge symmetries and satisfy Lorentz invariance.

In the simplest form, the SM Lagrangian can be written as

$$\begin{aligned} \mathcal{L} = &-\frac{1}{4} G^a_{\mu\nu} G^{\mu\nu}_a - \frac{1}{4} W^b_{\mu\nu} W^{\mu\nu}_b - \frac{1}{4} B_{\mu\nu} B^{\mu\nu} \\ &+ i\bar{L} D_\mu \gamma^\mu e_R + i\bar{Q} D_\mu \gamma^\mu Q + i\bar{u}_R D_\mu \gamma^\mu u_R + i\bar{d}_R D_\mu \gamma^\mu d_R \\ &+ (D_\mu \Phi)^\dagger D_\mu \Phi - V(\Phi) + (-\lambda_e \bar{L} \Phi e_R - \lambda_d \bar{Q} \Phi d_R - \lambda_u \bar{Q} \Phi^\dagger u_R + \text{h.c.}) \,. \end{aligned} \tag{1.2}$$

The first line contains the kinetic terms for the gauge bosons with the indices $a$ and $b$ representing the eight and three generators of $SU(3)_C$ and $SU(2)_L$ respectively. The second line contains the fermion kinetic terms as well as their interactions with the gauge fields (contained in the covariant derivative $D_\mu$).[3] The final line represents the interactions of the complex Higgs doublet, $\Phi$, with the gauge bosons (first term), with itself (second term) and with the fermion fields (last term). The Higgs-fermion interactions are also known as Yukawa interactions.

From Eq. 1.2, we immediately notice the absence of mass terms for the fermions and the gauge bosons. Since the SM is chiral, i.e., left- and right-handed fields have different transformation properties, any mass term of the form $\bar{\Psi}\Psi = (\Psi_L \bar{\Psi}_R + \Psi_R \bar{\Psi}_L)$ manifestly breaks gauge invariance. Similarly, a gauge boson mass term also violates the local $SU(2)_L \times U(1)_Y$ symmetry.[4] Particle masses in the SM have to be therefore generated via the *Higgs mechanism*. The Higgs

[3] $D_\mu = \partial_\mu - i g_s T_a G^a_\mu - i g_2 T_b W^b_\mu - i g_1 Y_q B_\mu/2$ where $g_{s,1,2}$ are the coupling constants for the various gauge interactions, $G$, $W$, $B$ are the field strengths for the gluon, weak boson and hypercharge fields, and $T_{a,b}$ are the generators of the gauge groups.

[4] This can be seen by applying the transformation $A^a_\mu \to A^a_\mu - f^{abc} A^b_\mu(x)\omega^c(x) + \frac{1}{g}\partial_\mu \omega^a(x)$ to the kinetic term in $\mathcal{L}$ where $f^{abc}$ are the structure constants for $SU(N)$ and $\omega$ is an infinitesimal parameter.

mechanism postulates the spontaneous breaking of the $SU(2)_L \times U(1)_Y$ symmetry to a residual $U(1)_Q$, where $Q$ denotes electric charge. The complex Higgs doublet with 4 degrees of freedom (dof) reduces to a scalar Higgs field (1 dof), and the remaining 3 dof are absorbed to produce the weak gauge boson masses. The photon, of course, remains massless. Additionally the Yukawa interactions with the Higgs which relate left- and right- handed fermions simplify to produce mass terms for the fermions.

The breaking of the electroweak symmetry is caused by a *phase transition*. Apart from the electroweak phase transition, the SM has another phase transition in the strong sector known as the QCD phase transition. We summarise these briefly in the next section.

### 1.1.1 Phase Transitions in the SM

#### The QCD Phase Transition

Although we have defined the QCD sector in terms of quarks and gluons, at low energies, free quarks and gluons do not exist. Instead, the strong interaction between them leads to the formation of colour-neutral bound states, called *hadrons*, in a process called *confinement*. Hadrons can either be formed from a quark-antiquark pair, known as *mesons*, or from three quarks, called *baryons*.

The exact mechanism for confinement is not properly understood but it stems from the non-abelian nature of $SU(3)$ [16]. In particular, the QCD phase transition is linked to the breaking of the chiral symmetry—which is an exact symmetry in the limit of massless quarks—and the formation of a quark condensate in vacuum, $\langle q\bar{q}\rangle$. Qualitatively, the energy required to separate a pair of quarks rises linearly with distance. As a result, at some point it becomes energetically cheaper to generate a new quark pair from the vacuum to form two colour-neutral bound states, than to have free quarks. Additionally, QCD is asymptotically free implying that the strength of interactions between quarks and gluons decreases with increasing energies. Put differently, at very high energies the strong coupling constant tends to zero. Taken together, this results in confinement at low energies whereas free, deconfined particles exist at high energies.

As a result of confinement, we cannot use the standard QCD Lagrangian at low energies. Instead, we use an effective field theory framework to construct a Lagrangian which includes baryons and mesons as the relevant degrees of freedom. This is done using Chiral Perturbation Theory [17]. The QCD phase transition is not directly relevant for this thesis apart from the fact that one should be mindful of the relevant degrees of freedom at a given temperature (or energy) scale when describing interactions. We will elaborate on this further in Chapter 4.

**The Electroweak Phase Transition**

To understand the phase transition in the electroweak sector (or the Higgs mechanism), it is necessary to first understand the phenomenon of *spontaneous symmetry breaking* (SSB). SSB occurs when the ground state of a theory is asymmetric under certain transformations even though the Lagrangian (which determines the dynamics of the theory) remains symmetric. The simplest example for when SSB is realised in nature is that of a ferromagnet. The theory which describes how two neighbouring spins interact is rotationally invariant, however, the ground state of a ferromagnet consists of spins aligned in a certain direction which explicitly breaks the rotational symmetry.

The Higgs mechanism is conceptually similar. To start with, we write down the Lagrangian for a set of N scalar fields, $\phi^i(x)$,

$$\mathcal{L} = \frac{1}{2}(\partial_\mu \phi^i)^2 + \frac{1}{2}\mu^2(\phi^i)^2 - \frac{\lambda}{4}[(\phi^i)^2]^2 \,, \tag{1.3}$$

with an implicit sum over $i$. This Lagrangian is symmetric under a rotation in N dimensions,

$$\phi^i \to R^{ij}\phi^j \,. \tag{1.4}$$

The lowest energy field configuration, or the ground state of the system, is then defined such that the potential

$$V(\phi^i) = -\frac{1}{2}\mu^2(\phi^i)^2 + \frac{\lambda}{4}[(\phi^i)^2]^2 \,, \tag{1.5}$$

is minimized, which results in

$$(\phi_0^i)^2 = \frac{\mu^2}{\lambda} \,. \tag{1.6}$$

Eq. 1.6 shows that the given set of fields $\phi^i$ can have a non-zero global value, called the *vacuum expectation value* (vev), at this minima. Since Eq. 1.6 specifies the magnitude of the vector $\phi_0^i$ but not the direction, it is possible to choose

$$\phi_0^i = (0, 0, \ldots, 0, v) \text{ with } v = \frac{\mu}{\sqrt{\lambda}} \,. \tag{1.7}$$

We can then define a set of shifted fields

$$\phi^i(x) = (\pi^k(x), v + \sigma(x)) \,, \quad k = 1, \ldots, N-1 \,, \tag{1.8}$$

and rewrite the Lagrangian 1.3 in terms of the $\pi$ and $\sigma$ fields.

$$\begin{aligned}\mathcal{L} =& \frac{1}{2}(\partial_\mu \pi^k)^2 + \frac{1}{2}(\partial_\mu \sigma)^2 - \frac{1}{2}(2\mu)^2\sigma^2 - \\ & \sqrt{\lambda}\mu\sigma^3 - \sqrt{\lambda}\mu(\pi^k)^2\sigma - \frac{\lambda}{4}\sigma^4 - \frac{\lambda}{2}(\pi^k)^2\sigma^2 - \frac{\lambda}{4}[(\pi^k)^2]^2 \,.\end{aligned} \tag{1.9}$$

Comparing Eqs. 1.3 and 1.9, we see that the original $O(N)$ symmetry is *hidden* (manifest only in how the coefficients in Eq. 1.9 relate to the two parameters, $\mu$ and $\lambda$, in Eq. 1.3), leaving only the $O(N-1)$ symmetry which rotates the $\pi$ fields among themselves.

Additionally, the only massive degree of freedom is $\sigma$ as the $\pi$ fields remain massless. The appearance of massless fields is a key feature of SSB, described by the *Goldstone Theorem* which states that a theory must contain one massless particle for each spontaneously broken continuous symmetry. In the example above, we go from $O(N)$ which has $N(N-1)/2$ independent continuous transformations to $O(N-1)$ which has $(N-1)(N-2)/2$.[5] Essentially, we break $N-1$ symmetries corresponding to the appearance of $N-1$ $\pi$ fields.

In the SM, the Higgs field, a complex scalar doublet, breaks the $SU(2)_L \times U(1)_Y$ symmetry to a residual $U(1)_Q$ by acquiring a vev. The three broken symmetries give rise to three massless Goldstone bosons, and the shifted Higgs field can be written as

$$\Phi = \frac{1}{\sqrt{2}} \begin{pmatrix} \phi^1 + i\phi^2 \\ v + h + i\phi^3 \end{pmatrix} , \tag{1.10}$$

where $h$ is the broken Higgs fields, $v$ is the vev and $\phi^i$ are the Goldstone bosons. It is possible to show that the Higgs doublet can be rotated to

$$\Phi \to \frac{1}{\sqrt{2}} \begin{pmatrix} 0 \\ v + h \end{pmatrix} \tag{1.11}$$

such that the Goldstone bosons are "absorbed" into the SM gauge bosons, $W^{\pm}$ and $Z$, providing them with a mass. Further, the Yukawa interaction in Eq. 1.2 for leptons and quarks simplify to give mass terms. To illustrate, we consider the electron Yukawa term

$$\mathcal{L} \supset -\lambda_e \bar{L}_1 \Phi e_{R_1} + \text{h.c} \tag{1.12}$$

which after SSB reduces to

$$L \supset -\frac{1}{\sqrt{2}} \lambda_e v \, \bar{e}_L e_R + \text{h.c} + \dots , \tag{1.13}$$

resulting in the electron mass $m_e = \lambda_e v/2$.

SSB, therefore, provides a simple mechanism to account for fermion and boson masses. However, we still have steered clear of answering *how* the symmetry breaking occurs. In our example of the ferromagnet, the reason that the rotational invariance of the system is broken at low energies is related to the temperature of the system. Below a critical temperature, we find that the spins in a ferromagnet align in a particular direction. It would not be unreasonable to guess then that the reason for SSB in the SM is also related to external effects. Put another way, to deduce the electroweak scale, or "when" SSB happens, we need to figure out the dynamics of our theory beyond the vacuum-only description we have studied so far.

[5] For $N = 1$, we do not have any rotations, for $N = 2$, we can perform a rotation in a single direction, for $N = 3$, in 3 directions and so on.

## 1.2 The Standard Model at Finite Temperature

Conventional field theory presupposes that interactions happen in vacuum[6], an ideal approximation to calculate observables such as cross-sections or event rates at experiments. However, as discussed in the introduction to this chapter, the early universe comprised of a hot dense plasma of particles and therefore interactions happened in the presence of a background thermal bath. These interactions alter the phenomenology of particles in-medium in substantive ways. For instance, positive mass-corrections to particles in-medium result in the opening up of decay channels not available at zero-temperature.[7] Formulating a finite temperature field theory (FQFT) can be used to include these background effects into cosmological calculations. It also provides an answer to the question asked at the end of Section 1.1.1: At what scale does the SM electroweak symmetry spontaneously break? In this section, we provide a short summary of the methods of FQFT before revisiting the electroweak phase transition.

### 1.2.1 Quantum Systems in Thermal Equilibrium: Imaginary Time Formalism

We begin by first thinking about a description of quantum particles in equilibrium. From statistical physics, we know that such an ensemble of particles with temperature, $T = 1/\beta$, can be described completely in terms of its partition function,

$$Z(\beta) \equiv \mathrm{Tr}\,\rho(\beta) = \mathrm{Tr}\,e^{-\beta\mathcal{H}} = \int \mathrm{d}\,x \langle x|e^{-\beta\mathcal{H}}|x\rangle\,, \tag{1.14}$$

where $\rho(\beta)$ is the density matrix, $\mathcal{H}$ is the Hamiltonian of the system, and Tr represents a trace (or a sum over the expectation values in any complete basis as shown in the final equality). Any observable is then given by an ensemble average

$$\langle A\rangle_\beta = \frac{1}{Z(\beta)}\mathrm{Tr}\,\rho(\beta)A = \frac{1}{Z(\beta)}\mathrm{Tr}\,e^{-\beta\mathcal{H}}A\,. \tag{1.15}$$

Further, the correlation function of any two observables is given by the thermal average, $\langle AB\rangle_\beta = Z^{-1}(\beta)\mathrm{Tr}\,\rho(\beta)AB$. The cyclicity of the trace leads to an interesting identity for the correlation function. For Heisenberg operators, $A_H(t) = e^{i\mathcal{H}t}A(0)\,e^{-i\mathcal{H}t}$, we can write

$$\begin{aligned}
\langle A_H(t)B_H(t')\rangle_\beta =& \frac{1}{Z(\beta)}\mathrm{Tr}\,e^{-\beta\mathcal{H}}A_H(t)B_H(t') \\
=& \frac{1}{Z(\beta)}\mathrm{Tr}\,e^{-\beta\mathcal{H}}B_H(t')e^{-\beta\mathcal{H}}A_H(t)e^{\beta\mathcal{H}} \\
=& \frac{1}{Z(\beta)}\mathrm{Tr}\,e^{-\beta\mathcal{H}}B_H(t')A_H(t+i\beta) \\
=& \langle B_H(t')A_H(t+i\beta)\rangle_\beta\,,
\end{aligned} \tag{1.16}$$

[6] Incidentally, physics also does not happen in vacuum and how we do science is shaped by the societies we do science *in* [18].

[7] This is a well-known result from stellar physics in the context of photon masses [19], but it can be generally applied to any particle in-medium.

where in the third line we have used the time evolution specified above to obtain $A_H(t) = e^{i\mathcal{H}t}A(0)\,e^{-i\mathcal{H}t} \Rightarrow e^{-\beta\mathcal{H}}A_H(t)e^{\beta\mathcal{H}} = A_H(t+i\beta)$. This is known as the KMS (Kubo-Martin-Schwinger) relation and it plays a major role in finite temperature field theories.

The connection between this statistical system and QFT can be seen clearly by considering the path integral formalism for zero-temperature QFT. In the path integral formalism, transition amplitudes at zero temperature are written as

$$\langle\phi(\vec{x}_1,\,t)|\phi(\vec{x}_2,\,0)\rangle = \langle\phi_1|e^{-i\mathcal{H}t}|\phi_2\rangle = N'\int\mathcal{D}\phi e^{i\mathcal{S}}\,, \tag{1.17}$$

where $\phi$ is the quantum field variable, $N'$ is a normalization constant determined from the "vacuum-to-vacuum" transition and $\mathcal{S}$ is the action defined by the Lagrangian of the system,

$$\mathcal{S}[\phi] = \int \mathrm{d}t \int \mathrm{d}^3x\,\mathcal{L} \tag{1.18}$$

The crucial observation is that the operator $e^{-\beta\mathcal{H}}$ in the definition of the partition function in Eq. 1.14, is equivalent to the time evolution operator $e^{-i\mathcal{H}t}$ in Eq. 1.17. In other words, the partition function of a quantum system at equilibrium can be described in a path integral formulation by making the replacement, $t \to i\beta$ [20],

$$\begin{aligned} Z(\beta) =& \mathrm{Tr}\, e^{-\beta\mathcal{H}} = \int \mathrm{d}\phi_1 \langle\phi_1|e^{-\beta\mathcal{H}}|\phi_1\rangle \\ =& N'\int\mathcal{D}\phi\, e^{-\mathcal{S}_E} \end{aligned} \tag{1.19}$$

where $\mathcal{S}_E[\phi] = \int_0^\beta \mathrm{d}t \int \mathrm{d}^3x\,\mathcal{L}[\phi]$ is the Euclidean (imaginary time) action defined over a *finite* time interval (corresponding to the inverse temperature of the system). Additionally, to represent a trace, the initial and final state should be the same. This means that the field variables must satisfy the periodicity and anti-periodicity conditions

$$\phi(\vec{x},\,\beta) = \pm\phi(\vec{x},0)\,, \tag{1.20}$$

for boson and fermion fields respectively. Note that the second component corresponds to imaginary time. The path integral representation of the partition function depicts the parallels between zero-temperature and finite-temperature QFT. In zero-temperature QFT, the end points in the path-integral formulation of the correlation function are not integrated over, however at finite temperature this very integration gives rise to the (anti-) periodicity conditions for the fields resulting in discrete energy levels as we shall see below.

It is possible to show that the thermal two-point Greens function, $\mathcal{G}_\beta(\tau,\tau')$, where $\tau$, $\tau'$ denote imaginary times, depends only on the difference, $\tau - \tau'$. Additionally, since $\tau$, $\tau' \in [0,\beta]$, one can use Eq. 1.16 to show that the two-point function in this formalism is also (anti-)periodic[8]

[8]This (anti-) periodicity is not directly related to the (anti-) periodicity in the field variables but instead comes from the KMS relation. See [11] for details.

[11],

$$\mathcal{G}_\beta(\vec{x},\,\tau) = \pm\mathcal{G}_\beta(\vec{x},\,\tau+\beta)\,. \tag{1.21}$$

Since the Greens functions are defined on finite time, their Fourier transform involves discrete frequencies,

$$\tilde{\mathcal{G}}_\beta(\vec{p},\,\omega_n) = \int_0^\beta \mathrm{d}\tau \int \mathrm{d}^3x\, e^{i(\omega_n\tau - \vec{p}.\vec{x})}\mathcal{G}_\beta(\vec{x},\,\tau)\,, \tag{1.22}$$

$$\mathcal{G}_\beta(\vec{x},\,\tau) = \frac{1}{\beta}\sum_{n=-\infty}^{\infty}\int \frac{\mathrm{d}^3p}{(2\pi)^3}\, e^{-i(\omega_n\tau - \vec{p}.\vec{x})}\tilde{\mathcal{G}}_\beta(\vec{p},\,\omega_n)\,. \tag{1.23}$$

Denoted by $\omega_n$, these are referred to as the Matsubara frequencies and are determined by the (anti-) periodicity conditions of the Greens function from Eq. 1.21,

$$\omega_n = \begin{cases} \frac{2n\pi}{\beta}, & \text{for bosons,} \\ \frac{(2n+1)\pi}{\beta}, & \text{for fermions,}\,. \end{cases} \tag{1.24}$$

The propagators in momentum space can then be calculated in the usual way by performing a Wick rotation,

$$\begin{aligned} \tilde{G}_\beta^{\text{boson}}(\vec{p},\,\omega_n) &= \frac{1}{\vec{p}^2 + m^2 + \omega_n^2}\,, \\ \tilde{G}_\beta^{\text{fermion}}(\vec{p},\,\omega_n) &= \frac{\gamma^0 + \vec{\gamma}.\vec{p} + m}{\vec{p}^2 + m^2 + \omega_n^2}\,, \end{aligned} \tag{1.25}$$

It follows from this discussion that finite temperature QFT looks like zero-temperature QFT with finite imaginary time.

To summarise, the imaginary time formalism consists of defining a partition function in the path integral representation with a Euclidean action over finite time. The Feynman rules can then be read off the path integral. The vertices remain the same as in the zero temperature Euclidean theory but the propagators pick up a non-trivial temperature dependence as a result of the (anti-) periodic boundary conditions. Finally, the loop integrals can be generalised by using the transformation,

$$\int \frac{\mathrm{d}^4p}{(2\pi)^4}\, f(\vec{p},\,\omega_n) \to \frac{1}{\beta}\sum_{n=-\infty}^{\infty}\int \frac{\mathrm{d}^3p}{(2\pi)^3}\, f(\vec{p},\,\omega_n)\,. \tag{1.26}$$

### 1.2.2 Masses at Finite Temperature

We illustrate this method by calculating the one-loop mass correction to a particle in a self-interacting scalar field theory described by the Lagrangian

$$\mathcal{L} = \frac{1}{2}\partial_\mu\phi\partial^\mu\phi - \frac{m^2}{2}\phi^2 - \frac{\lambda}{4!}\phi^4 \tag{1.27}$$

The corrections to the mass term come from a simple one-loop diagram arising from the four-vertex in the Lagrangian (see left panel of Fig. 1.2). Using the propagator for a scalar field and rotating to the Euclidean space we get

$$\begin{aligned}\Delta m^2 &= \frac{\lambda}{2\beta}\sum_n \int \frac{\mathrm{d}^3p}{(2\pi)^3}\frac{1}{(\frac{2n\pi}{\beta})^2 + \vec{p}^2 + m^2} \\ &= \frac{\lambda}{2\beta}\left(\frac{\beta}{2\pi}\right)^2 \sum_n \int \frac{\mathrm{d}^3p}{(2\pi)^3}\frac{1}{n^2 + (\frac{\beta\omega_p}{2\pi})^2}\,,\end{aligned} \tag{1.28}$$

where

$$\omega_p = (\vec{p}^2 + m^2)^{1/2}\,. \tag{1.29}$$

By using

$$\sum_{n=-\infty}^{\infty}\frac{1}{n^2+y^2} = \frac{\pi}{y}\coth\pi y\,, \tag{1.30}$$

we can calculate the one-loop mass correction as

$$\begin{aligned}\Delta m^2 &= \frac{\lambda}{4}\int\frac{\mathrm{d}^3p}{(2\pi)^3}\frac{1}{\omega_p}\coth\left(\frac{\beta\omega_p}{2}\right) \\ &= \frac{\lambda}{4}\int\frac{\mathrm{d}^3p}{(2\pi)^3}\frac{1}{\omega_p} + \frac{\lambda}{2}\int\frac{\mathrm{d}^3p}{(2\pi)^3}\frac{1}{\omega_p}\frac{1}{e^{\beta\omega_p}-1} \\ &= \Delta m_0^2 + \Delta m_\beta^2\,.\end{aligned} \tag{1.31}$$

The first term in the equation above, is the usual zero-temperature one-loop correction whereas the second term is the temperature dependent correction. Although it is difficult to obtain a closed-form expression for the second term, we can make a high-temperature expansion to obtain a positive mass correction,

$$\Delta m_\beta^2 \approx \frac{\lambda}{24\beta^2} = \frac{\lambda T^2}{24}\,, \tag{1.32}$$

Intuitively, this is what we would expect for a particle moving in a medium.

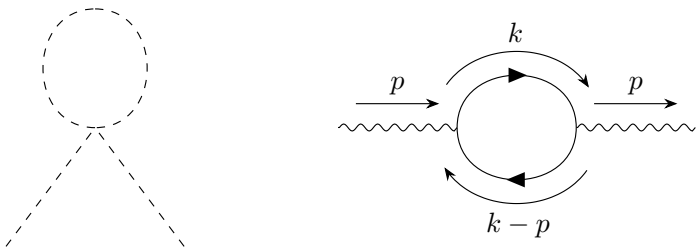


FIGURE 1.2: One loop correction to the mass term of a simple scalar field (left), and to the photon self-energy (right).

**Effective Masses for Massless Particles**

In-medium effects are also responsible for generating an *effective* mass for particles that are massless in vacuum. The most well-known example of this is the appearance of massive photons, called *plasmons*, in stellar systems [19]. This mass term can be traced back to a modification of the photon self-energy as a result of its interactions with the particles in the medium: the response of the plasma to a propagating electric field and the dynamical shielding of that field.

The photon self-energy in vacuum (assuming only electron-positrons in the loop) is given by,

$$\Pi_{\mu\nu}(p) = -ie^2 \int \frac{\mathrm{d}^4k}{(2\pi)^3} \mathrm{Tr}[\gamma_\mu G(-q)\gamma_\nu G(k)] \tag{1.33}$$

where $G(x)$ represent the electron propagators in the loop and $q = p - k$, with the various momenta as defined in the right panel of Fig. 1.2. As a result of the ward identity, $p^\mu \Pi_{\mu\nu}(p) = 0$, the self-energy has two independent components: the longitudinal (L) and transverse (T) mode corresponding to electric and magnetic interactions respectively,

$$\Pi_{\mathrm{L}}(p) = \Pi_{00}(p), \quad \Pi_{\mathrm{T}}(p) = \frac{1}{2}\left(\delta_{ij} - \frac{p_i p_j}{p^2}\right)\Pi_{ij}(p), \quad (i, j = 1, 2, 3). \tag{1.34}$$

We can reformulate Eq. 1.33 in the imaginary time formalism to obtain

$$\Pi_{\mu\nu}(p) = -\frac{4e^2}{\beta} \sum_{n=\infty}^{\infty} \int \frac{\mathrm{d}^3k}{(2\pi)^3} (k_\mu q_\nu - q_\mu k_\nu - g_{\mu\nu}) G(k) G(-q)\,, \tag{1.35}$$

where the sum runs over the discrete Matsubara frequencies, $k^0 = (2n+1)\pi/\beta$. It is difficult to obtain a closed form expression for this equation although in the high temperature limit ($T \gg m_e,\, p^0$), it is possible to solve for $\Pi_{\mathrm{L}}$ and $\Pi_{\mathrm{T}}$ [21, 22],

$$\Pi_{\mathrm{L}}(p) = -3m_\gamma^2 \left[1 - \frac{p_0}{2p} \ln \frac{p_0 + p}{p_0 - p}\right] \tag{1.36}$$

$$\Pi_{\mathrm{T}}(p) = \frac{3}{2} m_\gamma^2 \frac{p_0^2}{p^2} \left[1 - \left(1 - \frac{p^2}{p_0^2}\right) \frac{p_0}{2p} \ln \frac{p_0 + p}{p_0 - p}\right] \tag{1.37}$$

where $m_\gamma = eT/3$ denotes the effective thermal mass. The effective photon propagator will then have longitudinal and transverse contributions which in the static limit ($p^0 \to 0$) read

$$D^*_{\rm L}(p) = \frac{1}{p^2 + 3m_\gamma^2}, \tag{1.38}$$

$$D^*_{\rm T}(p) = -\frac{1}{p^2} \tag{1.39}$$

These equations tell us that the long range electric interaction is shielded in the infrared limit by the Debye mass, $m_D^2 = 3m_\gamma^2$, whereas the magnetic interaction is not.

The expression for the photon thermal mass can be readily generalised to include additional relativistic particles in the loop [23],

$$m_\gamma^2 = \sum_f \frac{e^2 q_f^2}{9} T^2 \,, \tag{1.40}$$

where the sum runs over all relativistic fermions each with a $U(1)$ charge given by $q_f$.

Similar to the photon self-energy, the fermion self-energies also get dressed in-medium. While calculating the fermion thermal masses, it is important to keep in mind that before the electroweak phase transition left- and right- handed fermions belong to different representations of the SM gauge group. This leads to different thermally induced masses. For the leptons we have [24],

$$m^2_{\ell,{\rm L}} = \frac{m_Z^2 + 2m_W^2 + m_\ell^2 + m_{\ell'}^2}{2v_h^2} T^2 \,, \tag{1.41}$$

$$m^2_{\ell,{\rm R}} = \frac{m_Z^2 - m_W^2 + \frac{1}{2}m_\ell^2}{2v_h^2} T^2 \,, \tag{1.42}$$

where $m_{\ell,\,\ell'}$ are the zero-temperature masses of the leptons belonging to the same $SU(2)$ doublet, $v_h$ is the Higgs vacuum expectation value, and $m_Z$ and $m_W$ denote the zero-temperature masses of the $Z$ and $W$ bosons. In particular, the masses of left-handed fermions belonging to the same $SU(2)$ doublet are equal. For the first-generation of quarks we get,

$$m^2_{q,{\rm L}} = \frac{1}{6} g_s^2 T^2 + \frac{3m_W^2 + \frac{1}{9}(m_Z^2 - m_W^2) + m_u^2 + m_d^2}{8v_h^2} T^2 \,, \tag{1.43}$$

$$m^2_{u,{\rm R}} = \frac{1}{6} g_s^2 T^2 + \frac{\frac{4}{9}(m_Z^2 - m_W^2) + \frac{1}{2}m_u^2}{2v_h^2} T^2 \,, \tag{1.44}$$

$$m^2_{d,{\rm R}} = \frac{1}{6} g_s^2 T^2 + \frac{\frac{1}{9}(m_Z^2 - m_W^2) + \frac{1}{2}m_d^2}{2v_h^2} T^2 \,, \tag{1.45}$$

where $m_{u,d}$ are the zero-temperature masses of up and down quarks and $g_s$ is the strong-coupling constant. The induced masses for the other two generations can be analogously defined.

After the phase transition, the mass corrections are simply [24],

$$\Delta m_\ell^2 = \frac{e^2\,T^2}{8}\,, \tag{1.46}$$

$$\Delta m_q^2 = \frac{g_s^2 T^2}{6}\,. \tag{1.47}$$

We end this section with a few comments on symmetries in the Finite Temperature QFT framework. Evidently, introducing a thermal bath of particles destroys Lorentz invariance since the rest frame of the bath is always preferred. Nevertheless, finite temperature field theory can in fact be formulated in a Lorentz covariant way in terms of the four-velocity of the system, $u^\mu = (1,\,0,\,0,\,0)$, and its (Lorentz-invariant) temperature, $T$. Given $u^\mu$, any four-vector, e.g., the particle four-momentum $p^\mu$, can be decomposed into a component parallel to it and one perpendicular to it.

$$\begin{aligned} p_\parallel^\mu &= (p.u)u^\mu \equiv \omega u^\mu \\ p_\perp^\mu &= p^\mu - \omega u^\mu\,. \end{aligned} \tag{1.48}$$

Then, in the rest frame of the heat bath where $u^\mu = (1,\,0,\,0,\,0)$, the energy of a particle is given by $p^0 = \omega$, and its three-momenta by $\vec{p} = p_\perp^\mu$. Therefore, $\omega$ can be understood as a Lorentz invariant energy and $p_\perp^\mu$ as the Lorentz invariant spatial momentum. This formulation has interesting consequences in terms of phenomenology. For instance, as we have already seen, the self-energy of particles in-medium now depend independently on two parameters ($\omega$ and $p_\perp^\mu$) instead of just on $p^\mu$, which leads to distinct plasmon masses and screening lengths.

Secondly, finite temperature effects, especially the positive mass correction as derived above, are crucial for restoring symmetries at high temperatures. The best example for this the restoration of the spontaneously broken $SU(2)_L \times U(1)_Y$ in the SM, which we discuss in detail in Section 1.2.3.

Finally, note that in the imaginary time formalism discussed above, we have traded the time variable for temperature. Consequently, this formalism can only be used to describe *static* systems. To track both time and temperature, we instead use *real time formalisms* in which we add a temperature variable to our theory [11, 13]. What this means in practice is a doubling of the Hilbert space to go from a purely vacuum ground state $|\Omega\rangle$ to a thermal vacuum given by $|\Omega, \beta\rangle$. Qualitatively, the result of using a real-time formalism is similar: we end up with temperature dependent propagators but in this case we can clearly separate the temperature-dependent and -independent parts. At the level of the Lagrangian, we end up doubling the degrees of freedom to have "ordinary" (or in-vacuum) vertices as well as "thermal" vertices for the interactions. Observables can then be calculated in the standard way of QFT. Real time formalisms are useful in studying dynamical systems but are far more technically complicated. For this thesis we will limit ourselves to an imaginary time formalism.

### 1.2.3 Electroweak Phase Transition Revisited

In Section 1.1.1, we reviewed the process of spontaneous symmetry breaking and the generation of particle masses in the Standard Model. In this section, we will quantify the scale of the electroweak phase transition.

Consider the tree-level Higgs Potential,

$$V_0(\phi_c) = -\frac{m^2}{2}\phi_c^2 + \frac{\lambda}{4}\phi_c^4 \tag{1.49}$$

specified in terms of the classical background field, $\phi_c$, defined such that the complex Higgs doublet is given by

$$\Phi = \begin{pmatrix} \phi^1 + i\phi^2 \\ \frac{\phi_c + h + i\phi^3}{\sqrt{2}} \end{pmatrix} . \tag{1.50}$$

Here, $\phi^i$ are the Goldstone bosons as before and $h$ is the Higgs field. Note that the tree level minimum is defined by the vev, $v^2 = m^2/\lambda$. Here, we shall express the masses in terms of the constant background field $\phi_c$ as

$$\begin{aligned} m_h^2(\phi_c) &= 3\lambda\phi_c^2 - m^2 \\ m_\chi^2(\phi_c) &= \lambda\phi_c^2 - m^2 \end{aligned} \tag{1.51}$$

For $\phi_c = v$, we obtain the usual expressions $m_h^2(v) = 2\lambda v^2 = 2m^2$, and $m_\chi^2(v) = 0$. Similarly, we can re-express the gauge boson and fermion masses in terms of $\phi_c$,

$$\begin{aligned} m_W^2(\phi_c) &= \frac{g^2}{4}\phi_c^2 \\ m_Z^2(\phi_c) &= \frac{g^2 + g'^2}{4}\phi_c^2 \\ m_f^2(\phi_c^2) &= \frac{y_f^2}{2}\phi_c^2 \, . \end{aligned} \tag{1.52}$$

We make this distinction between $\phi_c$ and $v$ to elucidate how temperature effects can change $\phi_c$, thus always reserving $v$ for the zero-temperature, tree-level minimum of the Higgs potential. To calculate the scale of the phase transition, we need to evaluate the one-loop effective Higgs potential in the finite temperature theory framework,

$$V_{\text{eff}}^\beta = V_0(\phi_c) + V_1^\beta(\phi_c) \tag{1.53}$$

where $V_1^\beta(\phi_c)$ includes the one-loop contributions from scalars, gauge bosons and fermions

to the tree-level Higgs potential at finite temperature. At zero-temperature, we have the following contributions from scalars, fermions and gauge bosons

$$\begin{aligned} V_1^{\text{scalar}}(\phi_c) =& \frac{1}{2}\int \frac{\mathrm{d}^4p}{(2\pi)^4}\log[p^2+m^2(\phi_c)] \\ V_1^{\text{vector}}(\phi_c) =& \tilde{g}_{gb}\frac{1}{2}\mathrm{Tr}\int \frac{\mathrm{d}^4p}{(2\pi)^4}\log[p^2+M_{gb}^2(\phi_c)] \\ V_1^{\text{fermion}}(\phi_c) =& -2\tilde{g}_f\frac{1}{2}\mathrm{Tr}\int \frac{\mathrm{d}^4p}{(2\pi)^4}\log[p^2+M_f^2(\phi_c)] \end{aligned} \tag{1.54}$$

where $M_{gb}$ and $M_f$ are the diagonal mass matrices of the gauge bosons and fermions respectively. The prefactors count the degrees of freedom of the particles in the loop, $\tilde{g}_{gb} = 3$ for gauge bosons, and $\tilde{g}_f = 1(2)$ for Weyl (Dirac) fermions. Note that these integrals need to be regularised to cancel out divergences.

We can now reformulate these integrals in the imaginary time formalism.

### Scalar Fields

Using the replacement from Eq. 1.26, we obtain for the scalar field contribution,

$$V_1^{\beta}(\phi_c) = \frac{1}{2\beta}\sum_{n=-\infty}^{\infty}\int \frac{\mathrm{d}^3p}{(2\pi)^3}\log(\omega_n^2+\omega^2)\,, \tag{1.55}$$

where $\omega_n$ are the bosonic Matsubara frequencies and we have defined $\omega^2 = \vec{p}^2 + m^2(\phi_c)$. The sum over the logarithm can be simplified to [10]

$$V_1^{\beta}(\phi_c) = \int \frac{\mathrm{d}^3p}{(2\pi)^3}\left[\frac{\omega}{2}+\frac{1}{\beta}\log\left(1-e^{-\beta\omega}\right)\right]. \tag{1.56}$$

The first term in the integral is the temperature-independent part and is exactly equal to the standard one-loop correction in zero-temperature QFT. The temperature-dependent part can be expressed in the form of a thermal bosonic function $J_B$,

$$\frac{1}{\beta}\int \frac{\mathrm{d}^3p}{(2\pi)^3}\log\left(1-e^{-\beta\omega}\right) = \frac{1}{2\pi^2\beta^4}J_B[m^2(\phi_c)\beta^2]\,, \tag{1.57}$$

with,

$$J_B[m^2\beta^2] = \int_0^{\infty}\mathrm{d}x\,x^2\log\left(1-e^{-\sqrt{x^2+\beta^2m^2}}\right). \tag{1.58}$$

$J_B$ has closed forms for both high- and low- temperature expansions which are particularly useful in analytically examining the evolution of the Higgs potential in the early universe. We

find

$$J_B\left(\frac{m^2}{T^2}\right) \underset{T\gg m}{=} -\frac{\pi^4}{45} + \frac{\pi^2}{12}\frac{m^2}{T^2} - \frac{\pi}{6}\left(\frac{m^2}{T^2}\right)^{3/2} - \frac{1}{32}\frac{m^4}{T^4}\log\frac{m^2}{a_b T^2} - 2\pi^{7/2}\sum_{l=1}^{\infty}(-1)^l\frac{\zeta(2l+1)}{(l+1)!}\Gamma\left(l+\frac{1}{2}\right)\left(\frac{m^2}{4\pi^2T^2}\right)^{l+2}, \tag{1.59}$$

$$J_B\left(\frac{m^2}{T^2}\right) \underset{T\ll m}{=} -\sum_{l=1}^{\infty}\frac{1}{l^2}\frac{m^2}{T^2}K_2\left(\frac{l\,m}{T}\right), \tag{1.60}$$

where $a_b = 16\pi^2\exp(3/2-2\gamma_E)$ ($\log a_b = 5.4076$), $\zeta$ is the Riemann $\zeta$- function and $K_2$ is the modified Bessel function of the second kind.

**Fermion fields**

Similarly, for the fermion fields we can write,

$$V_1^{\beta}(\phi_c) = -\frac{2\tilde{g}}{2\beta}\sum_{n=-\infty}^{\infty}\int\frac{\mathrm{d}^3p}{(2\pi)^3}\log(\omega_n^2+\omega^2), \tag{1.61}$$

with $\omega_n$ being the fermionic Matsubara frequencies and $\omega = \vec{p}^2 + M_f^2$. Once again, the integral splits into a temperature-independent and a temperature-dependent part,

$$V_1^{\beta}(\phi_c) = -2\tilde{g}\int\frac{\mathrm{d}^3p}{(2\pi)^3}\left[\frac{\omega}{2}+\frac{1}{\beta}\log\left(1+e^{-\beta\omega}\right)\right], \tag{1.62}$$

with the latter being expressed in the form of a thermal fermionic function $J_F$,

$$-2\tilde{g}\frac{1}{\beta}\int\frac{\mathrm{d}^3p}{(2\pi)^3}\log\left(1+e^{-\beta\omega}\right) = -2\tilde{g}\frac{1}{2\pi^2\beta^4}J_F[M_f^2(\phi_c)\beta^2], \tag{1.63}$$

$$J_F[m^2\beta^2] = \int_0^{\infty}\mathrm{d}x\,x^2\log\left(1+e^{-\sqrt{x^2+\beta^2\omega^2}}\right). \tag{1.64}$$

The high- and low- temperature expansions for $J_F$ are given by,

$$J_F\left(\frac{m^2}{T^2}\right) \underset{T\gg m}{=} \frac{7\pi^4}{360} - \frac{\pi^2}{24}\frac{m^2}{T^2} - \frac{1}{32}\frac{m^4}{T^4}\log\frac{m^2}{a_f T^2} - \frac{\pi^{7/2}}{4}\sum_{l=1}^{\infty}(-1)^l\frac{\zeta(2l+1)}{(l+1)!}(1-2^{-2l-1})\Gamma\left(l+\frac{1}{2}\right)\left(\frac{m^2}{\pi^2T^2}\right)^{l+2}, \tag{1.65}$$

$$J_F\left(\frac{m^2}{T^2}\right) \underset{T\ll m}{=} -\sum_{l=1}^{\infty}\frac{(-1)^l}{l^2}\frac{m^2}{T^2}K_2\left(\frac{l\,m}{T}\right), \tag{1.66}$$

with $a_f = \pi^2\exp(3/2-2\gamma_E)$ ($\log a_f = 2.6351$).

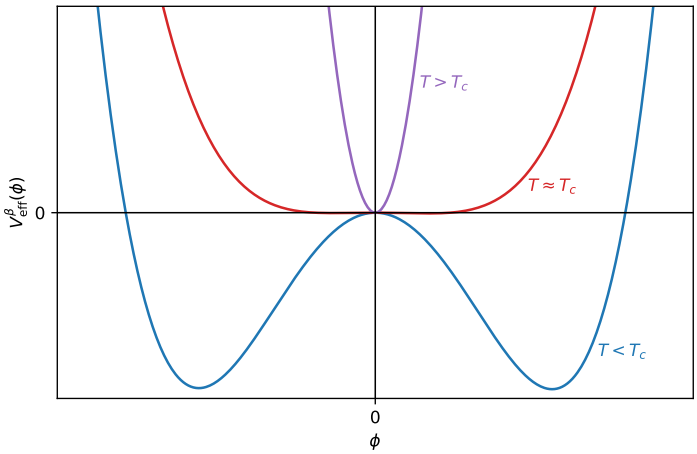


FIGURE 1.3: The one-loop effective Higgs potential as a function of temperature. The critical temperature, $T_c$, is defined as the temperature for which the zero-temperature minimum of the potential becomes unstable. For smaller temperatures, the $SU(2) \times U(1)$ symmetry is broken.

### Vector fields

Analogously, the gauge boson contribution is given by,

$$V_1^{\beta}(\phi_c) = 3\frac{1}{2}\left(\int \frac{\mathrm{d}^3 p}{(2\pi)^3}\log[p^2 + M_{gb}^2(\phi_c)] + \frac{1}{2\pi^2\beta^4}J_B[M_{gb}^2(\phi_c)\beta^2]\right). \tag{1.67}$$

### The evolution of the Higgs potential with temperature

Now that we have everything in place, we can finally study the part temperature plays in electroweak symmetry breaking. We can construct the effective one-loop Higgs potential at finite temperature using Eqs. 1.55, 1.61, 1.67 and assuming that only heavy particles contribute. The zero-temperature part can be evaluated in a given regularisation scheme. For example, in cut-off regularisation,

$$V_1(\phi_c) = \frac{1}{64\pi^2}\sum_i n_i\left(m_i^4(\phi_c)\left(\log\frac{m_i^2(\phi_c)}{m_i^2(v)} - \frac{3}{2}\right) + 2m_i^2(\phi_c)m_i^2(v)\right), \tag{1.68}$$

where the sum runs over all particle species which give a large enough contribution, i.e., particles with large zero-temperature masses or large Yukawa couplings, $i = W^{\pm}, Z, t, h$, and $n_i$ are the particle degrees of freedom, $n_W = 6, n_Z = 3, n_h = 1, n_t = -12$. In the high-temperature limit, we can approximate the temperature dependent part by the thermal bosonic and fermionic functions.[9] The total effective Higgs potential at high-temperatures can

[9]This analytic expression for the potential necessarily breaks down at zero-temperature where the high-temperature expansions are invalid. This can be quite clearly seen in the formulation of $\lambda(T)$ which has a divergence at $T = 0$.

then be simplified to

$$V^{\beta}_{\text{eff,high}-\text{T}} = D(T^2 - T_0^2)\phi_c^2 - ET\phi_c^3 + \frac{\lambda(T)}{4}\phi_c^4\,, \tag{1.69}$$

with

$$\begin{aligned} D &= \frac{2m_W^2 + m_Z^2 + 2m_t^2}{8v^2}\,, \\ E &= \frac{2m_W^3 + m_Z^3}{4\pi v^3}\,, \\ T_0^2 &= \frac{m_h^2 - 8Bv^2}{4D}\,, \\ B &= \frac{3}{64\pi^2 v^4}\left(2m_W^4 + m_Z^4 - 4m_t^4\right), \\ \lambda(T) &= \lambda - \frac{3}{16\pi^2 v^4}\left(2m_W^4 \log\frac{m_W^2}{A_B T^2} + m_Z^4 \log\frac{m_Z^2}{A_B T^2} - 4m_t^4 \log\frac{m_t^2}{A_F T^2}\right), \end{aligned} \tag{1.70}$$

where $\log A_B = \log a_b - 3/2$ and $\log A_F = \log a_f - 3/2$, with $a_F$ and $a_b$ defined as before. Note that we have removed the $\phi_c$-independent terms from the potential.

Fig. 1.3 shows this potential for different values of the temperature. What we are interested in is the equilibrium value of $\phi_c$ given by the minimum of $V^{\beta}_{\text{eff}}$. (Remember that a minimum at zero means that the $SU(2)_L \times U(1)_Y$ symmetry is unbroken.) Notably, this minimum is now a function of temperature, $\langle\phi_c(T)\rangle$ implying that even if the field has a non-zero minimum at zero-temperature, the minimum can shift to zero as the temperature is increased. Or in other words, symmetry can be restored at large temperatures. From Fig. 1.3, we can already see that for temperatures smaller than a critical temperature, the minimum at $\phi_c = 0$ becomes unstable. A quick glance at Eq. 1.68 shows that this should happen for $T \lesssim T_0 \equiv T_c$ when the prefactor of the $\phi_c^2$ term changes sign.

This symmetry breaking is exactly what happens when we look at the cosmological history. The early universe was hot and dense leading to the Higgs field having a minimum at absolute zero. During this time, all particles only had *thermal* masses, consequence of their interactions with the plasma as discussed in section 1.2.2. As the universe expanded and cooled, the temperature dropped below a certain critical temperature causing the minimum to shift to a new non-zero value and leading to a *phase transition*. The nature of the phase transition—whether it was first- or second-order (discontinuous or continuous)—is determined by the exact Lagrangian used. The SM phase transition with the current known particles and interactions is believed to be second order. We can estimate the temperature of the phase transition analytically by using the high-temperature expansion of the potential described in Eq. 1.69.

The critical points of the potential can be calculated in the standard way,

$$\begin{aligned} \frac{\partial V_{\text{eff, high}-\text{T}}(\phi_c, T)}{\partial\phi_c}\Big|_{\phi} &= 2D(T^2 - T_0^2)\phi - 3ET\phi^2 + \lambda(T)\phi^3 = 0 \\ \Rightarrow \phi &= \frac{3ET \pm \sqrt{9E^2T^2 - 8D\lambda(T)(T^2 - T_0^2)}}{2\lambda(T)}\,, \end{aligned} \tag{1.71}$$

so that we can define the critical temperature more accurately by, $T_c = T_1$, where $T_1$ is the temperature at which a local minimum appears defined by,

$$T_1^2 = \frac{8\lambda(T_1) D\, T_0^2}{8\lambda(T_1) D - 9E^2}\,. \tag{1.72}$$

This equation can be numerically solved for SM values of the parameters to obtain $T_1 \approx 163\,\mathrm{GeV}$. For $T > T_1$, the potential is symmetric and has a single minimum at $\phi = 0$. For smaller temperatures, the minimum shifts to non-zero values, approximately given by

$$\phi_c^2(T) = \frac{2D(T_0^2 - T^2)}{\lambda(T)}\,, \tag{1.73}$$

relaxing to the one specified by the vev as $T \to 0$. Note that in this expression we have assumed $\lambda(T)$ to be approximately constant. This analytic formulation of the temperature-dependent vev is therefore not valid as $T \to 0$. Additionally, there are some subtleties regarding this calculation which we have skipped over. The presence of the cubic term implies that this transition will be first order. This means that at $T = T_1$, a potential barrier develops between the local minimum and the minimum at the origin. $T_0$ then is the temperature at which this barrier disappears. In the SM model, the value of $E$, which determines the strength of the cubic term, is negligible as a result of higher order corrections which we have ignored. What this means in practice is that to a very good approximation $T_0 \approx T_1 \equiv T_{\mathrm{EW}}$.

The temperature dependence of the vev implies that the Higgs mass and indeed all other particle masses after the phase transition are also functions of temperature. Before the phase transition, the complex Higgs has a thermal mass given by

$$m_H^2(T) = \left.\frac{\mathrm{d}^2 V_{\mathrm{eff,\,high-T}}}{\mathrm{d}\phi_c^2}\right|_{\phi_c=0} = 2D(T^2 - T_0^2)\,. \tag{1.74}$$

As we move toward smaller temperatures, the high-temperature expansion used to arrive at Eq. 1.69, begins to break down. Nevertheless, we can approximate the Higgs mass in terms of the temperature-dependent vev from Eq. 1.73,

$$m_h^2(T) \approx 2\lambda(T)\phi_c^2(T) = 4D(T_0^2 - T^2)\,. \tag{1.75}$$

A more accurate result for the temperature-dependent Higgs mass and vev at low temperatures can be obtained by numerically minimising the full effective potential and not just the high-temperature expansion. We compare the numerical results with the analytic formulas discussed above in Fig. 1.4. As expected, the two show a remarkable agreement at large temperatures but differ considerably as $T \to 0$.

The SM particle masses also pick up a temperature dependence after the phase transition from the Higgs vev (given by the formulas in Eq. 1.52). This temperature dependence is independent of the thermal fermion masses that arise as a result of particle interactions in

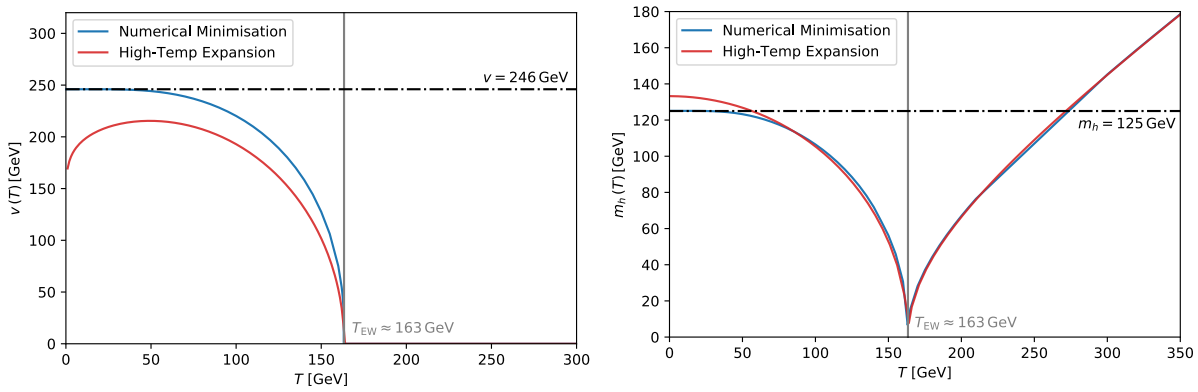


FIGURE 1.4: The evolution of the Higgs vev (left) and the Higgs mass (right) as a function of temperature. The red line corresponds to the analytic approximation as discussed in the text, and the blue line results from a numerical implementation of the effective Higgs potential.

the plasma. For sufficiently large Yukawa couplings, the Higgs-induced masses generally dominate over the thermal mass correction at low temperatures.

### A Note On Divergences

In this section, we have ignored completely the question of possible ultraviolet (UV) or infrared (IR) divergences in FQFT. It turns out that temperature does not introduce any new UV divergences in our theory. This can be seen, for instance, in the temperature dependent part of the mass correction in Eq. 1.31 which is well behaved as $T \to \infty\,(\beta \to 0)$. The UV divergences present at zero-temperature, of course, have to be regularised in the usual manner. IR divergences in FQFT, on the other hand, get significantly worse. These are related to the appearance of the so called ring or daisy diagrams that, in order to regulate the divergences, need to be resummed to all orders. In fact, these diagrams are exactly the reason the cubic term in the effective potential vanishes, leading to a smooth transition. A proper calculation of the phase transition, therefore, involves additional technicalities which we have skipped over. In particular, not accounting for these effects is why the Higgs mass in our prescription has a value of around $m_h \approx 10\,\text{GeV}$ at the critical temperature instead of zero (see Fig. 1.4). These details, although interesting, are irrelevant for the kinds of calculations we will be doing in this thesis.

With a handle on the temperature evolution at very small scales, i.e., a formulation of finite temperature quantum field theory, we now turn our attention to significantly larger scales and see how the universe collectively evolved throughout its history.

## 1.3 Particle Cosmology in a Nutshell

Organising the universe in a form that is not stupendously overwhelming appears to be a daunting task and yet, over centuries and with the help of many, oft-unrecognised, scientists,

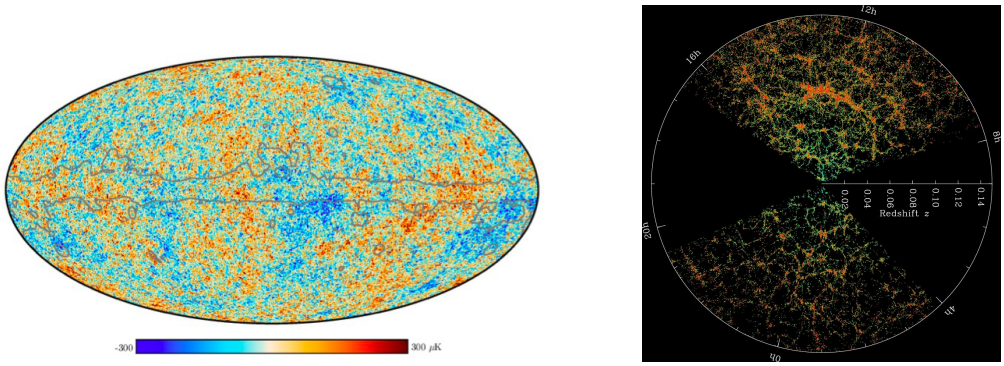


FIGURE 1.5: Left: CMB anisotropies as measured by Planck [25]. The temperature fluctuations across the field of view are of the order of $10^{-5}$ K. Right: Galaxy survey by Sloan Digital Sky Survey. Each dot is a galaxy and the colour bar shows the local density. Image from www.sdss.org.

we have arrived at the Standard Model of Cosmology. Commonly called ΛCDM —denoting the two currently unknown but most abundant components of the universe: dark energy (Λ) and cold dark matter (CDM)— it manages to describe all of our observations with a handful of parameters.

The foundational principle behind ΛCDM is the Cosmological Principle which states that the universe at sufficiently large scales should be homogenous and isotropic. This is well-supported by evidence, for example by the minuteness of temperature fluctuations in the Cosmic Microwave Background (CMB), and by the uniformity of structure as captured by galaxy surveys (Fig. 1.5). It is, of course, important to note that inhomogeneities and anisotropies exist at small scales, for instance galaxy clusters are very different from cosmic voids. In fact these small perturbations amidst a homogenous background turn out to be exceptional tests for both ΛCDM as well as any proposed additions to it. They are particularly useful in studies of non-cold dark matter models as we shall discuss in Chapter 2. For the moment, however, we will only consider the homogenous background in order to flesh out the mathematical framework we would require later.

As opposed to its spatial homogeneity, we know for a fact that the universe is evolving in time. We have already made a passing reference to the evolution of the universe as a function of its temperature. Additionally, we know that spacetime itself is constantly expanding— the farther out we look into space, the faster the galaxies appear to be moving away from us. We also know that this expansion has been happening throughout the history of the universe and therefore the equations which govern the universe must account for it. The expanding universe, as formulated by using general relativity, can be best described by defining *comoving* coordinates in a Friedmann-Lemaitre-Robertson-Walker (FLRW) metric

$$ds^2 = -c^2dt^2 + a(t)^2(dx^2 + dy^2 + dz^2) \tag{1.76}$$

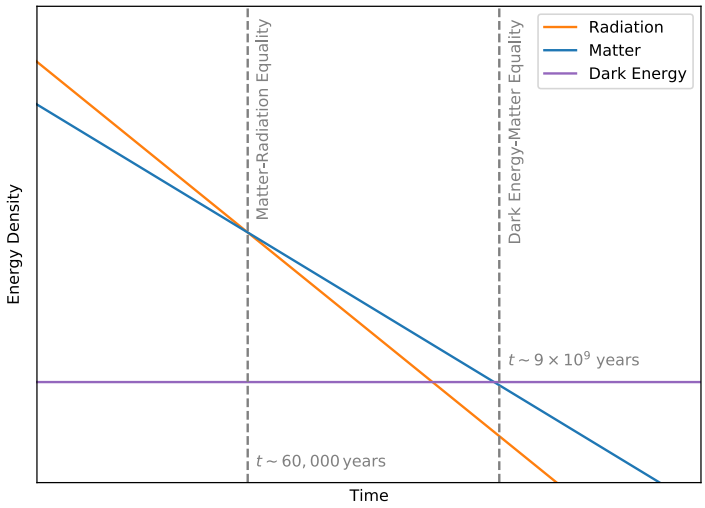


FIGURE 1.6: The dilution of radiation, matter and dark energy density as a function of time.

where $a$ is a time-dependent scale factor encapsulating the expansion of the universe. In this metric, Einstein's equationa

$$G_{\mu\nu} = 8\pi G T_{\mu\nu} - \Lambda g_{\mu\nu} \tag{1.77}$$

relate the properties of spacetime (encoded in Einstein's tensor $G_{\mu\nu}$) to the properties of matter (given by the stress-energy tensor $T_{\mu\nu}$). $G$ is the universal gravitational constant and the second term on the right represents the contribution of the cosmological constant $\Lambda$ with $g_{\mu\nu}$ being the Minkowski metric. Under the assumptions of homogeneity and isotropy, one can then derive the Friedmann relation [26], quantifying the expansion rate of the universe

$$H^2(t) \equiv \left(\frac{\dot{a}}{a}\right)^2 = \frac{8\pi G}{3}(\rho_{\rm R} + \rho_{\rm M}) - \frac{k}{a^2} + \frac{\Lambda}{3}\,, \tag{1.78}$$

in terms of the radiation and matter energy densities $\rho_{\rm R}$ and $\rho_{\rm M}$, the comoving spatial curvature $k$ and the cosmological constant $\Lambda$. All of the terms on the right of Eq. 1.78 (except the last) depend either implicitly or explicitly on the scale factor $a$; the implicit dependence in the first term can be obtained by considering energy conservation in an expanding universe, which gives $\rho_{\rm R} \propto a^{-4}$ and $\rho_{\rm M} \propto a^{-3}$.

In essence, the Friedmann equation tells us that the rate of expansion of the universe changes depending on which of these terms dominate. Using the scaling relations, we can already sketch out the contribution of radiation, matter and dark energy to the total energy density of the universe as a function of time, or equivalently the scale factor $a$, where $a \to 0$ denotes the earliest timescales at which our theories work. We plot the evolution of these energy densities in Fig. 1.6. This is an important puzzle piece in studying the thermal history of the universe, since the rate of expansion, which is related to which terms dominate in Eq. 1.78, is closely tied with the efficiency of interaction rates in the early universe.

From Fig. 1.6, we see that the universe was dominated by radiation for the first several tens of thousand years. During this time we can ignore the contribution from the matter and dark energy densities. Additionally, our universe has been observed to be spatially flat. Therefore, we can write the Hubble rate at these early times as,

$$H^2 \approx \frac{8\pi G}{3}\rho_{\rm R}\,. \tag{1.79}$$

In the following section, we will discuss the analytic form of $\rho_{\rm R}$ and thereby arrive at a simple analytic formula for $H$.

The Friedmann equation allows us to deduce the scale factor $a(t)$ (or the Hubble parameter $H$) at any time once we have measured $\rho_{\rm R}$, $\rho_{\rm M}$, $\Lambda$ and $H$ today. The observed spatial flatness of our universe defines a *critical density* given by

$$\rho_c(t) = \frac{3H^2(t)}{8\pi G}\,, \tag{1.80}$$

which allows us to define a density parameter, $\Omega \equiv \rho/\rho_c$. The Friedmann equation can then be reformulated in terms of the present day energy densities as

$$\frac{H^2(t)}{H_0^2} = \Omega_{0,\,\rm R}a^{-4} + \Omega_{0,\,\rm M}a^{-3} + \Omega_{0,\,\rm k}a^{-2} + \Omega_{0,\,\Lambda}\,, \tag{1.81}$$

where $H_0$ and $\Omega_{0,\,i}$ correspond to present-day values of the Hubble parameter and densities respectively.

### 1.3.1 Phase Space Distributions in Equilibrium

The earliest timescales that we can currently formulate (without a theory of quantum gravity) correspond to a regime in which the universe was extremely hot and dense. This means that the universe can be studied as a thermodynamic system in (or near) equilibrium characterised by a temperature $T$. The expansion of the universe leads to a subsequent drop in this temperature, resulting in various non-equilibrium phenomena that are crucial in explaining the structure of the universe we see today.

To understand the evolution of the universe, from a hot and dense plasma to the formation of light elements and beyond, we need to track how various particle densities evolve in time and how reactions between particles which deplete or enhance their densities proceed. Essentially, we need to compare the rate of these reactions, $\Gamma$, with the expansion rate of the universe, $H$, to determine when and for how long these reactions are efficient. Generally, if $\Gamma \gg H$, the timescale of the given process, $t = 1/\Gamma$, is much smaller than the characteristic timescale of expansion $1/H$, making these processes efficient and in equilibrium. On the other hand, if $\Gamma \ll H$, the universe expands much faster causing the particles to *decouple*.

Calculations of interaction rates are central to particle cosmology. The first step in any such calculation is to define a phase-space distribution function for the particle under study, $f_\chi(t,\,p)$

which is a function only of the absolute value of the particle momentum $p$ and time, $t$.[10] From the phase-space distribution we can calculate the particle number and energy densities as functions of time

$$n_\chi(t) = g_\chi \int \frac{\mathrm{d}^3 p}{(2\pi)^3} f_\chi(t,\, p) \tag{1.82}$$

$$\rho_\chi(t) = g_\chi \int \frac{\mathrm{d}^3 p}{(2\pi)^3} E_\chi f_\chi(t,\, p)\,, \tag{1.83}$$

where $g_\chi$ represents the internal (spin) degrees of freedom of $\chi$. The exact form of $f_\chi$ depends on the system under study. For particles in thermal equilibrium with a given temperature $T$, as is the case for the SM in the early universe, $f_\chi$ is known from statistical mechanics to have the form

$$f_\chi = \frac{1}{e^{\frac{E-\mu}{T}} \pm 1} \tag{1.84}$$

where $E = \sqrt{p^2 + m_\chi^2}$ is the energy of the particle, $\mu$ is the chemical potential, and the $+$ $(-)$ sign is for fermions (bosons). Note that in this formulation the time dependence is encoded in the temperature variable, $T$. Assuming $\mu = 0$, we can solve the integrals in Eqs. 1.82 and 1.83 in the relativistic ($T \gg m_\chi$) and non-relativistic ($T \ll m_\chi$) limits.

For $T \gg m_\chi$:

$$n_\chi = \frac{\zeta(3)}{\pi^2} g_\chi T^3 \times \left(\frac{3}{4}\right) \quad (\text{for fermions})\,, \tag{1.85}$$

$$\rho_\chi = \frac{\pi^2}{30} g_\chi T^4 \times \left(\frac{7}{8}\right)\,, \tag{1.86}$$

where $\zeta$ is the Riemann-zeta function. Conversely, for $T \ll m_\chi$:

$$n_\chi = g_\chi \left(\frac{m_\chi T}{2\pi}\right)^{3/2} e^{-m_\chi/T}\,, \tag{1.87}$$

$$\rho_\chi = m_\chi n_\chi\,. \tag{1.88}$$

Using the relativistic equation for energy density and Eq. 1.79, we can now write down a simple expression for the Hubble expansion during radiation domination,

$$H \approx 1.66 \sqrt{g_*^\rho}\, \frac{T^2}{M_{\mathrm{Pl}}}\,, \tag{1.89}$$

where $M_{\mathrm{Pl}} = 1.22 \times 10^{19}$ is the Planck mass (related to the gravitational constant by $M_{\mathrm{Pl}} = 1/\sqrt{G}$) and $g_*^\rho$ represents the effective relativistic degrees of freedom contributing to the radiation energy density.

[10] This dependence can be deduced from the Cosmological Principle. Homogeneity implies that $f_\chi$ should be the same everywhere and therefore independent of $x$. Isotropy implies that $f_\chi$ should be the same in every direction and therefore only dependent on the modulus of the momentum and not on its direction.

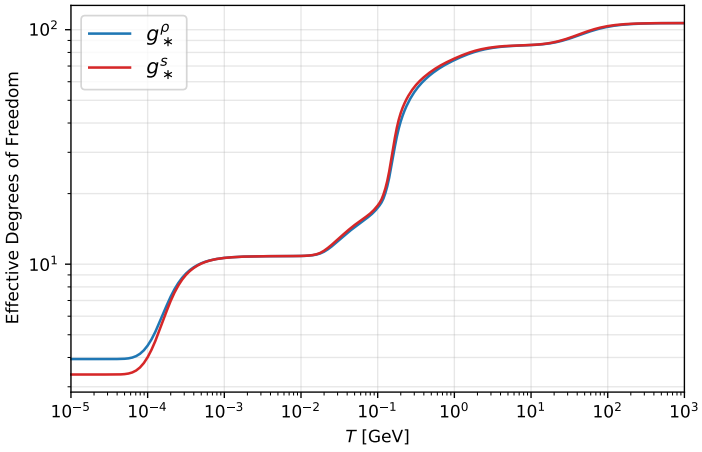


FIGURE 1.7: The effective energetic and entropic degrees of freedom in the SM as functions of temperature.

When discussing particle cosmology, another quantity of interest is the total entropy density given by

$$s = \frac{\rho + P}{T}, \tag{1.90}$$

where $\rho$ and $P$ are the total energy density and pressure of the species in the thermal bath. During radiation domination, $P = \rho/3$ and the entropy density has the simple form,

$$s = \frac{2\pi^2}{45} g_*^s T^3 \,, \tag{1.91}$$

where $g_*^s$ are effective number of relativistic degrees of freedom contributing to the entropy. The importance of this parameter lies in the fact that the total entropy density in a comoving volume remains conserved (as opposed to the *number density*). This conservation implies that $g_*^s T^3 a^3 =$ constant. Therefore, as long as $g_*^s$ is constant, the temperature scales as $T \propto a^{-1}$. However, if $g_*^s$ changes (for example, if one or many particles become non-relativistic), the temperature instead varies as $T \propto (g_*^s)^{-1/3} a^{-1}$.

It is important to note that the entropic and energetic degrees of freedom, $g_*^s$ and $g_*^\rho$, are not necessarily equal. In particular, if any of the particle species have a temperature $T_\chi$ different from the temperature of the background thermal bath $T$, we have

$$g_*^s = \sum_{\text{rel. bosons}} g_\chi \left(\frac{T_\chi}{T}\right)^3 + \frac{7}{8} \sum_{\text{rel. fermions}} g_\chi \left(\frac{T_\chi}{T}\right)^3 , \tag{1.92}$$

$$g_*^\rho = \sum_{\text{rel. bosons}} g_\chi \left(\frac{T_\chi}{T}\right)^4 + \frac{7}{8} \sum_{\text{rel. fermions}} g_\chi \left(\frac{T_\chi}{T}\right)^4 . \tag{1.93}$$

This difference in the evolution of $g_*^{s,\,\rho}$ in the SM is plotted in Fig. 1.7. The various features in

the plot correspond to particles becoming non-relativistic. Although the two degrees of freedom follow each closely, differences arise at smaller temperatures when heavier particles begin to decouple from the thermal bath. We will qualitatively investigate this decoupling in the following section.

### 1.3.2 Quantifying Interaction Rates

As mentioned previously, we are interested in the interaction rate $\Gamma \sim n\sigma v$, where $n$ is the number density of the particle, $\sigma$ is its interaction cross-section and $v$ its average velocity. At sufficiently large temperatures, $T > \mathrm{O}(100\,\mathrm{GeV})$, all particles are ultra-relativistic, meaning that $v \sim 1$ and the number density scales as $T^3$ (from Eq. 1.85). Consider a simple $2 \to 2$ interaction mediated by a massless gauge boson. The cross-section of this process can be written as $\sigma \sim \alpha^2/T^2$ where $\alpha = \lambda^2/4\pi$ is the gauge coupling squared. The interaction rate is then

$$\Gamma \sim \alpha^2 T\,. \tag{1.94}$$

At these early times, the universe would still be dominated by radiation and therefore, from Eq. 1.89, $H \sim T^2/M_{\mathrm{Pl}}^2$. Comparing the interaction rate with the Hubble rate we get

$$\frac{\Gamma}{H} \sim \frac{\alpha^2 M_{\mathrm{Pl}}}{T} \sim \frac{10^{16}\,\mathrm{GeV}}{T}\,, \tag{1.95}$$

assuming a typical weak-scale value for the coupling, $\alpha \sim 0.01$. It is clear from this equation that SM particles, which have order one couplings, remain in equilibrium for $T \sim 100 - 10^{16}$ GeV.

Additionally, we can redo the calculation at a smaller temperature to illustrate when particles decouple. After the Electroweak Phase Transition, weak interactions are mediated by massive gauge bosons, $W^{\pm}$ and $Z$. The interaction can be approximated by a four-point interaction such that the cross-section is given by $\sigma \sim G_F^2 T^2$, where $G_F = \alpha/m_W^2$ is Fermi's constant and the $1/m_W$ comes from the low-momentum limit of the propagator. Once again comparing the interaction with Hubble[11], we get

$$\frac{\Gamma}{H} \sim \frac{\alpha^2 M_{\mathrm{Pl}} T^3}{m_W^2} \sim \left(\frac{T}{1\,\mathrm{MeV}}\right)^3\,. \tag{1.96}$$

This ratio drops below 1 at temperatures of around 1 MeV, indicating that particles interacting via the weak force decouple from the thermal bath at this temperature. After decoupling, the number density of the particles "freezes-out". If the particles are stable, this number then gives the cosmological relic abundance of particles today.

In this section, we have only approximated interaction rates and decoupling temperatures. A more rigorous treatment is needed in order to determine relic abundances accurately. This

[11] Note that the universe is still dominated by radiation and therefore the expression for $H$ remains the same.

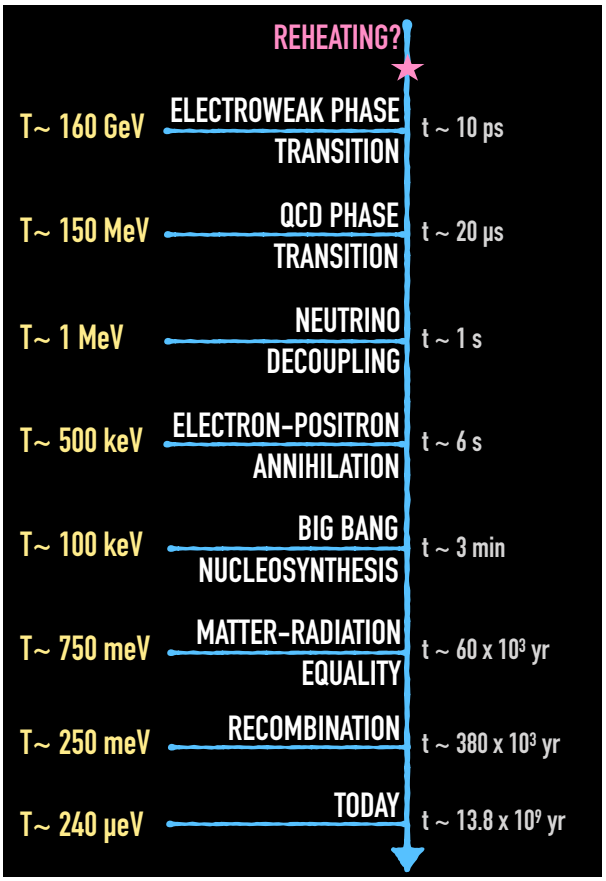


FIGURE 1.8: An outline of the major epochs in our universe's cosmological history.

is done by solving a Boltzmann Equation, which determines the rate of change of a given phase-space distribution by accounting for all possible interactions causing the change. We will elaborate on the Boltzmann Equation in Chapter 2 in the context of dark matter.

## 1.4 From The Earliest Times Until Today

We are finally ready to present a brief account of the thermal history of the universe. Fig. 1.8 summarises the various events along with the relevant times and temperatures. An asterisk (*) after the name represents hypothesised events, the exact natures of which are yet to be worked out. A dagger (†), on the other hand, indicates events expected to have occurred based on the current understanding of the SM but which have not yet been experimentally confirmed.

- **Inflation*:**
  The inflationary paradigm was hypothesised to provide an explanation for the apparent fine-tuning of the initial conditions of our universe. Qualitatively, it sought to explain why causally disconnected regions in space are homogenous (the *Horizon Problem*) and why the universe is flat (the *Flatness Problem*), by postulating a period of exponential

expansion in the very early universe. This expansion could be triggered by a scalar field which dominated the energy density of the universe at the time undergoing a phase transition. Once inflation ends, the energy density of this field gets transferred to the particles of the SM in a process called *reheating*. The interactions between the particles then thermalise the SM with a given temperature known as the *reheating* temperature, $T_{\rm RH}$. From our current understanding of cosmology, the value of the reheating temperature can be anywhere between $\sim 10^{16}\,\mathrm{GeV}$ to $\sim O(\mathrm{MeV})$, where the upper bound comes from inflationary models and the lower bound from the requirement of formation of light elements (nucleosynthesis) [27].
Technically, Inflation precedes the "Hot Big Bang era": a term colloquially used to describe the universe once the SM has thermalised. We mention it as part of the thermal history only for completeness and to introduce the idea of reheating temperature, which will be useful in the discussion of dark matter models in the following chapters.

- **Baryogenesis*:**
  Mechanisms of Baryogenesis aim to address the matter-antimatter asymmetry of the universe. If baryons and anti-baryons were equally abundant in the primordial thermal bath, efficient annihilations would result in our current universe being entirely populated by radiation. Instead we see an abundance of baryons. Viable models of Baryogenesis postulate that this asymmetry was likely generated before the electroweak phase transition but none have currently been experimentally confirmed [28, 29].

- **Electroweak Phase Transition†:**
  As discussed in Sec. 1.2.3, a phase transition happens in the SM at a temperature of around $160\,\mathrm{GeV}$ from the breaking of the $SU(2) \times U(1)$ symmetry, resulting in various particles becoming massive.

- **QCD Phase Transition†:**
  A second phase transition happens in the SM at $T \lesssim 150\,\mathrm{GeV}$ when quarks and gluons confine to hadrons, as mentioned in Sec. 1.1.1

- **Neutrino Decoupling:**
  As the temperature drops further, interactions in the SM begin to lose efficiency. Neutrinos only interact with other particles in the SM via the weak interactions and therefore they are the first SM particles to decouple at $T \sim 1\,\mathrm{MeV}$, following the calculation presented in Sec. 1.3.1. Once the neutrinos leave thermal equilibrium, their distribution remains "frozen" and their temperature scales simply with the scale factor, $T_\nu \propto a^{-1}$.

- **Electron-Positron Annihilation:**
  Shortly after neutrinos decouple, the temperature drops below the electron/positron mass, $m_e \sim 0.5\,\mathrm{MeV}$. This implies that while electrons and positrons can annihilate efficiently into photons, the inverse process, i.e., creation of electron-positron pairs, $\gamma\gamma \to e^+e^-$ is less likely. As a result, the number density of electrons and positrons decreases until nearly all positrons vanish and a small fraction of electrons remain to maintain electric neutrality of the plasma. Additionally, the photon temperature, or

equivalently, the temperature of the thermal bath, rises slightly because of this energy injection. The total radiation density at this point is given by the density of photons and neutrinos and can be written using Eq. 1.86 as:

$$\rho_{\rm R} = \frac{\pi^2}{30} g_\gamma T_\gamma^4 + \frac{\pi^2}{30} g_\nu \frac{7}{8} T_\nu^4 \tag{1.97}$$

$$= \frac{\pi^2}{30} \left( 2 + \frac{7}{4} N_{\rm eff} \left( \frac{4}{11} \right)^{4/3} \right) T_\gamma^4 \,, \tag{1.98}$$

where we have used entropy conservation[12] to evaluate $T_\nu/T_\gamma$. $N_{\rm eff}$ is the effective number of neutrino species in the universe and is sensitive to the presence of any additional relativistic particles in the thermal bath. Current measurements from Planck [25] places a bound on $N_{\rm eff} = 3.00^{+0.57}_{-0.53}$ highly compatible with the theory prediction of $N_{\rm eff} = 3.044$ [30].[13] We will discuss how $N_{\rm eff}$ can be used as a probe of DM in Chapter 2.

- **Big Bang Nucleosynthesis (BBN):**
  Roughly 3 minutes after the end of inflation, protons and neutrons began to combine resulting in the formation of nuclei of light elements such as hydrogen, helium, lithium and their isotopes. Heavier elements were formed later in stellar cores. Measurements of the abundances of these light elements provide a very precise way to test both ΛCDM and the SM of particle physics since the formation of these elements is sensitive to particle properties such as the proton mass and weak coupling as well as to the expansion rate of the universe. Through BBN, we can access the universe at the earliest timescales thus making it a useful tool also in the context of beyond-the-standard-model (BSM) studies. We discuss this briefly in the context of dark matter in Chapter 2.

- **Recombination:**
  After nucleosynthesis, the thermal plasma contains photons, non-relativistic electrons, hydrogen nuclei, and helium nuclei. Electromagnetic interactions keep all of these particle species in equilibrium. Additionally, there are interactions to produce as well as ionise hydrogen of the form $ep \leftrightarrow H\gamma$. As the temperature drops, the photons lose energy and cannot efficiently ionise Hydrogen, resulting in a net production of neutral Hydrogen atoms.

- **Photon Decoupling:**
  As long as free electrons are present in the plasma, Thomson scattering $e^-\gamma \to e^-\gamma$ is efficient enough to thermalise the photons. After recombination, the number density of electrons drops causing the photons to decouple and freestream. These photons are observed today as the CMB and provide a snapshot of the universe 380,000 years after the end of inflation. The CMB is also sensitive to new physics and is therefore very useful to constrain the same. Further discussion is provided in Chapter 2.

[12] The total entropy in a comoving volume, i.e., the number of possible states, remains conserved.
[13] The SM has three neutrino species which would give $N_{\rm eff} = 3$. However, neutrino decoupling is not instantaneous and $T_\nu$ receives some contribution from $e^+e^-$ annihilation thus altering $N_{\rm eff}$ slightly.

- **Reionization:**
  After photons decouple, the universe remains relatively dark and undisturbed until the first stars begin to form. These emit photons which partially reionize hydrogen. However, this reionization is not enough to re-establish thermal equilibrium and only a fraction of the CMB photons scatter off the newly freed electrons. Nevertheless, reionisation marks the end of the "Dark Ages" of the universe with the lighting of the first stars.

- **Today:**
  And so we end up today, with a universe that is mostly empty, mostly dark, but with enough mystery to have kept us hooked for centuries. Our Standard Models for both particle physics and cosmology have worked out excellently so far, but there are still many details to be worked out. In particular, the "dark components" of $\Lambda$CDM –dark matter and dark energy– are relatively unknown. We will now turn our attention toward dark matter and see how it has managed to dramatically affect the cosmology of our universe while simultaneously remaining frustratingly elusive.

# Chapter 2

# Whispers from the Dark: Hidden Sectors In The Early Universe

For the last several pages, we have been alluding to the presence of non-baryonic or dark matter (DM). The aim of this chapter is to describe the evolution of DM in detail, in particular to discuss production mechanisms that saturate the DM abundance we see in the universe. We begin in section 2.1 with a brief, somewhat historical, review of the evidences of DM gleaned from cosmology and astrophysics along with a discussion of properties DM particles should have. Next, in section 2.2 we discuss the production of DM in the early universe in two limits: when DM is in thermal equilibrium with the SM heat bath and when it is not. Finally, we close this chapter by detailing how BBN and CMB probe DM cosmology and what they say about the microphysics of DM (section 2.3).

## 2.1 Evidence and Properties of Dark Matter

Discussions on DM, which now span several timescales as well as length-scales, arose initially as a result of curious anomalies that popped up in studies of astrophysical systems. In 1933, Fritz Zwicky noted that the velocity dispersion of stars in the Coma Cluster was much higher than what one would expect from its observed mass [31]. To ensure the stability of the system despite the large velocities of its constituents, its mass would have to be much larger than the observed mass. Similar discrepancies were noted in other clusters [32] and so the problem of the "missing mass" gained traction.

Many decades later, Vera Rubin and Kent Ford published what became the most striking evidence for "hidden mass" [33]. They looked at rotation curves for spiral galaxies, i.e., the variation of stars' orbital velocities with their distance from the centre. From standard Newtonian gravity, the orbital velocity of a star is inversely proportional to its distance from the centre,

$$v_c(r) = \sqrt{\frac{G\,M}{r}}\,.$$

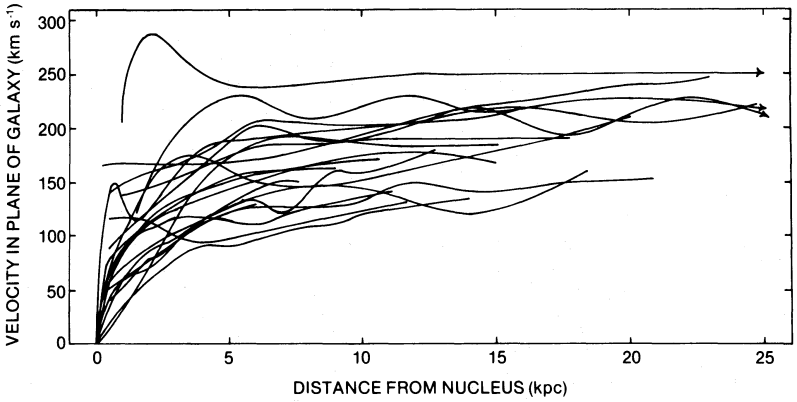


FIGURE 2.1: Galactic rotation curves as measured by V.C Rubin and K. Ford. The curves flatten out at large distances instead of decreasing as would be expected. Image taken from [33].

Here, $M$ is the enclosed mass of the system and $G$ is the gravitational constant. For distances larger than the size of the galactic disk (where the visible mass is concentrated) $M$ should be constant and so $v_c \propto r^{-1/2}$. Instead, Rubin and Ford found that the velocities of stars in the outer regions of spiral galaxies saturate to a constant value hinting at the presence of some invisible mass which extends far beyond the galactic disk (Fig. 2.1).

Owing to these observations it soon became evident that there must exist a different kind of matter, one which was weakly interacting and massive. It began to be known as Dark Matter and although, invisible matter would have been a more accurate description, the name stuck.[1] Through the years, the evidence favouring the existence of this mysterious matter has only grown.

In 1964, Arno Penzias and Robert Woodrow Wilson made the first observation of the CMB [35]. As mentioned in Chapter 1, the CMB is relic radiation from the Big Bang and therefore provides a snapshot of the universe 380,000 years ago. The power spectrum extracted from the CMB map (shown in Fig. 2.2) depicts the fluctuation in the CMB temperature at different angular scales in the sky. Its (very specific) shape is the result of oscillations in the hot gas of the early universe. These oscillations depend on the *total* matter to radiation ratio: radiation pushes the baryonic matter out of gravitational potential wells whereas gravity (or equivalently concentration of mass) pulls it back in. Since the amount of radiation is fixed in the Standard Model, the amplitudes and frequencies of these oscillations are highly sensitive to the matter content and so the dark matter density of the universe [36]. In fact, analysis of the CMB is what quantified the missing mass of the universe to be around eighty percent, $\Omega_{\rm DM}h^2 = 0.1200 \pm 0.0012$ [5].

Another piece of evidence demonstrating the weakly interacting nature of dark matter comes from colliding galaxy clusters. The most notable of these is the Bullet Cluster collision, a high-energy collision which took place some hundred million years ago and is now touted

[1] Although Zwicky is frequently credited with coining the term Dark Matter (or *Dunkle Materie* in German), "dark" or invisible objects had frequently been invoked in the preceding century, under the label of Dark Matter, to explain anomalies in motions of planets and stars. See [34] for a short review.

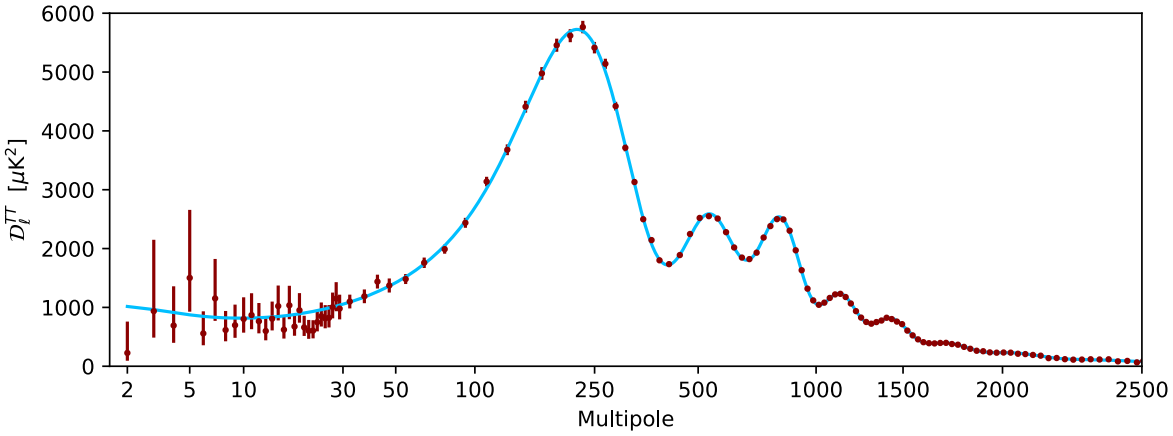


FIGURE 2.2: Planck CMB power spectra. Image taken from [5].

as a smoking gun signature of dark matter, not least because of its unusual shape (Fig. 2.3). Cluster collisions are a fascinating place to look for hidden or dark matter because different components of a cluster behave differently during a collision. The galaxies themselves pass through unhindered since they occupy a tiny volume compared to the total volume of the cluster. On the other hand, the particles present in the hot galactic plasma (which make most of the baryonic matter of a cluster) smash and ricochet and therefore, radiate a lot of energy in the form of X-rays. It is then possible to create a mass-profile of the clusters from this radiated energy. It is also possible to create a second mass-profile by using gravitational lensing: studying how the light from background objects is distorted because of the clusters' masses [37]. If the matter content of the clusters were to be purely baryonic (or visible), these two profiles would overlap. What is found instead, is that they are in exact opposition [38].

In Fig. 2.3, the pink regions represent the concentration of the baryonic mass. The blue regions denote the concentration of the total mass. The zero-overlap between the two implies the presence of a non-baryonic, invisible, non-interacting source of mass; non-interacting matter would pass right through during the collision while the baryonic mass interacts and gets tangled up at the centre of the collision. Moreover, a study of the Bullet Cluster purports that since the total mass of the two colliding clusters is concentrated at the edges of the collision, *most* of its mass is non-baryonic or dark. The separation between the clumps of non-baryonic mass of the two clusters further goes on to show that dark matter does not interact too strongly with itself either. If particles in the dark sector were to be strongly interacting, they would be caught up in the middle much like the baryons.[2]

Yet another source of evidence for dark matter is structure formation. The idea behind structure formation is simple. Small fluctuations in the early universe result in regions of under- and over-densities. As the universe expands, these fluctuations also grow on account of gravity and result in clumping of matter which eventually forms stars, galaxies, galaxy clusters, etc. However, the early universe is radiation dominated, as discussed in chapter 1, and radiation exerts pressure which tends to homogenise or wash out these fluctuations. In the

[2]We will return to the question of DM self-interactions in Chapter 6.

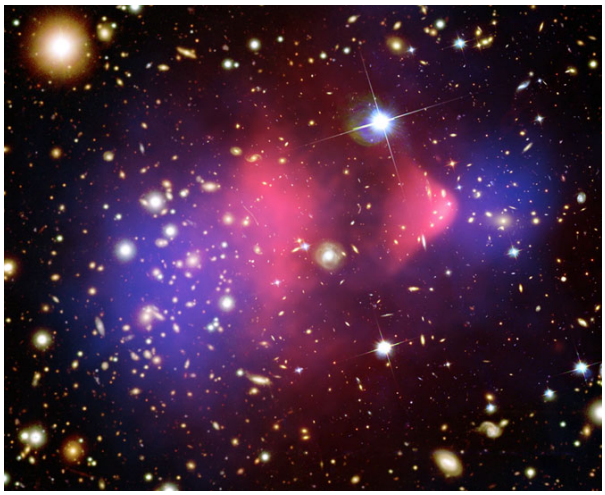

FIGURE 2.3: Bullet Cluster: X-ray image (pink) superimposed over the mass distribution calculated by gravitational lensing (blue). Image taken from chandra.harvard.edu

absence of something like dark matter which doesn't interact with radiation, structure formation would be highly suppressed. Moreover, structure formation also constrains the velocity or kinetic energy of dark matter. Relativistic dark matter would also wash out fluctuations and cause the suppression of structure [39]. And so, to explain the present-day structure of the universe, invoking *cold*, dark matter is necessary.

To summarise, observational evidence implies the following DM properties:

1. By definition, it is stable and electrically neutral. If it does have a charge this would be significantly smaller than the charge of an electron.
2. It is non-baryonic with a relic abundance given by $\Omega_{\rm DM}h^2 = 0.12$.
3. It is dissipationless and collisionless (meaning it does not lose energy through radiation or collisions) as well as cold (non-relativistic).

Additionally, assuming that DM is composed of particles,[3] it is possible to obtain bounds on its mass [42]. One of the best known lower bounds comes from phase-space considerations of DM particles confined to a halo. Known as the Tremaine-Gunn bound, it quantifies the extent to which fermionic DM particles can be compressed into a halo (based on the Pauli Exclusion Principle) and results in $m_{\rm DM} \geq 0.27^{+0.30}_{-0.14}$ keV at $95\%$ CL [43, 44]. A weaker lower bound on bosonic DM can be obtained from the observed structure of the universe. If the DM is extremely light, its de Broglie wavelength would be large enough to impact structure formation. This results in $m_{\rm DM} \gtrsim 10^{-21}$ eV [45, 46]. On the other end of the spectrum, DM is only essentially limited by the Planck scale with $m_{\rm DM} \leq M_{\rm Pl}$ [47].

[3] Of course, dark matter does not *have* to be a particle. Theories exist which attribute the evidence of dark matter to manifestations of gravity [40] or non-particle objects such as primordial black holes [41]. But particle physics models of dark matter remain the favoured explanation.

The fact that the DM mass can vary over such staggering orders of magnitude coupled with the the lack of other constraints means that a whole host of models can act as viable DM candidates. Furthermore, given the diversity of particles in the visible sector, it is not unreasonable to assume that DM is also organised in a complicated dark sector. All of this results in an expansive DM model space with DM models having different particle phenomenologies even though their macroscopic behaviour remains degenerate. The benefit, of course, is that we can talk about DM cosmology in a somewhat model-independent fashion. In the rest of this chapter, we will do exactly this and discuss the evolution of the dark sector based on some simplifying assumptions, followed with the effects of DM on cosmological probes.

## 2.2 Production Mechanisms of Dark Matter

The Planck data postulates the relic abundance of DM to be $\Omega_{\rm DM}h^2 = 0.12$ [5]. The question then is how does one devise a production mechanism for DM which explains this abundance. From the last chapter, we know that the way certain particles in the SM, such as the neutrinos, get their present-day abundance is by freeze-out, i.e., annihilations in equilibrium compete with the expansion rate of the universe until they become inefficient.[4] If DM were to be a part of the SM heat bath, or a thermal relic, it would undergo a similar evolution. However, it is quite possible that the interactions between the dark and the visible sectors are not strong enough for them to equilibrate. In such a scenario, DM can be produced "out-of-equilibrium" by decays or annihilations of SM particles until these processes lose out to the expansion rate of the universe. This is known as *freeze-in* [48].

In this section, we study the evolution of DM in these two limiting regimes. We begin with a more rigorous calculation of the rate of change of the number density of a generic particle species in section 2.2.1, followed with a discussion on freeze-out and freeze-in in sections 2.2.2 and 2.2.3 respectively. We conclude with a few statements on DM production beyond freeze-in and freeze-out in section 2.2.4.

### 2.2.1 The Boltzmann Equation

The evolution of the phase-space density for any particle species is obtained by solving the Boltzmann equation. In its simplest form, the Boltzmann equation can be written as [26],

$$\mathrm{L}[f_\chi] = \mathrm{C}[f_\chi]\,, \tag{2.1}$$

where $f_\chi$ denotes the phase-space distribution of the particle under consideration, $\mathrm{L}$ is the Liouville operator representing the time rate of change of $f_\chi$, and $\mathrm{C}$ is the Collision operator denoting the number of particles lost or gained per unit time per phase-space volume due to collisions or decays.

[4] Note that all SM particles do not obtain their abundances this way. Instead, as pointed out in Chapter 1, the abundance of most of them is set by an initial asymmetry (baryogenesis).

The covariant form of the Liouville operator is,

$$\mathrm{L} = p^\alpha \frac{\partial}{\partial x^\alpha} - \Gamma^\alpha_{\beta\gamma} p^\beta p^\gamma \frac{\partial}{\partial p^\alpha} \,. \tag{2.2}$$

Since the phase-space density $f_\chi$ is homogenous and isotropic, as mentioned in Chapter 1, $f_\chi = f_\chi(|\mathbf{p}|, t) = f_\chi(E, t)$, and in the FLRW metric,

$$\mathrm{L}[f_\chi] = E \frac{\partial f_\chi}{\partial t} - \frac{\dot{a}}{a} |\mathbf{p}|^2 \frac{\partial f_\chi}{\partial E} \,. \tag{2.3}$$

Using the definition of number density from Eq. 1.82, we can write down the Boltzmann equation from Eq. 2.3 as,

$$\dot{n}_\chi + 3Hn_\chi = g_\chi \int \frac{\mathrm{d}^3 p}{(2\pi)^3} \frac{\mathrm{C}[f_\chi]}{E} \,. \tag{2.4}$$

where $H$ is the standard Hubble parameter defined in Chapter 1,[5]

$$H = 1.66 \sqrt{g^\rho_*} \frac{T^2}{M_{\mathrm{Pl}}} \,. \tag{2.5}$$

It is conventional to treat the decrease in the number density due to the expansion of the universe implicitly by considering the comoving number density, $Y_\chi = n_\chi / s$, instead, with $s$ being the total entropy density of the universe as previously defined,

$$s = g^s_* \frac{2\pi^2}{45} T^3 \,. \tag{2.6}$$

Since $s$ and $n_\chi$ both scale as $a^{-3}$ (in the limit of no collisions and $g^s_* \approx$ constant), the comoving number density $Y$ is scale-invariant.

Additionally, we can further simplify the Boltzmann equation by considering a dimensionless variable for the temperature, $x = m_\chi / T$. With these changes, and assuming that the total degrees of freedom in the universe remains constant over the temperature regions of interest,[6] $\frac{\mathrm{d}g_*}{\mathrm{dT}} \sim 0$, we get:

$$\dot{n}_\chi + 3H\, n_\chi = s\, Hx \frac{\mathrm{d}Y_\chi}{\mathrm{d}x} \,. \tag{2.7}$$

Note that when evaluating the Boltzmann equation numerically, as we shall do for specific DM models in Part III, we will be considering the complete evolution of $g^{s,\,\rho}_*$ as discussed in Chapter 1 and plotted in Fig. 1.7.

[5] Note that we are still using the definition of $H$ during radiation domination. For DM production calculations, as we shall see below, the temperature ranges of interest almost always correspond to a radiation dominated universe.

[6] This can be for example, if most of dark matter is produced at a given temperature (due to resonance) or within a range of temperatures where no particles become non-relativistic.

Next, we consider the collision term. For a general process $\chi + a_1 + a_2 + a_3 + \cdots \leftrightarrow b_1 + b_2 + b_3 + \ldots$, the collision term for a particle $\chi$ is [26]:

$$g_\chi \int \frac{\mathrm{d}^3 p_\chi}{(2\pi)^3 E_\chi} \mathrm{C}[f_\chi] = -\int \frac{\mathrm{d}^3 p_\chi}{(2\pi)^3 2E_\chi} \frac{\mathrm{d}^3 p_{a_1}}{(2\pi)^3 2E_{a_1}} \frac{\mathrm{d}^3 p_{a_2}}{(2\pi)^3 2E_{a_2}} \cdots \frac{\mathrm{d}^3 p_{b_1}}{(2\pi)^3 2E_{b_1}} \frac{\mathrm{d}^3 p_{b_2}}{(2\pi)^3 2E_{b_2}} \cdots$$
$$(2\pi)^4 \delta^{(4)}(p_\chi + p_{a_1} + p_{a_2} \cdots - p_{b_1} - p_{b_2} - \ldots)$$
$$[|\mathcal{M}|^2_{\chi + a_1 + a_2 + a_3 + \cdots \to b_1 + b_2 + b_3 + \ldots} f_\chi f_{a_1} \ldots (1 \pm f_{b_1})(1 \pm f_{b_2}) \ldots$$
$$- |\mathcal{M}|^2_{b_1 + b_2 + b_3 + \cdots \to \chi + a_1 + a_2 + a_3 + \ldots} f_{b_1} f_{b_2} \ldots (1 \pm f_\chi)(1 \pm f_{a_1}) \ldots] \tag{2.8}$$

where statistical dependence enters through the $(1 \pm f)$ factors with $(+)$ for bosons and $(-)$ for fermions (corresponding to Bose-enhancement and Pauli-blocking effects respectively), and $\mathcal{M}$ is the square of the matrix element summed (**not averaged**) over the initial and final state spins. Eq. 2.1 is then formulated as:

$$sHx \frac{\mathrm{d}Y_\chi}{\mathrm{d}x} = -\int \frac{\mathrm{d}^3 p_\chi}{(2\pi)^3 2E_\chi} \frac{\mathrm{d}^3 p_{a_1}}{(2\pi)^3 2E_{a_1}} \frac{\mathrm{d}^3 p_{a_2}}{(2\pi)^3 2E_{a_2}} \cdots \frac{\mathrm{d}^3 p_{b_1}}{(2\pi)^3 2E_{b_1}} \frac{\mathrm{d}^3 p_{b_2}}{(2\pi)^3 2E_{b_2}} \cdots$$
$$(2\pi)^4 \delta^{(4)}(p_\chi + p_{a_1} + p_{a_2} \cdots - p_{b_1} - p_{b_2} - \ldots)$$
$$[|\mathcal{M}|^2_{\chi + a_1 + a_2 + a_3 + \cdots \to b_1 + b_2 + b_3 + \ldots} f_\chi f_{a_1} \ldots (1 \pm f_{b_1})(1 \pm f_{b_2}) \ldots$$
$$- |\mathcal{M}|^2_{b_1 + b_2 + b_3 + \cdots \to \chi + a_1 + a_2 + a_3 + \ldots} f_{b_1} f_{b_2} \ldots (1 \pm f_\chi)(1 \pm f_{a_1}) \ldots] \,, \tag{2.9}$$

and the DM number density is obtained by integrating this equation from the reheating temperature, $T_{\mathrm{RH}}$, to the temperature today, $T_0 \sim 0$.

For a DM particle with mass $m_\chi$, the present-day DM energy density is given by $\rho^0_\chi = m_\chi n^0_\chi = m_\chi Y^0_\chi s^0$, where$s^0 = 2891.2\,\mathrm{cm}^{-3}$ is the entropy density today. The DM relic abundance can therefore be calculated as:

$$\Omega_{\mathrm{DM}} = \frac{\rho^0_\chi}{\rho^0_c} \,,$$
$$\Rightarrow \Omega_{\mathrm{DM}} = \frac{Y^0_\chi \, m_\chi s^0}{\rho^0_c} \,, \tag{2.10}$$

where, $\rho^0_c = 1.053 \times 10^{-5}\, h^2\,\mathrm{GeV\,cm}^{-3}$ is the critical energy density today as defined in Chapter 1.

Note that the right-hand side of Eq. 2.9 still appears substantially difficult to solve. In the following sections, we will review how to simplify this for both freeze-out and freeze-in along with mentioning a few caveats. In doing so, we will be focusing primarily on $2 \to 2$ interactions. Decays can be included in a completely analogous way (see, for example, [48, 49]).

### 2.2.2 Freeze-out: Conventions and Caveats

We begin our discussion following the model of a SM particle, i.e., we assume that DM was part of the SM thermal bath at early times. Considering a simple process of the type $1 + 2 \leftrightarrow$

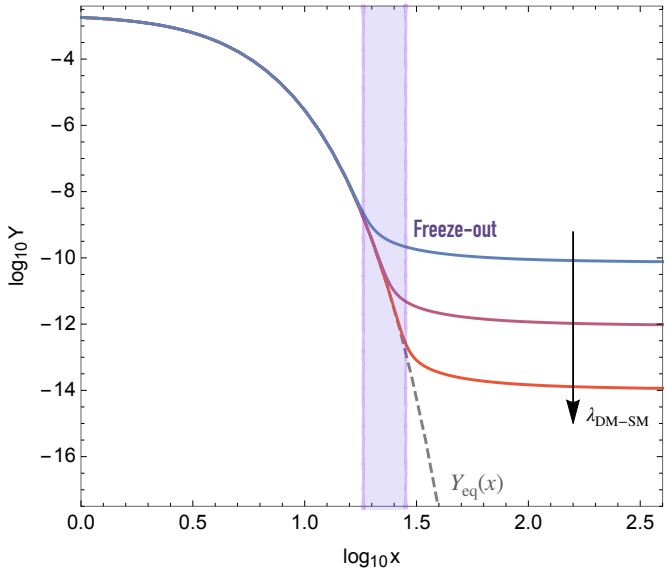


FIGURE 2.4: Representative sketch of DM freeze-out, with the DM comoving number density $Y$, plotted as a function of inverse temperature, $x = m/T$. The different colours correspond to different values of the DM-SM coupling with larger coupling values resulting in delayed freeze-out and thereby a smaller final DM density. Figure adapted from [50].

$3 + 4$, the collision term for particle 1 is [51],

$$g_1 \int \mathcal{C}[f_1] \frac{\mathrm{d}^3 p_1}{(2\pi)^3} = -\int \prod_{i=1}^{4} \frac{\mathrm{d}^3 p_i}{(2\pi)^3\, 2E_i} (2\pi)^4 \delta^4(p_1 + p_2 - p_3 - p_4) \times f_1 f_2 (1 \pm f_3)(1 \pm f_4) \left|M_{12\to 34}\right|^2 - f_3 f_4 (1 \pm f_1)(1 \pm f_2) \left|M_{34\to 12}\right|^2 . \tag{2.11}$$

Assuming the annihilation products quickly equilibrate, we can make the replacement $f_3 f_4 = f_3^{\rm eq} f_4^{\rm eq}$. Additionally, the principle of detailed balance allows us to write $f_3^{\rm eq} f_4^{\rm eq} = f_1^{\rm eq} f_2^{\rm eq}$, which simplifies the equation above to

$$g_1 \int \mathcal{C}[f_1] \frac{\mathrm{d}^3 p_1}{(2\pi)^3} = -\langle \sigma v_{\rm møl} \rangle (n_1 n_2 - n_1^{\rm eq} n_2^{\rm eq}) , \tag{2.12}$$

where $n_{1,2}$ are particle number densities with $n_{1,2}^{\rm eq}$ specifying their equilibrium values and $\langle \sigma v_{\rm møl} \rangle$ is the thermally averaged cross-section inclusive of *all* final states, $\sigma = \sum_f \sigma_{12\to f}$, given by

$$\langle \sigma v_{\rm møl} \rangle = \frac{\int \sigma v_{\rm møl} e^{-E_1/T} e^{-E_2/T} \mathrm{d}^3 p_1 \mathrm{d}^3 p_2}{\int e^{-E_1/T} e^{-E_2/T} \mathrm{d}^3 p_1 \mathrm{d}^3 p_2} , \tag{2.13}$$

where the Møller velocity is an explicitly covariant quantity defined by

$$v_{\rm møl} \equiv \frac{\sqrt{(p_1.p_2)^2 - m_1^2 m_2^2}}{E_1 E_2} . \tag{2.14}$$

Note that in these formulas we have implicitly assumed a Maxwell-Boltzmann distribution for the particles, $f = e^{-E/T}$, and ignored the statistical factors of $(1 \pm f)$. This is a good assumption for when $E > T$.

For the case of annihilation of identical particles, $m_1 = m_2 = m$, the thermal average can be solved for analytically [51],

$$\langle \sigma v_{\text{møl}} \rangle = \frac{1}{8m^4 T^2 K_2(m/T)} \int_{4m^2}^{\infty} \mathrm{d}s\, \sigma\,(s - 4m^2)\sqrt{s} K_1\left(\frac{\sqrt{s}}{T}\right) \tag{2.15}$$

where $K_{1,2}$ are the modified Bessel functions of the second kind. From now on, we shall suppress the subscript møl and assume $v_{\text{møl}} \to v$. Finally, in terms of the comoving number density, $Y$, and the inverse temperature, $x$, we have the following compact form of the Boltzmann equation,

$$\frac{\mathrm{d}Y(x)}{\mathrm{d}x} = -\frac{s\,\langle \sigma v \rangle}{H\,x}\left(Y^2(x) - Y_{\text{eq}}^2(x)\right) \tag{2.16}$$

**Factors of two**: The Boltzmann equation is notorious for having apparently strange factors of two pop up every now and then mostly because of the presence of multiple phase-space integrals and the implicit definition of the cross-section. The way it is conventionally formulated, as in the landmark paper by Gondolo and Gelmini [51], is as follows: First, looking at only the collision term, the cross-section is the usual one, summed over final spins and averaged over initial spins without a factor $1/2$ for identical *initial* particles. (The symmetry factor for final state particles is, however, included.) For identical particles in the initial state, $n_1 = n_2 = n$, Eq. 2.16 remains unchanged. For non-identical particles however, the *total* particle density is given by $n = n_1 + n_2$. Since for particles in chemical equilibrium, $n_1 = n_2$, this implies $n = 2n_1$, resulting in an overall factor of $1/2$ on the right hand side of Eq. 2.16.

Thermal freeze-out is an attractive scenario for DM production. One of the reasons for this is that weak-scale values of couplings and masses generically reproduce the observed DM abundance. This can be easily seen from Eq. 2.16 under certain assumptions [42]. First, the non-relativistic thermally averaged cross-section can be expanded in powers of $x$, $\langle \sigma v \rangle_0 \sim \sigma_0 x^{-n}$ where $n = 0$ for s-wave annihilation, $n = 1$ for p-wave annihilation, and so on. Additionally, the DM density follows the equilibrium distribution before freeze-out, $Y(x \lesssim x_f) \simeq Y_{\text{eq}}(x)$, and is much larger than the equilibrium distribution afterwards, $Y(x \gtrsim x_f) \gg Y_{\text{eq}}(x))$ (see Fig. 2.4 ). Hence, assuming a cross-section that is dominantly s-wave, $\langle \sigma v \rangle = \sigma_0$, and neglecting $Y_{\text{eq}}$, we can obtain the DM density by integrating the simplified Bolztmann equation,

$$\frac{\mathrm{d}Y}{\mathrm{d}x} \simeq -\frac{\lambda}{x^2} Y^2, \tag{2.17}$$

where we have made the $x$-dependence explicit in the prefactor by defining,

$$\lambda \equiv \frac{\sigma_0 s_0}{H(m_\chi)}, \tag{2.18}$$

with $s = s_0 x^{-3}$ and $H(m_\chi) = H(x)\, x^2$. Integrating from freeze-out until today yields,[7]

$$Y_{\text{today}} \simeq \frac{x_f}{\lambda}\,. \tag{2.20}$$

The freeze-out temperature is defined approximately by the condition, $\langle\sigma v\rangle n_{\text{eq}}(x_f) \simeq H(x_f)$. For a particle species that is non-relativistic at freeze-out, this is

$$\langle\sigma v\rangle \left(\frac{m_\chi^2}{2\pi x_f}\right)^{3/2} e^{-x_f} = \sqrt{g_*^\rho}\,\frac{1.66\, m_\chi^2}{M_{\text{Pl}}\, x_f^2}\,, \tag{2.21}$$

which results in $x_f \sim 20 - 30$ for $m_\chi \sim O(\text{GeV})$ and $\langle\sigma v\rangle \sim \alpha^2/m_\chi^2$ for $\alpha \sim 10^{-3} - 10^{-2}$. The correct DM abundance then places a bound on the thermally averaged cross-section,

$$\Omega_\chi h^2 = \frac{3\times 10^{-26}\,\text{cm}^3\,\text{s}^{-1}}{\langle\sigma v\rangle}\,, \tag{2.22}$$

which is naturally satisfied by a weak-scale cross-section, $\langle\sigma v\rangle = \alpha_\chi^2/m_\chi^2$, with $\alpha_\chi \sim 0.01$ and $m_\chi \sim 100\,\text{GeV}$.[8] This is known as the *WIMP miracle* and DM so produced is called a WIMP (Weakly Interacting Massive Particle).

Although Eq. 2.16 is fairly general, there do exist DM models for which the relic abundance calculation departs from the one presented above. First pointed out by Griest and Seckel [52], these exceptions arise when DM models have any of the following properties:

1. **Resonances**: In models where the mass of the DM particle lies close to a resonance, $m_A \simeq 2m_\chi$, the annihilation cross-section is enhanced for temperatures close to the resonance. This demands a proper treatment of the temperature integral in the Boltzmann equation since resonant annihilations might still be efficient after freeze-out. Phenomenologically, such models are interesting since they allow for a suppression of annihilation rates at late times and might alleviate certain constraints. We will discuss the Boltzmann equation for resonant annihilation next and elaborate on its phenomenological implications in the context of a specific model in Chapter 5 (see also [53]).

2. **Thresholds**: Thresholds also affect the relationship between the annihilation cross-section today and its value at freeze-out. For example, if DM dominantly annihilates into a slightly heavier state, $\phi$, the annihilation has an exponential phase-space suppression since this annihilation is kinematically forbidden at small temperatures. Since the relic abundance is inversely proportional to the cross-section, this suppression results in an enhancement in the final relic density. Such DM is categorised as *forbidden dark matter* (see, for example, [54]).

[7] Note that in general, we need to perform the full calculation,

$$Y_{\text{today}} \propto \left[\int_{x_f}^{\infty} \frac{\langle\sigma v\rangle}{x^2}\right]^{-1}\,, \tag{2.19}$$

to obtain the DM density.

[8] For a Dirac DM candidate the numerator in Eq. 2.22 has an additional symmetry factor of 2, resulting in $6\times 10^{-26}\,\text{cm}^3\,\text{s}^{-1}$.

3. **Co-annihilations**: Co-annihilations are important for models where the annihilating partner for DM is a particle with a mass close to the DM mass. Additionally, the co-annihilation cross-section is large enough for the freeze-out of the two species to be interconnected. In this case, the thermally averaged cross-section can be either enhanced or suppressed depending on whether or not the co-annihilating partner annihilates efficiently as compared to DM [55].

**Relic Abundance For Resonant Annihilations:**

We now turn our attention to the first exception to the relic density calculation. Consider a generic DM model where the DM particle, $\chi$, has a mass close to resonance, $2m_\chi \simeq m_A{}'$. For the moment, we remain agnostic about the underlying properties of both these particles.[9] We can parametrise how close we are to resonance by

$$\epsilon_R = \frac{m_{A'}^2 - 4m_\chi^2}{4m_\chi^2} \,. \tag{2.23}$$

The DM relic abundance is then set by the process, $\chi\chi \to A' \to ff$ where $f$ denotes a SM final state. For the total decay width of the mediator given by $\Gamma_{A'}$, we can use a Breit-Wigner form for the annihilation cross-section,

$$\sigma v_{\rm lab} = F(\epsilon) \frac{m_{A'}\Gamma_{A'}}{(s - m_{A'}^2)^2 + m_{A'}^2\Gamma_{A'}^2} \,, \tag{2.24}$$

where $\epsilon = (s - 4m_\chi^2)/4m_\chi^2$ is a dimensionless measure of the kinetic energy of the collision, $v_{\rm lab} = 2\sqrt{\epsilon\,(1+\epsilon)}/(1+2\epsilon)$ is the relative velocity in the rest frame of one of the two annihilating particles, and $F(\epsilon)$ is a model-dependent prefactor which includes the relevant couplings and masses for the initial and final states under consideration. In terms of these parameters[10], the thermally averaged cross-section in Eq. 2.15 is given by,

$$\langle \sigma v \rangle = \frac{2x}{K_2^2(x)} \int_0^\infty \sigma v \sqrt{\epsilon}(1+2\epsilon) K_1(2x\sqrt{1+\epsilon})\, {\rm d}\epsilon \,. \tag{2.25}$$

Previously, we saw that DM is generally non-relativistic at freeze-out, $x_f = m_\chi/T \sim O(10)$. This implies that we can use the non-relativistic limit, $\epsilon \ll 1$, to get

$$\langle \sigma v \rangle = \frac{2x^{3/2}}{\pi^{1/2}} \int_0^\infty \sigma v \sqrt{\epsilon} e^{-x\,\epsilon}\, {\rm d}\epsilon \,. \tag{2.26}$$

Additionally, by approximating $F(\epsilon) \approx F(0)$, we can perform the integration above numerically to obtain

$$\langle \sigma v \rangle_{\rm n.r.} \approx \frac{x^{3/2}\pi^{1/2}}{2m_\chi^2} F(0) {\rm Re}\left[ z_R^{1/2} w(z_R^{1/2} x^{1/2}) \right] \,, \tag{2.27}$$

[9] Although the $A'$ should already hint at the kind of model we will be interested in later!
[10] Note that we are now using $v = v_{\rm lab}$ and not $v_{\rm møl}$

where

$$w(z) = \frac{2i\,z}{\pi}\int_0^\infty \frac{e^{-t^2}}{z^2-t^2}\,\mathrm{d}t\,, \tag{2.28}$$

is the Fadeeva function and $z_R = \epsilon_R + i\,(1+\epsilon_R)\gamma_{A'}$ where we have defined a dimensionless decay width $\gamma_{A'} \equiv \Gamma_{A'}/m_{A'}$.

The non-relativistic limit mentioned above might not be valid over the entire range of parameter space. For instance, for an incredibly narrow width, $\gamma_{A'} \ll 1$, and for $\epsilon_R \sim 1$, it is possible to obtain a substantial contribution from DM particles in the relativistic tail of the distribution (that have the energy to produce the mediator on-shell). In such a scenario, it is better to use the narrow-width approximation for the cross-section:

$$\sigma v \approx \frac{\pi}{m_{A'}^2}\,F(\epsilon_R)\delta(\epsilon-\epsilon_R)\,, \tag{2.29}$$

yielding

$$\langle\sigma v\rangle_{\text{res.}} = \frac{\pi}{m_{A'}^2}F(\epsilon_R)\frac{2x}{K_2^2(x)}\sqrt{\epsilon_R}\,(1+2\epsilon_R)K_1(2x\sqrt{1+\epsilon_R})\,. \tag{2.30}$$

These two approximations, Eq. 2.27 and Eq. 2.30, can capture the behaviour of the thermally averaged cross-section in the entire domain.[11] Using Eq. 2.17 for the general cross-sections discussed above, the relic abundance is given by

$$\Omega h^2 \approx 1.7\times10^{-10}\text{GeV}^{-2}\left(\int_{x_f}^{x_0}\sqrt{g_{\text{eff}}}\frac{\langle\sigma v\rangle}{x^2}\mathrm{d}x\right)^{-1}\,, \tag{2.31}$$

with $g_{\text{eff}} \sim g_*^\rho$ denoting the effective degrees of freedom present in the thermal plasma. The freeze-out temperature, $x_f$, is defined by

$$\frac{63\sqrt{5}\,x_f^{-1/2}e^{-x_f}g_\chi}{32\pi^3}\frac{1}{g_{\text{eff}}^{1/2}}m_\chi m_{\text{Pl}}\langle\sigma v\rangle = 1\,, \tag{2.32}$$

where $g_\chi$ denotes the spin degrees of freedom of $\chi$, and $M_{\text{Pl}} = 1.22\times10^{19}\,\text{GeV}$ denotes the Planck mass.

To demonstrate the effect of resonant annihilations, we plot in Fig. 2.5 the thermally averaged cross-section as a function of $x$ in three different cases: s-wave annihilation ($\langle\sigma v\rangle = \sigma_0$), p-wave annihilation ($\langle\sigma v\rangle = \sigma_0 x^{-1}$), and resonant annihilation (Eq. 2.27). For each case, we normalise the cross-section so as to reproduce the correct value of the relic abundance.[12] From

[11] For a given model, the validity of this statement can be explicitly checked by calculating $\langle\sigma v\rangle$ numerically. We will do exactly this when talking about a concrete model in Chapter 5.

[12] Note that this necessarily requires some assumptions with respect to the underlying DM model. For the purposes of this plot, we assume $m_\chi \sim 50\,\text{MeV}$. Additionally, for the calculation of $\langle\sigma v\rangle_{\text{resonant}}$ we use $\epsilon_R = 0.001$ and consider a kinetically mixed dark photon model (discussed in detail in Chapter 5).

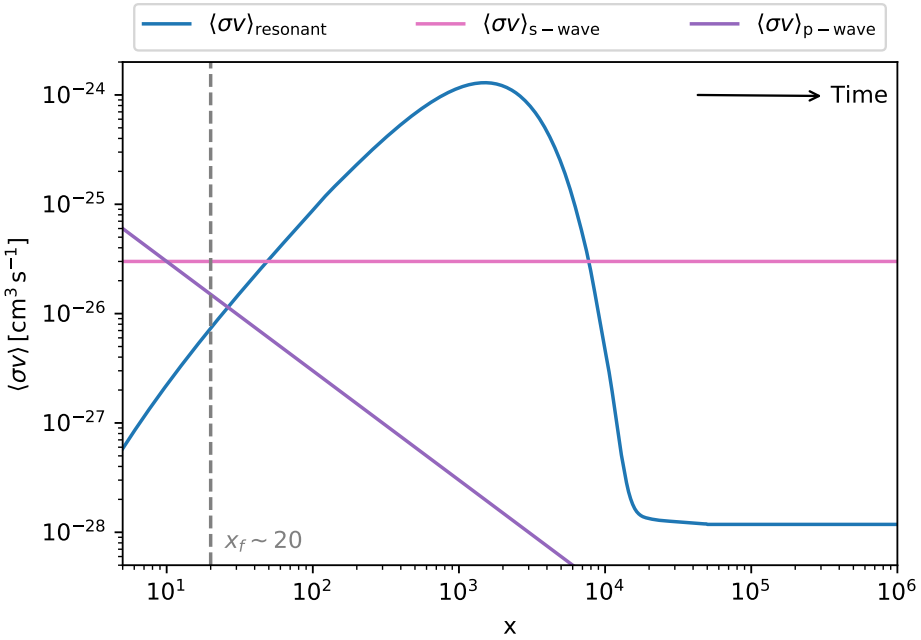


FIGURE 2.5: Thermally averaged cross-section as a function of $x$ corresponding to s-wave, p-wave and resonant annihilations.

Fig. 2.5, it is easy to see that resonant annihilations can substantially reduce the DM abundance after decoupling, thereby *decreasing* the DM-SM couplings required to reproduce the relic abundance. This has interesting phenomenological consequences in terms of viable parameter space for thermal DM models— a topic that we will address in Chapter 5.

### 2.2.3 Freeze-in: The Old And The New

Although thermal freeze-out is an attractive mechanism for DM production, it is by no means the only one. The foundational assumption of freeze-out—thermal equilibrium with the SM—is, in the end, simply an assumption, and one that is simple to violate. In principle, one can propose DM models with extremely tiny (weaker than weak) couplings to the SM that ensure that the two sectors never equilibrate. In this limit, DM is called a FIMP (Feebly Interacting Massive Particle). Additionally, we can use this disparity in couplings along with the fact that DM does not have a thermal abundance to make the assumption that the initial phase space density of DM is negligible, $f_\chi \ll 1$. DM is then produced by a leakage of energy from the SM, i.e., by SM particles annihilating or decaying, until these processes lose out to the expansion rate of the universe (see Fig. 2.6). Conversely to freeze-out, this mechanism is known as *freeze-in*.

We can obtain obtain a rough order-of-magnitude estimate for freeze-in couplings from the condition of non-equilibrium, $\Gamma_{ff\to\chi\chi} \lesssim H$, where $\Gamma_{ff\to\chi\chi} \sim \sigma v n_f$ and $f$ denotes a SM state. Since this condition must hold at the earliest times, we can approximate the particles to be relativistic, therefore assuming $v \sim 1$ and $n_f \approx T^3/\pi$. Additionally, the cross-section for a

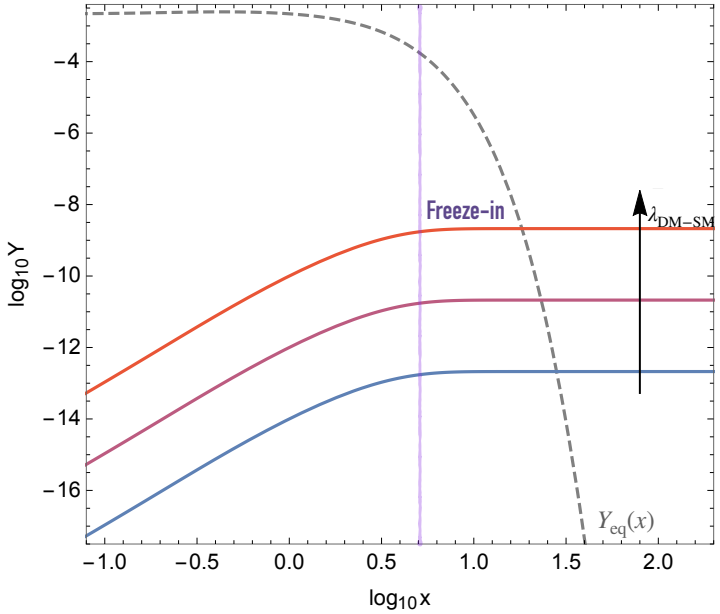


FIGURE 2.6: Representative sketch of DM freeze-in, with the DM comoving number density $Y$, plotted as a function of inverse temperature, $x = m/T$. The different colours correspond to different values of the DM-SM coupling. In contrast with freeze-out, freeze-in relies on DM *production* and hence larger couplings imply larger values of the relic abundance. Figure adapted from [50].

portal coupling $\lambda$ will scale as $\sigma \sim \lambda^2/T^2$. This results in,

$$\frac{\Gamma_{ff\to\chi\chi}}{H} \sim \frac{\lambda^2 10^{16}\,\text{GeV}}{T}\,. \tag{2.33}$$

Assuming that the two sectors are not in equilibrium at the electroweak phase transition, yields $\lambda < 10^{-7}$, which is much smaller than the weak scale coupling. Nevertheless, such tiny couplings may arise naturally in many BSM theories like supersymmetry or string theory as pointed out initially in [48].

FIMP models have gathered a lot of interest in the last few years primarily due to the absence of a clear DM signal at detection experiments which probe order one (or thermal) couplings between DM and SM. We will further elaborate on detection strategies in Chapter 7, but for now, our interests lie in simplifying the Boltzmann equation from Eq. 2.9 for the case of freeze-in.

As in the previous section, we start with a simple $2 \to 2$ process of the form, $12 \to 34$. Since freeze-in relies on DM production, we are interested in tracking the number density of the final state particles. Additionally, if the final state comprises of FIMPs, $f_3,\ f_4 \ll 1$. The collision term for this process is

$$\begin{aligned} g_3 \int \mathcal{C}[f_3]\frac{\mathrm{d}^3p_3}{(2\pi)^3} &= \int \prod_{i=1}^{4} \frac{\mathrm{d}^3p_i}{(2\pi)^3\,2E_i}\,(2\pi)^4\delta^4(p_1+p_2-p_3-p_4)\times f_1 f_2\,|M_{12\to34}|^2 \\ &= \int \mathrm{d}n_1 \mathrm{d}n_2 \sigma_{12\to34} v_{\text{møl}}\,, \end{aligned} \tag{2.34}$$

where in the second line we have used the definition of the Møller velocity from Eq. 2.14 as in the freeze-out case, and the standard definition of the unpolarised cross-section for the given process. By using the usual definition for the thermal average,

$$\langle \sigma v_{\text{møl}} \rangle = \frac{\int \sigma v_{\text{møl}}\, f_1 f_2\, \mathrm{d}^3 p_1 \mathrm{d}^3 p_2}{\int f_1 f_2\, \mathrm{d}^3 p_1 \mathrm{d}^3 p_2}\,, \tag{2.35}$$

we can write down Eq. 2.34 as $\langle \sigma v_{\text{møl}} \rangle n_1^{\text{eq}} n_2^{\text{eq}}$, resulting in the Boltzmann equation,

$$\frac{\mathrm{d}Y_\chi}{\mathrm{d}x} = \mathcal{C}_{ab} \frac{s\langle \sigma v \rangle}{Hx} \left(Y_{\text{SM}}^{\text{eq}}\right)^2\,, \tag{2.36}$$

where we have introduced $\mathcal{C}_{ab} = 1(2)$ to account for identical (non-identical) DM particles and $\langle \sigma v \rangle$ is defined as in Eq. 2.15 (with the particle masses relating to the SM particles in the initial state). Note that $Y_{\text{SM}}^{\text{eq}}$ is the equilibrium density for an identical SM initial state $f$. If the SM particles are non-identical, the *total* equilibrium density for $f$ would be $Y^{\text{eq}} = Y_f^{\text{eq}} + Y_{\bar{f}}^{\text{eq}} = 2Y_f^{\text{eq}}$ and therefore we will have an additional factor of $1/4$ on the right if we use $Y^{\text{eq}}$.[13]

Conventional descriptions of freeze-in follow the methodology laid out above to calculate relic abundances. However, as we show below, an equivalent framework can be derived by formulating our equations in terms of the DM *annihilation cross-section*, $\langle \sigma v \rangle_{\chi\chi \to \text{SMSM}}$, instead of the production cross-section. At first sight, this might appear to add an unnecessary degree of complexity in the phenomenological understanding of Eq. 2.36. However, in certain cases, the annihilation cross-section may be easier to calculate while maintaining a higher degree of numerical accuracy (see Chapter 4 for one such model).

Additionally, until now we have assumed a Maxwell-Boltzmann distribution for the particle phase space and neglected the statistical factors, $(1 \pm f)$, in the collision term to arrive at the analytic formulas listed above. For standard thermal freeze-out, such an assumption is robust since freeze-out occurs for temperatures smaller than the DM mass. However, inclusion of proper statistics becomes necessary when DM is produced dominantly at larger temperatures. Further, massless particles have to always be described by the relevant Fermi-Dirac or Bose-Einstein statistics. In such a case, one can usually rely on numerical tools like MICROMEGAS 5.0 [56] or DARKSUSY [57] to solve the Boltzmann equation. However, as we shall show below, it is still possible to derive semi-analytic results. We will perform this calculation for the case when we also reformulate the collision term in the Boltzmann equation in terms of DM annihilation, since this results in a slightly simpler expression. For the standard freeze-in calculation, see references [58] and [59].

#### Reformulating Freeze-in In Terms of DM Annihilation

Consider a freeze-in process, $\psi\psi \to \chi\chi$, where $\psi$ denotes generic SM initial states and $\chi$ denotes DM, and we remain agnostic as to whether any of the particles are identical or not. To clean up notation, we will denote the four-momenta of the DM particles with $(E, \mathbf{p})$ and

[13] Of course, factors of 2 continue to be annoying even for freeze-in.

$(\tilde{E}, \tilde{\mathbf{p}})$, and that of the SM particles with $(\omega, \mathbf{k})$ and $(\tilde{\omega}, \tilde{\mathbf{k}})$. The SM initial states will have a thermal distribution given by,

$$g(\omega) = \frac{1}{e^{\omega/T} - \varepsilon_\psi}\,, \tag{2.37}$$

where $\varepsilon_\psi = +1(-1)$ for bosons (fermions). A negligible initial abundance for FIMPs implies that $f_\chi \ll 1$. Additionally, since the DM abundance is always sub-thermal, $f \ll g$. Therefore, in the notation presented above, the collision term (Eq. 2.34) can then be written as,

$$C[f_\chi] = \int \frac{\mathrm{d}^3 p}{(2\pi)^3 2E} \int \frac{\mathrm{d}^3 \tilde{p}}{(2\pi)^3 2\tilde{E}} \int \frac{\mathrm{d}^3 k}{(2\pi)^3 2\omega} \int \frac{\mathrm{d}^3 \tilde{k}}{(2\pi)^3 2\tilde{\omega}} (2\pi)^4 \delta^{(4)}(\tilde{p} + p - \tilde{k} - k) \times |\mathcal{M}|^2_{\psi\psi\to\chi\chi}\, g(\omega) g(\tilde{\omega})\,. \tag{2.38}$$

We are interested in expressing the equation above in terms of DM annihilation cross-section. Since the matrix element is invariant under time (or equivalently under CP), $|\mathcal{M}|^2_{\psi\psi\to\chi\chi} = |\mathcal{M}|^2_{\chi\chi\to\psi\psi}$. Additionally, it is possible to write,

$$g(\omega)g(\tilde{\omega}) = g(\omega)g(\tilde{\omega}) e^{(\omega+\tilde{\omega})/T} e^{-(E+\tilde{E})/T} = (1-\varepsilon_\psi g(\omega))\,(1-\varepsilon_\psi g(\tilde{\omega}))\, f^{\mathrm{MB}}_\chi(E)\, f^{\mathrm{MB}}_\chi(\tilde{E})\,, \tag{2.39}$$

where the first equality arises from energy conservation and in the second equality we introduce a Maxwell-Boltzmann distribution for DM particles,[14]

$$f^{\mathrm{MB}}_\chi(E) = e^{-E/T}\,. \tag{2.40}$$

This results in the collision term,

$$\mathcal{C}[f_\chi] = \int \frac{\mathrm{d}^3 p}{(2\pi)^3 2E} \int \frac{\mathrm{d}^3 \tilde{p}}{(2\pi)^3 2\tilde{E}} \int \frac{\mathrm{d}^3 k}{(2\pi)^3 2\omega} \int \frac{\mathrm{d}^3 \tilde{k}}{(2\pi)^3 2\tilde{\omega}} (2\pi)^4 \delta^{(4)}(\tilde{p} + p - \tilde{k} - k) \times |\mathcal{M}|^2_{\chi\chi\to\psi\psi}\, f^{\mathrm{MB}}_\chi(E)\, f^{\mathrm{MB}}_\chi(\tilde{E})\,(1-\varepsilon_\psi g(\omega))\,(1-\varepsilon_\psi g(\tilde{\omega}))\,, \tag{2.41}$$

which is identical to the annihilation term in the case of freeze-out, Eq. 2.11, but with the inclusion of statistical factors. The in-medium DM annihilation cross-section in the centre-of-mass (CMS) frame is given by

$$\sigma_{\chi\chi\to\psi\psi}(p, \tilde{p}) = \frac{(2\pi)^4}{4N_\psi F} \int \frac{\mathrm{d}^3 k}{(2\pi)^3 2\omega} \int \frac{\mathrm{d}^3 \tilde{k}}{(2\pi)^3 2\tilde{\omega}} \delta^{(4)}(\tilde{p} + p - \tilde{k} - k)\, \left|\overline{\mathcal{M}}\right|^2 (1-\varepsilon_\psi g(\omega))\,(1-\varepsilon_\psi g(\tilde{\omega}))\,, \tag{2.42}$$

where $\left|\overline{\mathcal{M}}\right|^2 = |\mathcal{M}|^2 / g^2_\chi$ is the usual *spin-averaged* amplitude, $F = \sqrt{(p.\tilde{p})^2 - m^4_\chi}$, and $N_\psi = 1(2)$ for non-identical (identical) SM states. Using this definition of the cross-section and the

[14] Note that this distribution is not physical, i.e., this is not the *real* DM distribution which for the case of freeze-in will never be thermal. Instead, we introduce this quantity as a hypothetical distribution that a DM particle would have if it were thermal.

standard expression for the Møller velocity, $v_{\text{møl}} = F/(E\tilde{E})$, Eq. 2.41 can be written as

$$\begin{aligned}\mathcal{C}[f_\chi] &= g_\chi^2 \int \frac{\mathrm{d}^3 p}{(2\pi)^3} \int \frac{\mathrm{d}^3 \tilde{p}}{(2\pi)^3} f_\chi^{\text{MB}}(E)\, f_\chi^{\text{MB}}(\tilde{E}) \sigma_{\chi\chi\to\psi\psi} v_{\text{møl}} \\ &= \langle \sigma v \rangle \left(n_\chi^{\text{MB}}\right)^2 , \end{aligned} \tag{2.43}$$

where once again we have suppressed the subscript for the Møller velocity and defined the thermally averaged cross-section as

$$\langle \sigma v \rangle_{\chi\chi\to\psi\psi} \equiv \frac{g_\chi^2}{\left(n_\chi^{\text{MB}}\right)^2} \int \frac{d^3 p}{(2\pi)^3} \int \frac{d^3 \tilde{p}}{(2\pi)^3} f_\chi^{\text{MB}}(E) f_\chi^{\text{MB}}(\tilde{E})\, v_{\text{møl}} \sigma_{\chi\chi\to\psi\psi}(p,\, \tilde{p})\,. \tag{2.44}$$

$n_\chi^{\text{MB}}$ is the equilibrium number density for a Maxwell-Boltzmann distribution of particles, given by Eq. 1.82,

$$n_\chi^{\text{MB}} = \frac{g_\chi m_\chi^2 T}{2\pi^2} K_2\left(\frac{m_\chi}{T}\right) . \tag{2.45}$$

The difference between the thermally averaged cross-section in Eq. 2.44, and the usual one in, for example, Eq. 2.13 is that the former explicitly depends on the frame of reference through the statistical factors $(1 - \varepsilon_\psi g)$ included in the in-medium cross-section. The distribution functions $g(\omega)$ only take the form of Eq. 2.37 in the cosmic rest frame, where the four-velocity is given by $u^\mu = (1,\, 0,\, 0,\, 0)^T$. In a general frame, the distribution functions will have the form $g(u \cdot k)$, where $u$ is the four-velocity of the cosmic fluid and $k$ is the particle four-momentum. Therefore, the in-medium thermally averaged cross-section is, in general, a function of *two* parameters: the centre of mass energy $s$, and a boost parameter, $\eta$, that specifies the relation between the cosmic rest frame and the centre of mass frame,[15]

$$\sigma_{\chi\chi\to\psi\psi} = \sigma_{\chi\chi\to\psi\psi}(s,\, \eta)\,. \tag{2.46}$$

In usual studies of DM production in which the statistical factors are ignored, the cross-section is simply the centre-of-mass cross-section, $\sigma^{\text{CMS}}_{\chi\chi\to\psi\psi} = \sigma^{\varepsilon_\psi\to 0}_{\chi\chi\to\psi\psi}$. It is worth emphasising that in-medium effects are a consequence of background particle densities and are therefore encoded in the particle distribution functions that enter while calculating reaction amplitudes and rates. If the particle distributions are assumed to be always Maxwell-Boltzmann, the distinction between fermions and bosons is lost and hence also the modification of the available phase-space for a given process due to Pauli-blocking or Bose-enhancement.

The freeze-in Boltzmann equation in terms of DM annihilation has the form,

$$\frac{\mathrm{d}Y_\chi}{\mathrm{d}x} = \tilde{\mathcal{C}}_{ab} \frac{s\langle \sigma v \rangle}{Hx} (Y_\chi^{\text{MB}})^2 , \tag{2.47}$$

with $\tilde{\mathcal{C}}_{ab} = 1/2\,(1)$ for non-identical (identical) DM particles.[16]

[15] We can compare this to the covariant formulation of finite temperature field theory as discussed in Chapter 1.
[16] The symmetry factor for $\psi_{i,\,j}$ is already accounted for in the definition of the cross-section as we shall discuss.

Additionally, as is derived in Appendix A, the in-medium cross-section has the following simplified form,

$$\sigma_{\chi\chi\to\psi\psi}(s,\,\gamma) = \frac{1}{8\pi s N_\psi}\frac{|\mathbf{k}_{\rm CM}|}{\sqrt{s-4m_\chi^2}}\int_{-1}^{1}\frac{\mathrm{d}\cos\theta}{2}\left|\overline{\mathcal{M}}\right|^2(s,\,\cos\theta)G(\gamma,\,s,\,\cos\theta)\,, \tag{2.48}$$

where $\gamma = \cosh\eta$ specifies the boost from the cosmic rest frame to the CMS frame and the statistical factors are encapsulated in the function $G$ defined as

$$\begin{aligned} G^{-1} &\equiv (1-\varepsilon_\psi g(u\cdot k))^{-1}\left(1-\varepsilon_\psi g(u\cdot\tilde{k})^{-1}\right)^{-1} \\ &= 1-\varepsilon_\psi^2 e^{-2E\gamma/T} - 2\varepsilon_\psi e^{-E\gamma/T}\cosh\left[\frac{|\mathbf{k}_{\rm CM}|\cos\theta\sqrt{\gamma^2-1}}{T}\right]. \end{aligned} \tag{2.49}$$

This results in the thermal average,

$$\langle\sigma v\rangle_{\chi\chi\to\psi\psi} = \frac{8x^2}{K_2^2(x)}\int_1^\infty \mathrm{d}\tilde{s}\,\sqrt{\tilde{s}(\tilde{s}-1)}\int_1^\infty \mathrm{d}\gamma\sqrt{\gamma^2-1}e^{-2x\sqrt{\tilde{s}}\gamma}\sigma_{\chi\chi\to\psi\psi}(s,\,\gamma)\,, \tag{2.50}$$

This general form reproduces the standard thermally averaged cross-section when $\varepsilon_\psi = 0$, resulting in $\sigma(s,\,\gamma)\to\sigma(s)$. In this case, the $\gamma$ integral can be solved analytically,

$$\int_1^\infty \mathrm{d}\gamma\sqrt{\gamma^2-1}e^{-2x\sqrt{\tilde{s}}\gamma} = \frac{1}{2x\sqrt{\tilde{s}}}K_1(2x\sqrt{\tilde{s}})\,, \tag{2.51}$$

resulting in the exact Bessel function as in the integrand of Eq. 2.15, and therefore the usual thermally averaged cross-section.

In this section, we have discussed the general form of the freeze-in Boltzmann equation as well as provided an alternate formulation for the same in terms of the DM annihilation cross-section. The latter is more convenient to use for models with well-described annihilation cross-sections especially when these have already been calculating to higher orders. We will return to this formulation in Chapter 4 in the context of a Higgs portal DM model.

### 2.2.4 WIMPs, FIMPs, and Other Things

Both WIMPs and FIMPs have been targets of extensive study in the last decade, explore as they do opposing limits of DM-SM coupling strengths. In the last few sections, we have developed the mathematical framework required to calculate the DM relic abundance in both these cases, along with discussing caveats that such calculations entail. However, the DM density at the end of production is not guaranteed to be equal to the DM abundance today. Instead, if interactions within the dark sector are efficient enough, a second phase of annihilation or production could be triggered changing the DM density [49]. For example, if equilibrium is established within the dark sector *while* DM is being produced by freeze-in, DM may begin to annihilate. This simultaneous production and annihilation can then result in a period of

quasi-static equilibrium before the DM density eventually freezes-out [60]. Such non-standard evolution histories already arise even in very "simple" DM models like the scalar singlet [61].

Furthermore, as might be expected, the DM model space is not limited to generic WIMPs and FIMPs. The relic abundance of DM could be generated through a variety of different mechanisms such as by number changing processes in the dark sector (Self-Interacting Dark Matter [62] and Strongly Interacting Massive Particles [63]), by annihilations of kinetically decoupled DM (Elastically Decoupling Relics [64]), or by even more exotic processes such as the evaporation of primordial black holes [65]. The point is, of course, that it is possible to devise a whole host of production mechanisms as long as one ensures the reproduction of the measured DM relic abundance[17] and consistency with other constraints.

## 2.3 Early Universe Probes of Dark Matter

Until now we have treated the visible and the dark sectors separately: a useful categorisation to clearly demarcate the known and the unknown (more or less). However, as we have seen from this chapter, our production framework for DM always includes some form of (non-gravitational) coupling to the SM as a result of which the two sectors are not strictly independent. Indeed, it is quite possible for DM to leave an imprint on early universe cosmology. The fact that we have an incredible understanding of the universe in this era, along with extremely precise cosmological measurements, means that we can already search for these imprints and derive general bounds on the microphysics of DM. In this section, we will provide a qualitative description on how to use BBN and the CMB to calculate largely model-independent bounds on DM particle properties. For a more rigorous treatment of the same, see [66] and [67].

We will mostly be interested in the case of thermal relic DM, only providing a few caveats for non-thermal DM as we go along. From Chapter 1, we know that BBN is sensitive to the evolution of the heat bath at temperatures in the MeV range, i.e., when various SM particle species begin to decouple. We also know from section 2.2.2, that DM freeze-out occurs for $x \sim 20$, which corresponds to a temperature of $T \sim$ MeV for DM masses, $m_\chi \lesssim 20\,\text{MeV}$. Additionally, the CMB is sensitive to new physics around and after recombination at eV scales. This implies that light thermal DM can be constrained by cosmology.

In Fig. 2.7, we sketch the temperature evolution of the SM heat bath around the times relevant for BBN, along with the major reactions describing each temperature range. We start with temperature of a few MeV when all particles are in thermal equilibrium. The neutrons and protons are already non-relativistic at this point with their relative number densities given by

[17] Or, at the very least, ensure that DM is not over-abundant. Production mechanisms which lead to dark sub-components may still be interesting.

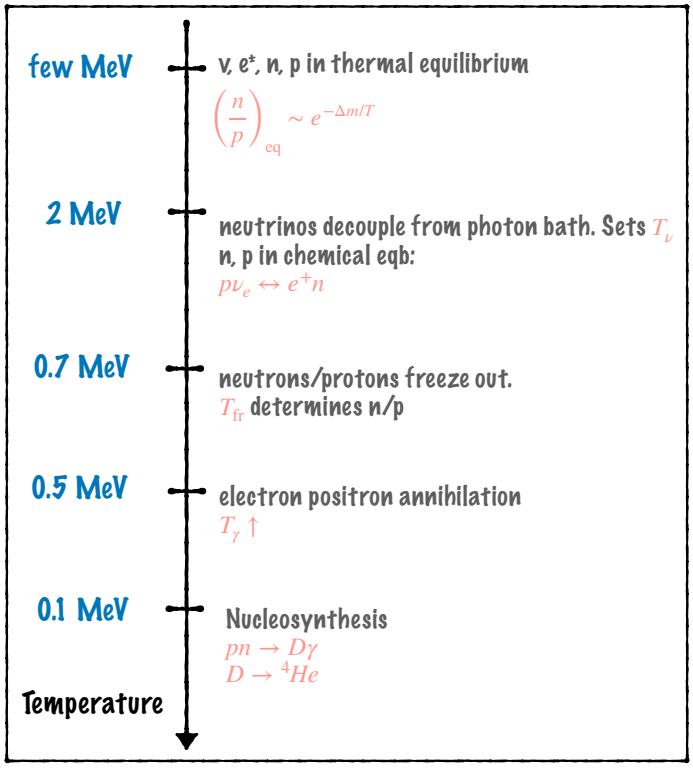


FIGURE 2.7: A sketch of the relevant processes that occur in the SM heat bath for times relevant for BBN. See text for details.

the equilibrium distribution,

$$\left(\frac{n}{p}\right)_{\rm eq} \sim e^{-(m_n - m_p)/T} \,. \tag{2.52}$$

At around 2 MeV, neutrinos decouple from the thermal bath, setting the neutrino temperature $T_\nu$. At slightly lower temperatures neutrons and protons freeze-out, determining the final $n/p$ abundance. This number directly relates to the final abundance of light nuclei and therefore is a sensitive probe for any new physics. Soon after, at around a temperature of 0.5 MeV, electrons and positrons annihilate thereby increasing the photon temperature $T_\gamma$. Finally, nucleosynthesis occurs by processes such as, $pn \to D\gamma$ and $D \to {}^4He$. This is followed with recombination (at much lower temperatures) that sets the observed value of $T_\gamma$.

With this incredibly brief and qualitative review of the important processes, we can now ask the question: what exactly do the cosmological probes constrain? As mentioned in Chapter 1, measurements of the CMB constrain the effective relativistic degrees of freedom $N_{\rm eff} \sim (T_\nu/T_\gamma)^4$. Further, we also have very precise measurements for the primordial helium and deuterium abundances, denoted by $Y_{\rm P}$ and $D/H|_{\rm P}$, respectively which are related to the $n/p$ ratio and therefore dependent on the physics of BBN.

Adding light thermal species can then change these observations in various ways.

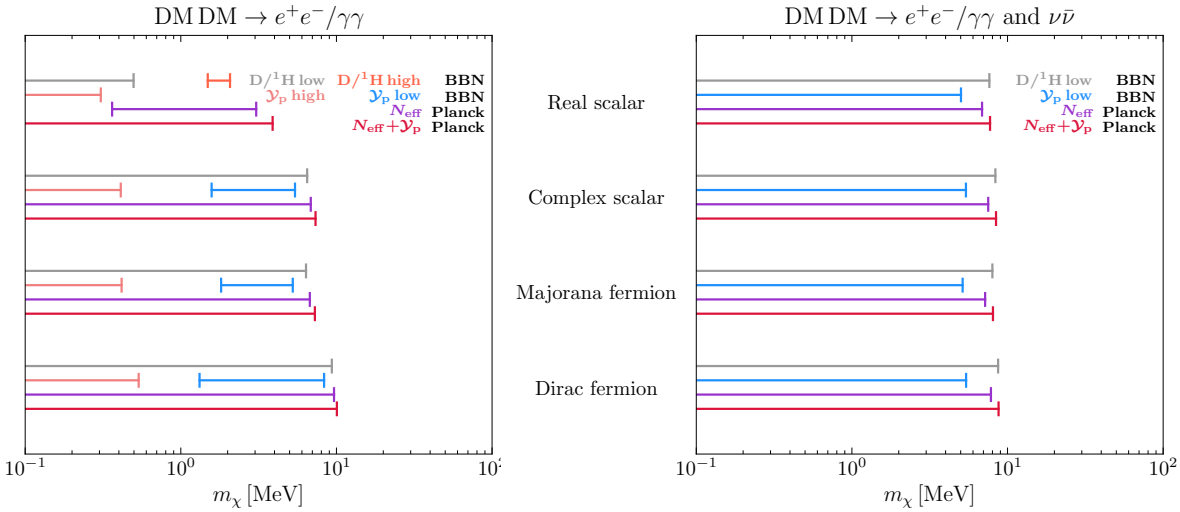


FIGURE 2.8: Bounds on a thermal DM particle annihilating into electrons/positrons (left) and additionally into neutrinos (right). The "high" and "low" correspond to over- and under-production of light elements. See the source of the figure, Ref. [67], for additional details.

### 2.3.1 Big Bang Nucleosynthesis

The prediction of light element abundances from the SM is modified in the presence of additional light species due to one (or more) of the following reasons:

1. **Contributing to the Hubble rate**: Any light species will contribute to the radiation density of the universe and therefore the Hubble rate, $H \propto \sqrt{\rho_{\rm R}}$. This contribution could be significant enough to change the temperature at which neutrons freeze-out, thereby altering the neutron abundance and consequently the final helium abundance. Our measurements of the helium abundance then place a bound on the number density of this additional species, which translates directly into a bound on particle mass *if* it is in thermal contact with the SM heat bath.

2. **Destroying light element abundances**: Annihilations into photons or electro-positron pairs can induce an electromagnetic cascade producing energetic photons, which can destroy light abundances by photo-disintegration through processes such as $D\gamma \to pn$. The exact calculation for these processes is quite involved and here we only quote the results from [67] in Fig. 2.8 for scalar, vector and fermion DM candidates.

3. **Delaying neutrino decoupling**: Additional interactions between any extra degree of freedom and neutrinos can keep the latter in thermal equilibrium with the SM heat bath for longer, delaying neutrino decoupling and decreasing $T_\nu$. This changes $N_{\rm eff}$ and therefore also the predictions of BBN.

As can be deduced, these effects are interlinked and the strength of each effect depends on the specifics of the DM model. However, it turns out that for thermal DM, these effects give a soft lower bound on the DM mass, $m_\chi \gtrsim 10\,\text{MeV}$ irrespective of whether DM is a scalar,

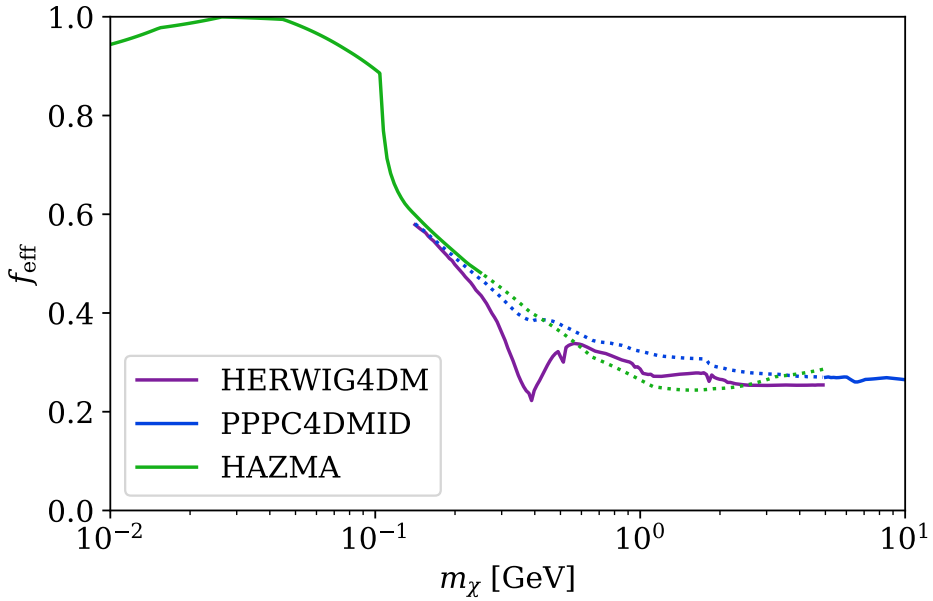


FIGURE 2.9: Efficiency function needed to calculate CMB constraints as a function of DM mass calculated using the energy injection spectra from three different numerical tools. Dotted lines represent extrapolation beyond the range of validity of each code.

vector or fermion. This is shown in Fig. 2.8 which we reproduce from [67]. The only assumptions made on the DM model in the two panels of this figure is whether DM annihilates only electromagnetically into $e^+e^-/\gamma\gamma$ (left) or also into neutrinos (right).

### 2.3.2 Cosmic Microwave Background

The CMB photons are a treasure trove of information for early universe physics. As mentioned previously, the CMB is sensitive to $N_{\rm eff}$ and therefore can be used alongside BBN to constrain DM models that change $T_\nu$ and/or $T_\gamma$ (see [68] for a comprehensive review). Additionally, CMB anisotropies can be used to constrain any DM model that injects energy into the plasma during or after recombination through annihilations or decays.

For a particle of mass $m_\chi$, the rate of energy injected in the photon-baryon plasma is characterised by the effective parameter constrained by Planck [25],

$$p_{\rm ann} = C_\chi f_{\rm eff} \left(\frac{\Omega_\chi h^2}{\Omega_{\chi,\,\rm Planck} h^2}\right)^2 \frac{\langle\sigma v\rangle_{\rm CMB}}{m_\chi} < 3.2 \times 10^{-28}\,{\rm cm}^3\,{\rm s}^{-1}\,{\rm GeV}^{-1} \tag{2.53}$$

where $C_\chi = 1/2\,(1)$ for identical (non-identical) particles, $f_{\rm eff}$ denotes the fraction of energy deposited in the plasma and $\langle\sigma v\rangle_{\rm CMB}$ is the thermally averaged annihilation cross-section at recombination. Additionally, since $p_{\rm ann}$ is generally quoted under the assumption that the additional thermal species saturates the DM abundance, we introduce a density fraction to generalise the above relation to a thermal species which is only a DM subcomponent.

The fraction of energy deposited in the plasma, $f_{\rm eff}$, has to be calculated as a function of the DM mass. For this, we require the energy injection spectra from DM annihilations into positrons and photons, $\mathrm{d}N_{e^+}/\mathrm{d}E$ and $\mathrm{d}N_\gamma/\mathrm{d}E$ respectively, which can be convoluted with energy-dependent efficiency factors [3, 69] to obtain,

$$f_{\rm eff}(m_\chi) = \frac{1}{2m_\chi}\int_0^{m_\chi} \mathrm{d}E\, E\left[2f_{\rm eff}^{e^+}(E)\frac{\mathrm{d}N_{e^+}}{\mathrm{d}E} + f_{\rm eff}^{\gamma}(E)\frac{\mathrm{d}N_\gamma}{\mathrm{d}E}\right] . \tag{2.54}$$

The injection spectra for electrons and muons can be calculated analytically but the calculation for taus and quarks is more involved. In particular for $0.25\,\mathrm{GeV} < m_\chi < 5\,\mathrm{GeV}$, the effects of various QCD resonances have to be included. These calculations can be performed using different public tools in different mass ranges. We depict the results from three of them in Fig. 2.9: PPC4DMID [70], HERWIG4DM [71, 72] and HAZMA [73].

With this calculation of $f_{\rm eff}$ and for a given DM model, Eq. 2.53 can be translated to a bound on DM mass and coupling. We will return to this equation in the context of a dark photon model in Chapter 4 but we can already see from Eq. 2.53 that a vanilla MeV-scale WIMP model with a thermal s-wave cross-section, $\langle\sigma v\rangle \sim 10^{-26}\,\mathrm{cm}^3\,\mathrm{s}^{-1}$ is excluded.

Our main takeaway here is that it is incredibly difficult to have thermal DM lighter than a few MeV. Any lighter DM particles then necessarily have to be out-of-equilibrium during recombination. This is easily achieved in FIMP models where the DM density is always smaller than its equilibrium value. This is, however, not to say that such limits on the DM mass cannot be obtained for FIMPs. Indeed, cosmological probes can be used to constrain freeze-in DM models, as was shown in [74] for the case of vector mediators. Particularly, non-thermal light DM models can be constrained by studying their impact on the formation of structure. In general, however, these constraints are significantly weaker and can be easily evaded.

# Part II

# The Middle

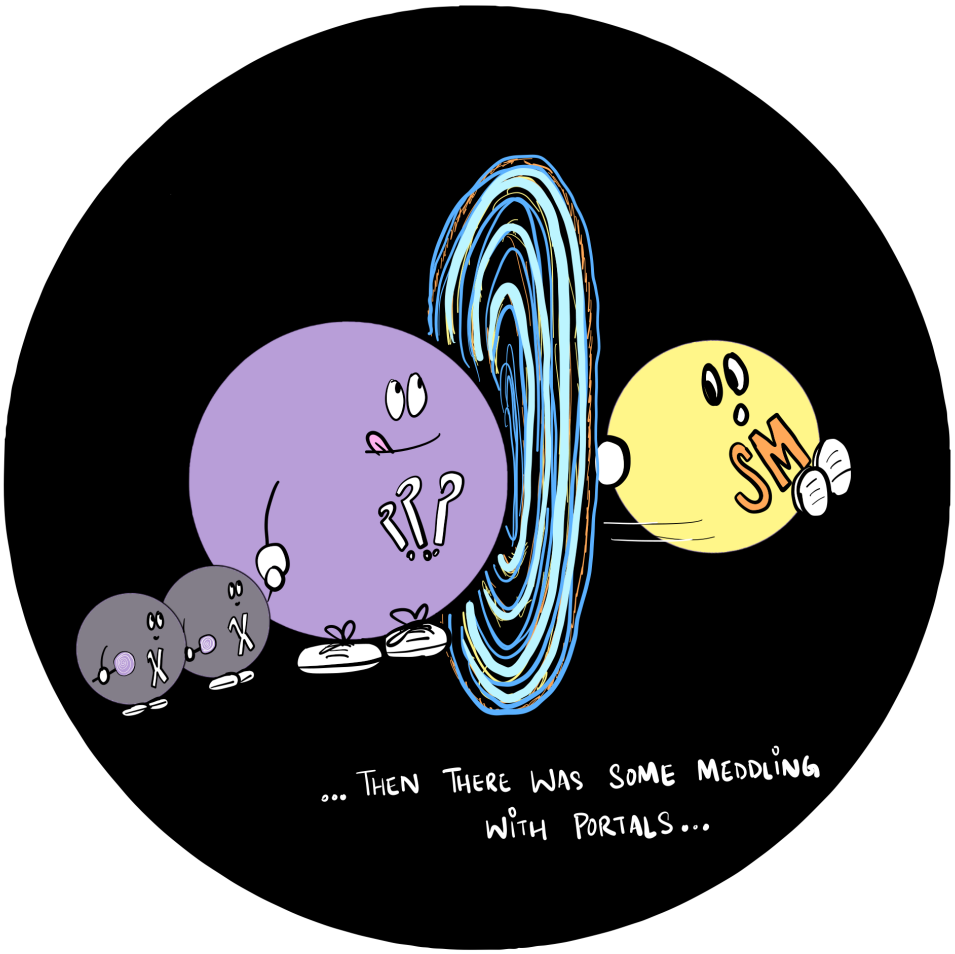

# Chapter 3

# Mediators Galore

With the foundation that we have developed over the last two chapters, we are now ready to concretely explore the DM model space from a particle physics perspective. Many DM models were initially derived from varied attempts to solve other outstanding problems in the SM [75]. For instance, WIMP candidates naturally appear in supersymmetric extensions of the SM developed in response to the hierarchy problem [76]. In the same vein, there are sterile neutrino DM models which serve to additionally explain neutrino masses and baryon asymmetry [77], and axion DM models that solve the strong CP problem [78]. In the last few years, however, DM phenomenology has found its own niche independent of its relationship to these problems.

Most experimental searches for DM rely on its assumed non-gravitational coupling to the SM. One of the most convenient ways to categorise DM models is then through the potential nature of these interactions. This results in different "portals" based on the mediating particle between the two sectors. In this thesis, we will be interested in the two most studied portals: *the Higgs Portal* which, as the name suggests, has the Higgs boson as the mediator, and *the Dark Photon Portal* which, likewise, has a vector mediator [79–83]. The DM candidate itself could be a scalar, vector or fermion, and the strength of the portal interaction determines whether or not the DM is thermally produced. Additionally, the mediating particle can be searched for at experiments independent of its connection to DM, making the portal interpretation of these mediators a complementary addition to existing searches looking for BSM physics [84–92].

Furthermore, the presence of a mediator necessarily implies interactions within the dark sector. These self-interactions can result in interesting phenomenology at large scales and therefore provide another avenue to search for new physics [93]. Contrary to DM phenomenology at terrestrial experiments, these effects would be independent of the mediator coupling to the SM and hence any derived constraints would be complementary.

In this next part, we will explore all of these effects in detail. Chapters 4 and 5 will discuss the Higgs portal and the Dark Photon portal respectively. Chapter 7 will elaborate on DM self-interactions in a model-independent fashion accounting for both scalar and vector mediators.

# Chapter 4

# Higgs Portal

The lowest dimension gauge-invariant operator in the SM consisting of the Higgs field, $\Phi^\dagger\Phi$, is uniquely situated to couple to additional particles in a renormalisable or superrenormalisable fashion [83]. This gives rise to the Higgs Portal, which for a renormalisable theory has the form,

$$\mathcal{L} \supset \frac{\lambda_{hs}}{2} |\Phi|^2 S^2 \,, \tag{4.1}$$

where $S$ is a scalar singlet neutral under $SU(3)_c \times SU(2)_L \times U(1)_Y$.[1] Higgs portal DM models with a scalar singlet have been extensively studied both in the case of freeze-in and freeze-out [94, 95]. In these models, the scalar singlet may be the DM candidate itself or simply a mediator coupled to the true DM candidate [96, 97]. These models offer a very rich phenomenology.[2] Indeed, even very simple scalar singlet DM models lend themselves to exciting cosmological histories as well as interesting low-energy behaviour [61, 82, 98–101].

In this chapter, we will explore the parameter space of a scalar singlet DM model in the context of freeze-in. In particular, we are interested in looking at the phenomenology of such a model away from the Higgs resonance, i.e., away from the mass range where the scalars are produced dominantly via Higgs decays. Further, we will include higher-order effects and non-perturbative corrections in our calculations for the DM relic abundance along with accounting for the electroweak and the QCD phase transition.

For the rest of this chapter we will distinguish between *in-medium effects* corresponding to the inclusion of the appropriate statistical factors in the Boltzmann equation, and *thermal effects* corresponding to finite temperature corrections to particle masses and the Higgs vev.

[1] One could also have a Higgs portal coupling to vectors, $|\Phi|^2 A_\mu A^\mu$, or to fermions, $|\Phi|^2 \chi\bar{\chi}$, but models with such interactions necessarily demand a UV completion because of the gauge boson mass term in the former and the explicitly non-renormalisable coupling in the latter.

[2] As can be seen from the number of papers that have been written about them.

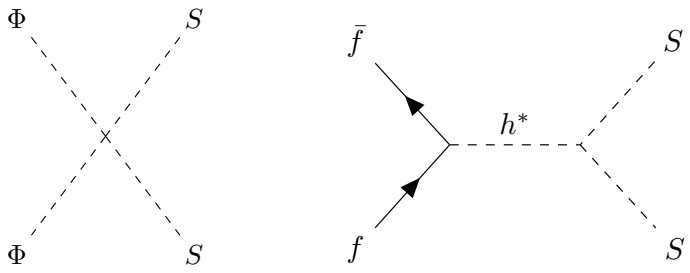


FIGURE 4.1: Dominant production channels before (left) and after (right) the electroweak phase transition.

## 4.1 Scalar Singlet Dark Matter

We consider the most general, renormalisable Lagrangian for a scalar singlet, $S$, stabilised by a $\mathbb{Z}_2$ symmetry [102–104],

$$\mathcal{L} = \frac{1}{2}\partial_\mu S \partial^\mu S + \frac{1}{2}\mu_S^2 S^2 + \frac{1}{2}\lambda_{hs} S^2 |\Phi|^2 + \frac{1}{4}\lambda_s S^4 \,. \tag{4.2}$$

After the electroweak phase transition, $|\Phi|^2 \to (v+h)^2/2$, the Lagrangian has the form,

$$\mathcal{L} = \frac{1}{2}\partial_\mu S \partial^\mu S + \frac{1}{2}(\mu_S^2 + \frac{1}{2}v^2\lambda_{hs})S^2 + \frac{1}{2}v\lambda_{hs}\, hS^2 + \frac{1}{4}\lambda_{hs}h^2S^2 + \frac{1}{4}\lambda_s S^4 \,, \tag{4.3}$$

where the scalar picks up a mass correction. As discussed in Chapter 1, the Higgs vev is a function of temperature. Therefore, the scalar mass becomes a function of temperature (independent of whether or not the scalar is in thermal equilibrium with the SM heat bath),

$$m_S(T) = \sqrt{\mu_S^2 + \frac{1}{2}\lambda_{hs} v(T)^2} \,. \tag{4.4}$$

As mentioned previously, we are interested in the case in which the scalar is produced through freeze-in. Consequently, the condition for non-equilibrium demands that the interaction rate of the scalars is always sub-Hubble. For sufficiently large reheating temperatures, this simply translates into the requirement $\lambda_{hs} \lesssim 10^{-7}$, as discussed in section 2.2.3. However, much larger values of the couplings are allowed if the reheating temperature is small, in which case the sub-Hubble nature of the rates is guaranteed by the Boltzmann suppression of the interacting particles. The scalar quartic coupling, $\lambda_s$ is largely irrelevant to the phenomenology, and therefore the parameters of interest for this model are simply $m_s$ and $\lambda_{hs}$.

From Eqs. 4.2 and 4.3, it can be clearly seen that the phenomenology of this model differs before and after the electroweak phase transition. In particular, to first order in portal coupling, the only production channel before the phase transition is $\Phi\Phi^\dagger \to SS$ (left panel of Fig. 4.1). In contrast, after the phase transition, a whole host of channels open up from Higgs decays (if kinematically allowed) to annihilation of SM particles, $f\bar{f} \to h^* \to SS$ (right panel of Fig. 4.1). This implies that the Boltzmann equation for the comoving number density of the scalar, $Y_s$, has to be solved independently in two separate regimes, $T \gtrsim T_{\rm EW}$ and $T \lesssim T_{\rm EW}$ with the

continuity of $Y_s$ imposed as a boundary condition. Additionally, we know from Chapter 1, that a second phase transition occurs in the QCD sector of the SM at a temperature of roughly $T \sim 150\,\text{MeV}$ corresponding to the confinement of free quarks and gluons into hadrons. This results in another change in the available degrees of freedom in the model—the production channels will now have hadronic initial states instead—and therefore we must make another distinction between $T_{\text{EW}} \gtrsim T \gtrsim T_{\text{QCD}}$ and $T \lesssim T_{\text{QCD}}$.

As discussed in Chapter 2, the Boltzmann equation for freeze-in is conventionally formulated in terms of the DM production cross-section, $\sigma_{f\bar{f}\to SS}$. However in this case, for reasons discussed below, it is much more precise to use the alternate formulation of the Boltzmann equation given by Eq. 2.47,

$$\frac{\mathrm{d}Y_\chi}{\mathrm{d}x} = \frac{s\langle\sigma v\rangle_{SS\to f\bar{f}}}{Hx}(Y_\chi^{\text{MB}})^2\,, \tag{4.5}$$

that depends on the DM annihilation cross-section.[3] This is useful not only because we have a semi-analytic formula for $\langle\sigma v\rangle$ that naturally includes the in-medium Bose-enhancement/Pauli-blocking effects (Eq. A.19), but also because we can formulate the DM annihilation cross-section into generic SM final states (except into $hh$) in terms of the off-shell Higgs decay width, $\Gamma_{h^*}(\sqrt{s})$, as [95],

$$\sigma v_{\text{rel}} = \frac{2\lambda_{hs}^2 v^2}{\sqrt{s}} \frac{\Gamma_{h^*}(\sqrt{s})}{(s-m_h^2)^2 + m_h^2\Gamma_h^2(m_h)}\,. \tag{4.6}$$

Here, $\Gamma_h(m_h)$, is the total decay width of the Higgs boson (including $h \to SS$ if allowed), and $v_{\text{rel}}$ is the relative velocity in the centre-of-mass frame. The benefit of such a formulation is that next-to-leading order effects on the SM side (for instance radiative corrections) can be easily included by using state-of-the-art calculations for the off-shell Higgs decay width. We will discuss exactly these effects in the following sections, along with discussing the finite temperature modifications to the partial off-shell Higgs decay widths. All of these calculations have been implemented in an upcoming release of DARKSUSY [57].

### 4.1.1 Off-shell Higgs Decays

To begin with, let us discuss the relevant off-shell Higgs decay modes at zero temperature and sufficiently large centre-of-mass energies $\sqrt{s} \gtrsim 2\,\text{GeV}$. The second condition ensures that we always have free quarks and gluons in the final state. The tree-level decay widths into fermions and gauge bosons is given by,

$$\Gamma(h \to f\bar{f}) = \frac{N_c m_f^2\sqrt{s}}{8\pi v^2}\left(1-4\eta_f\right)^{3/2}\,, \tag{4.7}$$

[3] Note that we have used $\tilde{\mathcal{C}}_{ab} = 1$ for the case of scalar singlet DM.

$$\Gamma(h \to VV) = \frac{\sqrt{s}^3}{32v^2\pi}\delta_V\sqrt{1-4\eta_V}(1-4\eta_V+12\eta_V^2)\,, \quad (V = W^\pm,\, Z) \tag{4.8}$$

where $\eta_X = m_X^2/s$, $N_c = 1\,(3)$ for leptons (quarks), $\delta_W = 2$ and $\delta_Z = 1$. Additionally, the leading-order (loop-induced) decay width into gluons is given by [105],

$$\Gamma(h \to gg) = \frac{\alpha_s^2(\sqrt{s})\sqrt{s}^3}{72v^2\,\pi^3}\left|\frac{3}{4}\sum_q A_{1/2}^h\left(\tfrac{1}{4\eta_q}\right)\right|^2, \tag{4.9}$$

where $\alpha_s(\sqrt{s})$ denotes the running strong coupling and

$$A_{1/2}^h(\tau) = 2(\tau + (\tau-1)f(\tau))\tau^{-2}\,, \tag{4.10}$$

with

$$f(\tau) = \begin{cases} \arcsin^2\sqrt{\tau} & \tau \le 1 \\ -\frac{1}{4}\left(\log\frac{1+\sqrt{1-\tau^{-1}}}{1-\sqrt{1-\tau^{-1}}} - i\pi\right)^2 & \tau > 1\,. \end{cases} \tag{4.11}$$

The decay width into photons can be written in an analogous way but gives a negligible contribution to the total decay width.

The analytic decay widths presented above receive significant higher-order corrections [105]. In particular, for large centre-of-mass energies, $\sqrt{s} \gg v$, when the decay into gauge bosons dominates, next-to-leading order (NLO) corrections arise from the emission of additional gauge bosons. Furthermore, for small centre-of-mass energies, QCD corrections to the quark final states become significant [95, 106]. These effects can be easily captured by calculating the off-shell decay widths using HDECAY [107, 108].

However, the results from HDECAY cannot be used in the calculation of the thermally averaged cross-section in certain regions of the parameter space. In particular,

- for large centre-of-mass energies, $\sqrt{s} \gtrsim 1\,\text{TeV}$, the off-shell decay widths calculated by HDECAY become unphysical, and,
- for small centre-of-mass energies, $\sqrt{s} \lesssim 2\,\text{GeV}$, and for temperatures below the QCD phase transition, HDECAY cannot be used to calculate the decay widths into the relevant degrees of freedom, i.e., hadrons.

We will next discuss how to resolve these issues.

### 4.1.2 Cross-sections at Large Energies: Unitarity Considerations

To see that the off-shell decay widths obtained from HDECAY are unphysical, we note that in the lab frame the DM annihilation cross-section into various SM final states can be written

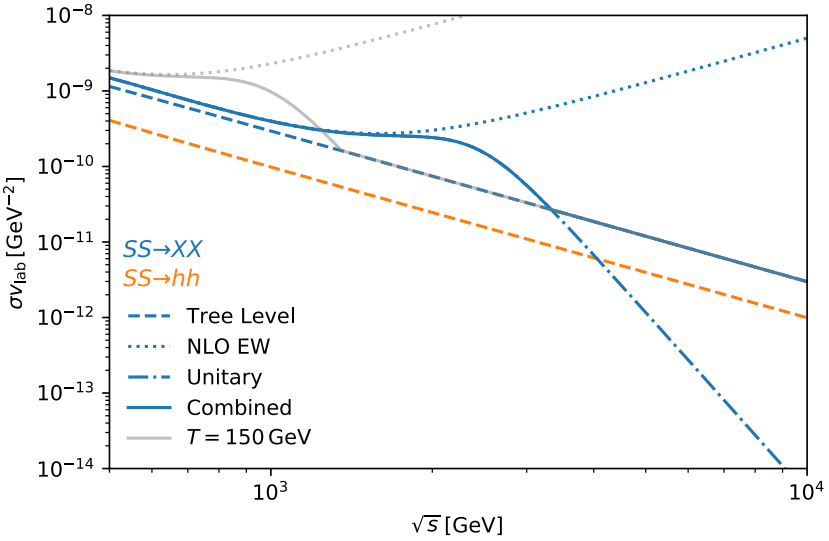


FIGURE 4.2: The DM annihilation cross-section at large centre of mass energies at tree level (dashed line), including NLO electroweak corrections (dotted line), and unitarised as described in text (solid line). The grey dotted and solid lines represent the NLO and the unitarised cross-section respectively at finite temperature, $T = 150\,\text{GeV}$ ($v \approx 100\,\text{GeV}$).

as,

$$\sigma(SS \to hh) v_{\rm lab} = \frac{\lambda_{hs}^2}{32\pi s}\,, \tag{4.12}$$

$$\sigma(SS \to XX) v_{\rm lab} = \frac{\lambda_{hs}^2 v^2}{\sqrt{s}} \frac{1}{(s-m_h^2)^2 + m_h^2 \Gamma_h^2} \Gamma_{h^*}(\sqrt{s})\,, \tag{4.13}$$

where $v_{\rm lab} = \sqrt{s(s-4m_S^2)}/(s-2m_S^2)$, and the second expression includes higher-order corrections in the SM couplings. Now, in order to ensure unitarity, a cross-section has to fall at least as fast as $1/s$ in the limit $s \to \infty$, which implies that in the cross-sections stated above, $\Gamma_{h^*}(\sqrt{s})$ should grow at most as $s^{3/2}$. This is exactly the case if we use the analytic expression for the decay widths presented in Eqs. 4.7–4.9. In particular, using these expressions, we recover the cross-section in the unbroken theory in the limit $s \to \infty$,

$$\sigma(SS \to hh) + \sigma(SS \to XX)^{\rm tree} \to \sigma(SS \to \Phi^\dagger \Phi)\,. \tag{4.14}$$

However, the NLO electroweak corrections implemented in HDECAY predict a more rapid growth for $\Gamma_{h^*}(\sqrt{s})$ (see the dotted line in Fig. 4.2). This implies that higher-order effects become increasingly more important at large $\sqrt{s}$.

Since these corrections are non-trivial to evaluate, we regulate this divergence in the following way. Using the approach from [109], we replace the on-shell Higgs decay width in the propagator by the off-shell Higgs decay width,

$$\sigma(SS \to XX)^{\rm unitary} v_{\rm lab} = \frac{\lambda_{hs}^2 v_0^2}{\sqrt{s}} \frac{1}{(s-m_h^2)^2 + m_h^2 \Gamma_{h^*}(\sqrt{s})^2} \Gamma_{h^*}(\sqrt{s})\,, \tag{4.15}$$

to ensure that the cross-section is well-behaved as $s \to \infty$. However, this modification forces the cross-section to fall faster than $1/s$ at large $s$ and we no longer recover the result from the unbroken theory (see the dashed-dotted line in Fig. 4.2). Therefore, we implement the total cross-section as,

$$\sigma(SS \to XX)^{\text{total}} = \max\left[\sigma(SS \to XX)^{\text{tree}}, \sigma(SS \to XX)^{\text{unitary}})\right] , \tag{4.16}$$

thereby ensuring that the NLO electroweak corrections are captured for $\sqrt{s} \lesssim 1\,\text{TeV}$, unitarity is not violated for $\sqrt{s} \gtrsim 1\,\text{TeV}$, and that the tree-level result in the unbroken theory is recovered in the limit $\sqrt{s} \to \infty$.

In general, the cross-section defined above can be compared to the usual unitarity bound on the DM annihilation cross-section [110], which for relativistic particles reads,

$$\sigma_{\text{ann}} v_{\text{lab}} < \frac{4\pi}{\sqrt{s}\sqrt{s - 4m_s^2}} . \tag{4.17}$$

This results in a bound on $\lambda_{hs}$ as a function of $\sqrt{s}$ which turns out to be the strongest for $\sqrt{s} \approx 2.2\,\text{TeV}$, yielding, $\lambda_{hs} < 10.9$. This bound is stronger than the tree-level bound, $\lambda_{hs} < 8\pi$, derived by considering the scattering process $Sh \to Sh$ in the limit $\sqrt{s} \to \infty$ [111], although still much larger than the freeze-in couplings relevant for our calculations.

Such a discussion on unitarity becomes important even for relatively small centre of mass energies when one includes temperature corrections to the theory. In particular, the relevant scale of this problem, i.e., when these bounds kick in, is not determined by $\sqrt{s}$ but instead by the ratio, $\sqrt{s}/v$. This is evident when looking at the analytic expressions for the off-shell Higgs decay width, Eqs. 4.7–4.9, which all scale as $\Gamma \propto v f(\sqrt{s}/v)$ for different functions $f(x)$. Therefore, the off-shell decay width at finite temperature can be written in terms of the zero-temperature one as

$$\Gamma_{h^*}(T, \sqrt{s}) = \Gamma_{h^*}\left(\sqrt{s}\frac{v(0)}{v(T)}\right)\frac{v(T)}{v(0)} . \tag{4.18}$$

It is evident then that the limit $\sqrt{s} \to \infty$ is degenerate with the limit $v(T) \to 0$ implying that the modifications introduced above become relevant for much smaller $\sqrt{s}$ close to the temperature of the electroweak phase transition (see for example the grey lines in Fig. 4.2). In particular, these modifications are what ensure a smooth transition between the broken and the unbroken phase.

### 4.1.3 Cross-Sections at Small Energies: The Effects of Chiral Symmetry Breaking

As mentioned before, for temperatures smaller than the electroweak phase transition, the decay into free quarks and gluons is forbidden. For $\sqrt{s} \gtrsim 2\,\text{GeV}$, however, it is a very good approximation to assume such decays with subsequent hadronisation. This treatment fails for $\sqrt{s} \lesssim 2\,\text{GeV}$ and instead we require the off-shell decay width into QCD bound states. These

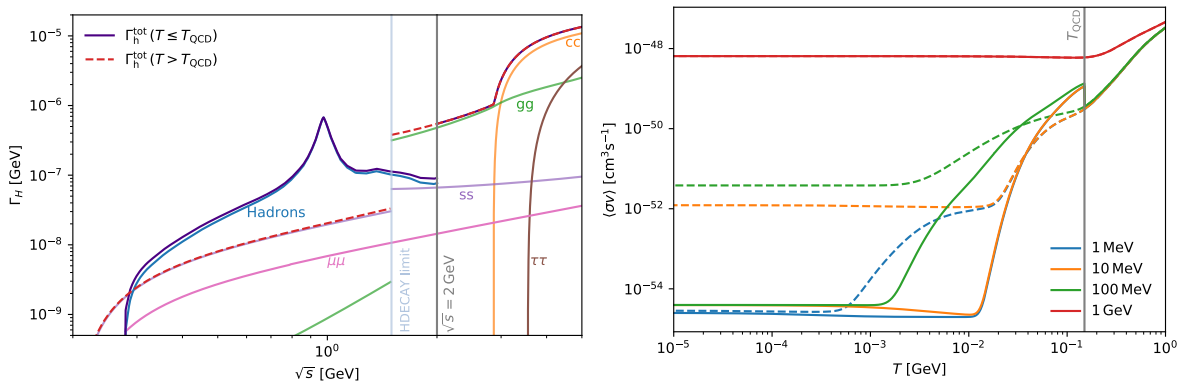


FIGURE 4.3: The off-shell Higgs decay width into various final states at small centre-of-mass energies. The total off-shell decay width at $T \leq T_{\rm QCD}$ ($T > T_{\rm QCD}$) is given by the solid indigo (dashed red) line. Right: The thermally averaged annihilation cross-section as a function of inverse temperature for different values of the DM mass accounting for the QCD phase transition (solid lines) and otherwise (dashed lines).

can be calculated using chiral perturbation theory with the relevant form factors evaluated using a dispersive analysis [112].

In the left panel of Fig. 4.3, we plot the off-shell Higgs decay width into free quarks and hadrons with the vertical grey line at $\sqrt{s} = 2\,\text{GeV}$ representing the limit at which the dispersive analysis used to calculate the hadronic decay width breaks down. Additionally, a light blue line indicates the limit at which calculations from HDECAY for quark and gluon final states cannot be trusted. For $T \geq T_{\rm QCD}$, we always use the off-shell decay channels into free quarks and gluons (the total decay width is represented by dashed red line). On the other hand, for $T \leq T_{\rm QCD}$, we use the hadronic decay width for $\sqrt{s} < 2\,\text{GeV}$ and the decay into free quarks otherwise (solid indigo line).

The resulting difference in the thermally averaged cross-section can be seen in the right panel of Fig. 4.3 for different DM masses, where the solid lines correspond to hadronic final states and the dotted lines to quark ones. Note that for this plot we ignore the in-medium effects in the calculation of the thermal average which is a good approximation for small temperatures. The temperature of the QCD phase transition is indicated by the grey vertical line. The discontinuity in $\langle\sigma v\rangle$ at the phase transition directly follows from the discontinuity in the total decay width between the free quark and hadronic approximations (left panel of Fig. 4.3). The lack of the light quarks and gluon decay channels when accounting for the QCD phase transition results in a substantial suppression of the total cross-section for MeV-scale DM at small temperatures. This might have a significant impact on the freeze-in abundance if the reheating temperature is small, as we will discuss in section 4.2.2.

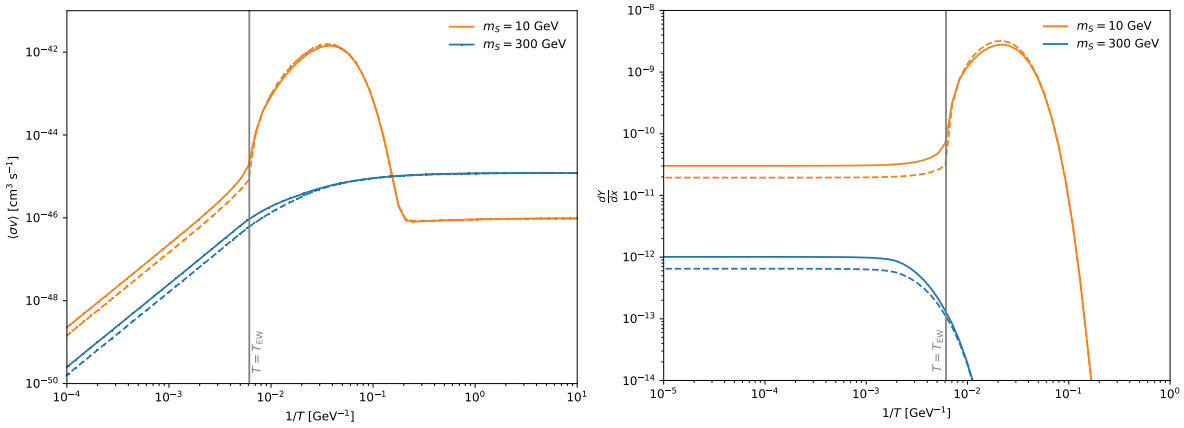


FIGURE 4.4: The thermally averaged DM annihilation cross-section (left) and the DM production rate (right) as a function of inverse temperature for two values of DM mass. The dotted lines represent the same quantities but without including in-medium effects.

## 4.2 Freeze-in Production

We now have all the necessary tools required to calculate the freeze-in abundance for a scalar singlet DM model. For $m_S < m_h/2$, the dominant production happens at a temperature $T \sim m_h/2$ via Higgs decays. The resulting relic abundance of the scalars can be easily calculated and receives only small corrections from thermal and in-medium effects [61, 113]. We will instead be focusing our attention on the case when the contribution from Higgs decays is subdominant. This can be either when such decays are kinematically forbidden, i.e., $m_S > m_h/2$, or if the reheating temperature is small such that the density of Higgs bosons is exponentially suppressed, $m_S, T_{\rm RH} \ll m_h$. We discuss these two scenarios below.[4]

### 4.2.1 High Reheating Temperature

For $T_{\rm RH} \gg m_S, m_h$, the freeze-in production is independent of the reheating temperature. This follows directly from the discussion in section 4.1.2: since the DM production cross-section is proportional to $1/s$, the production rate scales proportional to $T$ and is therefore sub-Hubble for high enough temperatures.

In Fig. 4.4, we plot the thermally averaged annihilation cross-section (left) and the DM production rate (right) as a function of temperature for two DM masses, $m_\chi = 10\,\text{GeV}$ and $m_\chi = 300\,\text{GeV}$. The dotted lines represent the case when in-medium effects are ignored. For $m_\chi = 10\,\text{GeV}$, the dominant production is through the production of an on-shell Higgs and therefore the rate falls rapidly once the typical centre-of-mass energy in the thermal bath is smaller than the Higgs mass, $T < m_h$. On the other hand, for $m_\chi = 300\,\text{GeV}$, the DM production is always via an off-shell Higgs boson. In this case, the temperature scaling of the

[4]Note that while we have focused on $2 \to 2$ processes, there is an interesting discussion to be had regarding the $1 \to 2$ process in a plasma and the corresponding modification of the propagator for the Higgs boson at finite temperature.

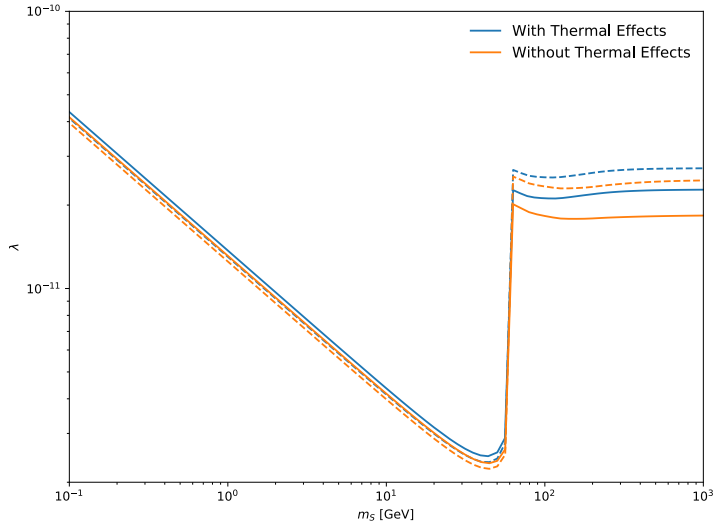


FIGURE 4.5: The coupling required to reproduce the relic abundance as a function of DM mass with and without accounting for thermal effects. The dotted lines denote the case when in-medium effects are ignored.

thermally averaged annihilation cross-section becomes trivial. However, the production rate gets exponentially suppressed as the temperature drops below the DM mass, $T \lesssim 300\,\text{GeV}$, as is expected from looking at the right hand side of Eq. 4.5. For both masses, we see that the in-medium effects amount to an enhancement in the annihilation cross-section and therefore the production rate at large temperatures. Additionally, our implementation of thermal masses and vev ensures a smooth transition at the electroweak phase transition (solid grey line).

For a given value of $\lambda_{hs}$ and $m_S$, integrating the production rate gives us the DM abundance today. In Fig. 4.5 we plot the coupling values required to reproduce the observed DM abundance as a function of DM mass when considering and ignoring in-medium effects (solid and dotted lines respectively). As expected, in-medium effects are less relevant when production happens via an on-shell Higgs ($m_S < m_h/2$), whereas significant deviations arise in the opposing limit, $m_S > m_h/2$. Further, thermal effects also become important for large DM masses in which case production happens at high temperatures.

### 4.2.2 Low Reheating Temperature

For the case of small reheating temperatures, the final freeze-in abundance becomes sensitive to $T_{\text{RH}}$. This is because the production can be written in terms of effective dimension-5 operators,

$$\mathcal{L} \supset \frac{1}{\Lambda_f} f \bar{f} S^2 \,, \tag{4.19}$$

where $\Lambda_f = m_h^2/(\lambda_{hs} m_f)$, resulting in a cross-section that becomes constant at large centre-of-mass energies and therefore a production rate dominated by the largest accessible temperatures, (see also right panel of Fig. 4.3). A lower bound on the reheating temperature is set

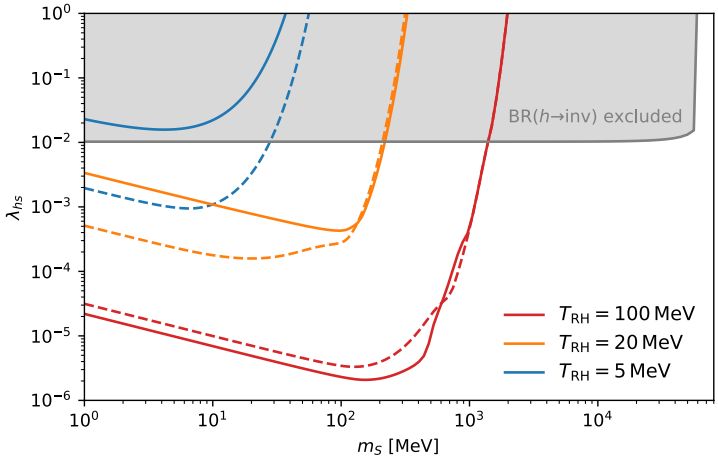


FIGURE 4.6: The coupling required to reproduce the relic abundance as a function of mass for different values of the reheating temperature. The dotted lines indicate the case in which the QCD phase transition is ignored and production via free quarks and gluons in allowed. The exclusion bound from searches for invisible Higgs decays is shown in grey.

at $T \sim 5\,\text{MeV}$ by the abundance of light elements [27], as also discussed in Chapter 1. From the right panel of Fig. 4.3, it is clear that for MeV-scale reheating temperatures, the effects of the QCD phase transition on DM production will become relevant. In particular, the suppression in the annihilation cross-section for small DM masses means that larger couplings will be required to saturate the DM abundance. Interestingly, such large couplings (for small scalar masses) mean that the SM Higgs decay width would be modified enough to be observable at colliders. In particular, LHC searches for invisible Higgs decays constrain the branching ratio [114],

$$\text{BR}(h \to \text{inv}) = \frac{\Gamma(h \to SS)}{\Gamma(h \to SS) + \Gamma_{h,\text{SM}}} < 0.11 \tag{4.20}$$

where,

$$\Gamma(h \to SS) = \frac{\lambda_{hs}^2 v^2}{32\pi m_h} \sqrt{1 - \frac{4m_S^2}{m_h^2}}\,, \tag{4.21}$$

resulting in a bound on the portal coupling, $\lambda_{hs} < 0.01$.

This is shown in Fig. 4.6 where we plot the coupling values that reproduce the DM abundance as a function of DM mass for different values of the reheating temperature. As expected, for sufficiently small reheating temperatures, there is a substantial difference between when we account for the QCD phase transition (solid lines) and when we do not (dotted lines). Additionally, the production rate for DM masses larger than the reheating temperature is exponentially suppressed resulting in a steep rise in the coupling. In such a case, the unitarity bound on the coupling, $\lambda_{hs} < 10$, becomes relevant. On the other hand, for small DM masses as well as low reheating temperatures, the couplings required to reproduce the DM abundance are substantially larger than the standard freeze-in couplings. Interestingly, the smallest masses

and couplings considered here are already excluded by LHC data.

## 4.3 Conclusions

The scalar singlet, as one of the simplest viable DM models, has received a lot of attention in the literature. In this chapter, we looked at improved estimates for the freeze-in abundance of these scalars focusing on the parameter space where the scalar production via Higgs decays is negligible. This could be either if the decays are kinematically forbidden or if the reheating temperature is small enough to ensure the exponential suppression of the density of the Higgs bosons. In both these scenarios, accurate relic density calculations rely on the inclusion of higher-order effects as well as a proper treatment of the electroweak and QCD phase transitions.

Higher order effects in the cross-section can be simply included in the relic density calculation by reformulating the Boltzmann equation in terms of the DM annihilation cross-section (as opposed to the conventional *production* cross-section). Since the annihilation cross-section is proportional to the partial off-shell Higgs decay width, an improved estimate of the DM production rate can be obtained by evaluating this decay width at NLO with the help of numerical tools such as HDECAY. Since these decay widths depend on the ratio $\sqrt{s}/v$, this prescription can be easily generalised for use at finite temperature. There are two caveats to these calculations. First, for large centre-of-mass energies, $\sqrt{s}/v \gtrsim O(\text{TeV})$, the NLO cross-section tends to diverge and we need to use a "unitarised" cross-section to ensure our results are always physical. On the other hand, at small centre-of-mass energies, $\sqrt{s} \lesssim O(\text{GeV})$, QCD corrections become important. In particular, for temperatures below that of the QCD phase transition, the relevant degrees of freedom are hadrons instead of quarks, and the off-shell decay width has to be calculated using chiral perturbation theory.

In-medium effects, corresponding to the statistical factors in the Boltzmann equation, can be easily included by a redefinition of the thermal average which we already discussed in Chapter 2. Thermal effects, accounting for the electroweak and QCD phase transitions, on the other hand, can be incorporated by simply replacing all masses with their temperature-dependent values as well as by solving the Boltzmann equation separately in three separate regimes: before the electroweak phase transition, after the electroweak phase transition but before the QCD phase transition, and after the QCD phase transition respectively.

We find that thermal and in-medium effects are highly relevant for large DM masses, $m_S > m_h/2$ and can change the DM abundance by upto a factor of 2 (Fig. 4.5). Additionally, for small DM masses, $m_S \sim O(\text{MeV})$, accounting for the QCD phase transition results in a substantial difference in the relic density estimate when considering low reheating temperatures. This difference can be as large as a few orders of magnitude in coupling for $T_{\text{RH}} \gtrsim 5\,\text{MeV}$ (Fig. 4.6). Surprisingly, the smallest masses and couplings considered here are already excluded by the LHC data.

Our calculations demonstrate the necessity of including in-medium and thermal effects in relic density calculations, as well as a need for numerical tools to obtain accurate and fast results. To this end, we have implemented all of these effects in an upcoming version of DARKSUSY, which can now be used to carry out precise freeze-in calculations.

# Chapter 5

# Dark Photon Portal

Another simple way to extend the SM is by adding particles charged under a new $U(1)'$ gauge symmetry. Interactions with the SM can then be mediated through a kinetic mixing between the field strengths of this $U(1)'$ and the SM hypercharge, represented by [79, 115] ,

$$\mathcal{L} \supset -\frac{\kappa}{2} F_Y^{\mu\nu} F'_{\mu\nu} \,, \tag{5.1}$$

where $\kappa$ denotes the coupling strength. Rotating the fields into the mass basis couples the gauge boson of the $U(1)'$—the dark photon—to the SM fermions thus providing a portal between the two sectors. Alternately, it is also possible for the SM particles to be explicitly charged under the new $U(1)'$. This is equivalent to saying that one of the remaining global symmetries of the SM is gauged. This could be, for instance, baryon number, $U(1)_B$, difference between baryon and lepton number, $U(1)_{B-L}$, or differences in family-lepton number $U(1)_{L_i - L_j}$ (where $i, j = e, \mu, \tau$) [116–118].[1]

In this chapter, we will study DM models employing both versions of the dark photon portal. We begin with a brief overview of kinetic mixing and mass mixing between the visible and dark photons in section 5.1. We then discuss the case of kinetic mixing in a light thermal DM model in section 5.2, making our calculations for the DM abundance and cosmological constraints from Chapter 2 more rigorous. We present the case where the SM is also gauged under the new $U(1)'$ in section 5.3 and map out the viable parameter space for such a model assuming DM is produced via freeze-in. The conclusions follow in section 5.4

Sections 5.2 and 5.3 closely follow the discussion in [3] and [1].

[1] Note that these gauge symmetries are only physically viable if the fermion spectrum of the theory is anomaly free. This implies that in the SM only one of the $U(1)_{L_i - L_j}$ symmetries is simultaneously viable [119]. Additionally, $U(1)_{B-L}$ can be made anomaly-free by adding three right-handed neutrinos. For anomaly free models of gauged baryon number, see [120].

## 5.1 The Structure of a Dark Photon Lagrangian

### 5.1.1 Kinetic Mixing

We will begin with a general description of a new $U(1)'$ gauge boson referred to as the dark photon. Under the assumptions of Lorentz invariance, we can write a mixing term between this $U(1)'$ and the SM hypercharge, as in Eq. 5.1. Next, we have to define whether or not this gauge boson is massive. From Chapter 1, we know that explicit mass terms for gauge bosons are prohibited by gauge symmetries. Nevertheless, it is possible to include massive dark photons in a theory by assuming that they obtain a mass via a secondary mechanism. One way to do this is by postulating a *dark higgs mechanism*, i.e., adding a scalar field that spontaneously breaks the $U(1)'$ symmetry yielding a mass term for the dark photon. The parameters of the theory can generally be chosen such that the phenomenology of the dark higgs is irrelevant to the low-energy description of the theory.[2] Another popular way to generate the dark photon mass without the addition of any new degrees of freedom is through the *Stuckelberg mechanism* [122, 123]. Since the Stuckelberg mass is not associated with the breaking of a symmetry, it is a free parameter of the model not subject to constraints from the scalar sector.

From this discussion, one can write down the following Lagrangian in complete generality,

$$\mathcal{L} = -\frac{1}{4}B_{\mu\nu}B^{\mu\nu} - \frac{1}{4}F'^{\mu\nu}F'_{\mu\nu} - \frac{\tilde{\kappa}}{2}B^{\mu\nu}F'_{\mu\nu} + \frac{m_{A'}^2}{2}A'^{\mu}A'_{\mu} - gJ^{\mu}_{\rm SM}B_{\mu}\,, \tag{5.2}$$

where $B_\mu$ represents the SM hypercharge and $J^\mu_{\rm SM}$ the SM charged current. The canonical kinetic terms are obtained by the transformation [84],

$$\begin{pmatrix} B_\mu \\ W^3_\mu \\ A'_\mu \end{pmatrix} \rightarrow \begin{pmatrix} 1 & 0 & -\frac{\tilde{\kappa}}{\sqrt{1-\tilde{\kappa}^2}} \\ 0 & 1 & 0 \\ 0 & 0 & \frac{1}{\sqrt{1-\tilde{\kappa}^2}} \end{pmatrix} \begin{pmatrix} B_\mu \\ W^3_\mu \\ A'_\mu \end{pmatrix}\,, \tag{5.3}$$

where $W^3_\mu$ is the neutral gauge boson of $SU(2)_L$. The resulting mass matrix, $\mathcal{M}^2$, can be diagonalised by two rotations,

$$R_1(\xi)R_2(\theta_W) = \begin{pmatrix} 1 & 0 & 0 \\ 0 & \cos\xi & \sin\xi \\ 0 & -\sin\xi & \cos\xi \end{pmatrix} \begin{pmatrix} \cos\theta_W & \sin\theta_W & 0 \\ -\sin\theta_W & \cos\theta_W & 0 \\ 0 & 0 & 1 \end{pmatrix}\,, \tag{5.4}$$

[2] For extremely light dark photons, it is not possible to disentangle the effects of the dark Higgs (which in such a case would also be extremely light) from the phenomenology of the theory. In particular for $m_{A'} \sim O(\mathrm{eV})$, strong constraints arise on the kinetic mixing parameter as a result of the stellar production of this light dark higgs and the associated stellar cooling [121].

such that diag $(m_\gamma^2, m_Z^2, m_{A'}^2) = R_1(\xi)R_2(\theta_W)\mathcal{M}^2 R_2(\theta_W)^T R_1(\xi)^T$ where $\theta_W$ is the weak mixing angle, $\cos\theta = m_W/m_Z$, and $\xi$ is an additional angle,

$$\tan 2\xi = \frac{2\tilde{\kappa}\sin\theta_W}{1 - m_{A'}^2/m_Z^2}. \tag{5.5}$$

Using these transformations, we end up in a basis where the photon is massless and the dark photon and Z-boson receive small mass corrections of order $\kappa^2$. To leading order in $\kappa$ the transformations above are equivalent to the replacement [80, 124],

$$\begin{pmatrix} A \\ Z \\ A' \end{pmatrix} \to \begin{pmatrix} A - \kappa A' \\ Z - \kappa\tan\theta_W \dfrac{m_{A'}^2}{m_Z^2} A' \\ A' + \kappa\tan\theta_W \dfrac{m_Z^2}{m_Z^2 - m_{A'}^2} Z\,, \end{pmatrix} \tag{5.6}$$

where $\kappa \equiv \tilde{\kappa}\cos\theta_W$.[3] This implies that the SM charged current couples to the dark photon with a strength proportional to $e\kappa$. The neutral current (which couples to the Z-boson) also picks up a coupling to the dark photon, but one that is suppressed by an additional factor of $m_{A'}^2/m_Z^2$ in the regime $m_{A'} < m_Z$. Further, any particle that couples to the dark photon—for instance, a dark fermion charged under $U(1)'$—will invariable pick up a coupling to the Z-boson, although this will be suppressed by the fermion's coupling to the dark photon, $g_{\rm DM}$.

To summarise, we can always write the vacuum Lagrangian for a light kinetically mixed dark photon as,

$$\mathcal{L}_{\rm vac} = -\frac{1}{4}F^{\mu\nu}F_{\mu\nu} - \frac{1}{4}F'^{\mu\nu}F'_{\mu\nu} + \frac{m_{A'}^2}{2}A'^{\mu}A'_{\mu} + J^{\mu}_{\rm SM}(eA_\mu + e\kappa A'_\mu) + g_{\rm DM}J^{\mu}_{\rm DM}A'_\mu\,, \tag{5.7}$$

where $J^{\mu}_{\rm DM}$ denotes a dark current and we have ignored the dark photon and dark current coupling to the Z-boson as argued above.

### 5.1.2 Light Dark Photons In-Medium: Effects on Masses and Couplings

We will now extend the discussion above to include in-medium effects on the masses and couplings of dark photons. We consider the Lagrangian,

$$\mathcal{L} \supset -\sum_f \left(eq_f \bar{f}\gamma^\mu f A_\mu + g' q'_f \bar{f}\gamma^\mu f A'_\mu\right)\,, \tag{5.8}$$

where $q_f$ and $q'_f$ denote the fermion charges under $U(1)$ and $U(1)'$ respectively, and the sum over $f,\ \bar{f}$, includes the *complete* fermion spectrum of the model, i.e., both the SM fermions and the dark fermions. For the moment, we will be interested in the case when $g' \ll e$. Note that this Lagrangian is completely general to leading order in coupling since we have some

[3] Note that one can always start with the definition of kinetic mixing as $\tilde{\kappa} = \kappa/\cos\theta_W$ in Eq. 5.2 and indeed, this is what is implicitly assumed while studying phenomenology (see for example, [80]).

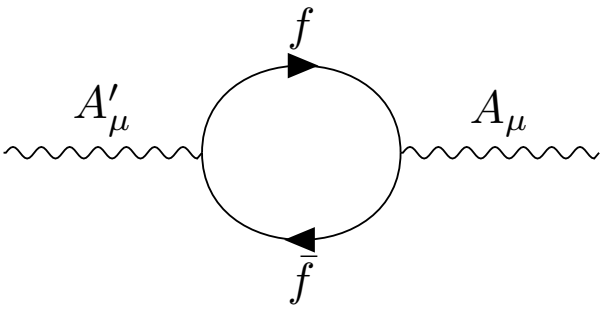


FIGURE 5.1: In-medium mass mixing between the visible and dark photon.

freedom in the definition of $g'q'_f$ to include the effects of any explicit kinetic mixing at the level of the Lagrangian.

From Chapter 1, we know that the SM photon develops an in-medium mass as a result of its interactions with the thermal plasma, (see right panel of Fig. 1.2):

$$m_A^2 \approx \sum_f \frac{e^2 q_f^2}{9} \equiv q_{\rm eff} \frac{e^2 T^2}{9} \,. \tag{5.9}$$

In this equation, the sum includes only relativistic fermions and $q_{\rm eff}$ denotes the effective number of charge degrees of freedom. A dark photon in-medium will similarly obtain a thermal mass correction given by,

$$\Delta m_{A'}^2 \approx \sum_f \frac{g'^2 q_f'^2}{9} T^2 \,. \tag{5.10}$$

This correction is, however, negligible for massive dark photons and small values of the coupling $g'$. Plasma effects will additionally induce a mass-mixing between the visible and the dark photons, as shown in Fig. 5.1,

$$\mathcal{L} \supset \delta m^2 A^\mu A'_\mu \,, \tag{5.11}$$

which can be similarly parameterised[4]

$$\delta m^2 \approx \sum_f \frac{e g' q_f q'_f}{9} T^2 \equiv q'_{\rm eff} \frac{e g' T^2}{9} \,. \tag{5.12}$$

The effective mixing degrees of freedom, $q'_{\rm eff}$, differ from the charge degrees of freedom, $q_{\rm eff}$ since the latter always monotonically increase with the temperature (as more and more particles become relativistic). In contrast, $q'_{\rm eff}$ can have negative contributions if $q_f$ and $q'_f$ have opposing signs. Additionally, since $g' \ll e$ by assumption, the mass mixing is always smaller than the plasmon mass, $\delta m^2 \ll m_A^2$.

[4]Eq. 5.12 reduces to the known forms in certain limits. For example it can be compared to Eq. (D2) in [125] if the plasma is assumed to be composed primarily of electrons.

This induced mass mixing can be removed through the rotation, $A \to A - \theta A'$ and $A' \to A' + \theta A$, with the mixing angle defined by,

$$\theta = \frac{\delta m^2}{m_A^2 - m_{A'}^2}\,, \tag{5.13}$$

resulting in the Lagrangian,

$$\begin{aligned}\mathcal{L} \supset & -\sum_f \left[eq_f \bar{f}\gamma^\mu f(A_\mu - \theta A'_\mu) + g'q'_f \bar{f}\gamma^\mu f(A'_\mu + \theta A_\mu)\right] \\ = & -\sum_f \left[(eq_f + \theta g'q'_f)\bar{f}\gamma^\mu f A_\mu + (g'q'_f - \theta eq_f)\bar{f}\gamma^\mu f A'_\mu\right]\,.\end{aligned} \tag{5.14}$$

In the limit of extremely light dark photons, $m_{A'} \ll m_A$, the mixing angle reduces to

$$\theta = \frac{g'}{e}\frac{q'_{\text{eff}}}{q_{\text{eff}}} = \frac{g'}{e}\frac{q'_f}{q_f} \tag{5.15}$$

such that if the dark charges are proportional to the electromagnetic charges, $q'_f = \kappa q_f$, as is the case for models with kinetic mixing, the dark photon coupling to the SM fermions vanishes,

$$g'q'_f - \theta eq_f = g'\kappa q_f - \frac{g'}{e}\frac{\kappa q_f}{q_f}eq_f = 0\,. \tag{5.16}$$

This is exactly the reason why kinetically mixed light dark photons evade thermalisation and therefore the strong constraints coming from BBN and CMB. In general, however, the temperature induced mixing is a non-trivial function of temperature.

We end this section by mentioning a few additional subtleties to be kept in mind while considering in-medium effects. First, as we have pointed out elsewhere in this thesis, it is always important to separate the physics before and after the electroweak phase transition. In the context of the photon-dark photon phenomenology, this results in replacing the particles and couplings with their unbroken counterparts. In particular, before the electroweak phase transition, the massive photon is replaced by a massive hypercharge boson with a mass given by [23],

$$m_Y^2 = q_{\text{eff}}\frac{g_Y^2 T^2}{9}. \tag{5.17}$$

Here, $g_Y$ is the hypercharge gauge coupling and $q_{\text{eff}}$ are the effective charge degrees of freedom before the phase transition,

$$q_{\text{eff}} = \sum_{f_L} Y_{f_L}^2 + \frac{1}{2}\sum_{f_R} Y_{f_R}^2 + 2Y_H^2\,, \tag{5.18}$$

with $Y_i$ representing the hypercharge assignments for left ($L$)- and right ($R$)- handed fermions, and the complex Higgs doublet ($H$). The medium-induced mass mixing is then between this gauge boson and the dark photon. Additionally, the SM fermions are replaced with their chiral

counterparts with different masses for the left- and right- handed components as discussed in section 1.2.2.

Second, just like in the case of kinetic mixing studied in section 5.1, in-medium effects after the phase transition will also induce a mixing between the dark photon and the Z-boson. This mixing, however, will be suppressed by the Z-boson mass following a similar line of reasoning as before and can therefore be neglected. Additionally, before the phase transition, one could in principle, think about a mixing between the third electroweak gauge boson $W^3_\mu$ and the dark photon, however the diagrams contributing to such a mixing cancel out [126].

Finally it is important to address when these in-medium effects are important. We re-emphasise that for extremely light photons $m_{A'} \lesssim$ keV, these effects ensure that models of kinetic mixing are viable [125]. Additionally, they are important while calculating stellar constraints on dark photons where the temperature scales of interest are large. In the context of thermal WIMP models with sufficiently heavy dark photons (MeV-scale masses or larger), these corrections are of little consequence since DM production happens dominantly at small temperatures.

In the following sections, we will study two dark photon models: one where DM production is via thermal freeze-out and we can therefore ignore these temperature corrections, and one where temperature-induced couplings are necessary to ensure the FIMP nature of DM.

## 5.2 Resonant Dark Photon Model

### 5.2.1 Relic Abundance Calculation

We first consider a DM model with a Dirac fermion, $\chi$, and a kinetically mixed dark photon, $A'$, specified by the Lagrangian [3, 53],

$$\mathcal{L}_{\rm DM} = -\frac{1}{4}F'_{\mu\nu}F'^{\mu\nu} + \frac{1}{2}m^2_{A'}A'^2 - \kappa e A'_\mu \sum_f q_f \bar{f}\gamma^\mu f + \bar{\chi}(i\partial\!\!\!/ - m_\chi)\chi - g_\chi A'_\mu \bar{\chi}\gamma^\mu \chi\,, \tag{5.19}$$

where the couplings are as defined in the previous section. We are interested in the case of sub-GeV DM where DM is produced via freeze-out.[5] As we have seen in section 2.3, sub-GeV DM faces strong cosmological constraints: BBN bounds dictate that any thermal particle must have a mass larger than a few MeV, whereas measurements of the CMB anisotropies strongly exclude the s-wave WIMP annihilation cross-section of $\langle\sigma v\rangle \sim 10^{-26}\,\mathrm{cm}^3\,\mathrm{s}^{-1}$. From the latter, it is easy to deduce that light WIMP models are only viable if there exists a mechanism to suppress annihilations at late times. In the model outlined above, such a velocity suppression can be achieved by considering resonantly-enhanced DM annihilation. If the dark photon mass is close to twice the dark matter mass, $m_{A'} \approx 2m_\chi$, DM annihilations to fermions, $\chi\chi \to A' \to ff$, will be resonantly enhanced at centre of mass energies close to $m_{A'}$. The correct relic

[5] This can be motivated by stringent terrestrial constraints on the WIMP DM parameter space as we will discuss in Chapter 7.

abundance can therefore be obtained for relatively small values of the couplings which result in suppressed annihilations at the time scales relevant for the CMB.

Additionally, since the CMB constraints are proportional to the square of the DM density (see section 2.3), they can be further alleviated if we assume that the Dirac fermion only constitutes a DM subcomponent. We can quantify this fractional abundance in terms of a free parameter,

$$R \equiv \frac{\Omega h^2}{0.12} \,. \tag{5.20}$$

Before calculating the relic abundance, let us have a quick look at the various parameters of interest in this model. We will limit ourselves to the case $m_{A'} \gtrsim 2m_\chi$ such that the dark photon can decay both invisibly and visibly. The leptonic decay width is given by,

$$\Gamma_{\ell\ell} = \frac{\kappa^2 e^2 m_{A'}}{12\pi} \sqrt{1 - \left(\frac{2m_\ell}{m_{A'}}\right)^2} \left(1 + \frac{2m_\ell^2}{m_{A'}^2}\right) \,. \tag{5.21}$$

The hadronic decay width can be characterised in terms of the ratio $\sigma(e^+e^- \to \text{hadrons})/\sigma(e^+e^- \to \mu^+\mu^-)$ for off-shell photons with centre-of-mass energy $\sqrt{s}$, given by $R(\sqrt{s})$. The total SM decay width of the dark photon is therefore given by,

$$\Gamma_{\text{SM}} = R(m_{A'})\Gamma_{\mu\mu} + \sum_\ell \Gamma_{\ell\ell} \,. \tag{5.22}$$

The invisible decay width is simply,

$$\Gamma_{\text{DM}} = \frac{g_\chi^2 m_{A'}}{12\pi} \sqrt{1 - \left(\frac{2m_\chi}{m_{A'}}\right)^2} \left(1 + \frac{2m_\chi^2}{m_{A'}^2}\right) \,. \tag{5.23}$$

Finally, we define the following parameters,

$$\Gamma_{A'} = \Gamma_{\text{SM}} + \Gamma_{\text{DM}} \,, \tag{5.24}$$

$$\gamma_{A'} = \frac{\Gamma_{A'}}{m_{A'}} \,, \tag{5.25}$$

$$B_e = \frac{\Gamma_{ee}}{\Gamma_{\text{SM}}} \,, \tag{5.26}$$

corresponding to the total dark photon decay width, a dimensionless dark photon decay width, and the branching ratio of a dark photon with a negligible invisible decay width into electrons respectively.

Since we are interested in thermal freeze-out via a resonance, we will use the methods outlined in the second half of section 2.2.2. We will once again parameterise the strength of the resonant enhancement by the dimensionless quantity

$$\epsilon_R = \frac{m_{A'}^2 - 4m_\chi^2}{4m_\chi^2} \,, \tag{5.27}$$

and the total cross-section as,

$$\sigma v_{\rm lab} = F(\epsilon)\frac{m_{A'}\Gamma_{A'}}{(s-m_{A'}^2)^2+m_{A'}^2\Gamma_{A'}^2}\,, \tag{5.28}$$

with,

$$F(\epsilon) = \frac{8\pi\alpha\kappa^2 g_\chi^2}{12\,\pi\,\Gamma_{A'}\,m_{A'}\,m_\chi}\frac{(2\epsilon+3)\left(m_e^2+2(\epsilon+1)m_\chi^2\right)\sqrt{(\epsilon+1)m_\chi^2-m_e^2}}{(2\epsilon+1)\sqrt{\epsilon+1}B_e\left(2\sqrt{\epsilon+1}m_\chi\right)}\,, \tag{5.29}$$

Remember that $\epsilon = (s-4m_\chi^2)/4m_\chi^2$ is the dimensionless kinetic energy of the collision and $v_{\rm lab}$ is the relative velocity in the rest frame of one of the particles.

We can then use Eq. 2.27 and Eq. 2.30 to obtain analytic results for the thermal average in the non-relativistic ($\langle\sigma v\rangle_{\rm n.r.}$) and resonant limits ($\langle\sigma v\rangle_{\rm res.}$) respectively. The former is valid for sufficiently small $\epsilon_R$ and when freeze-out occurs at low temperatures, whereas the latter works for larger $\epsilon_R$ when we obtain significant contributions from the relativistic tail of the particle distributions. On comparing with numerical results, we find that the non-relativistic approximation works well for $\epsilon_R < 0.1$ and $\gamma_{A'} > 0.01$. For $\gamma_{A'} < 0.01$, we use $\max(\langle\sigma v\rangle_{\rm res.}, \langle\sigma v\rangle_{\rm n.r.})$. We plot these approximations along with the full numerical calculation for $\langle\sigma v\rangle$ in Fig. 5.2 as functions of inverse temperature for a DM mass of $m_\chi = 50\,\mathrm{MeV}$. The purple dashed line is the standard thermally averaged s-wave cross-section for WIMPs. We clearly see that the resonant annihilations remain active after freeze-out has occurred (the pink shaded bands) until inverse temperatures close to $\epsilon_R^{-1}$. As expected, the non-relativistic approximation works very well for small temperatures whereas the resonant approximation is more accurate for larger temperatures.

Note that for a certain region of parameter space, when $\epsilon_R \ll 1$ and $\gamma_{A'} \ll \epsilon_R$, it is possible to make the narrow-width approximation in the non-relativistic limit to obtain,

$$\langle\sigma v\rangle \approx \frac{2\sqrt{\pi}x^{3/2}}{4m_\chi^2}\sqrt{\epsilon_R}e^{-x\epsilon_R}F(\epsilon_R)\,. \tag{5.30}$$

By then using the usual formula for the relic abundance,

$$\Omega h^2 \approx 1.7\times10^{-10}\mathrm{GeV}^{-2}\left(\int_{x_f}^{x_0}\sqrt{g_{\rm eff}}\frac{\langle\sigma v\rangle}{x^2}\mathrm{d}x\right)^{-1} \tag{5.31}$$

we get

$$\Omega h^2 = 1.7\times10^{-10}\mathrm{GeV}^{-2}\frac{1}{g_{\rm eff}^{1/2}}\left(\frac{2\pi\,(1+\epsilon_R)\,\mathrm{Erfc}(\sqrt{\epsilon_R x_f})\,F(\epsilon_R)}{m_{A'}^2}\right)^{-1}\,, \tag{5.32}$$

which implies

$$\Omega h^2 \propto \frac{1}{\mathrm{Erfc}(\sqrt{\epsilon_R x_f})\,F(\epsilon_R)} \overset{\epsilon_R\ll1}{\sim} \frac{\Gamma_{A'}}{\kappa^2\,g_\chi^2}\,. \tag{5.33}$$

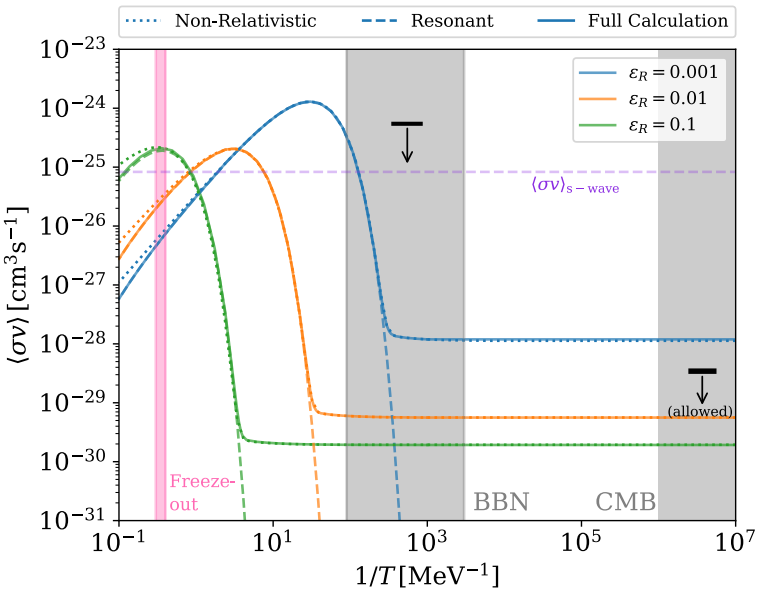


FIGURE 5.2: The thermally averaged cross-section as a function of temperature for three different values of $\epsilon_R$ calculated using the full expression (solid line) and the non-relativistic (dotted) and resonant (dashed) approximations. The DM mass is fixed to $m_\chi = 50\,\mathrm{MeV}$, the dark coupling to $g_\chi = 0.01$ and the kinetic mixing is fixed for each $\epsilon_R$ to reproduce the DM relic abundance. The grey shaded areas correspond to temperatures relevant for BBN and CMB with the horizontal bars corresponding to cross-sections required to satisfy the respective constraints assuming an s-wave cross-section (purple dashed line). We also indicate the temperature range relevant for freeze-out in light pink.

The equations above demonstrate some of the unique features of this DM model. First, we see from Eq. 5.32 that the relic abundance is nearly independent of the freeze-out temperature $x_f$ in the limit $\epsilon_R \ll 1$. This is because for $x > x_f$, the thermally averaged cross-section continues to grow until $x \sim \epsilon_R^{-1}$ as can also be seen from Fig. 5.2. Hence the final value of the relic abundance is independent of the lower bound on $x$. Second, from Eq. 5.33 we see that the relic abundance becomes independent of $g_\chi$ ($\kappa$) for $g_\chi \gg \kappa$ ($\kappa \gg g_\chi$). This introduces a degree of freedom in our model since one of the couplings can now be varied drastically while keeping the relic density fixed.

To get a sense of the scale of couplings that reproduce the correct relic abundance, we consider once again Fig. 5.2. For $m_\chi = 50\,\mathrm{MeV}$ and $g_\chi = 0.01$, we obtain the correct relic abundance for $\kappa = [3.6 \times 10^{-7}, 8.0 \times 10^{-7}, 4.5 \times 10^{-6}]$ for $\epsilon_R = [0.001, 0.01, 0.1]$. These couplings are smaller than general WIMP couplings: a straightforward consequence of the resonant enhancement in the annihilation. Additionally, we check the validity of our approximations by comparing the resulting relic abundance to the full numerical calculation for the parameter combinations represented in Fig. 5.2. The numerically evaluated thermal averages yield $\Omega h^2 = [0.121, 0.129, 0.122]$, the approximate ones yield $\Omega h^2 = [0.126, 0.124, 0.128]$, whereas Eq. 5.32 returns $\Omega h^2 = [0.127, 0.124, 0.130]$ for $\epsilon_R = [0.001, 0.01, 0.1]$, i.e., our analytic approximations agree to within $5\%$.

We will next have a more detailed look at the cosmological constraints on this model.

### 5.2.2 Cosmological Constraints

#### Big Bang Nucleosynthesis

From Chapter 2, we know that the formation of light elements in the early universe is sensitive to the presence of sub-GeV particles in a number of ways. Their contribution to the Hubble expansion rate of the universe sets largely model-independent bounds on their masses if these particles have a thermal abundance. For Dirac fermions, this turns out to be $m_\chi \gtrsim 10\,\mathrm{MeV}$ [66, 67] (see also Fig. 2.8).

Additionally, photo-disintegration sets a bound on DM annihilations at keV-scales. For velocity-independent annihilation, one obtains $\sigma v < 5.2 \times 10^{-25}\,\mathrm{cm}^3\,\mathrm{s}^{-1}$ [67]. To ensure that annihilations in our model are sufficiently suppressed at these temperatures, we limit ourselves to $\epsilon_R \geq 0.001$.

In Fig. 5.2, we shade the temperature region relevant for BBN with a light grey. The bound from photo-disintegration on a velocity-independent cross-section is represented by a black bar with an arrow denoting the allowed parameter space for cross-sections. Note that we currently evade all constraints from photo-disintegration by restricting ourselves to sufficiently small resonant enhancements. These constraints would have to be accounted for properly if one wants to extend the parameter space to include $\epsilon_R < 0.001$.

#### Cosmic Microwave Background

We have also discussed the general form of the constraints arising due to energy injection in the CMB by DM annihilations at late times in section 2.3. These are encoded in the effective parameter [25],

$$p_{\mathrm{ann}} = \frac{R^2}{2}\, f_\chi \frac{\langle \sigma v \rangle_{\mathrm{CMB}}}{m_\chi} < 3.2 \times 10^{-28}\,\mathrm{cm}^3\,\mathrm{s}^{-1}\,\mathrm{GeV}^{-1}\,, \tag{5.34}$$

where the factor $1/2$ accounts for the fact that the DM particle is not self-conjugate.

In this model, the cross-section at times relevant for the CMB constraints is approximately s-wave (see Fig. 5.2). We can therefore take the limit $v \to 0$ in Eq. 5.28 to obtain,

$$\langle \sigma v \rangle_{\mathrm{CMB}} = \frac{4\,\pi \alpha g_\chi^2 \kappa^2}{m_{A'}^3\, B_e\left(\frac{m_{A'}}{\sqrt{1+\epsilon_R}}\right)} \frac{(1+\epsilon_R)^{3/2}\,(m_{A'}^2 + 2\,(1+\epsilon_R)\,m_e^2)}{(1+\epsilon_R)^2\,\Gamma_{A'}^2 + \epsilon_R^2\, m_{A'}^2} \sqrt{\frac{m_{A'}^2}{1+\epsilon_R} - 4m_e^2}\,. \tag{5.35}$$

From this equation (as well as from Fig. 5.2), it can be seen clearly that the CMB constraints become stronger for smaller $\epsilon_R$, since $\langle \sigma v \rangle_{\mathrm{CMB}} \propto \epsilon_R^{-1}$ in the limit, $\gamma_{A'} \ll \epsilon_R \ll 1$.

We can calculate the fraction of energy deposited in the SM plasma as a function of the DM mass, $f_\chi(m_\chi)$, in a similar way as outlined in Chapter 2 with the help of publicly available tools such as PPPC4DMID, HERWIG, and HAZMA [70–73]. This places a bound on $R^2\langle\sigma v\rangle_{\rm CMB}$ as a function of DM mass.

It is possible to qualitatively estimate how the CMB bound translates to couplings. From Eq. 5.34, we know that the CMB would constrain $R^2\langle\sigma v\rangle_{\rm CMB}$. Assuming $\gamma_{A'} \ll \epsilon_R \ll 1$, we can write using Eq. 5.33, $R \propto \Omega h^2 \approx \Gamma_{A'}/(\kappa^2\, g_\chi^2)$. Additionally, in this limit, $\langle\sigma v\rangle_{\rm CMB} \propto g_\chi^2\kappa^2$, resulting in,

$$R^2\langle\sigma v\rangle_{\rm CMB} \propto \begin{cases} \dfrac{\kappa^2}{g_\chi^2} & \Gamma_{\rm DM} \ll \Gamma_{\rm SM} \\ \\ \dfrac{g_\chi^2}{\kappa^2} & \Gamma_{\rm SM} \ll \Gamma_{\rm DM} \end{cases} \tag{5.36}$$

These equations imply that the CMB constrains small values of $\kappa$ if the dark photon decays invisibly. Additionally, as we decrease $\epsilon_R$, the CMB constraints are first weakened as annihilations are enhanced around freeze-out and smaller couplings reproduce the relic abundance. However, a further decrease in $\epsilon_R$, results in resonant annihilations becoming efficient even during recombination, thereby yielding stronger CMB constraints. This is also evident from Fig. 5.2.

We will further discuss the complementarity of these constraints when we talk about terrestrial experiments in Chapter 7. Additionally, astrophysical constraints on this model arise from DM self-interactions which we discuss in detail in Chapter 6.

## 5.3 $B - L$ Dark Photon Model

We will now turn our attention to dark photon models in the freeze-in regime. Generally, feeble couplings of order $10^{-11}$, induced via a tiny kinetic mixing parameter, are used to ensure freeze-in production of DM [49, 50]. However, it turns out that the freeze-in mechanism is valid for even larger couplings provided that *both* the dark and the SM current couple weakly to the dark photon. In such a scenario, the production cross-sections scale as the fourth power of the coupling, $g'^4$, and therefore the correct relic abundance can be reproduced for couplings as large as $g' \sim 10^{-6}$ [1, 127]. This coupling structure arises naturally in extensions of the SM via an additional $U(1)'$ such that both the SM fermions and the dark sector carry $U(1)'$ charges.

We will exemplify this by taking the example of a $B - L$ gauge boson. A $U(1)_{B-L}$ gauge extension of the SM, coupled with the addition of three-handed neutrinos (RHNs) is commonly used to explain neutrino masses by the see-saw mechanism [77, 128]. We will, however, not be interested in the additional neutrino species or the scalar which provides the $A'$ and RHNs masses, and assume that these particles are sufficiently heavy to have no observable effects

| Particle | $N_c$ | $N_f$ | $Y$ | $B-L$ |
|---|---|---|---|---|
| $q_{\rm L}$ | 3 | 3 | $1/6$ | $1/3$ |
| $u_{\rm R}$ | 3 | 3 | $2/3$ | $1/3$ |
| $d_{\rm R}$ | 3 | 3 | $-1/3$ | $1/3$ |
| $e_{\rm L}$ | 1 | 3 | $-1/2$ | $-1$ |
| $e_{\rm R}$ | 1 | 3 | $-1$ | $-1$ |
| $\nu_{\rm R}$ | 1 | 3 | 0 | $-1$ |
| $H$ | 1 | 1 | $1/2$ | 0 |

TABLE 5.1: $B-L$ and hypercharge assignments before EWSB.

| Particle | $N_c$ | $N_f$ | $q_f$ | $B-L$ |
|---|---|---|---|---|
| $u$ | 3 | 3 | $2/3$ | $1/3$ |
| $d$ | 3 | 3 | $-1/3$ | $1/3$ |
| $e$ | 1 | 3 | $-1$ | $-1$ |
| $\nu_{\rm L}$ | 1 | 3 | 0 | $-1$ |
| $\nu_{\rm R}$ | 1 | 3 | 0 | $-1$ |

TABLE 5.2: $B-L$ and charge assignments after EWSB.

on the DM phenomenology.[6] Instead, we will introduce a Dirac fermion $\chi$ with a $U(1)_{B-L}$ charge $q'_\chi$ as our DM candidate. We remain agnostic about the value of $q'_\chi$, instead assuming the total $\chi - A'$ coupling to be given by $g_{\rm DM}$. Importantly, for $q'_\chi \neq -1$, the stability of $\chi$ is guaranteed by the $B-L$ symmetry. Using Eq. 5.8, we have the Lagrangian,

$$\mathcal{L} \supset \frac{1}{2} m_{A'}^2 A'_\mu A'^\mu - \sum_{f,\,\rm SM} g_{\rm BL} q'_f A'_\mu \bar{f}\gamma^\mu f - \underbrace{g_{\rm BL} q'_\chi}_{g_{\rm DM}} A'_\mu \bar{\chi}\gamma^\mu \chi \,. \tag{5.37}$$

Further, we can parameterise the DM charge as,

$$r \equiv \frac{g_{\rm BL}}{g_{\rm DM}} = \frac{1}{q'_\chi} \,. \tag{5.38}$$

The four free parameters of this model are $m_\chi$, $m_{A'}$, $g_{\rm BL}$ and $g_{\rm DM}$.

Tables 5.1 and 5.2 present the $B-L$ and $U(1)_Y$ charges of the SM fermions before and after the phase transition respectively. We first look at the coupling structure before the phase transition. In this case, following the discussion in section 5.1.2, and using Eq. 5.18, the mass-mixing is defined by,

$$\delta m^2 = q'_{\rm eff} \frac{g_Y g_{\rm BL} T^2}{9} = 4 \frac{g_Y g_{\rm BL} T^2}{9} \,, \tag{5.39}$$

resulting in,

$$\theta_{\rm BL} = \frac{8}{11} \frac{g_{\rm BL}}{g_Y} \,. \tag{5.40}$$

[6] Ref. [128] discusses in detail the case where the RHNs are the frozen in DM candidate.

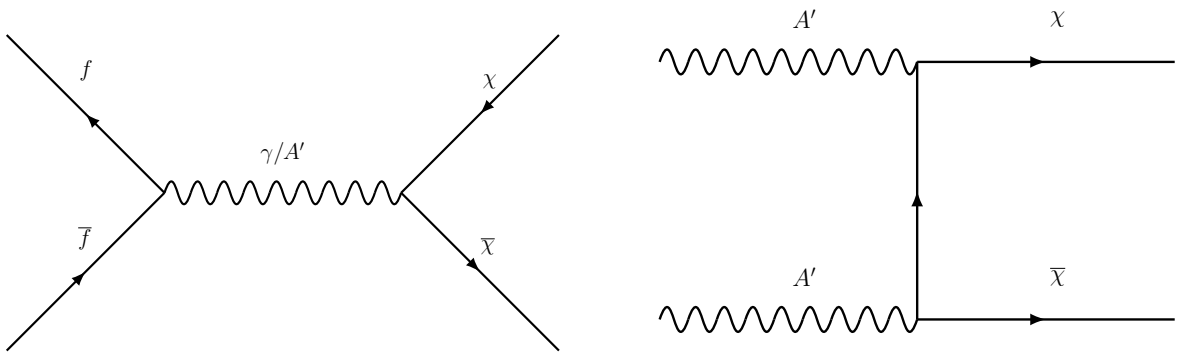


FIGURE 5.3: Freeze-in Production channels: Annihilations of SM fermions, $f$ and $\bar{f}$ (left) and annihilations of dark photons, $A'$ (right).

After the phase transition, and for temperatures above the bottom quark mass, we instead have,

$$\theta_{\rm BL} = \frac{1}{2}\frac{g_{\rm BL}}{e}\,, \tag{5.41}$$

where top quarks do not contribute to both $q_{\rm eff}$ and $q'_{\rm eff}$ on account of being non-relativistic. The effective coupling of the dark photon to the SM fermions is then given by Eq. 5.14, which for $\theta_{\rm BL}$ given above vanishes for all up-type quarks,

$$g_{\rm BL}q'_u - \theta_{\rm BL}eq_u = g_{\rm BL} \times \frac{1}{3} - \frac{1}{2}\frac{g_{\rm BL}}{e}e \times \frac{2}{3} = 0\,. \tag{5.42}$$

### 5.3.1 Relic Abundance Calculation

With a handle on the modifications to the coupling structure, we are now ready to investigate the parameter space of this model. As mentioned, we are interested in the freeze-in regime, where the dark sector is populated via decays and annihilations of particles in the thermal bath. It has been shown that for $m_\chi < 1$ TeV and $g_{\rm BL} \gtrsim 10^{-7}$, dark photons thermalise with the SM at the relevant temperature scales, $T \approx m_\chi$, via processes of the kind $qg \to qA'$ [80]. As long as $g_{\rm DM}$ is sufficiently small, however, the DM candidate itself does not enter thermal equilibrium and the conditions for freeze-in are still satisfied.

DM production then occurs via two kinds of processes differentiated by their coupling dependence:

1. **Annihilations or decays of SM particles**:
   These include processes of the form $f\bar{f} \to \chi\bar{\chi}$ with cross-sections that scale as $g^2_{\rm BL}g^2_{\rm DM}$ (left panel of Fig. 5.3). Additionally, in-medium effects imply that for large enough temperatures, massive photons (plasmons) can decay into DM, $A \to \chi\bar{\chi}$. Since the $A - \chi$ coupling is induced via a thermal mixing, the decay width of this process also scales as $g^2_{\rm BL}g^2_{\rm DM}$.

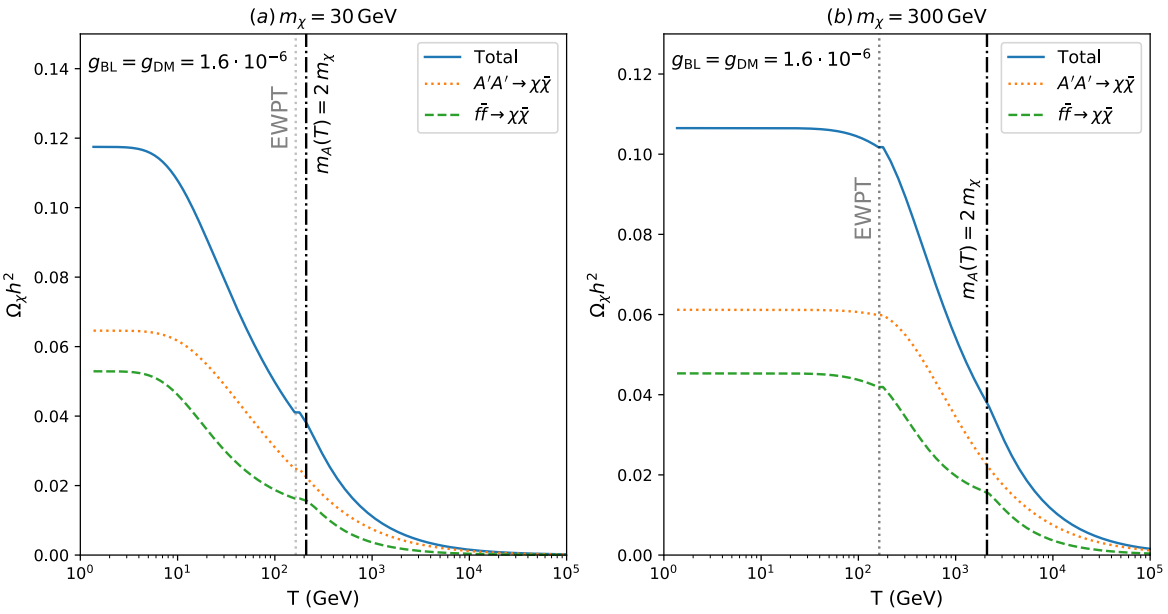


FIGURE 5.4: The DM abundance $\Omega h^2$ as a function of temperature for two different values of DM mass, (a) $m_\chi = 30\,\text{GeV}$ and (b) $m_\chi = 300\,\text{GeV}$. The temperature of the electroweak phase transition and the temperature at which plasmon decays become kinematically inaccessible are indicated by vertical lines.

2. **Annihilations of dark photons**:
   Since the dark photons are assumed to have a thermal abundance, processes of the kind $A'A' \to \chi\bar{\chi}$, also populate the dark sector (right panel of Fig. 5.3). These processes scale as $g_{\text{DM}}^4$ and dominate for $g_{\text{BL}} \ll g_{\text{DM}}$. We restrict ourselves to the regime where dark photon decays into DM are forbidden, $m_{A'} < 2m_\chi$.

The total abundance of DM is then given by the solution to the Boltzmann equation

$$\frac{s}{2}\frac{\mathrm{d}Y_\chi}{\mathrm{d}t} = \langle\sigma_{f\bar{f}}v\rangle n_f^2 + \langle\sigma_{A'A'}v\rangle n_{A'}^2 + \langle\Gamma_{A\to\chi\bar{\chi}}\rangle n_A\,, \tag{5.43}$$

with the usual definitions for the different variables. Note that plasmon decays are active for temperatures when $m_A(T) \sim \sqrt{20\,e^2T^2/27} > 2m_\chi$ corresponding to roughly $T \gtrsim 7m_\chi$. On the other hand, the annihilations are efficient until $T \approx m_\chi$ and typically dominate the total yield. This of course changes for smaller dark matter masses, in which case plasmon decays do in fact give the dominant contribution [129].

For $T \gg m_\chi$, the thermally averaged cross-sections scale as $\langle\sigma_{f\bar{f}}\rangle \sim g_{\text{BL}}^2 g_{\text{DM}}^2/T^2$ and $\langle\sigma_{A'A'}\rangle \sim g_{\text{DM}}^4/T^2$ respectively, resulting in the yields,

$$Y_{f\bar{f}} \propto \frac{g_{\text{BL}}^2 g_{\text{DM}}^2 M_{\text{Pl}}}{m_\chi}\,, \tag{5.44}$$

$$Y_{A'A'} \propto \frac{g_{\text{DM}}^4 M_{\text{Pl}}}{m_\chi}\,. \tag{5.45}$$

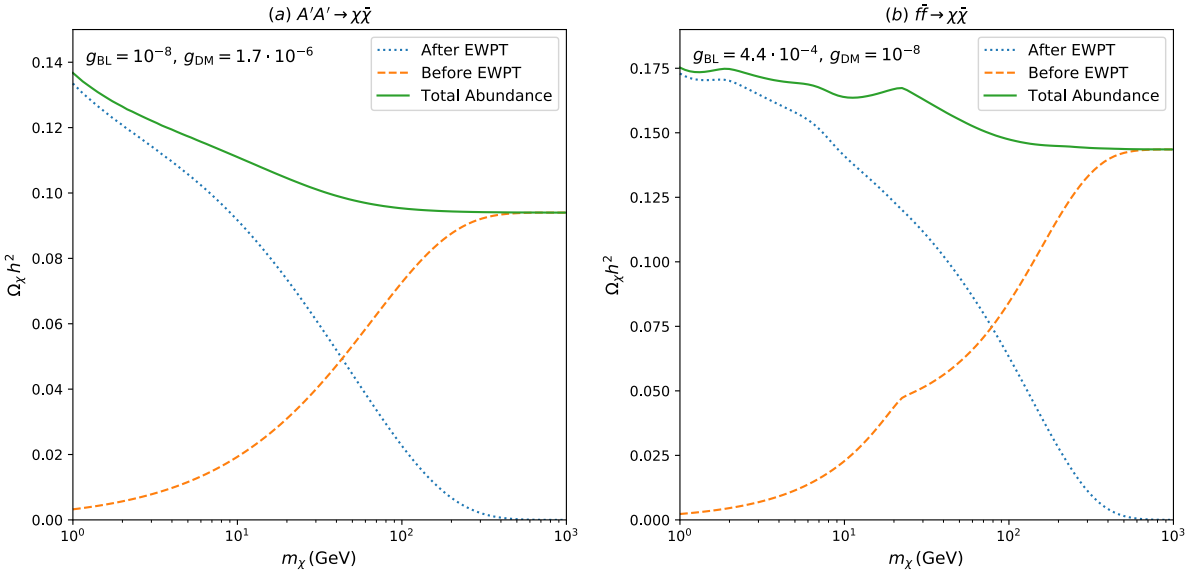


FIGURE 5.5: The total DM abundance as a function of DM mass for production dominated by (a) dark photon annihilation and (b) SM particle annihilation. The dashed and dotted lines represent the contribution to the total abundance before and after the electroweak phase transition respectively.

Therefore, we expect the final DM abundance, $\Omega h^2 \propto Y_\chi m_\chi$, to be independent of the DM mass.

The exact solution of the Boltzmann equation is, however, much more complicated as emphasised multiple times in this thesis. We need to account for the full statistical distributions of the particles, distinguish between production before and after the phase transition, as well as properly account for the thermal masses and induced couplings. We therefore solve this equation numerically using a modified version of MICROMEGAS 5.0 where we additionally implement temperature corrections to particle masses.

Fig. 5.4 displays the evolution of the DM abundance as a function of temperature for two DM masses, using couplings that reproduce the correct relic density, $g_{\rm BL} = g_{\rm DM} = 1.6 \times 10^{-6}$. For $m_{A'} < 1\,\text{GeV}$, the relic abundance is independent of the dark photon mass. We see that DM production is dominantly at $T \approx m_\chi$ and therefore before (after) the phase transition for $m_\chi = 300\,(30)$ GeV. The dashed-dotted black line represents the point where plasmon or hypercharge plasmon decays become forbidden. As argued above, this channel provides a sub-dominant contribution in our parameter range of interest. The other two channels give comparable contributions to the DM density although the dark photon channel turns out to be slight more efficient.

We also plot the relic abundance as a function of DM masses considering only the dark photon channel (left) and only SM fermion channels (right) in Fig. 5.5. As expected, the total abundance (solid green line) is largely independent of the DM mass. Further, heavier DM particles are mostly produced before the phase transition (orange dashed line) in contrast to lighter ones which are dominantly produced after the phase transition (blue dotted line). The wiggles in the right panel for DM masses below 10 GeV correspond to the change in the SM

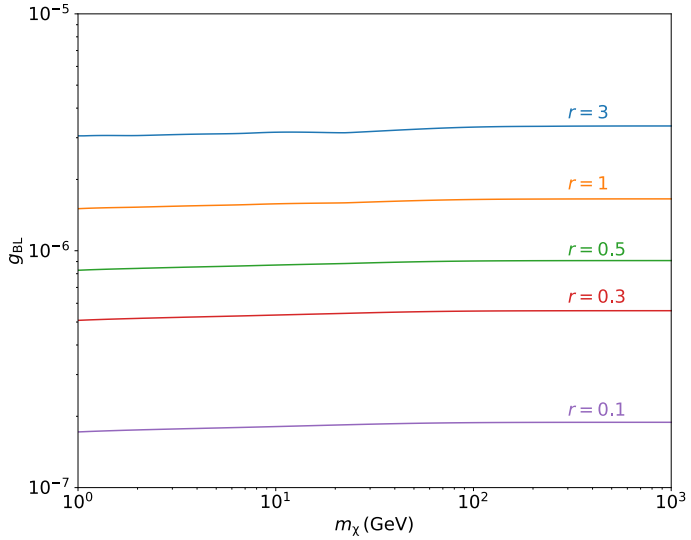


FIGURE 5.6: The gauge coupling $g_{\rm BL}$ that reproduces the observed value of the DM relic abundance for different values of the coupling ratio, $r = g_{\rm BL}/g_{\rm DM}$, plotted as a function of DM mass.

relativistic degrees of freedom that contribute to DM production. Neglecting the mass dependence, the relic abundance can be parameterised in terms of the ratio of the two couplings, as

$$\Omega_\chi h^2 \approx (0.16\, r^{-4} + 0.12\, r^{-2}) \left( \frac{g_{\rm BL}}{2 \times 10^{-6}} \right)^4 . \tag{5.46}$$

We can use this expression to estimate the magnitude of couplings required to obtain the measured relic abundance, $\Omega_\chi h^2 = 0.12$. For $r \ll 1$, the first term in the expression above, corresponding to dark photon annihilation, dominates. The correct relic abundance is obtained for $g_{\rm BL} \sim 10^{-6} r$ or equivalently $g_{\rm DM} \sim 10^{-6}$. In the opposite case, $r \gg 1$, SM particles give the dominant contribution and the couplings are roughly given by $g_{\rm BL} \sim 10^{-6}\sqrt{r}$, or $g_{\rm BL} g_{\rm DM} \sim 10^{-12}$.

In Fig. 5.6, we show the required values of $g_{\rm BL}$ as a function of DM mass for different values of the coupling ratio $r$. We restrict ourselves to $0.1 < r < 3$ which correspond to reasonable values for the dark matter charge, $q'_\chi = 1/r$. Intriguingly, gauge couplings in this regime are probed by various terrestrial experiments. We will discuss these further in Chapter 7.

Note that there aren't many cosmological constraints on this model. The small freeze-in couplings imply that DM annihilations into SM particles are necessarily suppressed during recombination. Further, the BBN constraints on thermal dark photons are easily evaded in the mass range of interest, $m_{A'} \gtrsim$ few MeV

## 5.4 Conclusions

In this chapter, we have explored the cosmology of a dark photon portal in the context of both thermal and non-thermal DM models. $U(1)'$ extensions of the SM have been extensively studied in the literature. For a DM particle charged under such a $U(1)'$, interactions with the SM particles can be established through a kinetic mixing between $U(1)_Y - U(1)'$, or by considering a $U(1)'$ under which the SM is also charged. In either case, the portal coupling can be treated as a free parameter.

For the case of a light dark photon, plasma effects induce an additional non-negligible mass mixing with the SM photon. As discussed in section 5.1, this mixing can result in a coupling structure substantially different from the vacuum case, in particular resulting in couplings that pick up a temperature dependence. For the case of a kinetically mixed dark photon, such an effect ensures that ultralight dark photons never thermalise with the SM thereby satisfying cosmological constraints. Even for a purely mass-mixed dark photon, this effect can selectively decouple the dark photon from certain SM particles and, therefore, affect DM cosmology.

In terms of DM production mechanisms, the dark photon portal can be used in the context of both WIMPs and FIMPs (sections 5.2 and 5.3 respectively). For WIMPs, models of light DM can be made cosmologically viable provided that the DM mass is close to twice the dark photon mass, i.e., if we consider the parameter space in which DM annihilations are resonantly enhanced. This resonant enhancement around freeze-out ensures that DM annihilations are suppressed during recombination thereby evading the stringent constraints arising from the CMB. Indeed, even moderate levels of enhancement can satisfy cosmological constraints, as shown in Fig. 5.2. The resonant enhancement also implies that the couplings required to reproduce the relic abundance are smaller than the traditional WIMP couplings. It is important to note here that very small couplings might result in a dark sector not in kinetic equilibrium with the SM thermal bath which would then require a modification of the relic density calculation. Additionally in such a case, the BBN constraints arising from photo-disintegration would also need to be evaluated properly. It is possible to do so by using specialised numerical tools such as ACROPOLIS [130]. On the flip side, for small resonant enhancements, $\epsilon_R > 0.1$, and therefore large couplings, uncertainties in the relic abundance calculation might arise from considering a fixed width of the dark photon propagator instead of a running one. These large couplings, however, would ensure efficient annihilations during recombination and therefore be excluded anyway.

For frozen-in heavy DM, on the other hand, MeV-scale thermal dark photons can easily reproduce the observed DM abundance with couplings that are substantially larger than the usual feeble couplings, as shown in Fig. 5.6. DM is produced through the annihilation of SM particles and dark photons. Which of these channels dominate depends on the relative strength of the $A'$-SM and $A'$-DM coupling. Additionally, plasmon and hypercharge plasmon decays give a sub-dominant contribution to the DM abundance. Since the DM abundance is always

sub-thermal, and DM is assumed to be heavy, cosmological constraints on DM do not apply. The BBN constraints on the dark photon are also easily avoided in the mass range of interest.

In both these scenarios, it turns out that the couplings required to satisfy the relic abundance requirement are exactly in the range of existing and future terrestrial searches (as we will detail in Chapter 7). Considering the rich phenomenology at both cosmological and laboratory scales, it is easy to see that the dark photon portal is an attractive avenue for both theoretical and experimental research into DM.

# Chapter 6

# Semi-Classical Treatment of Mediators

In the preceding chapters, we have focused primarily on DM-SM interactions. However, the very same mediators that couple the SM to DM also generate DM-DM interactions. Indeed, self-interactions are quite common in DM models. In particular, self-interactions mediated by long-range forces have long been posited as a solution to a number of problems in the collisionless cold DM paradigm. In this chapter, we will discuss a quantum-mechanical treatment for DM self-interactions in this regime along with their phenomenological implications on generic model parameters. We begin with a brief review of the so-called small-scale crisis in ΛCDM in section 6.1. In section 6.2, we formulate non-relativistic DM self-interactions in a quantum-mechanical way. Our calculations for long-range interactions and the resulting phenomenology follow in sections 6.3-6.5 respectively. Finally, we present our conclusions in section 6.6.

## 6.1 Small Scale Problems

Even though ΛCDM has proved to be an excellent success at predicting the large scale structure of the universe ($\gtrsim O(\mathrm{Mpc})$), inconsistencies arise at smaller scales [93, 131, 132]. The predictions obtained from cosmological N-body simulations—which are necessary to explore this regime as a result of the non-linearity of structure formation—differ from observations. Invoking self-interacting DM (SIDM) is one way to alleviate these discrepancies [133], although, as has been often pointed out, a more rigorous treatment of baryonic effects in simulations might also do the same [134–136].

We list the main discrepancies between CDM predictions and observations below.

1. **Cusp-Core Problem**: This refers to a discrepancy in the dark matter density profiles of dwarf galaxies obtained from DM-only numerical simulations and those obtained from observed rotation curves [137–139]. Simulations predict a density profile which increases like a steep power law toward the galactic centre, $\rho_{\mathrm{DM}} \propto r^{-1}$, i.e., a *cuspy* profile, whereas observations point to one that is flat or *cored*, $\rho_{\mathrm{DM}} \propto r^{0}$.

2. **Diversity Problem**: This refers to observations of halos that have the same maximum circular velocity but have significant variations in their inner density profiles [140].

Structure formation in CDM is a self-similar process implying that halos of a given mass should appear similar. Since the mass of a halo can be linked to its maximum circular velocity, $v_{\rm max}$, CDM predicts that halos with a given $v_{\rm max}$ should have the same densities at all radii. This is disputed by observations of disc galaxies where inferred core densities for similar $v_{\rm max}$ values, can vary by factor of $O(10)$ [141].

3. **Missing Satellites Problem**: CDM halos have a rich substructure since structure formation is a hierarchical process where halos grow via mergers of smaller halos. CDM thus predicts a number of satellites or small galaxies in our local group. However, far fewer satellites have been observed [93]. We should note that whether or not the missing satellite problem is still a problem is currently contested due to discoveries of more and more low-surface brightness galaxies [142, 143].

4. **Too-Big-To-Fail Problem**: This corresponds to the fact that N-body simulations based on ΛCDM predict a population of DM sub-halos around the Milky Way that are way too dense and massive to host the brightest observed satellites [144, 145].

Self-scattering of DM particles can act as an effective energy transfer mechanism, thus turning cusps into cores and changing the subhalo abundance. The missing satellite problem may also be alleviated by including additional properties like warm [146, 147] or decaying DM [148]. Since such solutions would probe the properties of DM independent of its interaction with the standard model, they offer interesting insights and constraints on possible DM models. Further, a general treatment of self-interactions is useful since it provides an easy way to map constraints onto different mediators. These will then be complementary to the mediator constraints arising from terrestrial experiments that probe the mediator's coupling to the SM.

Generally, constraints on SIDM are presented in terms of the *velocity-averaged* cross-section over mass, $\langle\sigma v\rangle/m$, as a function of average DM velocity, $\langle v\rangle$. Since the velocity dispersion varies with halo mass, studying differently-sized systems from dwarf galaxies to galaxy clusters provides a way to constrain self-interactions at different energy scales.

Fig. 6.1 shows the strength of self-interactions for different astrophysical systems as a function of their mean velocities, with straight lines representing a contact (or velocity-independent) self-interaction. The data in Fig. 6.1 appear to prefer a cross-section that is constant at small velocities but turns over to have a Rutherford-like ($v^{-4}$) dependence at large velocities. Further, the order of magnitude for the cross-section, $\sigma \sim 1\,\mathrm{cm^2 g^{-1}} \approx 10^{-24}\,\mathrm{cm^2}\,(m_\chi/\mathrm{GeV})$ appears to be much larger than the weak-scale cross-section of $10^{-36}\,\mathrm{cm^2}$, therefore implying a mediator mass lighter than the weak scale [149]. These properties are characteristic of long-range interactions, for example, of the form,

$$\mathcal{L}_{\rm int} = \begin{cases} g_\chi \bar{\chi}\gamma^\mu \chi \phi_\mu & \text{vector mediator}\,, \\ g_\chi \bar{\chi}\chi\phi & \text{scalar mediator}\,. \end{cases} \tag{6.1}$$

Before we proceed to the functional forms of the cross-section for these interactions, we point out two important questions that arise when making comparisons with data.


FIGURE 6.1: The inferred self-interaction cross-section from measurements of different astrophysical systems plotted as a function of their mean collisional velocity $\langle v \rangle$. Diagonal lines are contours for constant $\sigma/m$. The dotted line is a representative fit corresponding to a dark photon model. Figure adapted from [133].

1. **What do we mean by $\sigma$, i.e, what does the data actually constrain?**
   Many particle physics models of DM self-interactions predict a differential scattering cross-section, $\mathrm{d}\sigma/\mathrm{d}\Omega$, that depends non-trivially on both the scattering angle, $\theta$, and the velocity. To compare to data, we need to integrate out the angular dependence as well as conduct a phase-space averaging. The total integrated cross-section, $\sigma = \int \mathrm{d}\Omega \, (\mathrm{d}\sigma/\mathrm{d}\Omega)$, however, is not a good quantity to compare to since it receives a strong enhancement in the forward scattering limit ($\cos\theta \to 1$) for light mediators. This enhancement is irrelevant for the DM distribution in a halo since it leaves the DM particle trajectories unchanged. Instead, the *momentum transfer cross-section* [150, 151],

$$\sigma_{\mathrm{T}} = \int \mathrm{d}\Omega \, (1 - \cos\theta) \, \frac{\mathrm{d}\sigma}{\mathrm{d}\Omega} \,, \tag{6.2}$$

   which regulates this enhancement is often used as a suitable proxy in the literature. However, $\sigma_{\mathrm{T}}$ is also not a great figure of merit. It preferentially weights backward scattering that leaves DM distributions unchanged. Additionally, it is not well defined for identical particles as we shall show below. An alternative to $\sigma_{\mathrm{T}}$ is the *viscosity cross-section* [149],

$$\sigma_{\mathrm{V}} = \int \mathrm{d}\Omega \, \sin^2\theta \, \frac{\mathrm{d}\sigma}{\mathrm{d}\Omega} \,, \tag{6.3}$$

   which weights forward and backward scattering equally and takes into account the fact that perpendicular scatterings are the most efficient in thermalising a halo [152, 153].

Additionally, it is well defined for both identical and non-identical particles.

In the following sections, we will discuss both $\sigma_{\rm T}$ and $\sigma_{\rm V}$.

2. **How do we perform the velocity averaging?**
The rate of DM self-scattering in halos is proportional to $\langle\sigma v\rangle$, where the angular brackets denote a velocity average. However, halo dynamics are affected not by the rate of DM self-scattering but instead by the rate of energy and momentum transfer. Usually this is described by replacing $\sigma$ with $\sigma_{\rm T}$ or $\sigma_{\rm V}$ in the velocity average. In reality, however, the momentum and energy transfer rates turn out to be proportional to $\langle\sigma_{\rm T}v^2\rangle$ and $\langle\sigma_{\rm V}v^3\rangle$ respectively. We expand upon this further in section 6.4.

### A Quick Interlude

Before moving ahead, let us quickly revisit the resonant dark photon model presented in Chapter 5 to better contextualise the phenomenology of DM self-interactions. For such a model with Dirac fermion DM, two kinds of self-interactions are possible: particle-particle scattering via a $t$- or $u$-channel exchange of a dark photon, and particle-antiparticle scattering with an $s$- or $t$- channel dark photon exchange. Due to the resonant nature of the model, the $s$-channel exchange will always be dominant and we can write the averaged momentum transfer cross-section as,

$$\overline{\sigma_{\rm T}} = \frac{1}{2}\int_{-1}^{1}(1-|\cos\theta|)\frac{{\rm d}\sigma(\chi\bar{\chi}\to\chi\bar{\chi})}{{\rm d}\cos\theta}\,{\rm d}\cos\theta\,, \tag{6.4}$$

where the factor $1/2$ indicates that only half of the collisions involve a particle-antiparticle pair. Additionally, we have already solved one of the problems that arises when using $\sigma_{\rm T}$, i.e., the preferential weighting of backward scattering, by making the replacement, $\cos\theta \to |\cos\theta|$.[1] Looking at Fig. 6.1, we see that the leading constraint comes from galaxy clusters that probe velocities of the order of $1000\,{\rm km\,s^{-1}} \approx 3\times10^{-3}c$. These velocities are much smaller than the resonant enhancement $\epsilon_R$, and we can therefore approximate the velocity-averaged self-interaction cross-section as the cross-section in the limit $v\to 0$,

$$\overline{\sigma_{\rm T}} = \frac{3g_\chi^4}{64\pi(4m_\chi^2\epsilon_R^2+(1+\epsilon_R)\Gamma^2)}\,. \tag{6.5}$$

Since we have generalised the model in Chapter 5 to include a DM subcomponent, we need to compare the scattering rate inside a galaxy cluster for a fractional DM abundance. As a benchmark, we consider the Bullet Cluster and parameterise the scattering rate as,

$$\Gamma_{\rm SIDM} = \overline{\sigma_{\rm T}}\frac{R\,\rho_{\rm BC}}{m_\chi}\,, \tag{6.6}$$

[1] Note that we will not be using this replacement in the following sections since it cannot be generalised in the way that $\sigma_{\rm T}$ can be.

where $\rho_{\rm BC}$ is the DM density in the Bullet Cluster and $R$ denotes the DM fraction. The bound is then placed on the amount of mass lost during the cluster collision [154, 155],

$$R\frac{\Delta N}{N} = R(1 - e^{-R\overline{\sigma_{\rm T}}\sum_{\rm BC}/m_\chi}) < 0.3\,, \tag{6.7}$$

where $\sum_{\rm BC} = \int \rho_{\rm BC}\,{\rm d}x \approx 0.3\,{\rm g\,cm^{-2}}$ denotes the surface density of the bullet cluster. For large cross-sections, the total mass lost can never exceed $R$ and therefore the self-interaction constraint from the bullet cluster disappears for $R < 0.3$. For small self-interactions, the effect is proportional to $R^2$ and the constraint can be written as

$$R^2\frac{\overline{\sigma_{\rm T}}}{m_\chi} < 1\,{\rm cm^2\,g^{-1}}\,, \tag{6.8}$$

which is easily translatable to the DM mass and coupling.

With this brief aside into a concrete example for DM self-interactions, we now move toward a more general formulation and discuss in detail how to effectively parameterise SIDM.

## 6.2 Describing Non-Relativistic Interactions

The self-interactions we are interested in occur when DM is non-relativistic. In this case, we can describe the two particle scattering as a single particle with a reduced mass scattering off of a potential [156, 157]. The scattering cross-sections can then be evaluated either by solving for classical particle trajectories in this potential to determine the scattering angle $\theta$ for a given impact parameter, or by solving the Schroedinger Equation (SE) to determine the probability of scattering from the particle wavefunction. In the literature, much attention has been paid to the classical description [151, 158] even though it fails to account for certain phenomenological effects.

We begin this section with a short summary of the classical calculation before proceeding to the quantum-mechanical one. For the rest of this chapter, we will limit our discussion to centrally symmetric potentials.

### 6.2.1 Classical Description

Classical scattering has been studied in great detail in the plasma literature. It rests on the assumption that the de Broglie wavelengths of the scattering particles are much smaller than the length scales involved in the interaction such that they can be approximated with hard spheres. It is also characterised as the limit $k \to \infty$, where $k$ is the particle momentum in the reduced system. The scattering angle, $\theta(b)$ for a given impact parameter $b$, in a central potential $U(r)$ is then given by [159],

$$\theta(b) = \pi - \int_{r_0}^{\infty} {\rm d}r\,\frac{2b}{r^2\sqrt{1 - U(r)/E - b^2/r^2}}\,, \tag{6.9}$$

where, $E = \mu v^2/2$ is the kinetic energy in the CMS frame for the reduced mass, $\mu = m_\chi/2$, and relative velocity, $v$. Additionally, the lower limit of the integration, $r_0$, is the classical turning point, given by the largest root of the equation in the square root.

The differential scattering cross-section can be expressed in terms of the impact parameter $b$, $\mathrm{d}\sigma/\mathrm{d}\Omega = \mathrm{d}^2 b/\mathrm{d}\Omega$, which, from Eqs. 6.2 and 6.3, results in

$$\sigma_{\mathrm{T}} = \int \mathrm{d}\Omega \, (1 - \cos\theta) \, \frac{\mathrm{d}^2 b}{\mathrm{d}\Omega} = 2\pi \int_0^\infty \mathrm{d}b \, b \, (1 - \cos\theta(b)) \, , \tag{6.10}$$

$$\sigma_{\mathrm{V}} = \int \mathrm{d}\Omega \, \sin^2\theta \, \frac{\mathrm{d}^2 b}{\mathrm{d}\Omega} = 2\pi \int_0^\infty \mathrm{d}b \, b \sin^2\theta(b) \, . \tag{6.11}$$

Note that the lower limit of both the integrations above is set at $b = 0$. This is reflective of the fact that in a classical calculation, all length and momentum scales can be determined to an arbitrary degree of accuracy. This is in opposition to the quantum case where the uncertainty principle necessarily restricts the impact parameter to be larger than the uncertainty in the position $\Delta r$,

$$b \gtrsim \Delta r \gtrsim \frac{1}{2\Delta k} \gtrsim \frac{1}{2k}. \tag{6.12}$$

Therefore, the actual (quantum) cross-sections would be better approximated if the integration regime is restricted to $b \gtrsim 1/2k$. In the classical limit, $k \to \infty$, of course, we re-obtain the original expressions. This additional dependence of the cross-sections on the momentum is the first point of departure between the classical and quantum-mechanical calculations.

### 6.2.2 Quantum-Mechanical Description

The quantum description of the scattering problem is more general than the classical one. For one, it accounts for arbitrary particle momenta and potential strengths. It also generalises readily for the scattering of identical particles as we will see below. Although, we will be interested in the semi-classical regime[2] for interactions so that we can compare to the classical case, we will first provide a general framework for quantum calculations of elastic scattering.

Consider an incident, free particle described by a plane wave, $\psi = e^{-ikz}$, where $k = m_\chi v/2$ is the reduced momenta and $z$ specifies the direction of motion. After scattering on a potential, the particle can be described at some large distance $r$ by a spherical wave of the form $\psi = f(\theta) e^{ikr}/r$, where the scattering amplitude, $f(\theta)$, is a function of the scattering angle, i.e., the angle between z-axis and the direction of motion of the scattered particle. The exact wavefunction which must be a solution of the SE should then have the asymptotic form

$$\psi \approx e^{-ikz} + f(\theta) \frac{e^{ikr}}{r} \, . \tag{6.13}$$

[2]We provide an explicit definition for the semi-classical regime in section 6.3.

The probability of scattering, or the scattering cross-section, is simply given by $\mathrm{d}\sigma = |f(\theta)|^2 \, \mathrm{d}\Omega$ [157], where $f(\theta)$ can be determined by solving the SE.

For a centrally symmetric potential, any solution to the SE can be decomposed into a sum of products of spherical harmonics, $\psi \propto \sum_\ell \mathcal{R}_\ell(r) P_\ell(\cos\theta)$, with radial wavefunctions $\mathcal{R}_\ell(r)$ that satisfy,

$$\frac{1}{r^2}\frac{\partial}{\partial r}\left(r^2 \frac{\partial \mathcal{R}_\ell}{\partial r}\right) + \left(k^2 - m_\chi U(r) - \frac{\ell(\ell+1)}{r^2}\right)\mathcal{R}_\ell(r) = 0\,, \tag{6.14}$$

where $\mathcal{R}_\ell$ has the asymptotic form

$$\mathcal{R}_\ell \to \frac{\sin(kr - \frac{1}{2}l\pi + \delta_\ell)}{r}\,. \tag{6.15}$$

Here, the microphysics of scattering is encoded in the phase shifts, $\delta_\ell$. Using this relation for $\mathcal{R}_\ell$, the differential cross-section can be written as a sum over partial waves in the usual way [149, 157]

$$\frac{\mathrm{d}\sigma}{\mathrm{d}\Omega} = \frac{1}{k^2}\left|\sum_{\ell=0}^{\infty}(2\ell+1)e^{i\delta_\ell}P_\ell\left(\cos\theta\right)\sin\delta_\ell\right|^2\,, \tag{6.16}$$

with the total cross-section obtained by an integral over all angles. Further, using the properties of Legendre polynomials, we get for the momentum transfer and viscosity cross-sections,

$$\sigma_{\mathrm{T}} = \frac{4\pi}{k^2}\sum_{\ell=0}^{\infty}(\ell+1)\sin^2(\delta_{\ell+1} - \delta_\ell)\,, \tag{6.17}$$

$$\sigma_{\mathrm{V}} = \frac{4\pi}{k^2}\sum_{\ell=0}^{\infty}\frac{(\ell+1)(\ell+2)}{2\ell+3}\sin^2(\delta_{\ell+2} - \delta_\ell)\,. \tag{6.18}$$

**Identical particles**

We will now take a small detour to discuss the case of scattering of identical particles. The total two-particle wave function of a system can be written as a product of a spatial part and a spin part, $\Psi(\vec{r}_1, \vec{r}_2, s_1, s_2) = \psi(\vec{r}_1, \vec{r}_2)\epsilon(s_1, s_2)$. For identical bosons, the total wave function should be symmetric under particle exchange, implying that the spatial part needs to be even if the spin part is symmetric, and vice versa. Conversely, for fermions, the total wave function should be antisymmetric, meaning that the spatial part should be odd if the spin part is symmetric (and vice versa).

This is reflected in the partial wave expansion of the scattering cross-section which, for identical particles, can be written as,

$$\frac{\mathrm{d}\sigma}{\mathrm{d}\Omega} = \frac{1}{k^2}\left|\sum_{\ell=0}^{\infty}(2\ell+1)e^{i\delta_\ell}\left[P_\ell(\cos\theta) \pm P_\ell(-\cos\theta)\right]\sin\delta_\ell\right|^2\,, \tag{6.19}$$

where the second term accounts for the fact that if the particles are identical, a scattering by an angle $\theta$ is equivalent to one with an angle $\pi - \theta$. Further, the positive sign corresponds to an even spatial wave function ($\psi \sim (f(\theta) + f(\pi - \theta))e^{ikr}/r$), and the negative sign corresponds to an odd spatial wave function ($\psi \sim (f(\theta) - f(\pi - \theta))e^{ikr}/r$). Since $P_\ell(-x) = (-1)^\ell P_\ell(x)$, it follows that the contribution from all odd phase shifts vanishes for the even case, while the contribution from even phase shifts vanishes for the odd case. In other words, for identical bosons in a symmetric (antisymmetric) spin state, only the even (odd) partial waves contribute to the cross-section. Conversely, for identical fermions in a symmetric (antisymmetric) spin state, only the odd (even) partial waves contribute. In both cases,

$$\frac{\mathrm{d}\sigma}{\mathrm{d}\Omega}(\theta) = \frac{\mathrm{d}\sigma}{\mathrm{d}\Omega}(\pi - \theta) \tag{6.20}$$

as expected. This implies that $\int \mathrm{d}\cos\theta \frac{\mathrm{d}\sigma}{\mathrm{d}\Omega} \cos\theta = 0$, and therefore, $\sigma_{\mathrm{T}} = \sigma$. Hence, it is straight-forward to see why $\sigma_{\mathrm{T}}$ is not useful for the scattering of identical particles.

## 6.3 Self-interactions in a Yukawa Potential

We are finally ready to study the long-range interactions of the form given in Eq. 6.1. In the non-relativistic limit, these are well parametrised by a Yukawa potential,

$$U(r) = \pm\frac{\alpha_\chi}{r} e^{-m_\phi r}\,, \tag{6.21}$$

where $\alpha_\chi = g_\chi^2/4\pi$ is the dark fine structure constant and $m_\phi$ is the mediator mass. The potential can be attractive (+) or repulsive (−) depending on the nature of the DM particle $\chi$ and the mediator $\phi$. Scalar interactions ($\bar{\chi}\chi$ scattering) are purely attractive whereas vector interactions can be both attractive ($\bar{\chi}\chi$ scattering) and repulsive ($\chi\chi$ scattering).

It is well-known from the literature that analytic solutions to the SE for a Yukawa potential exist in the Born or perturbative regime, $\alpha_\chi m_\chi/m_\phi \ll 1$. It has also been shown that for small momentum, $k \ll m_\phi$, s-wave ($\ell = 0$) scattering dominates and accurate analytic approximations can be derived both for a Yukawa potential and in a more general framework [149, 160]. In the large momentum limit, $k \gtrsim m_\phi$, however, higher $\ell-$modes contribute making the calculation of the cross-section increasingly numerically intensive as one approaches the classical limit $k/m_\phi \to \infty$ [149]. In this regime, analytic expressions for only the momentum transfer cross-section have been previously found in the *strictly classical* limit following the methodology laid out in section 6.2.1 [161]. These forms of the cross-section are necessarily invalid in the semi-classical regime ($k/m_\phi \gtrsim 1$) as well as for identical particles.

We parameterise these different regimes by introducing two dimensionless parameters,

$$\kappa = \frac{k}{m_\phi}\,, \qquad \beta = \frac{2\alpha_\chi m_\phi}{m_\chi v^2}\,, \tag{6.22}$$

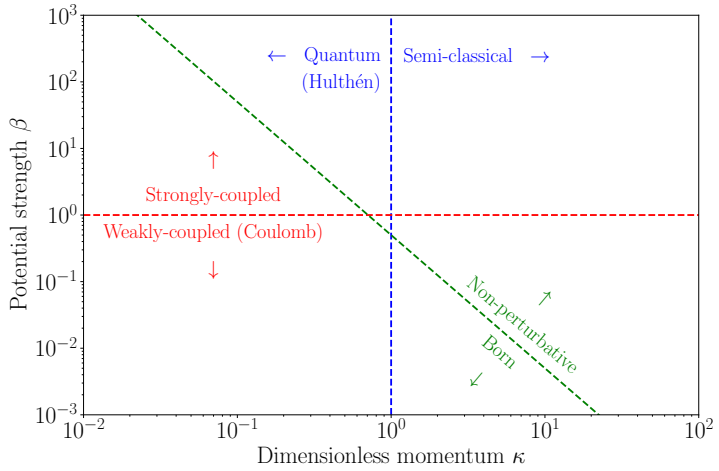


FIGURE 6.2: A sketch of the different regimes for DM self-interactions for a Yukawa potential in terms of the dimensionless parameters $\beta$ and $\kappa$. See text for details.

corresponding to the dimensionless momentum and the relative strength of the potential compared to the kinetic energy respectively. The different regimes in terms of these parameters are listed below and sketched in Fig. 6.2 where we also mention the different approximations used for computing the scattering cross-section.

$$\begin{aligned} \text{Weakly-coupled } (\beta \ll 1) \quad &\text{vs.} \quad \text{Strongly-coupled } (\beta \gg 1)\,, \\ \text{Born } (2\beta\kappa^2 \ll 1) \quad &\text{vs.} \quad \text{Non-perturbative regime } (2\beta\kappa^2 \gg 1)\,, \\ \text{Quantum } (\kappa \ll 1) \quad &\text{vs.} \quad \text{Semi-classical } (\kappa \gtrsim 1)\,. \end{aligned} \tag{6.23}$$

In the remainder of this chapter we will explore the semi-classical regime using a quantum-mechanical framework and derive analytic formulas for both $\sigma_{\rm T}$ and $\sigma_{\rm V}$.

As mentioned previously, to determine the scattering cross-section, we need to first evaluate the phase shifts, $\delta_\ell$. We start by rescaling the radial wave function, $u_\ell(R) = r\mathcal{R}_\ell(r)$. Parameterising the potential by using the definitions in Eq. 6.22, and introducing $R = rm_\phi$, the radial part of the SE becomes,

$$\frac{d^2u_\ell}{dR^2} + K^2(R)\,u_\ell(R) = 0\,, \tag{6.24}$$

where

$$K^2(R) = \kappa^2\left(1 - \frac{\ell(\ell+1)}{\kappa^2R^2} \mp \frac{2\beta}{R}e^{-R}\right)\,. \tag{6.25}$$

The asymptotic form of the rescaled wave function,

$$u_\ell(R) \xrightarrow[R\to\infty]{} \sin\left(\kappa R - \frac{\ell\pi}{2} + \delta_\ell\right)\,, \tag{6.26}$$

determines the phase shifts. In the semiclassical approximation[3], the wave function has the WKB form [159],

$$u_\ell^{\rm WKB}(R) = \frac{2}{K(R)^{1/2}} \cos\left(\int_{R_0}^{R} dR' K(R') - \frac{\pi}{4}\right) , \tag{6.27}$$

where $R_0 = r_0 m_\phi$ determines the classical turning point. The phase shift is the difference between the phase of this wave function and the phase of a free wave function, i.e., when $\beta = 0$,

$$\delta_\ell = \lim_{R\to\infty} \left(\int_{R_0}^{R} dR' K(R') - \frac{\pi}{4}\right) - \left(\int_{R_0}^{R} dR' K(R') - \frac{\pi}{4}\right)_{\beta=0} . \tag{6.28}$$

However, the WKB approximation breaks down near the origin for potentials which are dominated by the centrifugal term as $r \to 0$. This can be seen clearly by evaluating the second term in the equation above,

$$u_\ell^{\rm WKB}(R) \xrightarrow[R\to\infty]{} \sin\left(\kappa R - \frac{\pi}{2}\sqrt{\ell(\ell+1)} + \frac{\pi}{4}\right) . \tag{6.29}$$

This does not agree with the expected free wave function, $u_\ell(R) \to \sin(\kappa R - \frac{\ell\pi}{2})$, unless one makes the approximation $\ell \gg 1$. A solution to this problem was pointed out by Langer, who noted that the WKB method is valid over the entire domain if one makes the replacement, $\sqrt{\ell(\ell+1)} \to (\ell + 1/2)$ [162]. This is known in the literature as the *Langer modification* and amounts to the substitution,

$$K^2(R) \longrightarrow K^2_{\rm eff}(R) = \kappa^2 \left(1 - \frac{(\ell+\frac{1}{2})^2}{\kappa^2 R^2} \mp \frac{2\beta}{R} e^{-R}\right) . \tag{6.30}$$

Using this modification, the phase shifts in Eq. 6.28 are given by,

$$\delta_\ell = \kappa \int_{R_0}^{\infty} dR \left(\sqrt{1 \mp \frac{2\beta}{R} e^{-R} - \frac{(\ell+\frac{1}{2})^2}{\kappa^2 R^2}} - 1\right) + \frac{\pi(\ell+\frac{1}{2})}{2} - \kappa R_0 , \tag{6.31}$$

where $R_0$ is also determined using $K^2_{\rm eff}$.

With the phase shifts in hand, we now turn our attention back to $\sigma_{\rm T}$ and $\sigma_{\rm V}$. In the semiclassical limit, we are always interested in summing over a large range of $\ell$ modes, meaning that we can interpret $\delta_\ell$ as a continuous function of $\ell$, such that

$$\delta_{\ell+1} - \delta_\ell \approx \delta'(\ell + 1/2) , \tag{6.32}$$

$$\delta_{\ell+2} - \delta_\ell \approx 2\delta'(\ell + 1) , \tag{6.33}$$

[3]Here semiclassical refers to the fact that the wavefunctions, phase shifts and the scattering cross-sections are obtained in the limit where Planck's constant $\hbar$ is small compared to the action functions in the corresponding classical problem. Since the quantum-to-classical transition is singular at $\hbar = 0$, we cannot express quantum properties, such as wavefunctions, as perturbation series where the first term is the classical analogue. Instead, we use the *semiclassical* approximation where these singularities are accounted for. See Ref. [159] for a review.

where

$$\delta'(\ell) = \frac{\pi}{2} - \int_{R_0}^{\infty} dR \, \frac{\ell + \frac{1}{2}}{\kappa R^2 \sqrt{1 \mp \frac{2\beta}{R} e^{-R} - \frac{(\ell+1/2)^2}{\kappa^2 R^2}}} \, . \tag{6.34}$$

This approximation also means that the cross-sections in Eqs. 6.17 and 6.18 can be written as an integral over $\ell$,

$$\begin{aligned} \sigma_{\mathrm{T}} m_\phi^2 &\approx \frac{4\pi}{\kappa^2} \int_0^\infty \mathrm{d}\ell \, (\ell + \tfrac{1}{2}) \, \sin^2 \delta'(\ell) \\ &= \frac{4\pi}{\kappa^2} \int_{1/2}^\infty \mathrm{d}\ell \, \ell \, \sin^2 \delta'(\ell - 1/2) \, , \end{aligned} \tag{6.35}$$

$$\begin{aligned} \sigma_{\mathrm{V}} m_\phi^2 &\approx \frac{4\pi}{\kappa^2} \int_0^\infty \mathrm{d}\ell \, \frac{(\ell + 1/2)(\ell + 3/2)}{2\ell + 2} \, \sin^2 2\delta'(\ell + 1/2) \\ &\approx \frac{2\pi}{\kappa^2} \int_1^\infty \mathrm{d}\ell \, \ell \, \sin^2 2\delta'(\ell - 1/2) \, , \end{aligned} \tag{6.36}$$

where we have used $(\ell + 1/2)(\ell + 3/2)/(2\ell + 2) \approx (\ell + 1)/2$ in the final step. This translation from a sum to an integral is by no means unique but we find that it leads to results which are in remarkable agreement with the full numerical solutions of the SE. Additionally, one can show that the discrete sums are recovered when approximating the integrals by a Riemann sum with partition size $\Delta\ell = 1$.[4]

Before moving on, let us briefly discuss what happens to the formulas presented above in case of scattering of identical particles. From the last section, we already know that the most useful quantity that parameterises such a scattering is the viscosity cross-section $\sigma_{\mathrm{V}}$. Additionally, depending on the spin state of the incoming particles, only odd or even partial waves will contribute. In general, we can write

$$\sigma_{\mathrm{V}}^{\mathrm{even}} m_\phi^2 = \frac{8\pi}{\kappa^2} \sum_{\ell=0}^{\infty} \frac{(2\ell + 1)(2\ell + 2)}{4\ell + 3} \sin^2(\delta_{2\ell+2} - \delta_{2\ell}) \, , \tag{6.37}$$

$$\sigma_{\mathrm{V}}^{\mathrm{odd}} m_\phi^2 = \frac{8\pi}{\kappa^2} \sum_{\ell=0}^{\infty} \frac{(2\ell + 2)(2\ell + 3)}{4\ell + 5} \sin^2(\delta_{2\ell+3} - \delta_{2\ell+1}) \, , \tag{6.38}$$

where we have ensured that only even (odd) partial waves contribute by replacing $\ell \to 2\ell$ ($\ell \to 2\ell + 1$), and added an overall symmetry factor of $1/2$ to avoid double counting. Note

[4] From Ref. [2]: According to this approximation, an integral of the form $I = \int_{\ell_{\mathrm{min}}}^{\infty} f(\ell) \mathrm{d}\ell$ can be written as

$$I \approx \sum_{i=0}^{\infty} f\left(\ell_{\mathrm{min}} + \left(i + \tfrac{1}{2}\right) \Delta\ell\right) \Delta\ell = \sum_{\ell=0}^{\infty} f\left(\ell_{\mathrm{min}} + \ell + \tfrac{1}{2}\right) \, ,$$

where in the second step we have taken $\Delta\ell = 1$. Taking, for example, $\ell_{\mathrm{min}} = 0$ and $f(\ell) = (\ell + 1/2) \sin^2 \delta'(\ell)$ as in Eq. (6.35) then yields Eq. (6.17) with the approximation from Eq. (6.32).

that $\sigma_{\rm V}^{\rm even} + \sigma_{\rm V}^{\rm odd} = 2\sigma_{\rm V}$. Again, we can approximate the cross-section by an integral,

$$\begin{aligned}
\sigma_{\rm V}^{\rm even}\, m_\phi^2 &\approx \frac{8\pi}{\kappa^2} \int_0^\infty {\rm d}\ell\, \frac{(2\ell)(2\ell+1)}{4\ell+1} \sin^2 2\delta'(2\ell) \\
&\approx \frac{2\pi}{\kappa^2} \int_{1/2}^\infty {\rm d}\ell\, \ell \sin^2 2\delta'(\ell - 1/2)\,, \qquad (6.39) \\
\sigma_{\rm V}^{\rm odd}\, m_\phi^2 &\approx \frac{8\pi}{\kappa^2} \int_0^\infty {\rm d}\ell\, \frac{(2\ell+1)(2\ell+2)}{4\ell+3} \sin^2 2\delta'(2\ell+1) \\
&\approx \frac{2\pi}{\kappa^2} \int_{3/2}^\infty {\rm d}\ell\, \ell \sin^2 2\delta'(\ell - 1/2)\,. \qquad (6.40)
\end{aligned}$$

Realistically, incoming particles with a non-zero spin would always be unpolarised, i.e., the total wave function maybe either symmetric or antisymmetric. Hence, we should perform an averaging over the spin states which results in[5]

$$\sigma_{\rm V} \to \begin{cases} \sigma_{\rm V}^{\rm even} & \text{scalar DM}\,, \\ \frac{1}{4}\sigma_{\rm V}^{\rm even} + \frac{3}{4}\sigma_{\rm V}^{\rm odd} & \text{fermion DM}\,, \\ \frac{2}{3}\sigma_{\rm V}^{\rm even} + \frac{1}{3}\sigma_{\rm V}^{\rm odd} & \text{vector DM}\,. \end{cases} \qquad (6.41)$$

We finally turn our attention to the analytic approximations for the cross-sections in the semi-classical regime. Note that the following sections are quite technical and may be skipped in favour of simply the summary of the final analytic results presented in section 6.3.2.

### 6.3.1 Cross-sections in the Semi-Classical Regime

In this section, we will derive the analytic forms for $\sigma_{\rm T}$ and $\sigma_{\rm V}$ in the weakly coupled ($\beta \ll 1$) and strongly coupled regimes ($\beta \gg 1$). We will also discuss the intermediate regime $\beta \sim 1-50$ and provide a fitting formula for the cross-section for the same. Note that we are always in semi-classical regime, $\kappa \gtrsim 1$. The general steps of our calculations are:

1. Determine the distance of closest approach, $R_0$, i.e., the root of the effective potential, $K_{\rm eff}^2 = 0$ (Eq. 6.30), under the relevant assumptions.
2. Derive an analytic expression for $\delta_\ell$ and/or $\delta'_\ell$ as suitable.
3. Calculate the cross-sections by integrating over $\ell$. The integrals may be simplified by limiting the $\ell$ range by heuristic arguments, resulting in analytic expressions.

[5]This can be simply done by counting the number of symmetric and antisymmetric states for a given two-particle system. For example, scalars (bosons with 0-spin) only have a symmetric spin state. Identical fermions can either be in a symmetric singlet state $|s_{\rm tot},\, s_z\rangle = |00\rangle$ or in one of the antisymmetric triplet states $|11\rangle$, $|10\rangle$ or $|1-1\rangle$. Similarly for vectors, we will have 9 total states, 6 of which are symmetric and 3 antisymmetric.

**Weak Potential**

For $\beta \ll 1$, the effective potential can be approximated as

$$1 - \frac{(\ell+\frac{1}{2})^2}{\kappa^2 R^2} \mp \frac{2\beta}{R} e^{-R} \approx 1 - \frac{(\ell+\frac{1}{2})^2}{\kappa^2 R^2} , \tag{6.42}$$

which implies $R_0 \approx (l+1/2)/\kappa$. Additionally, we can expand the square root in Eq. 6.31 in $\beta$ to get,

$$\delta_\ell \approx \mp \int_{R_0}^{\infty} \mathrm{d}R \frac{\beta\kappa}{R} e^{-R} \frac{1}{\sqrt{1 - \frac{(\ell+\frac{1}{2})^2}{\kappa^2 R^2}}} = \mp \beta\kappa K_0 \left( \frac{\ell+\frac{1}{2}}{\kappa} \right) , \tag{6.43}$$

where $K_i$ denote the modified Bessel functions of the second kind and the negative (positive) sign corresponds to an attractive (repulsive) potential. The derivative of the phase shift is simply,

$$\delta'(\ell - 1/2) \approx \pm \beta K_1 \left( \frac{\ell}{\kappa} \right) . \tag{6.44}$$

The momentum transfer cross-section from Eq. 6.35 for both attractive and repulsive potentials is then given by,

$$\sigma_{\mathrm{T}} \approx \frac{4\pi}{\kappa^2 m_\phi^2} \int_{1/2}^{\infty} \ell \sin^2 \left[ \beta K_1 \left( \frac{\ell}{\kappa} \right) \right] \mathrm{d}\ell . \tag{6.45}$$

This integral can be further simplified by noting that $K_1$ is a monotonically decreasing function, and for $\beta\kappa < 1/2$,

$$\beta K_1 \left( \frac{\ell}{\kappa} \right) < \beta K_1 \left( \frac{1}{2\kappa} \right) < \beta K_1(\beta) < 1 . \tag{6.46}$$

Since $\ell > 1/2$, the argument of sine is small in the entire range of integration and by using $\sin x \approx x$, we can solve Eq. 6.45 to get

$$\sigma_{\mathrm{T}} \approx \frac{\pi\beta^2}{2\kappa^2 m_\phi^2} \left[ -K_1 \left( \frac{1}{2\kappa} \right)^2 + K_0 \left( \frac{1}{2\kappa} \right) K_2 \left( \frac{1}{2\kappa} \right) \right] \equiv \frac{2\pi\beta^2}{m_\phi^2} \eta \left( \frac{1}{2\kappa} \right) , \tag{6.47}$$

where the second step defines $\eta(x)$. For $\kappa \gg 1$,

$$\eta \left( \frac{1}{2\kappa} \right) \approx 2\log 4\kappa - 1 - 2\gamma_{\mathrm{E}} + \frac{1 - \gamma_{\mathrm{E}} + \log 4\kappa}{4\kappa^2} , \tag{6.48}$$

where $\gamma_{\mathrm{E}}$ is Euler's constant.

A completely analogous calculation for $\sigma_{\rm V}$ follows, yielding,

$$\sigma_{\rm V} \approx \frac{2\pi}{\kappa^2 m_\phi^2}\int_1^\infty \ell \sin^2\left[2\beta K_1\left(\frac{\ell}{\kappa}\right)\right]{\rm d}\ell \approx \frac{4\pi\beta^2}{m_\phi^2}\eta\left(\frac{1}{\kappa}\right) \ . \tag{6.49}$$

If instead $\beta\kappa > 1/2$, the expansion in the equation for $\delta_\ell$ is only valid for $\ell > \ell_{\rm min} \equiv \beta\kappa$. For small $\ell$, $(\delta_\ell - \delta_{\ell-1})$ becomes large and the integral over $\ell$ oscillates rapidly between 0 and 1. In this regime, the integral is best approximated by assuming $\sin^2 x \approx 1/2$,

$$\frac{4\pi}{\kappa^2 m_\phi^2}\int_{1/2}^{\ell_{\rm min}} \ell \sin^2\left(\delta_\ell - \delta_{\ell-1}\right){\rm d}\ell \approx \frac{\pi}{\kappa^2 m_\phi^2}\left(\ell_{\rm min}^2 - \frac{1}{4}\right) \ . \tag{6.50}$$

whereas for $\ell > \ell_{\rm min}$, the previous approximation holds and we get,

$$\frac{4\pi}{\kappa^2 m_\phi^2}\int_{\ell_{\rm min}}^\infty \ell \sin^2\left[\beta K_1\left(\frac{\ell}{\kappa}\right)\right]{\rm d}\ell \approx \frac{2\pi\beta^2}{m_\phi^2}\eta\left(\beta\right) \ . \tag{6.51}$$

The momentum transfer cross-section is therefore

$$\sigma_{\rm T} \approx \frac{2\pi\beta^2}{m_\phi^2}\left[\frac{\ell_{\rm min}^2 - \frac{1}{4}}{2\kappa^2\beta^2} + \eta\left(\beta\right)\right] \ . \tag{6.52}$$

We can further expand Eq. 6.52 assuming $\beta\kappa \gg 1$, in which case $\sigma_{\rm T}$ becomes purely a function of $\beta$,

$$\sigma_{\rm T} \approx \frac{2\pi\beta^2}{m_\phi^2}\left[2\log\frac{2}{\beta} - \frac{1}{2} - 2\gamma_{\rm E} + \beta^2\left(1 - \gamma_{\rm E} + \log\frac{2}{\beta}\right)\right] \ . \tag{6.53}$$

The crucial point here is that for $\beta < 1$ and a constant $\kappa$, $\sigma_{\rm T}$ scales more steeply than simply $\beta^2 \log\beta^{-1}$, contrary to the classical result (Eq. 6.101).

The two cases outlined above, Eq. 6.47 and 6.52 can be combined by defining,

$$\zeta_n(\kappa,\beta) \equiv \frac{\max(n,\beta\kappa)^2 - n^2}{2\kappa^2\beta^2} + \eta\left(\frac{\max(n,\beta\kappa)}{\kappa}\right) \ , \tag{6.54}$$

which leads to

$$\sigma_{\rm T} \approx \frac{2\pi\beta^2}{m_\phi^2}\zeta_{1/2}\left(\kappa,\beta\right) \ . \tag{6.55}$$

Analogously, for the viscosity cross-section the integration starts at $\ell = 1$ and therefore we need to use $2\beta K(\ell/\kappa) < 1$ to ensure that the argument of sine is small. This implies,

$$\sigma_{\rm V} \approx \frac{4\pi\beta^2}{m_\phi^2}\zeta_1\left(\kappa,2\beta\right) \ . \tag{6.56}$$

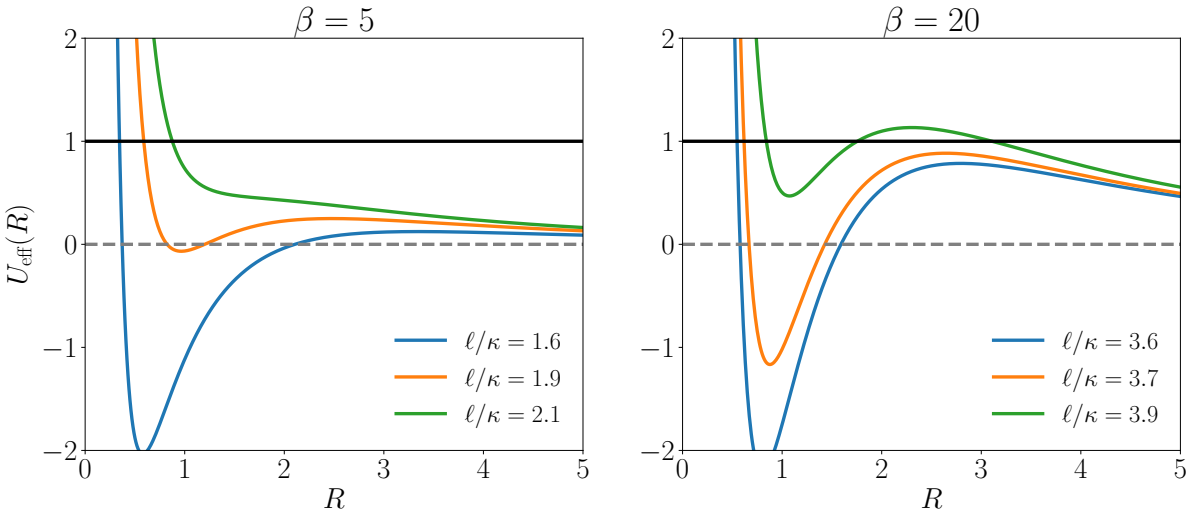


FIGURE 6.3: The effective potential as defined in Eq. 6.59 for two values of $\beta$. For $\beta \gtrsim 13.2$ a secondary barrier emerges resulting in a sudden jump in the distance of closest approach, $R_0$.

and similarly for the even and odd partial waves contributing we get,

$$\sigma_V^{\text{even}} \approx \frac{4\pi\beta^2}{m_\phi^2}\zeta_{1/2}\left(\kappa, 2\beta\right) \ , \tag{6.57}$$

$$\sigma_V^{\text{odd}} \approx \frac{4\pi\beta^2}{m_\phi^2}\zeta_{3/2}\left(\kappa, 2\beta\right) \ . \tag{6.58}$$

**Strong Potential**

Once again, we start with the effective potential which we reframe as,

$$U_{\text{eff}}(R) = \frac{(\ell+\frac{1}{2})^2}{\kappa^2 R^2} \mp \frac{2\beta}{R}e^{-R} \, . \tag{6.59}$$

so that $R_0$ is defined as the largest root of the equation $U_{\text{eff}}(R) = 1$. In this case, $R_0$ depends on the sign of $\beta$ and is different for attractive and repulsive potentials. We will therefore discuss these two case separately. Also note that for a strong potential, it can be shown numerically that the final cross-section is independent of $\kappa$ (see Fig. 6.4). This means we can always assume $\kappa \gg 1$ or equivalently take the lower limit of the cross-section integrals at $\ell = 0$.

1. **Attractive Potential**
   For an attractive potential, the effective potential can develop a secondary potential barrier for small values of $\ell$, leading to multiple roots (see Fig. 6.3). For $\beta < 13.2$, this effect is small enough that a unique root for $U_{\text{eff}}(R) = 1$ can still be defined for all values of $\ell$. For larger values of $\beta$ however there will be multiple roots to the equation. In this case, it is convenient to define $\ell = \ell_{\max}$ such that a *unique* root exists for $\ell < \ell_{\max}$. This can be

done by simultaneously solving the equations,

$$U_{\rm eff}(R) \equiv \left(\frac{\ell+1/2}{\kappa}\right)^2 \frac{1}{R^2} - 2\beta\frac{e^{-R}}{R} = 1 \tag{6.60}$$

$$\frac{{\rm d}U_{\rm eff}(R)}{{\rm d}R} = 0 \Rightarrow e^{-R} = \frac{1}{\beta}\left(\frac{\ell+1/2}{\kappa}\right)^2 \frac{1}{R(R+1)}\,, \tag{6.61}$$

where the second equation reflects the fact that a local maxima appears at $R > 0$. From these equations, we obtain,

$$\left(\frac{\ell+1/2}{\kappa}\right) = R_0\sqrt{\frac{R_0+1}{R_0-1}} \underset{R\gtrsim 1}{\approx} 1 + R_0 + \frac{1}{2R_0} \tag{6.62}$$

$$\Rightarrow R_0 \approx \frac{1}{2}\left(-1 + \frac{\ell+1/2}{\kappa} + \sqrt{-1 - \frac{2\ell+1}{\kappa} + \left(\frac{\ell+1/2}{\kappa}\right)^2}\right)\,. \tag{6.63}$$

Substituting this value of $R_0$ back in Eq. 6.61 we get,

$$\ell_{\rm max} = \kappa\left(1 + \log\beta - \frac{1}{2\,\log\beta}\right) - \frac{1}{2}\,. \tag{6.64}$$

We can now find $R_0$ for the case $\ell < \ell_{\rm max}$. Since, in such a case, $\ell/\kappa < 2\beta$, the equation $U_{\rm eff} = 1$ can only be satisfied for $R < 1$ in which case the Yukawa potential can be approximated with a Coulomb potential ($e^{-R}/R \approx 1/R$). This results in the simple expression,

$$R_0 \approx \frac{\ell^2}{2\beta\kappa^2} \qquad (\ell < \ell_{\rm max})\,. \tag{6.65}$$

In the opposite case, ($\ell > \ell_{\rm max}$), the largest root of the equation is for $R \gg 1$, or when the Yukawa potential is exponentially suppressed, resulting in

$$R_0 \approx \frac{\ell}{\kappa} \qquad (\ell > \ell_{\rm max})\,. \tag{6.66}$$

For $\ell > \ell_{\rm max}$, the distance of closest approach is so large that the phase shifts are tiny. These partial waves therefore do not contribute to the cross-sections and we can approximate

$$\sigma_{\rm T}^{\rm att.} m_\phi^2 \approx \frac{4\pi}{\kappa^2}\int_0^{\ell_{\rm max}} \ell\sin^2\delta'(\ell){\rm d}\ell\,. \tag{6.67}$$

We can now move on to calculating the phase shifts. In this case, it is easier to directly evaluate the phase shift derivative $\delta'(\ell)$,

$$\delta'(\ell) \approx -\frac{\pi}{2} - \frac{\ell}{\kappa}\gamma(\beta)\,, \tag{6.68}$$

where

$$\gamma(\beta) \equiv \frac{W(2\beta)+2}{W(2\beta)^2} \tag{6.69}$$

with $W(x)$ denoting the product logarithm. A detailed derivation is provided in Appendix A (reproduced from Ref. [2]). This approximation holds for $\frac{\ell}{\kappa}\gamma(\beta) < \pi/2$. We can therefore break the integral in Eq. 6.67 in two parts by defining $\ell' \equiv \frac{\ell}{\kappa}\gamma(\beta)$,

$$\sigma_{\mathrm{T}}^{\mathrm{att.}} m_\phi^2 \approx \frac{4\pi}{\gamma(\beta)^2}\int_0^{\pi/2} \ell' \sin(\pi/2+\ell')^2 \mathrm{d}\ell' + \frac{4\pi}{\kappa^2}\int_{\pi\kappa/(2\gamma(\beta))}^{\ell_{\max}} \ell \sin^2\delta'(\ell)\mathrm{d}\ell\,. \tag{6.70}$$

such that the first term evaluates to $(\pi^2-4)/16$, and in the second term we can once again make use of the approximation $\sin^2(x) \approx 1/2$. This yields,

$$\sigma_{\mathrm{T}}^{\mathrm{att.}} m_\phi^2 \approx \frac{\pi}{\kappa^2}\left(\ell_{\max}^2 - \frac{\kappa^2}{\gamma(\beta)^2}\right) \approx \pi\left[\left(1+\log\beta - \frac{1}{2\,\log\beta}\right)^2 - \frac{1}{\gamma(\beta)^2}\right]\,. \tag{6.71}$$

For $\beta \gg 1$, $\gamma(\beta) \approx 1/W(2\beta)$ and $W(2\beta) \approx \log\beta - \log\log\beta$ we obtain,

$$\sigma_{\mathrm{T}}^{\mathrm{att.}} m_\phi^2 \approx 2\pi \log\beta(\log\log\beta + 1)\,. \tag{6.72}$$

The calculation for the viscosity cross-section follows analogously, and we get

$$\sigma_{\mathrm{V}}^{\mathrm{att.}} m_\phi^2 \approx \frac{\pi}{2\kappa^2}\ell_{\max}^2 \approx \frac{\pi}{2}\left(1+\log\beta - \frac{1}{2\,\log\beta}\right)^2\,, \tag{6.73}$$

2. **Repulsive Potential**

For the repulsive case, $\beta > 1$ implies that the root of the equation $U_{\mathrm{eff}}(R) = 1$ is larger than one. We consider two regimes $\ell/\kappa \ll 1$ and $\ell/\kappa \gg 1$ which decide whether the Yukawa potential or the centrifugal potential dominates in the effective potential, Eq. 6.59. We can simply solve for $R_0$ in these two cases,

$$R_0 \approx W(2\beta) \qquad (\ell/\kappa \ll 1)\,, \tag{6.74}$$

$$R_0 \approx \frac{\ell}{\kappa} \qquad (\ell/\kappa \gg 1)\,. \tag{6.75}$$

Once again, we can use $\ell_{\max}$ to denote the transition between the two regions which happens when $W(2\beta) \approx R_0$. This gives,

$$\ell_{\max} \approx \kappa W(2\beta)\,. \tag{6.76}$$

A similar calculation as before results in the phase shift derivatives,

$$\delta'(\ell) \approx \frac{\pi}{2} + \frac{\ell}{\kappa}\int_{R_0}^{\infty}\frac{\mathrm{d}R}{R^2} \approx \frac{\pi}{2} - \frac{\ell}{\ell_{\max}}\,, \tag{6.77}$$

and consequently a momentum transfer cross-section,

$$\sigma_{\mathrm{T}}^{\mathrm{rep.}} m_\phi^2 \approx \pi \lambda_{\mathrm{T}} W(2\beta)^2 \,, \tag{6.78}$$

with $\lambda_{\mathrm{T}} \equiv (1 + \cos 2 + 2 \sin 2)/2 \approx 1.20$.

Analogously for the viscosity cross-section and for $\ell < \ell_{\mathrm{max}}$, we have,

$$2\delta'(\ell) \approx \pi - \frac{2\ell}{\ell_{\mathrm{max}}} \,. \tag{6.79}$$

Since this is close to $\pi$, the contribution of these phase-shifts is suppressed in the viscosity cross-section and we need to extend the integration region beyond $\ell_{\mathrm{max}}$. For $\ell > \ell_{\mathrm{max}}$, we can use the approximation for the weak potential (since the centrifugal term in the potential always dominates) and approximate

$$2\delta'(\ell) \approx 2\beta K_1\left(\frac{\ell}{\kappa}\right) \,. \tag{6.80}$$

Using these two equations, we can write for the viscosity cross-section

$$\sigma_{\mathrm{V}}^{\mathrm{rep.}} \approx \frac{2\pi}{\kappa^2 m_\phi^2}\left[\int_0^{\ell_{\mathrm{max}}} \ell \sin^2\left(\pi - \frac{2\ell}{\ell_{\mathrm{max}}}\right) \mathrm{d}\ell + \int_{\ell_{\mathrm{max}}}^{\infty} \ell \sin^2\left(2\beta K_1\left(\frac{\ell}{\kappa}\right)\right) \mathrm{d}\ell\right] \,, \tag{6.81}$$

where the first term evaluates to $\pi\lambda_{\mathrm{V}}\, W(2\beta)^2$ with $\lambda_{\mathrm{V}} = (9 - \cos 4 - 4\sin 4)/16 \approx 0.793$, and the second term can be calculated by noting that the argument for the sine becomes small for $\ell > \kappa \log 2\beta$ (and consequently, the contribution to the cross-section becomes negligible for larger $\ell$'s).[6] Hence,

$$\sigma_{\mathrm{V}}^{\mathrm{rep.}} m_\phi^2 \approx \pi\lambda_{\mathrm{V}}\, W(2\beta)^2 + \frac{\pi}{2}\left(\log^2 2\beta - W(2\beta)^2\right) \tag{6.82}$$

$$\approx \pi \log 2\beta \left(\lambda_{\mathrm{V}} \log 2\beta - (2\lambda_V - 1)\log\log 2\beta\right) \,. \tag{6.83}$$

Finally, for $\beta \gg 1$, the scattering of identical particles becomes trivial as we always have $\sigma_{\mathrm{V}}^{\mathrm{even}} \approx \sigma_{\mathrm{V}}^{\mathrm{odd}} \approx \sigma_{\mathrm{V}}$.

### Intermediate regime

The approximations we have made so far do not work for potentials of the order $\beta \sim 1$. In particular, on numerically solving the SE, we find that the $\sigma_{\mathrm{T}}$ already starts to differ between the attractive and repulsive potentials for $\beta \gtrsim 0.2$ which cannot be accounted for by assuming $\beta \ll 1$. Additionally, for $\beta \lesssim 50$, the momentum transfer cross-section exhibits a number of oscillations as a result of the maximal value of the phase shift derivative approaching $\pi$ ($\pi/2$) which enhances (suppresses) $\sigma_{\mathrm{T}}$. These cannot be accounted for in our treatment. In the

[6] For some $\ell > \tilde{\ell}_{\mathrm{max}}$, $2\beta K_1(\ell/\kappa) \to 0$. Since, $\beta > 1 \Rightarrow \ell'/\kappa \gg 1 \Rightarrow K_1(\ell/\kappa) \approx e^{-\ell/\kappa}\sqrt{\pi\kappa/2\ell}$. $\tilde{\ell}_{\mathrm{max}}$ can be obtained by solving $2\beta e^{-\ell/\kappa}\sqrt{\pi\kappa/2\ell} = 1$, which yields $\tilde{\ell}_{\mathrm{max}} \approx \kappa \log 2\beta$.

end, however, these peaks are irrelevant since the quantity of interest is always the velocity-averaged cross-section in which these features get smeared out.

Nevertheless, for the regime $0.2 \lesssim \beta \lesssim 50$, it is better to use an empirical fitting formula for $\sigma_{\rm T}$ and $\sigma_{\rm V}$ instead of trying to extend our analytic treatment. This can be done by further breaking this $\beta$ regime into two: $1 \lesssim \beta \lesssim 50$, where we know that the cross-sections are independent of $\kappa$, and $0.2 \lesssim \beta \lesssim 1$, where they are not.

For the former, we calculate the cross-sections numerically at $\beta = 1$ in the limit $\kappa \gg 1$ to obtain $\sigma_{\rm T}^{\rm att.} m_\phi^2/\pi = 2.8$ ($\sigma_{\rm T}^{\rm rep.} m_\phi^2/\pi = 1.1$) for the attractive (repulsive) case. Assuming that $\sigma_{\rm T} m_\phi^2/\pi$ scales as $a\log(\beta + b)$ for $1 < \beta < 50$, we can find the values of $a$ and $b$ by ensuring that the numerical result at $\beta = 1$ is reproduced as well as that the function connects continuously to the analytic expressions for large $\beta$. This gives,

$$\sigma_{\rm T}^{\rm att.} = 4.7\log(\beta + 0.82)\frac{\pi}{m_\phi^2} \qquad (1 < \beta < 50)\,, \tag{6.84}$$

$$\sigma_{\rm T}^{\rm rep.} = 2.9\log(\beta + 0.47)\frac{\pi}{m_\phi^2} \qquad (1 < \beta < 50)\,. \tag{6.85}$$

For $0.2 \lesssim \beta \lesssim 1$, the non-negligible dependence on $\kappa$ implies that a better approximation for the fitting function is obtained by multiplying the analytic expressions with $e^{c(\beta-0.2)}$. We determine $c$ by demanding continuity at $\beta = 1$, leading to,

$$\sigma_{\rm T}^{\rm att.} = \frac{2\pi\beta^2}{m_\phi^2}\zeta_{1/2}\left(\kappa, \beta\right) e^{0.64(\beta-0.2)} \qquad (0.2 < \beta \leq 1)\,, \tag{6.86}$$

$$\sigma_{\rm T}^{\rm rep.} = \frac{2\pi\beta^2}{m_\phi^2}\zeta_{1/2}\left(\kappa, \beta\right) e^{-0.53(\beta-0.2)} \qquad (0.2 < \beta \leq 1)\,. \tag{6.87}$$

An analogous calculation can be performed for the viscosity cross-section. Note that in this case, the intermediate regime is shifted to slightly smaller values of $\beta$. For $\beta = 0.5$, numerical evaluation of the cross-sections yields $\sigma_{\rm V}^{\rm att.} m_\phi^2/\pi = 1.1$ ($\sigma_{\rm V}^{\rm rep.} m_\phi^2/\pi = 0.73$) for the attractive (repulsive) potential, resulting in,

$$\sigma_{\rm V}^{\rm att.} = 2.5\log(\beta + 1.05)\frac{\pi}{m_\phi^2} \qquad (0.5 < \beta < 25)\,, \tag{6.88}$$

$$\sigma_{\rm V}^{\rm rep.} = 2.8\log(\beta + 0.80)\frac{\pi}{m_\phi^2} \qquad (0.5 < \beta < 25)\,, \tag{6.89}$$

and

$$\sigma_{\rm V}^{\rm att.} = \frac{4\pi\beta^2}{m_\phi^2}\zeta_n\left(\kappa, 2\beta\right) e^{0.67(\beta-0.1)} \qquad (0.1 < \beta \leq 0.5)\,, \tag{6.90}$$

$$\sigma_{\rm V}^{\rm rep.} = \frac{4\pi\beta^2}{m_\phi^2}\zeta_n\left(\kappa, 2\beta\right) e^{-0.37(\beta-0.1)} \qquad (0.1 < \beta \leq 0.5)\,, \tag{6.91}$$

where $n = 1$ for distinguishable particles and $n = \frac{1}{2}$ ($n = \frac{3}{2}$) for identical particles with even (odd) spatial wave function.

### 6.3.2 Summary

Our analytic results can be summarised as follows:

$$\sigma_{\mathrm{T}}^{\mathrm{att.}} = \frac{\pi}{m_\phi^2} \times \begin{cases} 2\beta^2 \zeta_{1/2}\left(\kappa, \beta\right) & \beta \leq 0.2 \\ 2\beta^2 \zeta_{1/2}\left(\kappa, \beta\right) e^{0.64(\beta - 0.2)} & 0.2 < \beta \leq 1 \\ 4.7 \log(\beta + 0.82) & 1 < \beta < 50 \\ 2 \log \beta (\log\log \beta + 1) & \beta \geq 50 \end{cases} \tag{6.92}$$

$$\sigma_{\mathrm{T}}^{\mathrm{rep.}} = \frac{\pi}{m_\phi^2} \times \begin{cases} 2\beta^2 \zeta_{1/2}\left(\kappa, \beta\right) & \beta \leq 0.2 \\ 2\beta^2 \zeta_{1/2}\left(\kappa, \beta\right) e^{-0.53(\beta - 0.2)} & 0.2 < \beta \leq 1 \\ 2.9 \log(\beta + 0.47) & 1 < \beta < 50 \\ \lambda_{\mathrm{T}} (\log 2\beta - \log\log 2\beta)^2 & \beta \geq 50 \end{cases} \tag{6.93}$$

with

$$\zeta_n(\kappa, \beta) = \frac{\max(n, \beta\kappa)^2 - n^2}{2\kappa^2\beta^2} + \eta\left(\frac{\max(n, \beta\kappa)}{\kappa}\right), \tag{6.94}$$

$$\eta(x) = x^2 \left[-K_1\left(x\right)^2 + K_0\left(x\right) K_2\left(x\right)\right], \tag{6.95}$$

$$\approx -2\log\left(\frac{x}{2}\right) - 1 - 2\gamma_{\mathrm{E}} + x^2\left[1 - \gamma_{\mathrm{E}} - \log\left(\frac{x}{2}\right)\right]. \tag{6.96}$$

$$\sigma_{\mathrm{V}}^{\mathrm{att.}} = \frac{\pi}{m_\phi^2} \times \begin{cases} 4\beta^2 \zeta_n\left(\kappa, 2\beta\right) & \beta \leq 0.1 \\ 4\beta^2 \zeta_n\left(\kappa, 2\beta\right) e^{0.67(\beta - 0.1)} & 0.1 < \beta \leq 0.5 \\ 2.5 \log(\beta + 1.05) & 0.5 < \beta < 25 \\ \frac{1}{2}\left(1 + \log\beta - \frac{1}{2\log\beta}\right)^2 & \beta \geq 25 \end{cases} \tag{6.97}$$

$$\sigma_{\mathrm{V}}^{\mathrm{rep.}} = \frac{\pi}{m_\phi^2} \times \begin{cases} 4\beta^2 \zeta_n\left(\kappa, 2\beta\right) & \beta \leq 0.2 \\ 4\beta^2 \zeta_n\left(\kappa, 2\beta\right) e^{-0.37(\beta - 0.1)} & 0.1 < \beta \leq 0.5 \\ 2.8 \log(\beta + 0.80) & 0.5 < \beta < 25 \\ \log 2\beta \left(\lambda_{\mathrm{V}} \log 2\beta - (2\lambda_V - 1) \log\log 2\beta\right) & \beta \geq 25 \end{cases} \tag{6.98}$$

with

$$\lambda_{\rm T} = (1 + \cos 2 + 2\sin 2)/2\,, \tag{6.99}$$

$$\lambda_{\rm V} = (9 - \cos 4 - 4\sin 4)/16\,, \tag{6.100}$$

where $n = 1$ for distinguishable particles and $n = \frac{1}{2}$ ($n = \frac{3}{2}$) for identical particles with even (odd) spatial wave function.

These expressions can be accessed via the online code CLASSICS (CalcuLAtionS of Self Interaction Cross Sections) available at https://github.com/kahlhoefer/CLASSICS.

### Comparison with pre-existing results and numerical solutions

In the classical limit, analytic expressions for $\sigma_{\rm T}$ are known from the literature. For an attractive Yukawa potential, we have [163]

$$\sigma_{\rm T} = \begin{cases} \frac{2\pi}{m_\phi^2}\beta^2\log(1+\beta^{-2}) & \beta \lesssim 10^{-2} \\ \frac{7\pi}{m_\phi^2}\frac{\beta^{1.8}+280(\beta/10)^{10.3}}{1+1.4\beta+0.006\beta^4+160(\beta/10)^{10}} & 10^{-2} \lesssim \beta \lesssim 10^2 \\ \frac{0.81\pi}{m_\phi^2}(1+\log\beta-(2\log\beta)^{-1})^2 & \beta \gtrsim 10^2 \end{cases}. \tag{6.101}$$

whereas for a repulsive Yukawa potential, the corresponding formulas are [163]:

$$\sigma_{\rm T} = \begin{cases} \frac{2\pi}{m_\phi^2}\beta^2\log(1+\beta^{-2}) & \beta \lesssim 10^{-2} \\ \frac{8\pi}{m_\phi^2}\frac{\beta^{1.8}}{1+5\beta^{0.9}+0.85\beta^{1.6}} & 10^{-2} \lesssim \beta \lesssim 10^4 \\ \frac{\pi}{m_\phi^2}(\log 2\beta - \log\log 2\beta)^2 & \beta \gtrsim 10^4 \end{cases}. \tag{6.102}$$

In Fig. 6.4, we compare our results for the momentum scattering cross-section with the classical ones and with a full numerical solution of the SE for both attractive and repulsive potentials and for different values of $\kappa$. Our results are in a much better agreement with the numerical results for $\beta \lesssim 1$ where $\sigma_{\rm T}$ has a non-trivial $\kappa$-dependence. Further, one can see clearly from Fig. 6.4, that our results approach the classical formulas in the limit $\kappa \to \infty$.

Going back to the point made at the beginning of this section, our results imply that nearly complete analytic coverage of the parameter space for the Yukawa potential is now possible. We demonstrate this in Fig. 6.5, where we plot both $\sigma_{\rm T} m_\phi^2$ and $\sigma_{\rm V} m_\phi^2$ as functions of $\kappa$ for different values of $\beta$. The dots once again represent the exact numerical solutions obtained from the SE and span both the semi-classical ($\kappa > 1$) and the quantum regime ($\kappa < 1$). For the former, the solid lines represent our analytic results once again in better agreement with the full numerical results than the classical cross-sections. The quantum regime is usually dominated by $s-$wave scattering and analytic formulas for the cross-section can be obtained by using a Hulthén approximation,[7] represented in Fig. 6.5 by dashed lines. Together with

[7] This treatment accurately captures the effects of resonances and antiresonances. See Ref. [149] for more details.

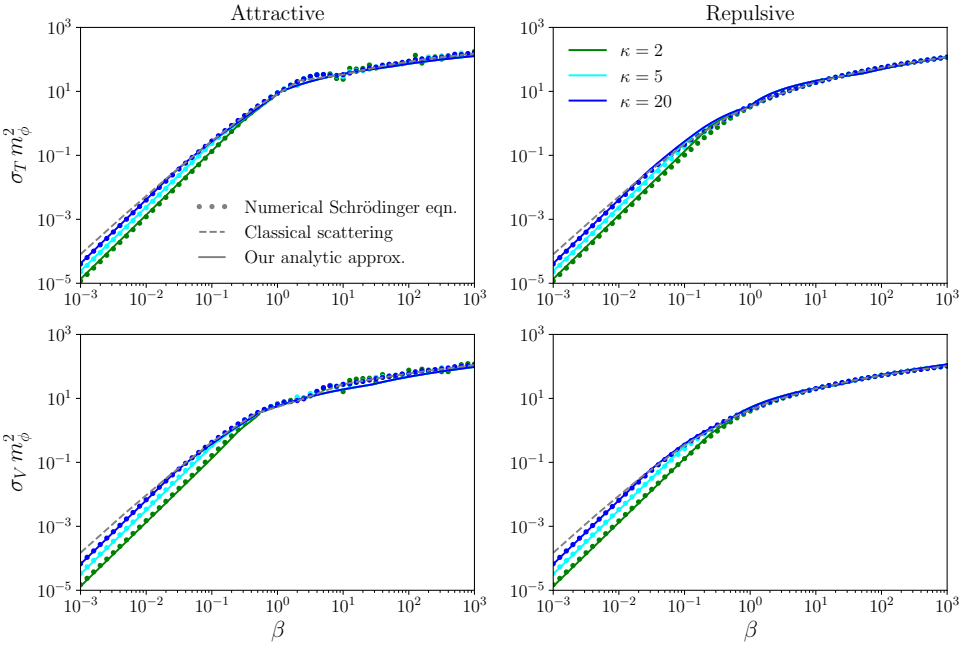


FIGURE 6.4: Dimensionless cross sections $\sigma_{\mathrm{T}} m_\phi^2$ and $\sigma_{\mathrm{V}} m_\phi^2$ as a function of $\beta$, for attractive and repulsive Yukawa potentials, for different values of $\kappa$. The solid lines correspond to our analytic results, the dots correspond to cross-sections obtained by numerically solving the SE, and the dashed lines reflect purely classical scattering.

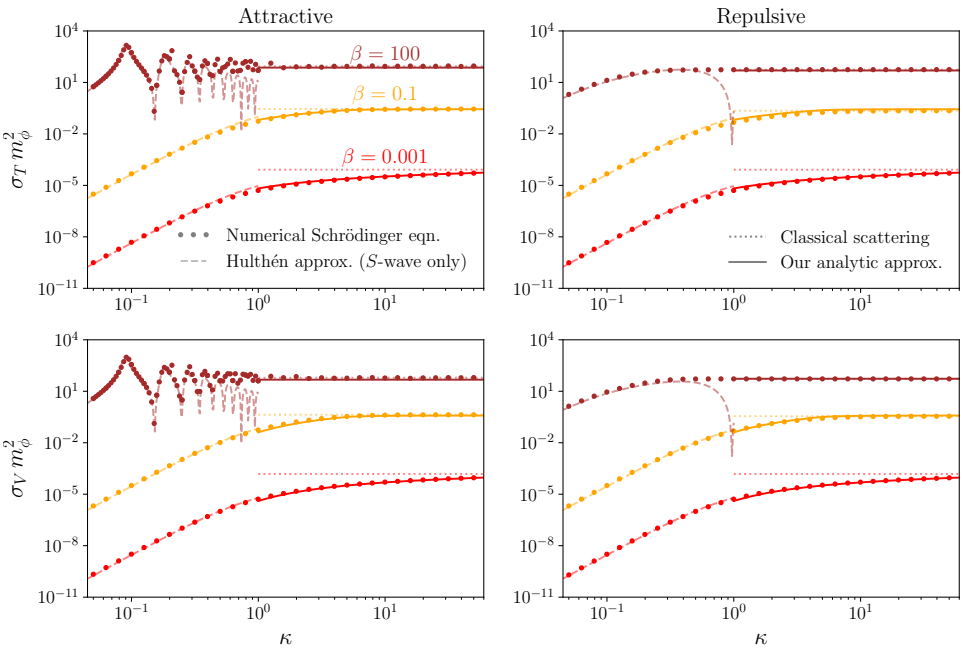


FIGURE 6.5: Dimensionless cross sections $\sigma_{\mathrm{T}} m_\phi^2$ and $\sigma_{\mathrm{V}} m_\phi^2$ as a function of $\kappa$, for attractive and repulsive Yukawa potentials, for different values of $\beta$. The solid lines correspond to our analytic results in the semi-classical regime, $\kappa > 1$, the dots correspond to cross-sections obtained by numerically solving the SE, and the dotted lines reflect purely classical scattering. Additionally, dashed lines for $\kappa < 1$ represent analytic approximation using a Hulthén potential.

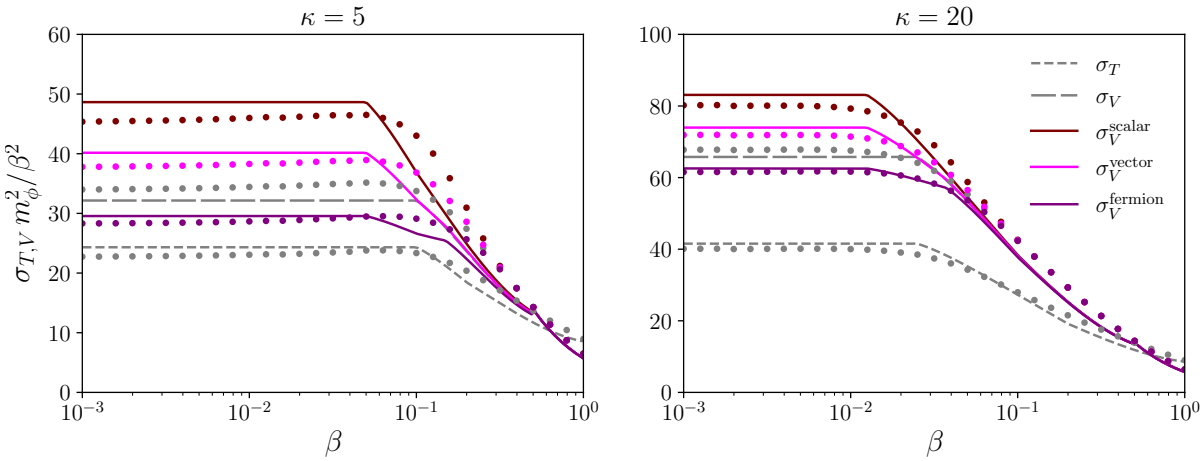


FIGURE 6.6: Cross sections for distinguishable versus identical particles for an attractive Yukawa potential, with $\kappa = 5$ (left) and $\kappa = 20$ (right). Grey coloured lines denote distinguishable cross sections $\sigma_{\rm T}$ (short-dashed) and $\sigma_{\rm V}$ (long-dashed), whereas the other coloured lines correspond to identical scattering, depending on the DM particle spin $s = 0, \frac{1}{2}, 1$. As before, solid lines correspond to analytic results and dots to numerical ones.

our semi-classical results, it is now possible to analytically describe Yukawa scattering for both $\kappa \lesssim 1$ and $\kappa \gtrsim 1$. Note that both these treatments break down at $\kappa = 1$ but sensible results for the cross-sections can still be obtained by a simple interpolation between the two regimes.

Finally, we highlight the differences between scattering of identical and non-identical particles in Fig. 6.6, where we plot the cross-sections rescaled by $\beta^2$, $\sigma_{\rm T,V} m_\phi^2/\beta^2$ for two different values of $\kappa$. The deviation arising due indistinguishability of particles is starkest for small values of $\kappa$. In this regime, only a small number of phase shifts contribute and therefore the differences between considering $\sigma_{\rm V}^{\rm even}$ or $\sigma_{\rm V}^{\rm odd}$ are important. For $\kappa = 5$, using the momentum transfer cross-section instead of the viscosity cross-section for identical particles can result in a difference as large as a factor of 2.

## 6.4 Velocity Averaging

With an accurate description of the relevant cross-sections in hand, we now turn toward the second question posed in section 6.1, i.e., what is the correct velocity-averaging procedure one needs when wanting to compare to data. As mentioned previously, we are interested not in the rate of scattering but in the rate of energy and momentum transfer.

To calculate this rate, consider a DM particle moving with a velocity $v$ in a halo with a background particle density of $\rho$ (currently assumed to be at rest). The probability of scattering for this particle is $\rho\sigma v/m_\chi$. We now shift to the centre-of-mass frame for this interaction which moves with a velocity $v_{\rm frame} = v/2$. The momentum and energy transfer during the collision can be written in terms of the velocity transfer $\Delta\mathbf{v} = \mathbf{v}_{\rm cms} - \mathbf{v}'_{\rm cms}$, where $\mathbf{v}_{\rm cms}$ and $\mathbf{v}'_{\rm cms}$ denote

the velocity of the incoming and outgoing DM particle in the cms frame. For a given scattering angle, $\theta_{\rm cms}$, it is possible to decompose $\Delta\mathbf{v}$ into a parallel and a transverse component, $\Delta v_{\parallel} = v_{\rm cms}(1-\cos\theta_{\rm cms})$, $\Delta\mathbf{v}_{\perp} = -v_{\rm cms}(\sin\theta_{\rm cms}\cos\phi, \sin\theta_{\rm cms}\sin\phi)$, where $\phi$ is the azimuthal angle. The parallel component is responsible for efficient transfer of momentum, whereas the transverse component corresponds to an efficient transfer of energy. By noting that the distribution of scattering angles is given by $\sigma^{-1}{\rm d}\sigma/{\rm d}\theta_{\rm cms}$, we can calculate the expectation values $\langle\Delta v_{\parallel}\rangle$ and $\langle\Delta\mathbf{v}_{\perp}^2\rangle$[8]:

$$\langle\Delta v_{\parallel}\rangle = \frac{v_{\rm cms}}{\sigma}\int\frac{{\rm d}\sigma}{{\rm d}\theta_{\rm cms}}(1-\cos\theta_{\rm cms}){\rm d}\theta_{\rm cms} = \frac{\sigma_{\rm T}v}{2\,\sigma}\,, \tag{6.103}$$

$$\langle\Delta v_{\perp}^2\rangle = \frac{v_{\rm cms}^2}{\sigma}\int\frac{{\rm d}\sigma}{{\rm d}\theta_{\rm cms}}\sin^2\theta_{\rm cms}{\rm d}\theta_{\rm cms} = \frac{\sigma_{\rm V}v^2}{4\,\sigma}\,, \tag{6.104}$$

where in the final equalities we have used the fact that the cms velocity for the DM particle is half its velocity in the rest frame of the halo. This yields for the relative change in momentum and energy,

$$\frac{\dot{p}}{p} = \frac{\rho}{m_\chi}\frac{v\sigma_{\rm T}}{2} \qquad \frac{\dot{E}_{\perp}}{E} = \frac{\rho}{m_\chi}\frac{v\sigma_{\rm V}}{4}\,. \tag{6.105}$$

These formulas are generalisable for the more realistic case where the background particle density is not at rest but has its own velocity distribution. In such a case, the rate at which these particles encounter each other is $\rho\sigma v_{\rm rel}/m_\chi$, where $\mathbf{v}_{\rm rel} = \mathbf{v}-\mathbf{w}$ and $\mathbf{w}$ is the velocity of the background particles. The centre of mass velocity is now given by $v_{\rm cms}/2$ which results in the relative momentum and energy transfer rates

$$\frac{\dot{p}}{p} = \frac{\rho}{m_\chi}\frac{v_{\rm rel}^2\sigma_{\rm T}(v_{\rm rel})}{2v}\,, \qquad \frac{\dot{E}_{\perp}}{E} = \frac{\rho}{m_\chi}\frac{v_{\rm rel}^3\sigma_{\rm V}}{4v^2}\,, \tag{6.106}$$

where the additional factor of $v_{\rm rel}/v$ accounts for the fact that the velocity transfer can never exceed the relative velocity in a collision.

For DM particles in a halo, both the incoming DM particle and the background particle densities approximately follow a Maxwell-Boltzmann distribution with a velocity dispersion $v_0$

$$f(v) = \sqrt{\frac{2}{\pi}}\frac{v^2e^{-v^2/(2v_0^2)}}{v_0^3}\,, \tag{6.107}$$

resulting in a typical momentum, $\langle p\rangle = 2\sqrt{2/\pi}m_\chi v_0$, and energy $\langle E\rangle = \frac{3}{2}m_\chi v_0^2$. We can then simply evaluate the momentum and energy transfer rates as,

$$\Gamma_p \equiv \frac{\langle\dot{p}\rangle}{\langle p\rangle} = \frac{\rho}{m_\chi}\frac{\langle\sigma_{\rm T}v_{\rm rel}^2\rangle}{4\sqrt{2/\pi}v_0} = \frac{\rho}{m_\chi}\int{\rm d}v_{\rm rel}\sigma_{\rm T}(v_{\rm rel})\frac{v_{\rm rel}^4}{8\sqrt{2}v_0^4}e^{-v_{\rm rel}^2/(4v_0^2)}\,, \tag{6.108}$$

$$\Gamma_E \equiv \frac{\langle\dot{E}_{\perp}\rangle}{\langle E\rangle} = \frac{\rho}{m_\chi}\frac{\langle\sigma_{\rm V}v_{\rm rel}^3\rangle}{6v_0^2} = \frac{\rho}{m_\chi}\int{\rm d}v_{\rm rel}\sigma_{\rm V}(v_{\rm rel})\frac{v_{\rm rel}^5}{12\sqrt{\pi}v_0^5}e^{-v_{\rm rel}^2/(4v_0^2)}\,. \tag{6.109}$$

[8] $\langle\Delta\mathbf{v}_{\perp}\rangle = 0$ since the azimuthal angle is uniformly distributed.

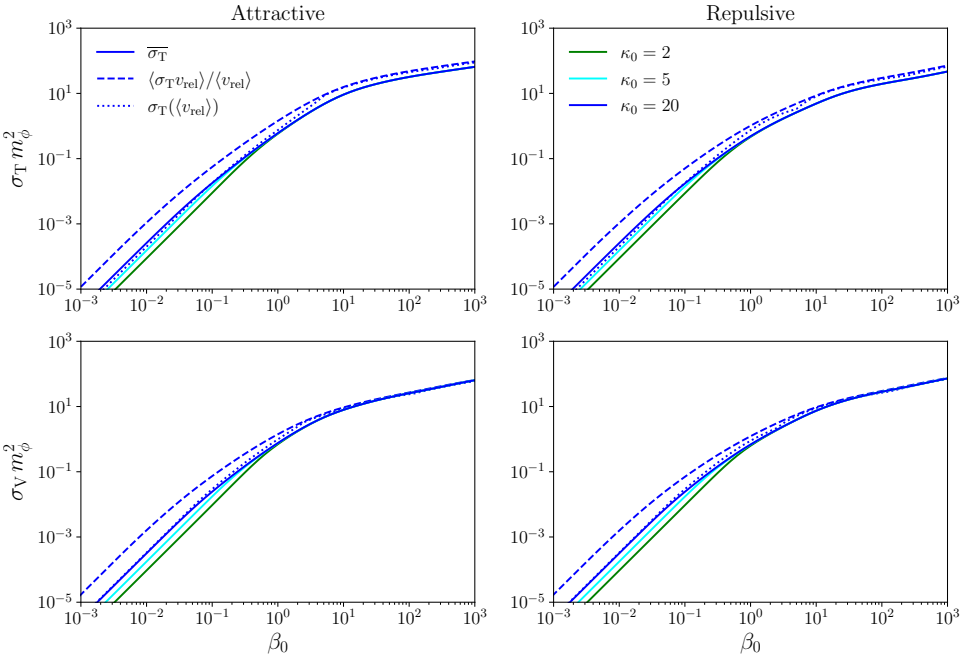


FIGURE 6.7: The averaged momentum transfer cross section (top) and viscosity cross section (bottom) for the attractive (left) and repulsive (right) Yukawa potential following different averaging prescriptions and for different values of $\kappa$. Our averaging procedure is represented using solid lines, whereas dashed and dotted lines correspond to alternatives approaches followed in the literature.

which can be reframed by defining,

$$\overline{\sigma_{\rm T}} = \frac{\langle \sigma_{\rm T} v_{\rm rel}^2 \rangle}{16\sqrt{2} v_0^2/\pi} \,, \qquad \overline{\sigma_{\rm V}} = \frac{\langle \sigma_{\rm V} v_{\rm rel}^3 \rangle}{24/\sqrt{\pi} v_0^3} \,, \tag{6.110}$$

as,

$$\Gamma_p = \frac{\rho}{m_\chi} \overline{\sigma_{\rm T}} \langle v_{\rm rel} \rangle \,, \tag{6.111}$$

$$\Gamma_E = \frac{\rho}{m_\chi} \overline{\sigma_{\rm V}} \langle v_{\rm rel} \rangle \,. \tag{6.112}$$

For cross-sections which can be written as $\sigma_{\rm T,V} = \frac{\pi}{m_\phi^2} f_{\rm T,V}(\beta, \kappa)$, we can simplify the averages to have the form

$$\begin{aligned} \overline{\sigma_{\rm T}} &= \frac{\pi}{m_\phi^2} \int {\rm d}x e^{-x^2/4} \frac{x^4}{32\sqrt{2/\pi}} f_{\rm T}(\beta_0/x^2, \kappa_0 x) \,, \\ \overline{\sigma_{\rm V}} &= \frac{\pi}{m_\phi^2} \int {\rm d}x e^{-x^2/4} \frac{x^5}{48} f_{\rm V}(\beta_0/x^2, \kappa_0 x) \,, \end{aligned} \tag{6.113}$$

where $x = v/v_0$, and $\beta_0$ and $\kappa_0$ are the effective parameters obtained when setting $v = v_0$. For $\kappa_0 \gg 1$ the velocity averaged cross section hence depends only on $\beta_0$ and (trivially) on $m_\phi$.

From the equations above, we see that rates of energy and momentum transfer place more weight on collisions with larger velocities. Consequently, the effects of collisions with small velocities is suppressed and we obtain a finite result for the rate even for the cases where the

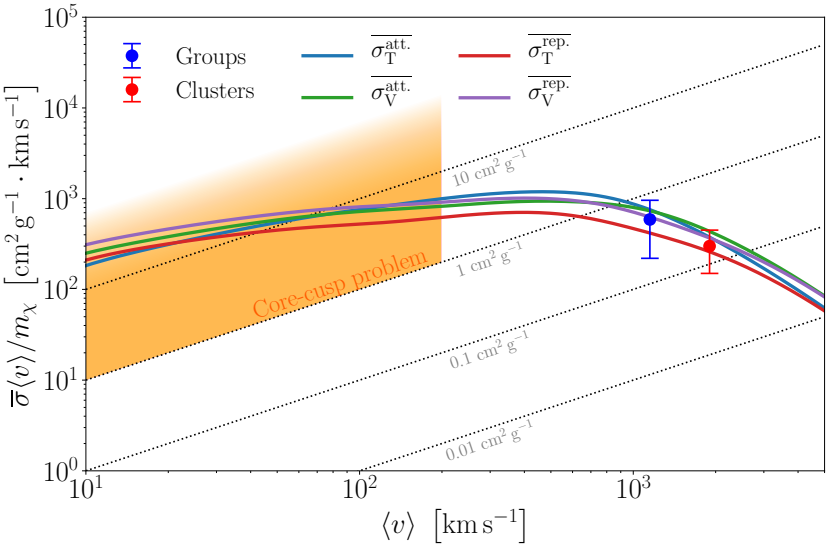


FIGURE 6.8: The averaged momentum transfer cross section (blue) and viscosity cross section (green) for $m_\chi = 190\,\text{GeV}$, $m_\phi = 3\,\text{MeV}$, $\alpha_\chi = 0.5$, plotted along with the inferred cross-sections at various scales [164].The shaded region corresponds to the range of cross-sections required to solve the core-cusp problem.

velocity scales as $v^{-4}$. This is contrary to the naive velocity average $\langle\sigma_{\rm T} v_{\rm rel}\rangle$ which diverges for small velocities.

In Fig. 6.7, we compare our velocity averaging procedure with those existing in the literature. The latter depend on either calculating $\sigma_{\rm T}$ at the average velocity in the halo $\langle v_{\rm rel}\rangle$ or by evaluating $\langle\sigma_{\rm T} v_{\rm rel}\rangle/\langle v_{\rm rel}\rangle$. As a side note, we point out that the oscillations we mentioned in section 6.3 for $\beta \sim O(10)$, have been smeared out as a result of the averaging, highlighting the fact that our analytic expressions are in perfect agreement with the numerical results.

## 6.5 Phenomenological implications

With an acceptable answer to both of the questions posed in section 6.1, we turn once again to Fig. 6.1, using which we can easily pinpoint our velocity scale of interest. This ranges from $v_0 = 20\,\text{km s}^{-1}$ (dwarf galaxies) to $v_0 = 1000\,\text{km s}^{-1}$ (galaxy clusters). Accommodating this range of velocities within the semiclassical regime demands the requirement $\kappa(v_0 = 20\,\text{km s}^{-1}) > 1$, resulting in,

$$\frac{m_\phi}{m_\chi} \lesssim 10^{-4}\,. \tag{6.114}$$

We also note from Fig. 6.1 that the self-interaction cross-sections scale rather weakly with velocities. This further restricts us to $\beta \gtrsim 1$. Assuming then that $\sigma_{\rm T} m_\phi^2 \approx c$, where $c$ is a constant of roughly order 100,[9] we can use the fact that $\sigma_{\rm T}/m_\chi \sim 1\text{cm}^2\,\text{g}^{-1}$, to obtain $m_\chi m_\phi^2 \sim 0.02\,\text{GeV}^3$. Coupled with Eq. 6.114, this implies $m_\phi \lesssim 10\,\text{MeV}$ or light mediators are necessary

[9]This is a good approximation since the cross-section scales very weakly as $\log\beta$ and therefore the $\beta$ dependence can be neglected.

TABLE 6.1: Velocity averaged self-interaction cross sections for $m_\chi = 190\,\mathrm{GeV}$, $m_\phi = 3\,\mathrm{MeV}$, $\alpha_\chi = 0.5$ at different astrophysical scales.

| System | $\langle v \rangle$ | $\beta_0$ | $\kappa_0$ | $\overline{\sigma_\mathrm{T}^\mathrm{att.}}/m_\chi$ $[\mathrm{cm^2\,g^{-1}}]$ | $\overline{\sigma_\mathrm{T}^\mathrm{rep.}}/m_\chi$ $[\mathrm{cm^2\,g^{-1}}]$ | $\overline{\sigma_\mathrm{V}^\mathrm{att.}}/m_\chi$ $[\mathrm{cm^2\,g^{-1}}]$ | $\overline{\sigma_\mathrm{V}^\mathrm{rep.}}/m_\chi$ $[\mathrm{cm^2\,g^{-1}}]$ |
|---|---|---|---|---|---|---|---|
| Dwarf galaxy | 50 | 2890 | 2.34 | 10.9 | 9.0 | 11.7 | 13.6 |
| Galaxy | 250 | 116 | 11.7 | 4.3 | 2.6 | 3.5 | 3.8 |
| Galaxy group | 1150 | 5.46 | 53.8 | 0.66 | 0.36 | 0.64 | 0.54 |
| Galaxy cluster | 1900 | 2.00 | 88.9 | 0.20 | 0.14 | 0.23 | 0.19 |

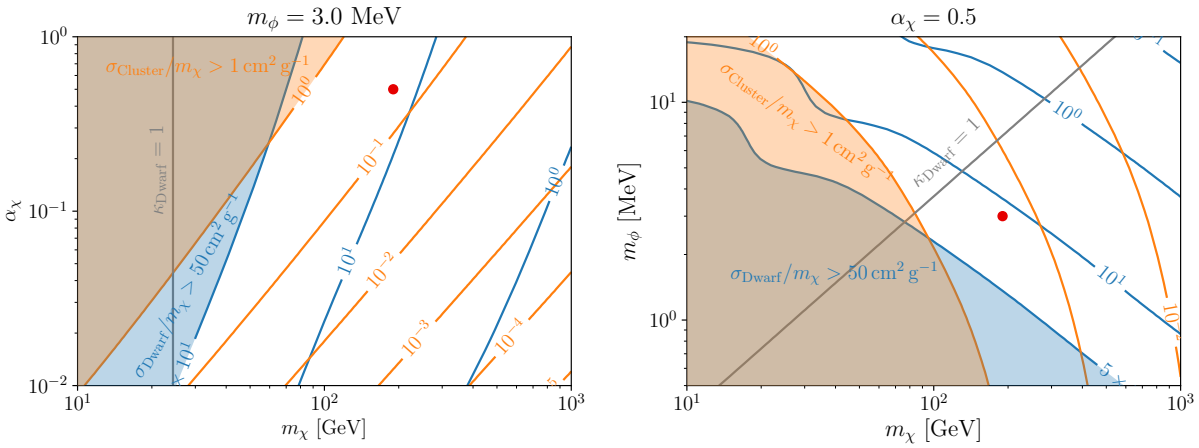


FIGURE 6.9: Self-interaction cross section at cluster scales (orange contours) and at dwarf scales (blue contours) as a function of the DM mass $m_\chi$ and the coupling $\alpha_\chi$ (left), and as a function of the DM mass and the mediator mass $m_\phi$ (right). Shaded regions represent approximate bounds from astrophysical observations. The gray line indicates the transition between the quantum regime (left) and the semi-classical regime (right) for dwarf galaxies. At cluster scales self-interactions are always in the semi-classical regime. For concreteness, we consider the viscosity cross section for a repulsive potential, but very similar plots are obtained in the other cases. The red dot indicates the benchmark point considered in Fig. 6.8 and Table 6.1.

to ensure that we obtain phenomenologically interesting cross-sections while staying in the semi-classical regime. We know from our discussion in Chapter 2 that such light mediators cannot be in thermal equilibrium with the SM heat bath owing to constraints arising from BBN. Nevertheless, they can still be viable in models with out-of-equilibrium DM such as freeze-in.

We condense this discussion in Fig. 6.8 and Table 6.1, where we represent the best-fit points for DM masses and couplings so as to satisfy constraints on both dwarf and cluster scales.

Additionally, it is also interesting to see how the constraints from dwarfs and clusters apply to the full parameter space of the model. In Fig. 6.9, we demonstrate such a parameter scan for the viscosity cross-section for a repulsive potential holding $m_\phi$ and $\alpha_\chi$ fixed respectively. In the left panel, we fix $m_\phi = 3\,\mathrm{MeV}$ and vary $\alpha_\chi$ and $m_\chi$. At dwarf scales, where $\beta_0 \gg 1$ (shaded in blue), $\sigma_\mathrm{V}$ depends very weakly on both $\alpha_\chi$ and $m_\chi$ (see Eq. 6.98) and therefore the

dominant scaling comes from the overall factor of $m_\chi^{-1}$. On cluster scales where $\beta \approx 1$ (shaded in orange), the dependence on the model parameters is more pronounced. The semi-classical regime is denoted by the grey vertical line where we set $\kappa = 1$ at dwarf scales. Everything to the right (left) of the line falls in the semi-classical (quantum) regime. As discussed before, we are always in the semi-classical regime at cluster scales.

A similar plot can be made by fixing $\alpha_\chi = 0.5$ and varying $m_\chi$ and $m_\phi$. From Eq. 6.98, it is easy to see that the cross-section now depends strongly on $m_\phi$ and we cannot obtain phenomenologically interesting cross-sections for $m_\phi > 10\,\mathrm{MeV}$ while staying within the semi-classical regime (bottom right of the grey line).

Our best fit point from Table 6.1 is represented by the red dot. Note that similar plots can be obtained for the other three cases: $\sigma_{\mathrm{T}}^{\mathrm{att.}}$, $\sigma_{\mathrm{T}}^{\mathrm{rep.}}$, and $\sigma_{\mathrm{V}}^{\mathrm{rep.}}$.

## 6.6 Conclusions

Self-interacting DM can work to resolve tensions between astrophysical observations and N-body simulations of CDM. In particular, self-interactions mediated by long range forces have the correct behaviour to fit observations at both dwarf and cluster scales. When comparing theoretical predictions of SIDM cross-sections to data, it is important to keep in mind the difference between the total cross-section and the cross-section that is relevant to the astrophysical processes under consideration. To this end, it is important to distinguish between the total cross-section $\sigma$, the momentum transfer cross-section $\sigma_{\mathrm{T}}$, and the viscosity cross-section $\sigma_{\mathrm{V}}$. $\sigma_{\mathrm{T}}$ is often used as a proxy for $\sigma$ since it regulates the (irrelevant) forward scattering divergence present for interactions via a light mediator, but it is ill-defined for identical particles and preferentially weighs backward scattering which leaves particle distributions unchanged. $\sigma_{\mathrm{V}}$ solves both of these issues while simultaneously being better suited for describing thermalisation processes within a halo. Additionally, it is equally important to specify how the velocity averaged cross-sections enter in the scattering rate. In particular, the velocity averaged cross-sections conventionally used in the literature, $\langle \sigma_{\mathrm{T,V}} v \rangle$ are imprecise and the rates of energy and momentum transfer are instead proportional to $\langle \sigma_{\mathrm{V}} v^3 \rangle$ and $\langle \sigma_{\mathrm{T}} v^2 \rangle$ respectively.

As for the actual expressions for the cross-sections, these can be obtained by solving the Schroedinger Equation for a Yukawa potential. However, in the phenomenologically interesting semi-classical regime, i.e., when the de Broglie wavelength of the particles are small compared to the characteristic length scales in the interaction, performing such a calculation is numerically intensive as it requires summing over a large number of partial waves. Usually, one uses analytic classical cross-sections in this regime which assume scattering of distinguishable particles in a hard-sphere approximation. These expressions necessarily break down for identical particle scattering as well as for momentum transfers close to the boundary of the semi-classical regime. A better approximation is to derive completely analytic solutions for both $\sigma_{\mathrm{T}}$ and $\sigma_{\mathrm{V}}$ that capture the necessary quantum corrections in this

regime by following the quantum-mechanical framework laid out in sections 6.2 and 6.3. Further, the results so obtained are in excellent agreement with the full numerical solution of the Schroedinger equation (as shown in Fig. 6.4 and 6.5), and lie in the phenomenologically interesting regime—explaining both observations at dwarf and cluster scales—for sufficiently small mediator masses (section 6.5)

Since analytic approximations for the cross-sections exist already in the Quantum and Born regimes (as defined in Fig. 6.2), with the results presented in this chapter, a complete analytic coverage of the Yukawa potential is possible. Additionally, the framework laid out above can be generalised to other potentials to speed up calculations even in cases where the phase shifts cannot be calculated analytically.

The analytical results presented in this chapter have been implemented in the new code CLASSICS available at https://github.com/kahlhoefer/CLASSICS.

# Part III

# The Now

# Chapter 7

# Detection Strategies

Until now we have been interested in the cosmological manifestations of DM, studying in detail what large scales in the universe can tell us about the particle properties of DM. Of course, the ideal way to know the exact nature of DM would be through conducting repeatable laboratories experiments, such that a clear DM signal could be used to resolve degeneracies between various models. Three major search strategies are employed in this regard to look for DM based on the kind of interaction that would give rise to a signal: indirect detection, direct detection, and collider searches (see Fig. 7.1).

**Indirect detection** looks for DM decay or annihilation products in regions with large DM densities such as the centres of galaxies [165]. These can be in the form of charged leptons, anti-protons, gamma rays, or neutrinos. The last two channels are of particular interest since both gamma rays and neutrinos travel through space relatively undisturbed owing to the absence of charge- and weak- interactions respectively. In fact, one of the most promising (potential) DM signals currently is a gamma ray excess originating from the Galactic centre [166, 167]. However, deciphering such signatures of DM proves to be quite challenging owing to the presence of large astrophysical backgrounds and associated uncertainties [168].

**Direct detection** looks for nuclear or electron recoil induced by a DM particle scattering off a target [169]. We provide an introduction to direct detection discussing light DM signatures from electron and nuclear scattering in section 7.1,

**Accelerator searches** look for DM produced as a result of the annihilation of SM particles at colliders in the form of missing energy or displaced vertices [170]. These are discussed in detail in section 7.2.

Using these descriptions, we constrain the dark photon models discussed in Chapter 5 in sections 7.3 and 7.4. We summarise our results in section 7.5

## 7.1 Direct Detection

Our local DM density, $\rho_0 = 0.3$ GeV/cm$^3$, is large enough to generate a sizeable flux through the Earth [171]. This means that even weakly interacting particles can lead to observable

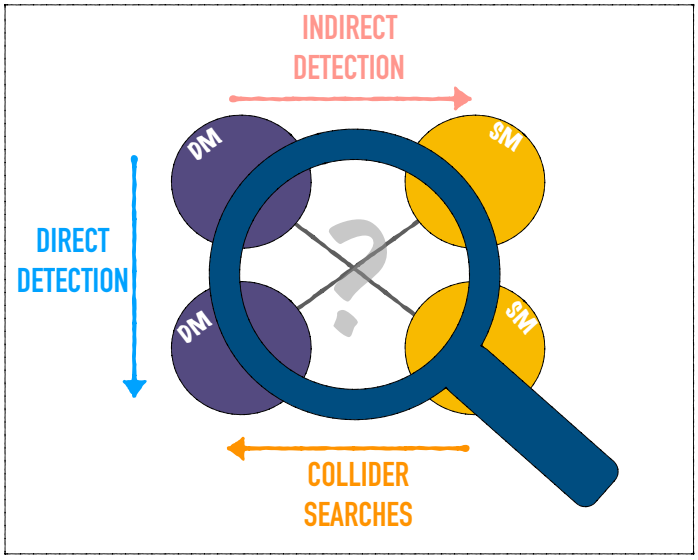


FIGURE 7.1: Different DM detection strategies, colloquially referred to as the *shake it, make it, break it* approach corresponding to Direct Detection, Collider Searches, and Indirect Detection respectively.

events as a result of scattering off a target. These could be in the form of heat (phonons produced in crystals), light (photons produced through excitation and de-excitation of target) and/or charge (ionisation of the target). Through direct detection experiments, we attempt to measure such signals. The quantity of interest is the differential scattering rate that parameterises the number of events observed at a specific energy per unit time and mass of the detector material [172–174],

$$\frac{\mathrm{d}R}{\mathrm{d}E_R} = \frac{\rho_0}{m_T m_{\mathrm{DM}}} \int_{v_{\mathrm{min}}} |\vec{v}|\, f(\vec{v}+\vec{v}_{\mathrm{E}}) \frac{\mathrm{d}\sigma(v,\, E_R)}{\mathrm{d}E_R}\, \mathrm{d}^3 v\,. \tag{7.1}$$

In this equation, $m_{\mathrm{DM}}$ and $m_T$ are the DM and the target nucleus mass respectively, $f(\vec{v}+\vec{v}_{\mathrm{E}})$ is the DM velocity distribution in the galactic rest frame, with $\vec{v}_{\mathrm{E}}$ being the relative velocity of Earth to the Galactic centre, and $\mathrm{d}\sigma/\mathrm{d}E_R$ is the differential particle scattering rate. The velocity distribution for the DM wind is assumed to be Maxwell-Boltzmann truncated at the galactic escape velocity, $v_{\mathrm{esc}} = 544\,\mathrm{km\,s^{-1}}$ [171]. Further, the lower limit of the velocity integral, $v_{\mathrm{min}}$, denotes the minimum DM velocity required in order for the target to scatter with a recoil energy $E_R$ and can be simply evaluated from kinematics,

$$v_{\mathrm{min}}(E_R) = \sqrt{\frac{m_N E_R}{2\mu^2}}\,, \tag{7.2}$$

where $\mu = m_T m_{\mathrm{DM}}/(m_T + m_{\mathrm{DM}})$ is the DM-target reduced mass.

The astrophysical and particle physics contributions to the scattering rate can be disentangled: the former enters through the velocity distribution and the local DM density, and the latter through the differential cross-section and a trivial normalisation in the prefactor. The astrophysical contribution is described by the Standard Halo Model with the definitions of $f(v)$

and $\rho_0$ as specified above.[1] The particle physics contribution is, of course, model-dependent. It is convenient to make a distinction between heavy ($m_{\rm DM} \gtrsim$ GeV) and light ($m_{\rm DM} \lesssim$ GeV) DM depending on which particle interactions result in observable signals. Phenomenologically, we expect DM-nuclei scattering to be the dominant process for heavy DM particles and DM-electron scattering for lighter ones. Conventional direct detection experiments have focused their attention on DM-nucleus scattering but recent years have seen a steady rise in experiments specifically looking for DM-electron scattering [175].

### DM-nucleon scattering

DM-nucleus scattering is further divided into spin-dependent (SI) and spin-independent (SD) scattering depending on whether DM couples to nucleon number, $A$, or to the nucleon spin. In the former case, the scattering is coherent on the nucleus and therefore the *DM-nucleus* cross-section is enhanced by $A^2$ with respect to the *DM-nucleon* cross-section, $\sigma_{N\chi} \propto A^2$. In contrast, the nucleon spins add incoherently inside the nucleus and therefore $\sigma_{N\chi} \propto J(J+1)$ for SD scattering where $J$ denotes the spin. With respect to concrete interactions, SI cross-sections may arise from scalar and vector couplings to quarks. On the other hand, SD cross-sections might originate from axial-vector couplings [171].[2] For a given DM model, we can express the differential cross-section in Eq. 7.1 in terms of a SI and a SD part,

$$\frac{\mathrm{d}\sigma}{\mathrm{d}E_R} = \frac{\mathrm{d}\sigma^{\rm SI}(v,\, E_R)}{\mathrm{d}E_R} + \frac{\mathrm{d}\sigma^{\rm SD}(v,\, E_R)}{\mathrm{d}E_R}\,. \tag{7.3}$$

The models discussed in this thesis do not have axial quark couplings and therefore we will only talk about SI scattering from here on.

We can obtain a general functional form of $\mathrm{d}\sigma^{\rm SI}/\mathrm{d}E_R$ by reminding ourselves that a non-relativistic two-body scattering can be modelled by a Yukawa potential (c.f. Chapter 6). For DM-nucleus scattering, this would be given by the potential [177]

$$V(r) = \alpha_{\rm eff}\frac{e^{-m_{\rm med}r}}{r}\,, \tag{7.4}$$

where $\alpha_{\rm eff}$ is representative of the effective DM-nucleon coupling (that includes for instance the number of nucleons that couple to DM). For a generic mediator which has SM and DM couplings given by $g_{\rm SM}$ and $g_{\rm DM}$ respectively, we get $\alpha_{\rm eff} = g_{\rm SM}g_{\rm DM}A/4\pi$ where $A$ is the number of nucleons inside the target nucleus. For a dark photon which only couples to charge, we will replace $A$ with the number of protons, $Z$. Additionally, $m_{\rm med}$ is the mediator mass for the interaction.The differential cross-section is then given by [178],

$$\frac{\mathrm{d}\sigma(v,\, E_R)}{\mathrm{d}q^2} = \frac{2m_N\tilde{\alpha}_{\rm eff}^2}{(q^2+m_{\rm med}^2)^2}\frac{1}{v^2}F^2(E_R)\,, \tag{7.5}$$

[1] Note that there are some uncertainties in these quantities, see e.g., [171, 174].
[2] For a list of effective operators that result in SI and SD interactions, see [176].

where $\tilde{\alpha}_{\text{eff}}^2 = 2\pi\alpha_{\text{eff}}^2/m_N$, $m_N$ is the nucleus mass and $q = \sqrt{2m_N E_R}$ is the momentum transfer. Additionally, we include a form factor $F^2(E_R)$ that parameterises the momentum-dependent response of the nucleus to the scattering [179].

Under the assumption that DM couples equivalently to protons and neutrons, we can relate the SI differential cross-section to a reference DM-proton cross-section $\sigma_{\chi p}$,

$$\frac{\mathrm{d}\sigma(v,\, E_R)}{\mathrm{d}E_R} = \frac{m_N}{2\mu_{\chi p}^2}\frac{1}{v^2}A^2\sigma_{\chi p}(E_R)F^2(E_R)\,, \tag{7.6}$$

with,

$$\begin{aligned}\sigma_{\chi p}(E_R) &= \frac{8\tilde{\alpha}_{\text{eff}}^2 m_N}{A^2}\frac{\mu_{\chi p}^2}{(q^2+m_{\text{med}}^2)^2} \\ &= \frac{1}{\pi}\frac{g_{\text{SM}}^2\, g_{\text{DM}}^2}{(q^2+m_{\text{med}}^2)^2}\mu_{\chi p}^2\,.\end{aligned} \tag{7.7}$$

Bounds from direct detection experiments are typically presented as constraints on $\sigma_{\chi p}$ (see Fig. 7.2) with the implicit assumption that $\sigma_{\chi p}$ is momentum-independent. This is true when $m_{\text{med}} \gg q^2$, (contact interaction) in which case the differential event rate can be simply written as,

$$\frac{\mathrm{d}R}{\mathrm{d}E_R} = \frac{\rho_0\,\sigma_{\chi p}^{\text{SI}}\,A^2F^2(E_R)}{2\mu_{\chi p}^2 m_\chi}g(v_{\text{min}})\,, \tag{7.8}$$

with the velocity integral, $g(v_{\text{min}}) = \int_{v_{\text{min}}}\mathrm{d}^3v f(\vec{v}+\vec{v}_{\text{E}})/v$. The strongest constraint in this limit is from the XENON1T experiment, which places a bound $\sigma_{\chi p} \lesssim 10^{-47}\,\text{cm}^2$ for a 30 GeV DM particle [180] (see also Fig. 7.2). Since generic WIMP models predict larger cross-sections—compare this, for instance, to the thermal cross-section discussed in section 2.2.2—direct detection experiments spell trouble for WIMPs.

As these experiments constrict the parameter space further, it has become imperative to lay the theoretical groundwork for DM models which naturally include tiny couplings and therefore evade these constraints. As might be guessed, FIMP models do this rather easily. Assuming a contact interaction, a generic FIMP coupling of order $\lambda \lesssim 10^{-7}$ will result in a scattering cross-section roughly equal to $\sigma_{\chi p} \sim \mu_{\chi p}^2\alpha\lambda^2/m^4 \lesssim 10^{-50} \times (30\,\text{GeV}/m)^4$, much below the limit discussed in the preceding paragraph. At first sight, this might appear to make FIMPs completely untestable, and therefore uninteresting, but fortunately for us, this turns out to not be the case.

As mentioned before, the limits presented above are for a contact interaction, valid when the mediator mass is much larger than the momentum transfer involved in the scattering. If the mediator is light, the DM-nucleus scattering is long-range and the cross-section in Eq. 7.7 scales as $E_R^{-2}$, resulting in an enhancement for small momentum transfers. Of course, arbitrarily small recoil energies cannot be probed and therefore a cut is placed on this enhancement by the detector threshold, i.e., the smallest recoil energies that a given detector

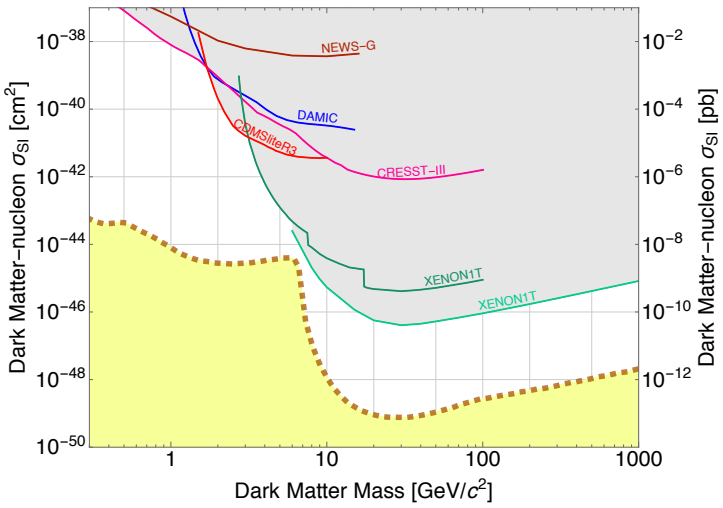


FIGURE 7.2: Direct detection limits on the spin-independent DM-nucleon scattering cross-section as a function of DM mass from various experiments [180–185]. The yellow shaded region represents the irreducible neutrino background for the XENON experiment. Image created using the Dark Matter Limit Plotter [186].

is sensitive to. For instance, XENON1T has a threshold of $E_{\rm th} = 1.1\,\text{keV}$ meaning that for $m_{\rm med} \ll \sqrt{2m_N E_{\rm th}} \approx 16\,\text{MeV}$, the differential event rate will *always* benefit from an enhancement. This enhancement can then directly compensate for the tiny freeze-in couplings to produce observable event rates at experiments [1, 187].

### DM-electron scattering

It is unlikely for a light DM particle to induce detectable nuclear recoils in heavy target atoms such as Xenon. The average nuclear recoil energy for a DM particle with a mass of 100 MeV would be $E_R = q^2/2m_N \simeq 1\,\text{eV} \times (m_\chi/100\,\text{MeV})^2\,(10\,\text{GeV}/m_N)$, close to or below threshold for most of the conventional direct detection experiments like XENON1T. However, MeV scale DM can trigger electron ionisation in the nucleus leading to potentially visible signatures [188]. For a DM particle with mass $m_\chi$ transferring a momentum $\vec{q}$ to an electron that is bound to a nucleus, energy conservation for the DM-atom system implies,

$$\Delta E_e + \frac{|m_\chi \vec{v} - \vec{q}|^2}{2m_\chi} + \frac{q^2}{2m_N} = \frac{1}{2} m_\chi v^2 \tag{7.9}$$

$$\Rightarrow \Delta E_e = \vec{q}.\vec{v} - \frac{q^2}{2\mu_{N\chi}}\,, \tag{7.10}$$

where $\vec{v}$ is the initial DM velocity and $\Delta E_e$ is the energy transferred to the electron. Note that $\Delta E_e$ is *not* equal to the electron recoil energy. Since the electron is in a bound state, the electron recoil energy is actually the difference of the energy transferred and the binding energy $E_{nl}$ of the electron, $E_{eR} = \Delta E_e - E_{nl}$. A bound on $\Delta E_e$ comes from maximising Eq. 7.10 with

respect to $q$,

$$\Delta E_e \lesssim \frac{1}{2}\mu_{N\chi}v^2 \underset{m_\chi \ll m_N}{\simeq} \frac{1}{2}m_\chi v^2 \sim 1\,\text{eV}\left(\frac{m_\chi}{1\,\text{MeV}}\right), \tag{7.11}$$

where in the final step we assume typical DM velocities of $10^{-3}$. This equation demonstrates that the entire kinetic energy of the incoming DM particle can be transferred to the electron, implying that for a given electron binding energy $E_{nl}$, a measurable signal can be produced for,

$$m_\chi \gtrsim 1\,\text{MeV} \times \frac{E_{nl}}{1\,\text{eV}}. \tag{7.12}$$

Even lighter DM (meV - keV masses) can be probed by looking for DM absorption by electrons in which case the DM mass can be directly converted into the electron recoil energy [175].

By building detectors using target material with a small binding energy, we can therefore extend the search region to smaller and smaller DM masses. This has in fact been done using semiconductors targets such as Germanium and Silicon which have the potential to probe DM masses on sub-MeV scales, but even traditional detections such as XENON can probe DM masses up to tens of MeV by increasing sensitivities to single-electron events [175, 189, 190].

Note that the bound state of the electron implies that the initial electron momentum is arbitrary and therefore the momentum transfer $q$ can take any value. Despite this arbitrariness in $q$, momentum transfers larger than a typical scale—set by the electron's momentum, $q_{\text{typ}} \sim Z_{\text{eff}}\alpha m_e \sim Z_{\text{eff}} \times 4\,\text{keV}$—are highly suppressed. Here $Z_{\text{eff}}$ is the effective charge seen by the electron. This can be explicitly seen by calculating electron form factors which capture the transition from one state to another

$$f_{1\to 2}(\vec{q}) = \int \mathrm{d}^3x \psi_2^*(\vec{x})\psi_1(\vec{x})e^{i\vec{q}.\vec{x}}, \tag{7.13}$$

where $\psi_1(\vec{x})$ and $\psi_2(\vec{x})$ are the initial bound state and final state wavefunctions respectively. We plot these form factors for the Xenon 5p shell in Fig. 7.3 for two different values of $\Delta E_e$ and therefore two values of the outgoing electron energy $\Delta E_e - E_{5p}$ where $E_{5p} \sim 12.5 \times 10^{-3}$ keV.[3] As mentioned previously, the form factor drops at large momentum transfers.

Similar to the DM-nucleon scattering cross-section, the DM-electron scattering cross-section is also parameterised in terms of a reference cross-section at a fixed momentum transfer,

$$\overline{\sigma}_e \equiv \frac{\mu_{\chi e}^2}{16\pi m_\chi^2 m_e^2}\overline{|\mathcal{M}_{\chi e}(q)|^2}\Big|_{q^2=\alpha^2 m_e^2}, \tag{7.14}$$

[3]The calculations for these form factors are non-trivial and significant discrepancies can arise between different approximations [191, 192].

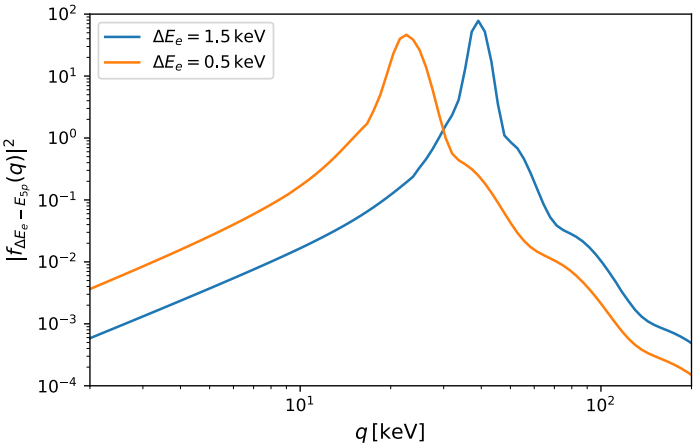


FIGURE 7.3: The electron ionisation form factor for a Xenon electron in the 5p shell as a function of the momentum transfer, for two different values of $\Delta E_e$.

under the assumption,

$$\overline{|\mathcal{M}_{\chi e}(q)|^2} = \overline{|\mathcal{M}_{\chi e}(q)|^2}\Big|_{q^2=\alpha^2 m_e^2} \times F_{\rm DM}(q)^2\,, \tag{7.15}$$

where $\overline{|\mathcal{M}_{\chi e}(q)|^2}$ is the squared matrix element for DM-electron scattering averaged over the initial and summed over final spin states. For a dark photon model, Eq. 7.14 simplifies to [188, 193],

$$\overline{\sigma}_e = \frac{16\pi\mu_{\chi e}^2\alpha\alpha_{\rm DM}}{(m_{A'}^2+\alpha^2 m_e^2)^2} \simeq \begin{cases} \dfrac{16\pi\mu_{\chi e}^2\alpha_{\rm SM}\alpha_{\rm DM}}{m_{A'}^4}\,, & m_{A'} \gg \alpha m_e \\ \dfrac{16\pi\mu_{\chi e}^2\alpha_{\rm SM}\alpha_{\rm DM}}{(\alpha m_e)^4}\,, & m_{A'} \ll \alpha m_e \end{cases}\,, \tag{7.16}$$

where $\alpha_{\rm SM}$ and $\alpha_{\rm DM}$ denote the $A'$-SM and $A'$-DM coupling respectively.[4] The DM form factor $F_{\rm DM}(q)$ encodes the (directionless) momentum dependence of the interaction with $F_{\rm DM}(q) = 1$ and $F_{\rm DM}(q) = (\alpha m_e/q)^2$ in the heavy ($m_{\rm med} \gg q$) and light ($m_{\rm med} \ll q$) mediator limits respectively. The differential event rate is then given by the equation [192],

$$\begin{aligned}\frac{{\rm d}R}{{\rm d}\Delta E_e} =& \frac{\overline{\sigma}_e}{8\mu_{\chi e}^2}\sum_{n,l}\frac{\rho_\chi}{m_\chi}\frac{1}{\Delta E_e - E_{nl}} \\ &\times \int {\rm d}q\, q\, |F_{\rm DM}(q)|^2 \left|f_{nl\to(\Delta E_e - E_{nl})}(\vec{q})\right|^2 g(v_{\rm min}(q,\,\Delta E_e))\,,\end{aligned} \tag{7.17}$$

where the sum is over all initially occupied shells {n, l} and $g(v_{\rm min})$ is the velocity integral as defined before.

DM-electron scattering plays an incredibly important role in constraining sub-GeV DM models. The latest XENON1T result which shows a $3\sigma$ excess for electron recoil energies between $2-3$ keV has further reinvigorated theoretical as well as experimental research into light DM

[4] For example, for a kinetically mixed dark photon, $\alpha_{\rm SM}\alpha_{\rm DM} = \kappa^2\alpha\alpha_{\rm DM}$.

[194]. Although, a keV-scale excess cannot be explained by the standard DM-electron scattering discussed above without being in dramatic conflict with other lower threshold searches such as SENSEI [195] and XENON1T [196], slightly more exotic models of DM fit the bill quite well [192]. Inelastic DM has gained traction in this regard where a heavier DM state can decay or a downscatter into a lighter one, thus converting a fraction of its mass into electron recoil [192].

Both DM-nucleon and DM-electron scattering place stringent bounds on DM models. Although we have talked about them independently, there is no clean divide between them. This is most clearly evident in the phenomenon of *Migdal scattering* where electron recoils arise as result of DM-nucleon interactions and the signature we search for includes a recoiling atom and a promptly ionised electron [191, 197–199]. In simple terms, the energy transferred by the DM to the target atom is distributed in such a way so as to induce a nuclear recoil as well as a simultaneous electron ionisation. DM-electron scattering and Migdal scattering are governed by the same sets of energy and momentum conservation equations. The difference between the two can be entirely captured in the electron ionisation form factor since the momentum transferred to the electron differs between the two cases, i.e., the dynamics of the the two processes are different depending on whether DM couples to the nucleus or directly to the electron. In particular, it is found that the momentum transferred to the recoiling electron for Migdal scattering is suppressed compared to the momentum transferred to the entire atom, $\vec{q}_e = (m_e/m_N)\vec{q}$. This, coupled with the fact that the nuclear form factor does not have a suppression for $q \lesssim$ MeV, implies that the Migdal scattering spectrum is dominated by the largest kinematically allowed momentum transfers. For $m_\chi \gtrsim 100\,\text{MeV}$, Migdal scattering results in appreciable variations in the constraints on the DM-nucleon cross-section [200].

## 7.2 Accelerator Constraints

A complementary way to search for DM is by producing it at colliders and at beam-dump or other fixed-target experiments. DM produced at accelerators can either escape leading to *missing transverse energy*, or decay into SM particles thereby providing a *displaced vertex* signature. Dark photon searches at accelerators, in particular, have garnered significant interest over the recent years with searches for sub-GeV dark photons seeing tremendous advancements [85, 201].

For light dark photons, $m_{A'} \lesssim 1\,\text{GeV}$, the best sensitivity is provided by beam-dump and fixed-target experiments. Beam-dump experiments involve dark photon production via bremsstrahlung off of protons or electrons or through decays of SM mesons (see Fig. 7.4). These dark photons then travel through a length of detector material before decaying visibly or invisibly.[5] The search signature has the form of a displaced vertex in the former case and missing energy in the latter case. In fixed-target experiments, production is typically through bremsstrahlung but the search signature is not a displaced vertex. Instead most experiments search for prompt

[5]Note that the invisible decay channel includes decays into DM as well as into neutrinos.

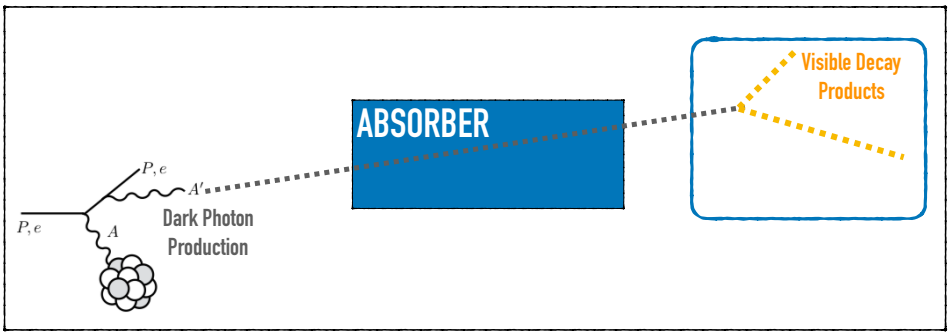


FIGURE 7.4: Representative sketch of a beam dump experiment. A dark photon is produced as a result of bremsstrahlung. It traverses a certain length of the detector before decaying into SM final states. The "absorber", as the name suggests, absorbs the SM background with the exception of neutrinos.

visible decays or kinematic features such as a resonance bump in the invariant mass spectrum, as well as missing energy corresponding to invisible decays or long-lived particles [84, 202]. Beam-dump experiments provide an upper and lower bound on the dark photon coupling to the SM (for an example, see Fig. 7.10). The upper bound is determined by the coupling for which the dark photon lifetime become smaller than the detector length, i.e., the dark photons decay before reaching the detector. On the other hand, the lower bound arises because smaller couplings correspond to a suppression in dark photon production once again making the detector insensitive to the corresponding signals.

MeV to GeV scale dark photons can also be produced at $e^+e^-$ colliders through radiative return or meson decay, with searches being sensitive to decays into leptons or missing energy in single-photon searches [203, 204]. Further, visibly decaying GeV scale dark photons are constrained by a number of searches at the LHC [170, 205]. Collider constraints are dominant for large dark photon masses and couplings.

As can be inferred from this discussion, the parameters of interest for accelerator searches are the dark photon decay width and branching ratio. In both kinds of searches, the number of signal events $N$ is proportional to the product of the production cross-section $\sigma_{A'}$ and the branching ratio into the relevant final state $\mathrm{BR}_{A'\to\mathcal{F}} \equiv \Gamma_{\mathcal{F}}/\Gamma_{A'}$,

$$N \propto \sigma_{A'}\,\mathrm{BR}_{A'\to\mathcal{F}}\varepsilon\,, \tag{7.18}$$

where we have also multiplied with the experimental efficiency $\varepsilon$ that encapsulates the probability that the dark photon decays within the detector volume. Dark photon constraints in the literature can be recast for specific models using available recasting procedures [202]. The public code DARKCAST implements these calculations for visible decay channels. Our modified version of DARKCAST includes invisible decays as well [3].

We will now use the framework developed in this and the previous section to constrain the dark photon models studied in Chapter 5.

## 7.3 Constraining Resonant Dark Photons

The first model introduced in Chapter 5 consisted of a sub-GeV Dirac DM interacting with the SM via a kinetically mixed resonant dark photon with $m_{A'} \approx 2m_\chi$ (section 5.2). As a reminder, we present the free parameters of the model once again:

- $m_{A'}$: The dark photon mass. Because of BBN constraints on additional thermal degrees of freedom in the early universe, we always assume $m_{A'} \gtrsim 10$ MeV. Additionally to ensure that the dark photon is kinematically accessible at B-factories, and that the Dirac fermion evades stringent direct detection constraints for $m_\chi > 5$ GeV, we further choose $m_{A'} \lesssim 10$ GeV.
- $\kappa$: The kinetic mixing between the dark and SM photons. In the dark photon mass range specified above, accelerator constraints imply $\kappa \lesssim 0.001$ irrespective of whether the dark photon decays visibly or invisibly [202].
- $g_\chi$: The dark photon-DM coupling. This is only constrained by perturbativity, $g_\chi < \sqrt{4\pi}$.
- $\epsilon_R$: The strength of the resonant enhancement in the model. This also relates the DM mass to the dark photon mass, $\epsilon_R = (m_{A'}^2 - 4m_\chi^2)/4m_\chi^2$. Although there are no constraints on $\epsilon_R$ a priori, both extremely small and extremely large values are disfavoured. The former will result in extremely large annihilation rates during BBN while the latter would imply large annihilation rates during recombination. We will, therefore, restrict ourselves to the range $0.001 \leq \epsilon_R \leq 0.1$.
- $R$: Fractional DM abundance. Although not an intrinsic model parameter, we use $R$ to account for the case that the Dirac fermion only forms a fraction of DM.

Additionally, we reiterate from section 5.2 that for a strong resonant enhancement, $\epsilon_R \ll 1$, the relic abundance is approximately given by

$$\Omega h^2 \sim \frac{\Gamma_{A'}}{\kappa^2 g_\chi^2}\,, \tag{7.19}$$

where $\Gamma_{A'}$ is the *total* dark photon decay width.

### 7.3.1 Accelerator Constraints

We start by describing the accelerator constraints. From Eq. 7.18, we know that the expected signal events are proportional to $\sigma_{A'}\,\mathrm{BR}_{A'\to\mathcal{F}\mathcal{E}}$. The dark photon production cross-section scales proportionally to $\kappa^2$. The dark sector parameters $g_\chi$ and $\epsilon_R$, on the other hand, enter the equation not independently but only through the invisible decay width $\Gamma_{\mathrm{DM}}$. This means that different combinations of $g_\chi$ and $\epsilon_R$ that map on to the same $\Gamma_{\mathrm{DM}}$ will result in the same experimental constraints on $\kappa$ and $m_{A'}$. Hence, we introduce the invisible dimensionless dark

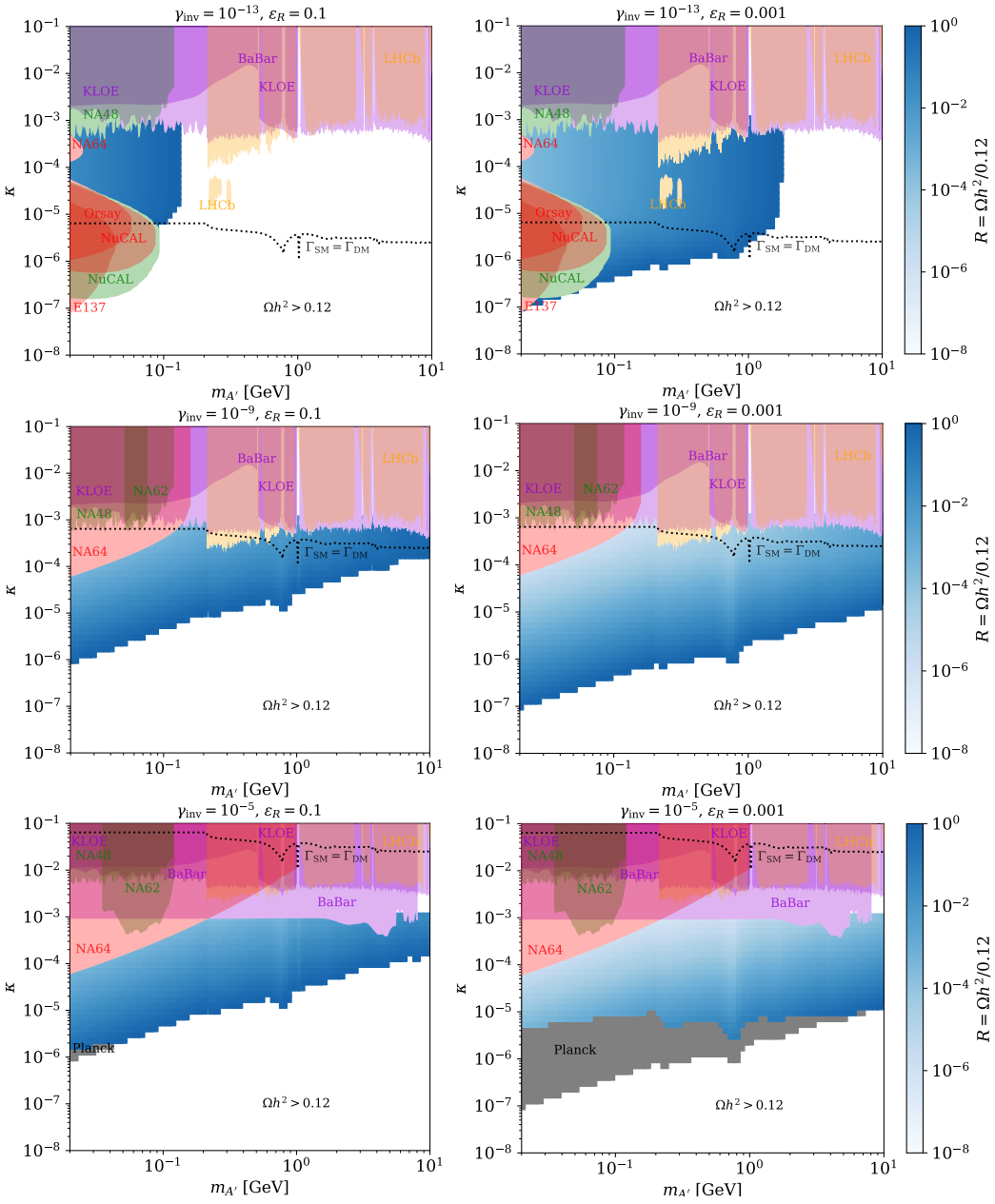


FIGURE 7.5: Exclusion bounds from fixed target and collider experiments for different values of $\gamma_{\rm inv}$ and $\epsilon_R$ plotted on top of parameter points resulting in $\Omega h^2 \leq 0.12$. The colours of the different contours correspond to the dark photon production mechanism: bremsstrahlung (red), meson decay (green), $e^+e^-$ colliders (violet), and LHC (orange). The Planck excluded regions are shaded grey.

photon decay width,

$$\gamma_{\rm inv} \equiv \frac{\Gamma_{\rm DM}}{m_{A'}} = \frac{g_\chi^2}{12\pi}\left(1-\frac{1}{1+\epsilon_R}\right)^{1/2}\left(1+\frac{1}{2(1+\epsilon_R)}\right) \tag{7.20}$$

and use it as a free parameter of the model instead of $g_\chi$. In the limit $\epsilon_R \ll 1$, we have $\gamma_{\rm inv} \propto g_\chi^2\sqrt{\epsilon_R}$.

In Fig. 7.5, we plot the accelerator constraints in the $m_{A'} - \kappa$ parameter plane using fixed values of $\gamma_{\rm inv}$ and $\epsilon_R$. Additionally, for each point, we also calculate the relic abundance using the formulas presented in section 5.2 denoting different relic densities by a colour gradient: dark blue corresponds to when the relic density is saturated, $\Omega h^2 = 0.12$, whereas a lighter blue denotes under-abundance. Parameter points which result in $\Omega h^2 > 0.12$ are excluded.

The rows in Fig. 7.5 correspond to different values of $\gamma_{\rm inv}$ with $\epsilon_R = 0.1$ (slight resonant enhancement) and $\epsilon_R = 0.001$ (strong resonant enhancement) in the left and right columns respectively. As mentioned above, the accelerator constraints for a fixed $\gamma_{\rm inv}$ are independent of $\epsilon_R$ and the primary difference between the left and the right panels comes through differences in the viable parameter space that satisfies the relic density requirement.

In the first row, we show plots for $\gamma_{\rm inv} = 10^{-13}$ which corresponds to values of $g_\chi$ between $10^{-6}$ and $10^{-5}$ depending on the choice of $\epsilon_R$. These values result in a dark photon that decays dominantly into SM final states. This is represented by the location of the dotted line which determines the couplings values for which the visible and invisible decay widths are equal. The strongest constraints, therefore, arise from fixed-target experiments searching for visible decays. Additionally, we can clearly see that for $\kappa \gtrsim 0.001$, nearly the entire parameter space is excluded by collider searches. Using Eq. 7.19, for a dark photon that decays visibly, we can write

$$\Omega h^2 \sim \frac{\Gamma_{\rm SM}}{\kappa^2 g_\chi^2} \sim \frac{m_{A'}^2}{g_\chi^2}\,, \tag{7.21}$$

meaning that the relic abundance becomes independent of $\kappa$. For a fixed $g_\chi$ then, the relic abundance is saturated for a particular value of $m_{A'}$ which yields the sharp cutoff for $m_{A'} \sim 100\,\text{MeV}$ and $m_{A'} \sim$ few GeV in the left and right panels respectively. As we proceed to the following rows of the plot corresponding to larger $\gamma_{\rm inv}$, this cut-off disappears since we transition to a regime where the dark photon decays invisibly, the relic abundance instead scaling as,

$$\Omega h^2 \sim \frac{\Gamma_{\rm DM}}{\kappa^2 g_\chi^2} \sim \frac{m_{A'}^2}{\kappa^2}\,. \tag{7.22}$$

For dominant invisible decays, the strongest constraints arise, as expected, from invisible searches such as NA64 [206].

Finally, in Fig. 7.5, we also show in grey the CMB constraints which place a bound on $R^2\langle\sigma v\rangle_{\rm CMB}$. As discussed in section 5.2.2, for a dark photon that decays invisibly, these constraints come

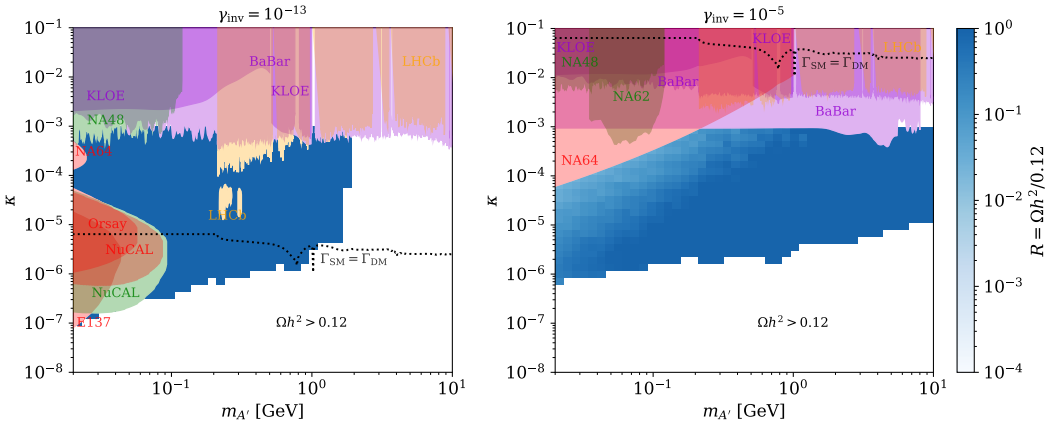


FIGURE 7.6: Same as Fig. 7.5 but with a scan over $\epsilon_R$. The shading corresponds to the largest allowed value of $\Omega h^2$.

in from below. For large $\gamma_{\rm inv}$ and strong resonant enhancements the CMB rules out large parts of the viable parameter space.

As mentioned before, for a fixed $\gamma_{\rm inv}$, the accelerator constraints do not depend on $\epsilon_R$. We can therefore scan over $\epsilon_R$ keeping only those parameter combinations for which the cosmological bounds and the relic density requirement, $\Omega h^2 \leq 0.12$ are satisfied. We can additionally ensure that the self-interaction constraints discussed in Chapter 6 are satisfied although it turns out that regions of parameter space that have large self-interactions are already excluded by other constraints. We present this scan in Fig. 7.6, once again in the $m_{A'} - \kappa$ plane. This time the shading represents the *largest* possible value for the relic abundance given the scan over $\epsilon_R$. For example, a point shaded dark blue means that there is at least one value of $\epsilon_R$ that saturates the DM relic abundance while simultaneously being consistent with all other constraints.

In the left panel of Fig. 7.6, we set $\gamma_{\rm inv} = 10^{-13}$ and the resulting plot is as one would expect from looking at Fig. 7.5. The boundary between the blue and the white regions is determined by the lower boundary on $\epsilon_R$. A smaller $\epsilon_R$ would shift the blue region further to the right and to the bottom since a stronger resonant enhancement would decrease the couplings required to produce the relic abundance. Note that in this case however, BBN bounds because of photo-disintegration would become non-trivial as a result of efficient late-time annihilations.

The right panel of Fig. 7.6 is for $\gamma_{\rm inv} = 10^{-5}$. In this case, CMB constraints are highly relevant for small values of $\kappa$ and determine the lower boundary of the allowed parameter space. Since decreasing $\epsilon_R$ would only increase the annihilation rate at recombination, $\epsilon_R < 0.001$ will not increase the viable parameter space in this plot. Additionally, we see that it is no longer possible to satisfy the relic density requirement everywhere. For large $\kappa$ and small $m_{A'}$, all values of $\epsilon_R$ result in a DM subcomponent. Note that having a DM subcomponent does not affect its ability to be observed at accelerator experiments since these rely on the production of DM particles rather than the detection of a local DM flux.

We would now like to scan over the other parameters of the model. To do this, it is necessary to shift to the direct detection parameter plane, i.e., $\sigma_e - m_\chi$, since the accelerator constraints can only be calculated for a fixed value of $\gamma_{\rm inv}$.

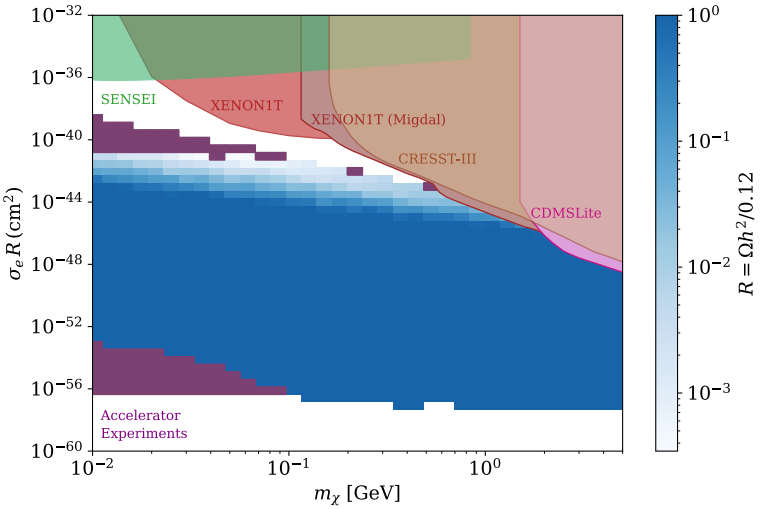


FIGURE 7.7: Allowed parameter space in the direct detection plane, $R\sigma_e - m_\chi$ with a scan over $\epsilon_R$ and $\gamma_{\rm inv}$. The purple shading indicates parameter regions completely excluded by accelerator experiments.

### 7.3.2 Direct Detection Constraints

For sub-GeV DM, as discussed in section 7.1, we will be interested in the bounds on DM-electron cross-section, which from Eq. 7.16 can be written as,

$$\sigma_e = \frac{4\mu_{\chi e}^2 \alpha \kappa^2 g_\chi^2}{(m_{A'}^2 + \alpha^2 m_e^2)^2}\,. \tag{7.23}$$

Additionally bounds on DM-nucleon scattering cross-section (which kick in for DM masses above a 100 MeV) can be converted to those on DM-electron scattering cross-section by a rescaling,

$$\sigma_e = \frac{A^2}{Z^2}\frac{\mu_{\chi e}^2}{\mu_{\chi p}}\sigma_{\chi p}\,, \tag{7.24}$$

where the additional factor reflects the fact that DM-nucleon scattering is conventionally assumed to scale as $A^2$ but for the case of dark photons, it actually scales as $Z^2$. Finally, bounds on the DM-nucleon cross-section arising from the Migdal effect can also be rescaled similarly into bounds on $\sigma_e$. Note that since we accommodate the case when DM is under-abundant, direct detection actually constraints $R\sigma_e$ instead of $\sigma_e$. This follows directly from Eq. 7.1 by reducing the local DM density from $\rho_0$ to $R\,\rho_0$.

In this section, we will consider bounds on $\sigma_e$ from XENON1T [182] and SENSEI [195]. Further, for $\sigma_{\chi p}$, we will consider CRESST-III [207], CDMSLite [208] and a recent search for the Migdal effect in XENON1T [200].

Following the procedure laid out in the previous section, we now scan over the following parameter ranges, where the upper and lower bounds are argued for in the preceding paragraphs,

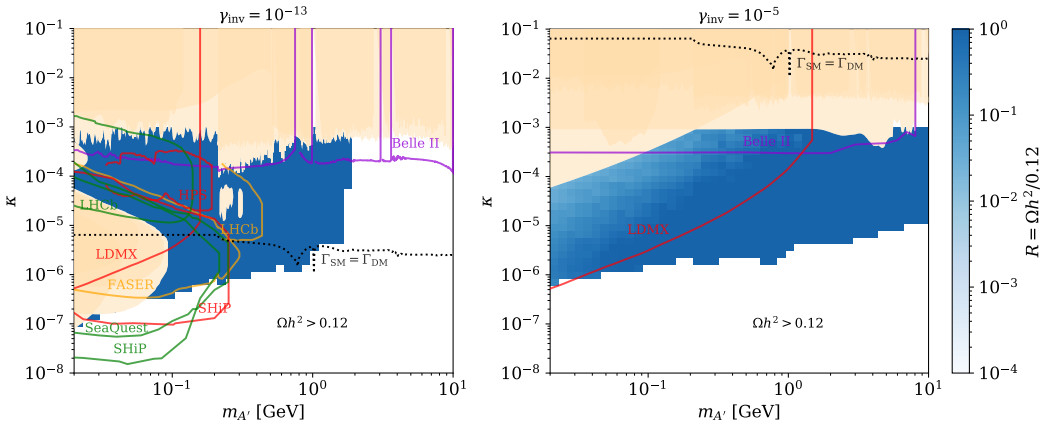


FIGURE 7.8: Same as figure 7.6, this time with existing constraints. Solid lines represent projected sensitivities of various experiments. The colours depend on the dark photon production mechanism as in figures 7.5 and 7.6.

- $m_\chi \in [10\,\text{MeV},\, 5\,\text{GeV}]$
- $\gamma_{\rm inv} \in [10^{-23},\, 0.1]$
- $\kappa \in [10^{-10},\, 0.001]$
- $\epsilon_R \in [0.001,\, 0.1]$

We present the viable parameter space with the scan outlined above in Fig. 7.7 with the same convention of the shading as before, i.e, we plot the parameter combination which results in the largest value of the relic abundance consistent with cosmological constraints. White regions in the plot then correspond to where no combination of parameter points survive after the application of cosmological and relic density constraints. Purple shaded regions represent regions where no viable parameter points survive after applying accelerator constraints. Note that accelerator bounds exclude points along the hidden dimensions in other regions of the parameter space but it is always possible to find a combination of parameters that are viable and map on to the same $R\sigma_e$. We know from earlier discussions that the observed relic density requires smaller couplings when $\epsilon_R \ll 1$ and larger ones when $\epsilon_R \to 1$. Since $\sigma_e \propto \kappa^2 g_\chi^2$, moving from top to bottom in Fig. 7.7 is equivalent to moving closer to resonance. The accelerator constraints in the bottom left of the plot which exclude dark photon masses upto a hundred MeV, correspond to ones coming from fixed-target experiments as can also be seen in Fig. 7.5. The accelerator constraints on the top, on the other hand, come from both fixed-target and $e^+e^-$ colliders. Further, moving to the top of the plot (or going toward large $\epsilon_R$) means that larger couplings are required to reproduce the relic abundance which are then in tension with CMB. As a result, the relic abundance cannot be saturated toward the top of the plot (indicated by the lighter shading).

Fig. 7.7 demonstrates that a large amount of viable parameter space exists even for moderate values of resonant enhancement ($\epsilon_R \geq 0.001$). This result is largely independent of the choice of lower bound on $\epsilon_R$ with the viable parameter space shrinking insignificantly if, for instance, we require $\epsilon \geq 0.01$ instead (see Appendix B of [3]).

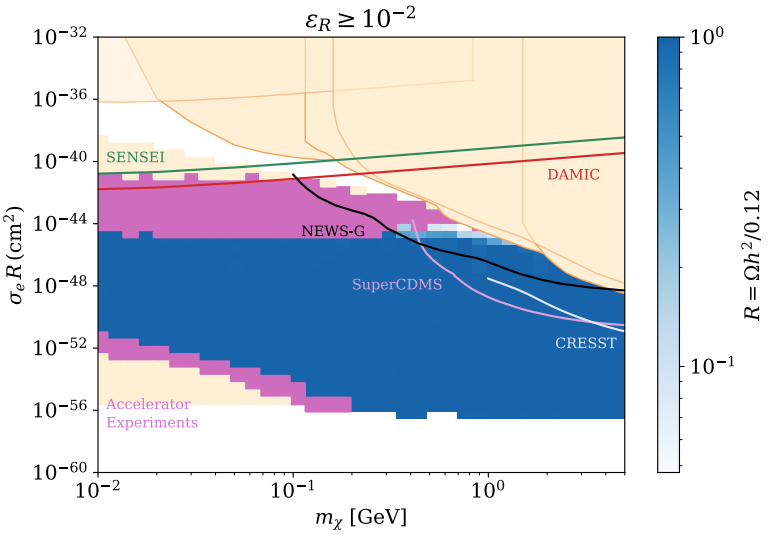


FIGURE 7.9: Same as figure 7.7 but this time with existing constraints shaded in orange. Solid lines represent projected sensitivities. The parameter regions that can be fully explored by future accelerator experiments are shaded in magenta.

Future experiments can further probe this parameter space for both large and small coupling values. Accelerator experiments such as Belle II [209], FASER [210], HPS [211], LHCb [212, 213], SeaQuest [214] and SHiP [89] have the potential to deeply explore the parameter space for visibly decaying sub-GeV dark photons. Belle II and LDMX [85, 215] with improved single-photons and missing energy searches will additionally be highly sensitive to invisible decays. As for direct detection, SENSEI, DAMIC [216], Super-CDMS [217], NEWS-G [218] and CRESST-III [219] will explore this parameter space further. We show these projections in Fig. 7.8 and Fig. 7.9. The direct detection bounds are obtained from the Dark Matter Limit Plotter [186], whereas the accelerator bounds come from our modified version of the DARKCAST code (see Appendix A of [3] for more details).

## 7.4 Constraining B-L Dark Photons

We will now consider the second dark photon model discussed in Chapter 5: that of $U(1)_{\mathrm{B-L}}$ dark photon with a thermally-induced mass mixing with the SM photon. The DM candidate in this model is a frozen-in Dirac fermion charged under $U(1)_{\mathrm{B-L}}$. The free parameters in this model are:

- $m_{A'}$: Mass of the dark photon. Since the $A'$ is assumed to be thermal, BBN places a lower bound on its mass, $m_{A'} >$ few MeV.
- $m_\chi$: Mass of the DM candidate. We are interested in the DM mass range, $1\,\mathrm{GeV} \leq m_\chi \leq 1\,\mathrm{TeV}$.
- $g_{\mathrm{BL}}$: The gauge coupling of the dark photon. The total coupling to any particle is then given by $g_{\mathrm{BL}} q'_f$, where $q'_f$ is the particle's $B - L$ charge. From relic abundance requirements, $g_{\mathrm{BL}} \sim 10^{-6} - 10^{-5}$.

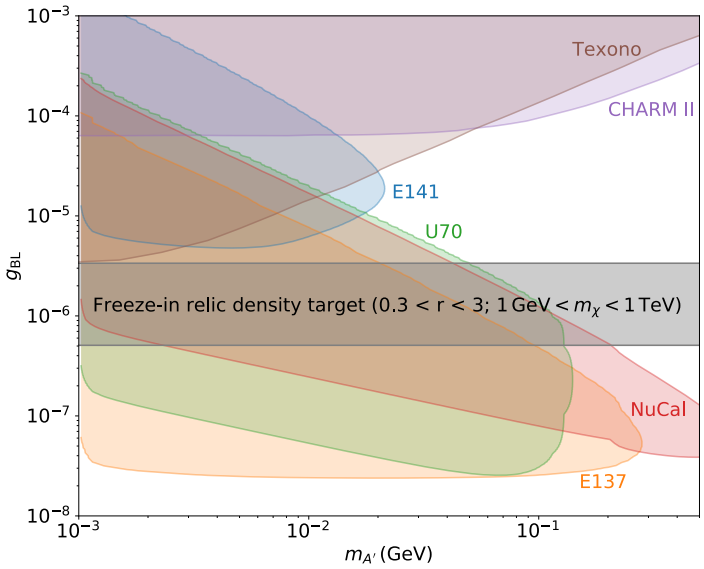


FIGURE 7.10: Exclusion bounds from fixed-target and beam-dump experiments plotted on top of the relic density target for $0.3 < r < 3$ and $1\,\text{GeV} < m_\chi < 1\,\text{TeV}$ in the $m_{A'}$-$g_{\text{BL}}$ parameter plane.

- $r \equiv g_{\text{BL}}/g_{\text{DM}} = 1/q'_{\text{DM}}$: The ratio of the gauge coupling to the total $A' - \chi$ coupling. Assuming that the $B - L$ charge of the DM particle is of order unity, it is reasonable to use, $0.3 < r < 3$.

Further, the DM abundance in this model is approximately given by Eq. 5.46,

$$\Omega_\chi h^2 \approx (0.16\, r^{-4} + 0.12\, r^{-2}) \left(\frac{g_{\text{BL}}}{2 \times 10^{-6}}\right)^4 . \tag{7.25}$$

### 7.4.1 Accelerator Constraints

The accelerator constraints on this model are straightforwardly obtained from the literature [84]. Since the dark photon is lighter than the DM particle, the only decays are into SM final states. Note that since neutrinos are charged under $B-L$, in this model we also obtain bounds from neutrino experiments such as TEXONO [220] and CHARM-II [221].

We plot these constraints in Fig. 7.10 in the $m_{A'} - \kappa$ parameter plane, along with the freeze-in target which demarcates the coupling range required to reproduce the relic abundance for $1\,\text{GeV} \leq m_\chi \leq 1\,\text{TeV}$ and $0.3 < r < 3$. Since the freeze-in production is independent of the dark photon mass, the band is exactly horizontal. The width of the band reflects the spread in DM masses and the coupling ratio (compare to Fig. 5.6). We reiterate that because of the structure of this model, i.e., small couplings of the dark photon to *both* SM and DM particles, we can have freeze-in production of DM while simultaneously having the capacity to produce observable signals at fixed-target and beam-dump experiments.

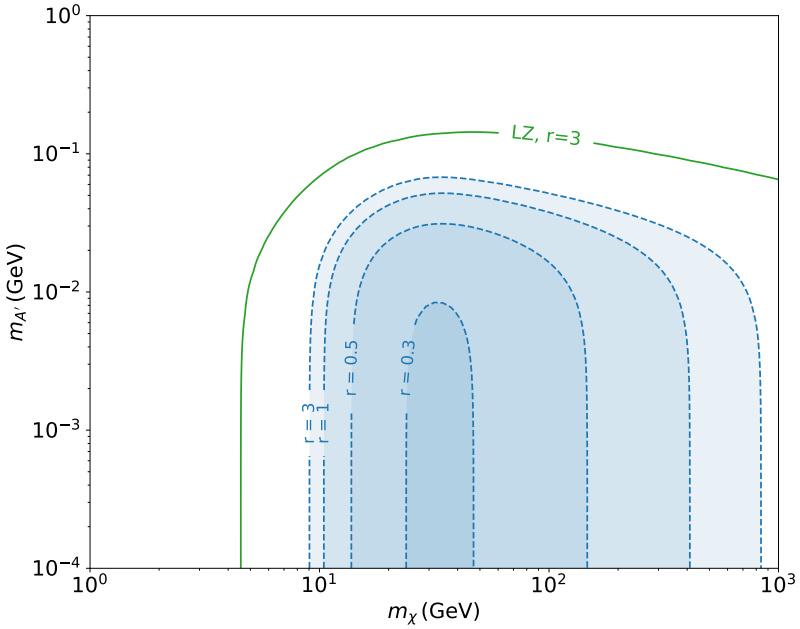


FIGURE 7.11: Parameter region excluded by XENON1T for different values of the coupling ratio $r = g_{\rm BL}/g_{\rm DM}$. The green line depicts the projected sensitivity of LZ for the case $r = 3$.

### 7.4.2 Direct Detection Constraints

As argued in section 7.1, freeze-in couplings can be probed at direct detection experiments in the limit of light mediators which result in an enhancement of the direct detection cross-section at low recoil energies. The DM-nucleus scattering cross-section for this model can be written using Eq. 7.6 and Eq. 7.7,

$$\frac{\mathrm{d}\sigma_N}{\mathrm{d}E_R} = \frac{g_{\rm BL}^2\, g_{\rm DM}^2 m_N A^2 F^2(E_R)}{2\pi v^2 (2m_N E_R + m_{A'}^2)^2}\,, \tag{7.26}$$

where the symbols have their usual meaning.[6] This cross-section will be enhanced at low recoil energies in the limit, $m_{A'} \ll \sqrt{2m_N E_R}$. The lowest observable recoil energy in XENON1T is $E_{\rm th} = 1.1\,\text{keV}$ which implies that for $m_{A'} \ll 16\,\text{MeV}$, the differential event rate will be independent of the mediator mass and benefit from the same enhancement as in the massless mediator limit, $m_{A'} \to 0$. For larger mediator masses, the event rates would be suppressed by $m_{A'}^{-4}$.

Using the publicly available code DDCALC [222, 223] and the XENON1T data, we place bounds in the $m_\chi - m_{A'}$ parameter plane for different values of the coupling ratio $r$ in Fig. 7.11. At each point in the parameter plane, we fix the remaining parameter, i.e., $g_{\rm DM}$, so as to reproduce the correct relic abundance. As expected, the constraints weaken for large values of $m_{A'}$ where the direct detection rates are suppressed. In terms of the couplings, for $r \gg 1$ (or $g_{\rm BL} \gg g_{\rm DM}$), the direct detection constraints depend on the same coupling combination as

[6] Note that neutrons (with a *udd* quark composition) have a $B - L$ charge and therefore couple to the dark photon. This results in the factor of $A^2$ instead of $Z^2$ that is usually present in kinetically mixed dark photon models

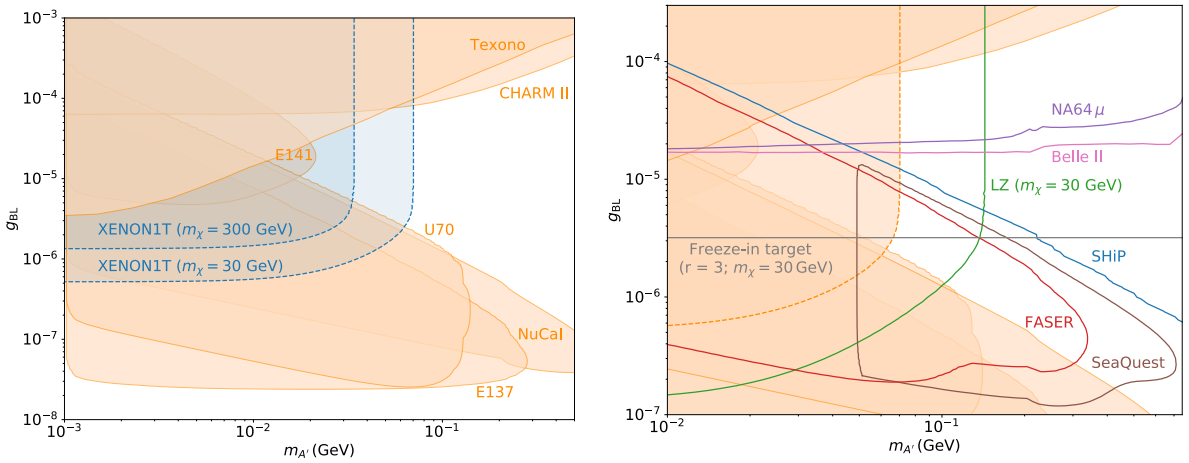


FIGURE 7.12: Complementarity of direct detection (blue) and accelerator (peach) constraints for a FIMP dark matter model. The direct detection constraints depend on the DM mass (contours shown for $m_\chi = 30\,\text{GeV}$ and $m_\chi = 300\,\text{GeV}$) and the coupling ratio (fixed to $r = 3$). The right panel shows projected sensitivities of various experiments.

the relic abundance, i.e., $g_{\text{BL}}^2 g_{\text{DM}}^2$ (see Eq. 7.25). Hence, by fixing the coupling combination by the relic density requirement, the direct detection constraints are only a function of $m_\chi$ and $m_{A'}$. This also results in the constraints saturating as $r \to 3$. For $r \ll 1$ on the other hand, the relic abundance scales as $g_{\text{DM}}^4$ whereas the direct detection cross-section scales as $g_{\text{DM}}^4 r^2$. This implies that the event rate reduces for small $r$ making this region more challenging to probe. Nevertheless, we see that the parameter space of this model is constrained by current experiments and is well within reach of future ones such as LZ (green line in Fig. 7.11) [224].

To demonstrate the complementarity between accelerator and direct detection searches for this model, we can plot constraints from the latter in the $m_{A'} - g_{\text{BL}}$ plane for different values of DM mass. We show this in the left panel of Fig. 7.12 for $m_\chi = 30\,\text{GeV}$ (for which we get the strongest direct detection constraints) and $m_\chi = 300\,\text{GeV}$. Once again, for each point in the plane we fix the coupling ratio (or equivalently, $g_{\text{DM}}$) in order to reproduce the correct relic abundance. The excluded parameter region becomes independent of the coupling strength for large $g_{\text{BL}}$ (corresponding to $r \gg 1$) and vanishes for small $g_{\text{BL}}$ ($r \ll 1$) as expected.

This plot can be immediately extended to include sensitivities of future experiments. In the right panel of Fig. 7.12, we demonstrate the reach of upcoming accelerator and direct detection experiments. It is easy to see that direct detection and accelerator searches probe the parameter space in complementary ways. Further, future experiments will carry out a thorough exploration of large parts of the currently allowed parameter space, making this model an attractive target for these searches.

## 7.5 Conclusions

In the last several years, DM detection strategies have witnessed huge advancements in all channels. With increasing sensitivities of these experiments, the traditional GeV-TeV WIMP search window is being pushed to both smaller masses and couplings. In particular, sub-GeV DM searches have gained a lot of traction with traditional direct detection experiments such as XENON1T being optimised to detect DM-electron scattering along with completely new experiments being set up to specifically look for electron recoil. At the same time, more and more precise searches for hidden particles at accelerator experiments are exploring new corners of parameters.

Dark photons arise naturally in the context of such searches since they provide a well-motivated portal between the visible and dark sectors. Accelerator searches for dark photons in particular have seen a tremendous increase in sensitivity in both invisible and visible decay channels quite independently of their connection to DM. This has resulted in a push toward developing and studying DM models with a dark photon portal. For many DM models, the constraints arising from accelerator and direct detection searches turn out to be highly complementary to each other and to those arising from cosmology. In this chapter, we have looked at the terrestrial constraints on two dark photon models representing two opposing DM production mechanisms: a resonant DM model (production through freeze-out) and a $U(1)'$ extended DM model (production via freeze-in).

In section 7.3, we showed that a resonant DM model can be probed in complementary ways at accelerators and direct detection experiments while being cosmologically viable. To this end, we conducted a global scan of the parameter space using state-of-the-art numerical tools like DARKCAST. Our results show that the accelerator experiments are highly sensitive to smaller couplings and therefore the case of a strong resonant enhancement, whereas the direct detection experiments probe larger couplings and regions of parameter space where the DM forms a subcomponent. These are summarised in Fig. 7.8 and Fig. 7.9 where the allowed parameter space is shaded in blue with the gradient representing the largest possible value of the DM abundance consistent with all constraints. Despite the complementarity of these constraints, however, large regions of parameter space remain viable, demonstrating that even simple models of light thermal DM consistent with cosmological and terrestrial constraints can be constructed with only moderate amounts of tuning. Additionally, while upcoming experiments will probe this parameter space further, new strategies are required for a complete and thorough exploration.

In section 7.4, we discussed direct detection and accelerator constraints for a FIMP dark matter model and showed that such models are highly testable despite the smallness of freeze-in couplings. In particular, we looked at a model in which both the DM and the SM particles are charged under an additional gauge group. In this case, accelerator constraints—which are based on dark photon production—already probe the freeze-in parameter space. Additionally, direct detection experiments obtain a sensitivity to the freeze-in couplings due to an enhancement in the scattering cross-section at low recoil energies. This is a direct result of

having an MeV-scale gauge boson in the model which, in the limit of being lighter than the smallest detectable momentum transfer, effectively acts as a massless mediator. While the accelerator constraints are independent of the DM mass and only probe the dark photon coupling to the SM, the direct detection constraints probe a combination of the two couplings, $g_{\rm SM} \times g_{\rm DM}$. These constraints are the strongest in the limit $g_{\rm SM} > g_{\rm DM}$ in which the direct detection cross-section and the relic abundance depends on exactly the same coupling combination. Our results are summarised in Fig. 7.12. Note that these constraints might differ if we assume a $U(1)'$ extension different from $B - L$.

From this discussion, it is evident that terrestrial search strategies for DM hold enormous promise for the future, and dark photons, in particular, make for an attractive target for BSM physics.

# Chapter 8

# Conclusions

We do not know what eighty percent of the universe is made of. Yet the story of DM is woven through our cosmological history, its effects manifest in the very structure of our universe. While this means that the macrophysics of DM is quite well understood—captured in the cold, collisionless DM paradigm—its microphysics remains shrouded in mystery.

In this thesis, I have attempted to detail the phenomenological implications of a few different DM models categorised according to their possible non-gravitational interactions with the SM. In order to capture the relevant physics at all scales, I have used cosmological time as a scaffolding, detailing the possible effects of DM on timescales ranging from a few seconds after the Big Bang to today, billions of years later.

In Part I, I laid down the theoretical groundwork required in order to study this DM phenomenology. Chapter 1 provided a brief review of the standard models of particle physics and cosmology with a focus on the physics at very early times. To this end, we discussed the framework of finite temperature field theory in order to accurately describe particle properties and interactions in a thermal plasma. In particular, we discussed the electroweak phase transition in the SM detailing the temperature-dependent evolution of the Higgs mass and vev. In Chapter 2, we reviewed the observational evidences for DM, and discussed the evolution of the dark sector in the context of two different production mechanisms: freeze-out, where the DM abundance is set by its annihilation and decay into SM particles, and freeze-in, where it is set by production from the SM particles. Since particle production at early times necessarily happens in a plasma, we presented a modified version of the freeze-in Boltzmann equation accounting for the corresponding in-medium effects. We also elaborated on constraining DM in the early universe by cosmological probes such as BBN and CMB. BBN is extremely sensitive to any additional light particles in the early universe and places an almost model-independent bound on the DM mass if it has a thermal abundance. Additionally, DM annihilations at late times can inject energy into the photon-baryon plasma and therefore DM can be constrained quite effectively using the CMB. From the discussions in Part I, the calculations of relic abundances for specific DM models as well as relevant cosmological bounds straightforwardly follow.

In Part II, we discussed the cosmology of concrete DM models grouped under two portals on the basis of whether the mediating particle between DM and the SM is a scalar or a vector.

After an extremely brief summary of portals in Chapter 3, we dove into the Higgs portal with the example of a scalar singlet DM model in Chapter 4. We were interested in looking at the scalar singlet in the freeze-in regime and in particular in regions of parameter space where the relic abundance is not set by decays of the Higgs bosons. To ensure this, we considered two scenarios: one, with a scalar mass larger than twice the Higgs mass, and second, with a reheating temperature much smaller than the Higgs mass. In both cases, we demonstrated that higher order corrections, in-medium and thermal effects are important in the relic density calculations. In particular, both the QCD and the electroweak phase transition in the SM needed to be accounted for properly to obtain accurate results. We showed that all of these effects can be simply included by reformulating the freeze-in Boltzmann equation in terms of the thermally averaged DM annihilation cross-section, which is calculated at finite temperature with the relevant statistical phase space factors. Interestingly, the largest of the couplings required to saturate the relic abundance for low reheating temperatures are already excluded by terrestrial experiments.

As part of ongoing work, we have implemented these calculations in the public code DARKSUSY. It would be interesting to further extend (and implement) this framework to study the evolution of other DM models at finite temperature. Of course, even though our work focused on (the dominant) $2 \to 2$ processes, an interesting discussion is to be had regarding $1 \to 2$ processes at finite temperature and the equivalence (or lack thereof) between the two.

In Chapter 5, we shifted our attention to another commonly studied portal, namely the dark photon portal. We studied the DM cosmology with a dark photon portal in both freeze-out and freeze-in scenarios. In the case of thermal freeze-out, we were interested in the sub-GeV DM regime. We demonstrated such light DM models can be cosmologically viable if the dark photon mass is close to twice the DM mass. Consequently, DM annihilations are resonantly enhanced at early times and smaller couplings are required to reproduce the DM relic abundance. For a moderate resonant enhancement, these small couplings evade constraints from BBN and CMB by suppressing late time annihilations. On the flip side, for the case of freeze-in, we considered a $U(1)'$ extension to the SM and specified how a thermal mass-mixing between the SM $U(1)$ and this $U(1)'$ can result in temperature-dependent couplings. In-medium and thermal effects were highly relevant for this model with DM production channels differing before and after the electroweak phase transition. In contrast to the previous model, we showed that couplings larger than the standard freeze-in ones are needed to reproduce the relic abundance. The two models together show that the conditions for freeze-in and freeze-out can be satisfied by a range of couplings not necessarily similar to the conventionally assumed ones.

Dark photon models, in general, are open to a number of exciting directions in future work. The parameter space for the resonant dark photon model discussed here can be expanded to include much stronger resonant enhancements and therefore even smaller couplings. This would require a more accurate calculation of the relic abundance, in particular accounting for the fact that the DM may no longer be in kinetic equilibrium during freeze-out [225, 226]. Additionally, for strong resonant enhancements, BBN constraints arising as a result of photodisintegration become relevant, along with novel constraints arising from energy losses in

supernovae [227]. For $U(1)'$ extensions, our framework can be used to evaluate abundances and constraints on other specific realisations such as $U(1)_{L_\mu - L_\tau}$ or $U(1)_B$.

Since the particles mediating the DM-SM interactions can also mediate DM-DM interactions, we switched gears and explored DM self-interactions in Chapter 6. We discussed the subtleties that crop up when comparing model predictions to data in terms of both the cross-section to be used (momentum-transfer or viscosity), and the procedure for averaging over velocities. The DM self-interactions constrained at various scales, from dwarf galaxies to galaxy clusters, hint toward a long-range interaction which can be modelled by a Yukawa potential. Additionally, many small-scale problems can be solved if these interactions fall within the semi-classical regime. We therefore derived general analytic formulas for both the momentum transfer and the viscosity cross-sections in the semi-classical regime from first principles. Together with existing results in the literature, our results provide a complete analytic coverage of self-interactions with a Yukawa potential.

Our framework for calculating these self-interactions can be used for interactions mediated by other kinds of potentials. In particular, even if analytic results are difficult to obtain, numerical evaluations of the phase-shift integrals may yield an accurate (and fast) approximation to solving the full Schroedinger equation in the semiclassical regime. Additionally, our results can be implemented in numerical simulations in order to better explore DM phenomenology on small scales.

Finally, in Part III, we entered current timescales with a discussion on DM detection strategies in Chapter 7. After introducing direct detection strategies and accelerator searches for DM, we placed bounds on the dark photon models introduced in Part II. The bounds from these two search strategies turned out to be highly complementary to each other as well as to the cosmological bounds derived in Part II, constraining even the small couplings present in freeze-in models. This is a remarkable result considering that models with light, extremely weakly coupled particles appear, at first sight at least, to be undetectable, and provides hope for the future with innovative and more precise experiments further exploring exactly these regions of the parameter space.

It is evident from the discussions in this thesis that we have neither exhausted the scope of existing ideas nor mapped out the full terrain of possibilities when it comes to DM. Even in the few models studied here, there remain huge opportunities for future work. Further, the recent XENON1T excess [194] has opened the door to even more exotic models of light DM. In particular, models with inelastic DM—where the dark sector is composed of particles with a small mass splitting—have gained a lot of traction [192]. The phenomenology of such models at direct detection experiments, especially considerations on their phase-space after potential upscatterings inside the Earth, poses an exciting direction for future work. Additionally, the cosmology of such models may be non-trivial with late-time de-excitations in the dark sector having potentially observable effects on structure formation.

Other anomalies in our measurements, such as the $g-2$ anomaly [228], that compel us to look for BSM particles also provide a rich ground for DM model-building. In the absence of

a clear DM signal, and with increasingly precise experiments probing different corners of the parameter space, we are, in a sense, limited only by our creativity. DM models which were "exotic" a few years ago are now being regularly probed by experiments. Simultaneously, new ideas are needed both on the theoretical as well as on the experimental side of DM research. The story of DM is still being written and it is an incredible privilege to be able to contribute to it, however small that contribution may be.

And lastly, finally, I would like to take a step back from the exciting world of DM research and implore whoever is reading this thesis to also reflect on the broader state of our shared planet and the conditions we do science in. While I was writing this thesis, the rivers of my country were choked with bodies of people lost to the pandemic as a result of criminal mismanagement by a complacent state. This came after more than two years of constant, hideous attacks on the dignity and freedoms and lives of marginalised groups there. A huge fraction of my PhD was spent with a visceral awareness of this collective grief and helplessness. And I am sure I was not the only one. These situations are truly international as was brought to the fore with the Black Lives Matter movement last year and more recently in the struggle for Palestinian liberation. My point is that while for much of the scientific community in the West, it continued to be business-as-usual, it has (always) been a completely different story for under-represented groups who do not have the luxury of detachment. My point is that as we increasingly talk about diversity and inclusion in scientific communities, it is imperative that we not limit these conversations to only when they are "safe" or convenient. Instead, we *must* express unconditional solidarity with oppressed groups everywhere. We *must* ensure that our community is not only welcoming but active and visible in its commitment to equality and justice.

We cannot remain aloof. And we cannot, indeed should not, look away.

# Appendix A

# In-medium Cross-Section And Thermal Average

In this appendix, we will discuss how to reduce the 12-dimensional integral in the collision term of Eq. 2.47, while making sure we include the frame-dependence at every step.

**In-Medium Cross-Section:**
The cross-section for a given process is most easily calculated in the CMS frame. The cross-section in Eq. 2.42 is exactly the CMS cross-section apart from the statistical factors which depend on the cosmic rest frame through $(u \cdot k)$ that enters in the distribution functions. We can transform these to the CMS frame by applying a Lorentz boost to the comic four-velocity, $u$, for each DM momenta $p$, $\tilde{p}$.

For any two momenta, $p$, $\tilde{p}$, in a general frame, we can introduce [58],

$$\begin{aligned} \overline{p} &= \frac{p+\tilde{p}}{2}\,, \\ \overline{k} &= \frac{p-\tilde{p}}{2}\,, \end{aligned} \tag{A.1}$$

such that the CMS frame is defined by,

$$\overline{p} = \Lambda(\overline{p}) \begin{pmatrix} E \\ 0 \\ 0 \\ 0 \end{pmatrix}\,, \tag{A.2}$$

where $E = \sqrt{s}/2$ is the particle energy in the CMS frame. For $\overline{p} = (\overline{p}^0, \overline{p}^3, \overline{p}^2, \overline{p}^1)^T$, the Lorentz transformation can be written in terms of the rapidity, $\eta$ and the angular variables $\theta$, $\phi$,

$$\Lambda(\overline{p}) = \begin{pmatrix} 1 & 0 & 0 & 0 \\ 0 & 1 & 0 & 0 \\ 0 & 0 & \cos\phi & -\sin\phi \\ 0 & 0 & \sin\phi & \cos\phi \end{pmatrix} \begin{pmatrix} 1 & 0 & 0 & 0 \\ 0 & \cos\theta & -\sin\theta & 0 \\ 0 & \sin\theta & \cos\theta & 0 \\ 0 & 0 & 0 & 1 \end{pmatrix} \begin{pmatrix} \cosh\eta & \sinh\eta & 0 & 0 \\ \sinh\eta & \cosh\eta & 0 & 0 \\ 0 & 0 & 1 & 0 \\ 0 & 0 & 0 & 1 \end{pmatrix}\,, \tag{A.3}$$

$$\Lambda(\overline{p})^{-1} = \begin{pmatrix} \cosh\eta & -\sinh\eta & 0 & 0 \\ -\sinh\eta & \cosh\eta & 0 & 0 \\ 0 & 0 & 1 & 0 \\ 0 & 0 & 0 & 1 \end{pmatrix} \begin{pmatrix} 1 & 0 & 0 & 0 \\ 0 & \cos\theta & -\sin\theta & 0 \\ 0 & -\sin\theta & \cos\theta & 0 \\ 0 & 0 & 0 & 1 \end{pmatrix} \begin{pmatrix} 1 & 0 & 0 & 0 \\ 0 & 1 & 0 & 0 \\ 0 & 0 & \cos\phi & \sin\phi \\ 0 & 0 & -\sin\phi & \cos\phi \end{pmatrix} . \tag{A.4}$$

The 6 degrees of freedom in $p$, $\tilde{p}$ get converted into $E$, $\eta$ and 4 angular variables $\theta$, $\phi$, $\theta_{\bar{k}}$, $\phi_{\bar{k}}$, where $\theta_{\bar{k}}$, $\phi_{\bar{k}}$ denote the spherical coordinate angles parameterizing $\overline{k}$. Because the DM particles are on-shell, $\overline{k}^0 = 0$ and $\left|\overline{\mathbf{k}}\right| = \sqrt{E^2 - m_\chi^2}$.

Using this Lorentz transformation, we can transform the distribution functions in Eq. 2.42 to the CMS frame:

$$\begin{aligned} g(\omega) = g(u\cdot k) \to g((\Lambda^{-1}u)\cdot k) &= \frac{1}{\exp[\frac{k^0\cosh\eta + k^3\sinh\eta}{T}] - \varepsilon_\psi} = \frac{1}{\exp[\frac{\omega\cosh\eta + |\mathbf{k}_{\rm CM}|\cos\theta\sinh\eta}{T}] - \varepsilon_\psi}, \\ g(\tilde{\omega}) = g(u\cdot \tilde{k}) \to g((\Lambda^{-1}u)\cdot \tilde{k}) &= \frac{1}{\exp[\frac{\tilde{k}^0\cosh\eta + \tilde{k}^3\sinh\eta}{T}] - \varepsilon_\psi} = \frac{1}{\exp[\frac{\tilde{\omega}\cosh\eta - |\mathbf{k}_{\rm CM}|\cos\theta\sinh\eta}{T}] - \varepsilon_\psi}, \end{aligned} \tag{A.5}$$

where $k$, $\tilde{k}$ are the SM momenta in the CMS frame and in the final equality we have used, $k^0(\tilde{k}^0) = \omega(\tilde{\omega})$ and $k^3 = -\tilde{k}^3 = |\mathbf{k}_{\rm CM}|\cos\theta$, with the CMS momenta given by the usual expression,

$$|\mathbf{k}_{\rm CM}| = \frac{1}{2\sqrt{s}}\sqrt{(s-(m_\psi - m_{\bar{\psi}})^2)(s-(m_\psi + m_{\bar{\psi}})^2}\,. \tag{A.6}$$

The statistical factors taken together can be expressed in terms of a function,

$$\begin{aligned} G^{-1} &\equiv (1-\varepsilon_\psi g(u\cdot k))^{-1}\left(1-\varepsilon_\psi g(u\cdot\tilde{k})^{-1}\right)^{-1} \\ &= 1 - \varepsilon_\psi^2 e^{-2E\gamma/T} - 2\varepsilon_\psi e^{-E\gamma/T}\cosh\left[\frac{|\mathbf{k}_{\rm CM}|\cos\theta\sqrt{\gamma^2-1}}{T}\right], \end{aligned} \tag{A.7}$$

where we have defined $\gamma = \cosh\eta$ for convenience. In terms of dimensionless variables, $\tilde{s} \equiv s/4m_\chi^2 = E^2/m_\chi^2$ and $x = m_\chi/T$, this becomes,

$$\begin{aligned} G^{-1}(\gamma, \cos\theta, s) = 1 &+ \varepsilon_\psi^2 e^{-2\sqrt{\tilde{s}}x\gamma} \\ &- 2\varepsilon_\psi e^{-\sqrt{\tilde{s}}x\gamma}\cosh\left[x\cos\theta\sqrt{\gamma^2-1}\frac{1}{2\sqrt{\tilde{s}}}\sqrt{\tilde{s}-\left(\frac{m_\psi - m_{\bar{\psi}}}{2m_\chi}\right)^2}\sqrt{\tilde{s}-\left(\frac{m_\psi + m_{\bar{\psi}}}{2m_\chi}\right)^2}\right] \end{aligned} \tag{A.8}$$

which in the limit, $m_\psi = m_{\bar{\psi}}$ reduces to,

$$G^{-1}(\gamma, \cos\theta, s) = 1 + \varepsilon_\psi^2 e^{-2\sqrt{\tilde{s}}x\gamma} - 2\varepsilon_\psi e^{-\sqrt{\tilde{s}}x\gamma} \cosh\left[x\cos\theta\sqrt{\gamma^2-1}\sqrt{\tilde{s} - \frac{m_\psi^2}{m_\chi^2}}\right] . \tag{A.9}$$

This yields the in-medium cross-section in the CMS frame,

$$\sigma_{\chi\chi\to\psi\psi}(s,\,\gamma) = \frac{1}{8\pi s N_\psi} \frac{|\mathbf{k}_{\rm CM}|}{\sqrt{s-4m_\chi^2}} \int_{-1}^{1} \frac{\mathrm{d}\cos\theta}{2} \left|\overline{\mathcal{M}}\right|^2 (s,\,\cos\theta) G(\gamma,\,s,\,\cos\theta)\,, \tag{A.10}$$

where we have reduced the phase space integrals to angular ones in the usual way. It can be easily seen that this cross-section is equivalent to the vacuum CMS cross-section when $\varepsilon_\psi = 0$ (which implies $G = 1$).

**In-medium Thermal Average:**
The thermal average in Eq. 2.44 can also be boosted to the CMS frame. We note that the differential phase space corresponding to $p,\,\tilde{p}$ can be reformulated in the CMS frame in terms of $\overline{p}$ and $\overline{k}$ as defined in Eq. A.1,

$$\frac{\mathrm{d}^3p}{(2\pi)^3 2E}\frac{\mathrm{d}^3\tilde{p}}{(2\pi)^3 2\tilde{E}} = 2^4 \frac{\mathrm{d}^4\overline{p}}{(2\pi)^4}\frac{\mathrm{d}^4\overline{k}}{(2\pi)^4}(2\pi)^2\delta\left((\overline{p}+\overline{k})^2 - m_\chi^2\right)\delta\left((\overline{p}-\overline{k})^2 - m_\chi^2\right)\,, \tag{A.11}$$

where the $\delta$ functions ensure energy conservation. Since $\overline{p}$ is time-like in the CMS frame, we can parameterise it in terms of the rapidity and CMS energy

$$\begin{aligned}
\overline{p}^0 &= \frac{\sqrt{s}}{2}\cosh\eta,\\
\overline{p}^1 &= \frac{\sqrt{s}}{2}\sinh\eta\sin\theta\sin\phi,\\
\overline{p}^2 &= \frac{\sqrt{s}}{2}\sinh\eta\sin\theta\cos\phi,\\
\overline{p}^3 &= \frac{\sqrt{s}}{2}\sinh\eta\cos\theta,
\end{aligned} \tag{A.12}$$

thereby reducing the $\overline{p}$-integral as,

$$\int \frac{\mathrm{d}^4\overline{p}}{(2\pi)^4} = \frac{1}{(2\pi)^4}\int \sinh^2\eta \left(\frac{s}{32}\right) \mathrm{d}s\,\mathrm{d}\eta\,\mathrm{d}\Omega_{\bar{p}}\,, \tag{A.13}$$

where $\Omega_{\bar{p}}$ is the solid angle in $\overline{p}$-space. Additionally, the $\delta$-functions can be used to reduce the $\overline{k}$-integral,

$$2^4\int \frac{\mathrm{d}^4\overline{k}}{(2\pi)^4}(2\pi)^2\delta\left((\overline{p}+\overline{k})^2 - m_\chi^2\right)\delta\left((\overline{p}-\overline{k})^2 - m_\chi^2\right) = \frac{2^2}{(2\pi)^2}\int \mathrm{d}\Omega_{\bar{k}}\frac{1}{\sqrt{s}}\sqrt{\frac{s}{4}-m_\chi^2}\,. \tag{A.14}$$

Eqs. A.13 and A.14 imply that for any function of momenta $g(p,\,\tilde{p})$, the integral over the phase-space can be converted into the CMS frame through

$$\int \frac{\mathrm{d}^3p}{(2\pi)^3 2E}\int \frac{\mathrm{d}^3\tilde{p}}{(2\pi)^3 2\tilde{E}}\, g(p,\,\tilde{p}) = \frac{m_\chi^4}{(2\pi)^6}\int_1^\infty \mathrm{d}\tilde{s}\,\sqrt{\tilde{s}(\tilde{s}-1)}\int_1^\infty \mathrm{d}\gamma\sqrt{\gamma^2-1}\int \mathrm{d}\Omega_{\bar{p}}\mathrm{d}\Omega_{\bar{k}}\, g(\bar{p},\,\bar{k})\Big|_{\bar{k}^0=0}\,, \tag{A.15}$$

where we have used $\gamma = \cosh\eta$, and expressed everything in terms of the dimensionless variable, $\tilde{s} = s/4m_\chi^2$, as before.

To calculate the thermal average, we also need to boost the (hypothetical) Maxwell-Boltzmann DM distribution, $f_\chi^{\mathrm{MB}}$ into the CMS frame. Following the same procedure as before, we have

$$\begin{aligned} u\cdot p &= (\Lambda^{-1}u)\cdot(\bar{p}+\bar{k}) = E\cosh\eta + \sqrt{E^2-m_\chi^2}\sinh\eta\cos\theta\,,\\ u\cdot\tilde{p} &= (\Lambda^{-1}u)\cdot(\bar{p}-\bar{k}) = E\cosh\eta - \sqrt{E^2-m_\chi^2}\sinh\eta\cos\theta\,, \end{aligned} \tag{A.16}$$

which yields for the distribution functions,

$$f_\chi^{\mathrm{MB}}(E) f_\chi^{\mathrm{MB}}(\tilde{E}) \to e^{-\frac{2E\cosh\eta}{T}} = e^{-2x\sqrt{\tilde{s}}\gamma}\,. \tag{A.17}$$

The thermal average can now be calculated using Eq. A.15 with,

$$\begin{aligned} g(p,\,\tilde{p}) =& 4g_\chi^2\sigma(p,\,\tilde{p})F f^{\mathrm{MB}}(p)_\chi f^{\mathrm{MB}}(\tilde{p})\\ \underset{\mathrm{CMS}}{=}& 4g_\chi^2\sigma(s,\,\gamma)m_\chi^2\sqrt{\tilde{s}(\tilde{s}-1)}e^{-2x\sqrt{\tilde{s}}\gamma}\,. \end{aligned} \tag{A.18}$$

Since the distribution functions, $f_\chi^{\mathrm{MB}}$, do not have any angular dependence, the angular integrals in $\bar{p}$- and $\bar{k}$-space can be done trivially to obtain $\int \Omega_{\bar{p}}\Omega_{\bar{k}} = (4\pi)^2$. Note that this is a particular feature of freeze-in reformulated in terms of DM annihilations, since we have invoked $f_\chi^{\mathrm{MB}}$ in an ad-hoc manner under the assumption that the actual DM distribution can be ignored. If this weren't true, we would instead have a Fermi-Dirac or Bose-Einstein distribution here for the SM particles with an explicit angular dependence (see [59]).

Using these substitutions, the thermally averaged cross-section has the form,

$$\langle\sigma v\rangle_{\chi\chi\to\psi\psi} = \frac{8x^2}{K_2^2(x)}\int_1^\infty \mathrm{d}\tilde{s}\,\sqrt{\tilde{s}(\tilde{s}-1)}\int_1^\infty \mathrm{d}\gamma\sqrt{\gamma^2-1}e^{-2x\sqrt{\tilde{s}}\gamma}\sigma_{\chi\chi\to\psi\psi}(s,\,\gamma)\,. \tag{A.19}$$

# Appendix B

# Derivation of phase shifts

Note: This Appendix has been reproduced from [2].

We start from the integral

$$I^\ell = \kappa \int_{R_0(\ell)}^{\infty} \mathrm{d}R \sqrt{1 + \frac{2\beta}{R} e^{-R} - \frac{(\ell+\frac{1}{2})^2}{\kappa^2 R^2}} \tag{B.1}$$

$$= \kappa \int_{R_0(\ell)}^{R_{\text{cut}}} \mathrm{d}R \sqrt{1 + \frac{2\beta}{R} e^{-R} - \frac{(\ell+\frac{1}{2})^2}{\kappa^2 R^2}} + \kappa \int_{R_{\text{cut}}}^{\infty} \mathrm{d}R \sqrt{1 + \frac{2\beta}{R} e^{-R} - \frac{(\ell+\frac{1}{2})^2}{\kappa^2 R^2}} \tag{B.2}$$

$$\equiv I_1^\ell + I_2^\ell \,, \tag{B.3}$$

where $R_0 = (\ell + 1/2)^2/(2\beta\kappa^2)$ and $R_{\text{cut}}$ is chosen such that $R_0 \ll R_{\text{cut}} \ll 1$.

In the first integral we can neglect the first term in the square root and approximate $e^{-R} \approx 1$, leading to

$$I_1^\ell = \kappa \int_{(\ell+\frac{1}{2})^2/(2\beta\kappa^2)}^{R_{\text{cut}}} \mathrm{d}R \sqrt{\frac{2\beta}{R} - \frac{(\ell+\frac{1}{2})^2}{\kappa^2 R^2}} \tag{B.4}$$

$$= (\ell + \tfrac{1}{2}) \int_1^{S_{\text{cut}}} \mathrm{d}S \frac{1}{S} \sqrt{S-1} \tag{B.5}$$

$$= (2\ell+1) \left( \sqrt{S_{\text{cut}} - 1} - \operatorname{asec}(\sqrt{S_{\text{cut}}}) \right) \,, \tag{B.6}$$

with $S_{\text{cut}} = R_{\text{cut}}(2\beta\kappa^2)/(\ell+\frac{1}{2})^2$. For $S_{\text{cut}} \gg 1$ we then find

$$I_1^\ell - I_1^{\ell-1} = -\pi + \sqrt{\frac{2}{\beta R_{\text{cut}}}} \frac{\ell}{\kappa} \,. \tag{B.7}$$

In the second integral, we have $(\ell+\frac{1}{2})^2 \ll \kappa^2 R^2$, such that we can approximate

$$I_2^\ell \approx \kappa \int_{R_{\text{cut}}}^{\infty} \mathrm{d}R \sqrt{1 + \frac{2\beta}{R} e^{-R}} - \frac{(\ell+1/2)^2}{2\kappa^2} \frac{1}{\sqrt{1 + \frac{2\beta}{R} e^{-R}} R^2} \,. \tag{B.8}$$

We then find

$$I_2^\ell - I_2^{\ell-1} \approx -\frac{\ell}{\kappa} \int_{R_{\text{cut}}}^{\infty} \mathrm{d}R \frac{1}{\sqrt{1 + 2\beta e^{-R}/R} R^2} \,. \tag{B.9}$$

To solve this integral, we again split it into two parts, separated at $R = R_\mathrm{t}$ defined by $2\beta e^{-R_\mathrm{t}}/R_\mathrm{t} = 1$, which can equivalently be written as $R_\mathrm{t} = W(2\beta)$:

$$I_2^\ell - I_2^{\ell-1} \approx -\frac{\ell}{\kappa}\int_{R_\mathrm{cut}}^{R_\mathrm{t}} \mathrm{d}R \frac{1}{\sqrt{1+\frac{2\beta}{R}e^{-R}}R^2} - \frac{\ell}{\kappa}\int_{R_\mathrm{t}}^{\infty} \mathrm{d}R \frac{1}{\sqrt{1+\frac{2\beta}{R}e^{-R}}R^2} \tag{B.10}$$

$$\approx -\frac{\ell}{\kappa}\int_{R_\mathrm{cut}}^{R_\mathrm{t}} \mathrm{d}R \frac{1}{\sqrt{2\beta e^{-R}}R^{3/2}} - \frac{\ell}{\kappa}\int_{R_\mathrm{t}}^{\infty} \mathrm{d}R \frac{1}{R^2} \tag{B.11}$$

$$\approx -\frac{\ell}{\kappa}\left[\sqrt{\frac{2}{R_\mathrm{cut}\beta}} - \sqrt{\frac{2e^{R_\mathrm{t}}}{R_\mathrm{t}\beta}} + \sqrt{\frac{\pi}{\beta}}\mathrm{erfi}(\sqrt{R_\mathrm{t}/2}) + \frac{1}{R_\mathrm{t}}\right] , \tag{B.12}$$

where $\mathrm{erfi}(x)$ denotes the imaginary error function. For $R_\mathrm{t} \gg 1$ we can approximate

$$\sqrt{\pi}\mathrm{erfi}\left(\sqrt{R_\mathrm{t}/2}\right) \approx \sqrt{\frac{2}{R_\mathrm{t}}}e^{R_\mathrm{t}/2}\left(1+\frac{1}{R_\mathrm{t}}\right) . \tag{B.13}$$

Now we make use of the defining property of $R_\mathrm{t}$ to substitute $e^{R_\mathrm{t}} = 2\beta/R_\mathrm{t}$ and obtain

$$I_2^\ell - I_2^{\ell-1} \approx -\frac{\ell}{\kappa}\left[\sqrt{\frac{2}{R_\mathrm{cut}\beta}} + \frac{R_\mathrm{t}+2}{R_\mathrm{t}^2}\right] . \tag{B.14}$$

As expected, the dependence on $R_\mathrm{cut}$ drops out when combining $I_1$ and $I_2$, giving

$$I^\ell - I^{\ell-1} = -\pi - \frac{\ell}{\kappa}\frac{W(2\beta)+2}{W(2\beta)^2} \equiv -\pi - \frac{\ell}{\kappa}\gamma(\beta) . \tag{B.15}$$

Adding $\pi/2$ following Eq. (6.31) yields Eq. (6.68).

# Bibliography


[1] Saniya Heeba and Felix Kahlhoefer. "Probing the freeze-in mechanism in dark matter models with U(1)' gauge extensions". In: *Phys. Rev. D* 101.3 (2020), p. 035043. DOI: 10.1103/PhysRevD.101.035043. arXiv: 1908.09834 [hep-ph].

[2] Brian Colquhoun et al. "Semiclassical regime for dark matter self-interactions". In: *Phys. Rev. D* 103.3 (2021), p. 035006. DOI: 10.1103/PhysRevD.103.035006. arXiv: 2011.04679 [hep-ph].

[3] Elias Bernreuther, Saniya Heeba, and Felix Kahlhoefer. "Resonant sub-GeV Dirac dark matter". In: *JCAP* 03 (2021), p. 040. DOI: 10.1088/1475-7516/2021/03/040. arXiv: 2010.14522 [hep-ph].

[4] Torsten Bringmann et al. "How to freeze-in scalar singlets: A closer look". In Prep (2021).

[5] Y. Akrami et al. "Planck 2018 results. I. Overview and the cosmological legacy of Planck". In: (2018). arXiv: 1807.06205 [astro-ph.CO].

[6] Gianfranco Bertone, Dan Hooper, and Joseph Silk. "Particle dark matter: Evidence, candidates and constraints". In: *Phys. Rept.* 405 (2005), pp. 279–390. DOI: 10.1016/j.physrep.2004.08.031. arXiv: hep-ph/0404175.

[7] Gianfranco Bertone et al. "Gravitational wave probes of dark matter: challenges and opportunities". In: *SciPost Phys. Core* 3 (2020), p. 007. DOI: 10.21468/SciPostPhysCore.3.2.007. arXiv: 1907.10610 [astro-ph.CO].

[8] Rebecca K. Leane and Juri Smirnov. "Exoplanets as Sub-GeV Dark Matter Detectors". In: *Phys. Rev. Lett.* 126.16 (2021), p. 161101. DOI: 10.1103/PhysRevLett.126.161101. arXiv: 2010.00015 [hep-ph].

[9] Michael E. Peskin and Daniel V. Schroeder. *An Introduction to quantum field theory*. Reading, USA: Addison-Wesley, 1995. ISBN: 978-0-201-50397-5.

[10] Mariano Quiros. "Finite temperature field theory and phase transitions". In: *ICTP Summer School in High-Energy Physics and Cosmology*. Jan. 1999. arXiv: hep-ph/9901312.

[11] Ashok K. Das. *Finite Temperature Field Theory*. New York: World Scientific, 1997. ISBN: 978-981-02-2856-9, 978-981-4498-23-4.

[12] Daniel Baumann. *Cosmology, Lecture Notes*. URL: http://cosmology.amsterdam/education/cosmology/.

[13] Mikko Laine and Aleksi Vuorinen. "Basics of Thermal Field Theory". In: *Lecture Notes in Physics* (2016). ISSN: 1616-6361. DOI: 10.1007/978-3-319-31933-9. URL: http://dx.doi.org/10.1007/978-3-319-31933-9.

[14] C. Prescod-Weinstein. *The Disordered Cosmos: A Journey into Dark Matter, Spacetime, and Dreams Deferred*. PublicAffairs, 2021. ISBN: 9781541724693. URL: https://books.google.de/books?id=e4rvDwAAQBAJ.

[15] P. A. Zyla et al. "Review of Particle Physics". In: *PTEP* 2020.8 (2020), p. 083C01. DOI: 10.1093/ptep/ptaa104.

[16] William J. Marciano and Heinz Pagels. "Quantum Chromodynamics: A Review". In: *Phys. Rept.* 36 (1978), p. 137. DOI: 10.1016/0370-1573(78)90208-9.

[17] A Pich. "Chiral perturbation theory". In: *Reports on Progress in Physics* 58.6 (1995), 563–609. ISSN: 1361-6633. DOI: 10.1088/0034-4885/58/6/001. URL: http://dx.doi.org/10.1088/0034-4885/58/6/001.

[18] Chanda Prescod-Weinstein. "Making Black Women Scientists under White Empiricism: The Racialization of Epistemology in Physics". In: *Signs: Journal of Women in Culture and Society* 45.2 (2020), 421–447. DOI: 10.1086/704991. URL: https://doi.org/10.1086/704991.

[19] Eric Braaten and Daniel Segel. "Neutrino energy loss from the plasma process at all temperatures and densities". In: *Phys. Rev. D* 48 (1993), pp. 1478–1491. DOI: 10.1103/PhysRevD.48.1478. arXiv: hep-ph/9302213.

[20] Mikko Laine and Aleksi Vuorinen. *Basics of Thermal Field Theory*. Vol. 925. Springer, 2016. DOI: 10.1007/978-3-319-31933-9. arXiv: 1701.01554 [hep-ph].

[21] André Peshier, Klaus Schertler, and Markus H. Thoma. "One-Loop Self Energies at Finite Temperature". In: *Annals of Physics* 266.1 (1998), 162–177. ISSN: 0003-4916. DOI: 10.1006/aphy.1997.5781. URL: http://dx.doi.org/10.1006/aphy.1997.5781.

[22] MARKUS H. THOMA. "APPLICATIONS OF HIGH-TEMPERATURE FIELD THEORY TO HEAVY-ION COLLISIONS". In: *Quark-Gluon Plasma 2* (1995), 51–134. DOI: 10.1142/9789812830661_0002. URL: http://dx.doi.org/10.1142/9789812830661_0002.

[23] Vyacheslav S. Rychkov and Alessandro Strumia. "Thermal production of gravitinos". In: *Phys. Rev. D* 75 (2007), p. 075011. DOI: 10.1103/PhysRevD.75.075011. arXiv: hep-ph/0701104.

[24] Per Elmfors, Kari Enqvist, and Iiro Vilja. "Thermalization of the Higgs field at the electroweak phase transition". In: *Nuclear Physics B* 412.1-2 (1994), 459–476. ISSN: 0550-3213. DOI: 10.1016/0550-3213(94)90512-6. URL: http://dx.doi.org/10.1016/0550-3213(94)90512-6.

[25] N. Aghanim et al. "Planck 2018 results. VI. Cosmological parameters". In: *Astron. Astrophys.* 641 (2020), A6. DOI: 10.1051/0004-6361/201833910. arXiv: 1807.06209 [astro-ph.CO].

[26] Edward W. Kolb and Michael S. Turner. *The Early Universe*. Vol. 69. 1990. ISBN: 978-0-201-62674-2.

[27] Andrei D. Linde. *Particle physics and inflationary cosmology*. Vol. 5. 1990. arXiv: hep-th/0503203.

[28] V. A. Kuzmin, V. A. Rubakov, and M. E. Shaposhnikov. "On the Anomalous Electroweak Baryon Number Nonconservation in the Early Universe". In: *Phys. Lett. B* 155 (1985), p. 36. DOI: 10.1016/0370-2693(85)91028-7.

[29] Thomas Konstandin and Geraldine Servant. "Natural Cold Baryogenesis from Strongly Interacting Electroweak Symmetry Breaking". In: *JCAP* 07 (2011), p. 024. DOI: 10.1088/1475-7516/2011/07/024. arXiv: 1104.4793 [hep-ph].

[30] S. Gariazzo, P. F. de Salas, and S. Pastor. "Thermalisation of sterile neutrinos in the early Universe in the 3+1 scheme with full mixing matrix". In: *JCAP* 07 (2019), p. 014. DOI: 10.1088/1475-7516/2019/07/014. arXiv: 1905.11290 [astro-ph.CO].

[31] F. Zwicky. "On the Masses of Nebulae and of Clusters of Nebulae". In: *Astrophys. J.* 86 (Oct. 1937), p. 217. DOI: 10.1086/143864.

[32] Sinclair Smith. "The Mass of the Virgo Cluster". In: *Astrophys. J.* 83 (1936), pp. 23–30. DOI: 10.1086/143697.

[33] V. C. Rubin, N. Thonnard, and W. K. Ford Jr. "Rotational properties of 21 SC galaxies with a large range of luminosities and radii, from NGC 4605 /R = 4kpc/ to UGC 2885 /R = 122 kpc/". In: *Astrophys. J.* 238 (1980), p. 471. DOI: 10.1086/158003.

[34] Gianfranco Bertone and Dan Hooper. "History of dark matter". In: *Reviews of Modern Physics* 90.4 (2018). ISSN: 1539-0756. DOI: 10.1103/revmodphys.90.045002. URL: http://dx.doi.org/10.1103/RevModPhys.90.045002.

[35] Arno A. Penzias and Robert Woodrow Wilson. "A Measurement of excess antenna temperature at 4080-Mc/s". In: *Astrophys. J.* 142 (1965), pp. 419–421. DOI: 10.1086/148307.

[36] Wayne Hu. "Concepts in CMB anisotropy formation". In: *Lect. Notes Phys.* 470 (1996), p. 207. DOI: 10.1007/BFb0102588. arXiv: astro-ph/9511130 [astro-ph].

[37] Matthias Bartelmann. "Gravitational Lensing". In: *Class. Quant. Grav.* 27 (2010), p. 233001. DOI: 10.1088/0264-9381/27/23/233001. arXiv: 1010.3829 [astro-ph.CO].

[38] Douglas Clowe, Anthony Gonzalez, and Maxim Markevitch. "Weak lensing mass reconstruction of the interacting cluster 1E0657-558: Direct evidence for the existence of dark matter". In: *Astrophys. J.* 604 (2004), pp. 596–603. DOI: 10.1086/381970. arXiv: astro-ph/0312273 [astro-ph].

[39] Joel R. Primack. "Dark matter and structure formation". In: *Midrasha Mathematicae in Jerusalem: Winter School in Dynamical Systems Jerusalem, Israel, January 12-17, 1997*. 1997. arXiv: astro-ph/9707285 [astro-ph].

[40] Robert H. Sanders and Stacy S. McGaugh. "Modified Newtonian dynamics as an alternative to dark matter". In: *Ann. Rev. Astron. Astrophys.* 40 (2002), pp. 263–317. DOI: 10.1146/annurev.astro.40.060401.093923. arXiv: astro-ph/0204521.

[41] Bernard Carr and Florian Kuhnel. "Primordial Black Holes as Dark Matter: Recent Developments". In: *Ann. Rev. Nucl. Part. Sci.* 70 (2020), pp. 355–394. DOI: 10.1146/annurev-nucl-050520-125911. arXiv: 2006.02838 [astro-ph.CO].

[42] Stefano Profumo. *An Introduction to Particle Dark Matter*. World Scientific, 2017. ISBN: 978-1-78634-000-9, 978-1-78634-001-6, 978-1-78634-001-6. DOI: 10.1142/q0001.

[43] Scott Tremaine and James E. Gunn. "Dynamical Role of Light Neutral Leptons in Cosmology". In: *Phys. Rev. Lett.* 42 (6 1979), pp. 407–410. DOI: 10.1103/PhysRevLett.42.407. URL: https://link.aps.org/doi/10.1103/PhysRevLett.42.407.

[44] James Alvey et al. "New constraints on the mass of fermionic dark matter from dwarf spheroidal galaxies". In: *Mon. Not. Roy. Astron. Soc.* 501.1 (2021), pp. 1188–1201. DOI: 10.1093/mnras/staa3640. arXiv: 2010.03572 [hep-ph].

[45] Takeshi Kobayashi et al. "Lyman-$\alpha$ constraints on ultralight scalar dark matter: Implications for the early and late universe". In: *Phys. Rev. D* 96.12 (2017), p. 123514. DOI: 10.1103/PhysRevD.96.123514. arXiv: 1708.00015 [astro-ph.CO].

[46] Eric Armengaud et al. "Constraining the mass of light bosonic dark matter using SDSS Lyman-$\alpha$ forest". In: *Mon. Not. Roy. Astron. Soc.* 471.4 (2017), pp. 4606–4614. DOI: 10.1093/mnras/stx1870. arXiv: 1703.09126 [astro-ph.CO].

[47] Edward W. Kolb, Daniel J. H. Chung, and Antonio Riotto. "WIMPzillas!" In: *AIP Conf. Proc.* 484.1 (1999). Ed. by H. Falomir, R. E. Gamboa Saravi, and F. A. Schaposnik, pp. 91–105. DOI: 10.1063/1.59655. arXiv: hep-ph/9810361.

[48] Lawrence J. Hall et al. "Freeze-In Production of FIMP Dark Matter". In: *JHEP* 03 (2010), p. 080. DOI: 10.1007/JHEP03(2010)080. arXiv: 0911.1120 [hep-ph].

[49] Xiaoyong Chu, Thomas Hambye, and Michel H.G Tytgat. "The four basic ways of creating dark matter through a portal". In: *Journal of Cosmology and Astroparticle Physics* 2012.05 (2012), 034–034. ISSN: 1475-7516. DOI: 10.1088/1475-7516/2012/05/034. URL: http://dx.doi.org/10.1088/1475-7516/2012/05/034.

[50] Nicolás Bernal et al. "The Dawn of FIMP Dark Matter: A Review of Models and Constraints". In: *Int. J. Mod. Phys. A* 32.27 (2017), p. 1730023. DOI: 10.1142/S0217751X1730023X. arXiv: 1706.07442 [hep-ph].

[51] Paolo Gondolo and Graciela Gelmini. "Cosmic abundances of stable particles: Improved analysis". In: *Nucl. Phys. B* 360 (1991), pp. 145–179. DOI: 10.1016/0550-3213(91)90438-4.

[52] Kim Griest and David Seckel. "Three exceptions in the calculation of relic abundances". In: *Phys. Rev. D* 43 (1991), pp. 3191–3203. DOI: 10.1103/PhysRevD.43.3191.

[53] Jonathan L. Feng and Jordan Smolinsky. "Impact of a resonance on thermal targets for invisible dark photon searches". In: *Physical Review D* 96.9 (2017). ISSN: 2470-0029. DOI: 10.1103/physrevd.96.095022. URL: http://dx.doi.org/10.1103/PhysRevD.96.095022.

[54] Elias Bernreuther et al. "Strongly interacting dark sectors in the early Universe and at the LHC through a simplified portal". In: *JHEP* 01 (2020), p. 162. DOI: 10.1007/JHEP01(2020)162. arXiv: 1907.04346 [hep-ph].

[55] Michael J. Baker and Andrea Thamm. "Leptonic WIMP Coannihilation and the Current Dark Matter Search Strategy". In: *JHEP* 10 (2018), p. 187. DOI: 10.1007/JHEP10(2018)187. arXiv: 1806.07896 [hep-ph].

[56] Geneviève Bélanger et al. "micrOMEGAs5.0 : Freeze-in". In: *Comput. Phys. Commun.* 231 (2018), pp. 173–186. DOI: 10.1016/j.cpc.2018.04.027. arXiv: 1801.03509 [hep-ph].

[57] Torsten Bringmann et al. "DarkSUSY 6 : An Advanced Tool to Compute Dark Matter Properties Numerically". In: *JCAP* 07 (2018), p. 033. DOI: 10.1088/1475-7516/2018/07/033. arXiv: 1802.03399 [hep-ph].

[58] Giorgio Arcadi et al. "Real Scalar Dark Matter: Relativistic Treatment". In: *JHEP* 08 (2019), p. 050. DOI: 10.1007/JHEP08(2019)050. arXiv: 1906.07659 [hep-ph].

[59] Oleg Lebedev and Takashi Toma. "Relativistic Freeze-in". In: *Phys. Lett. B* 798 (2019), p. 134961. DOI: 10.1016/j.physletb.2019.134961. arXiv: 1908.05491 [hep-ph].

[60] Nicolás Bernal et al. "Production regimes for Self-Interacting Dark Matter". In: *Journal of Cosmology and Astroparticle Physics* 2016.03 (2016), 018–018. ISSN: 1475-7516. DOI: 10.1088/1475-7516/2016/03/018. URL: http://dx.doi.org/10.1088/1475-7516/2016/03/018.

[61] Saniya Heeba, Felix Kahlhoefer, and Patrick Stöcker. "Freeze-in production of decaying dark matter in five steps". In: *JCAP* 11 (2018), p. 048. DOI: 10.1088/1475-7516/2018/11/048. arXiv: 1809.04849 [hep-ph].

[62] Eric D. Carlson, Marie E. Machacek, and Lawrence J. Hall. "Self-interacting dark matter". In: *Astrophys. J.* 398 (1992), pp. 43–52. DOI: 10.1086/171833.

[63] Yonit Hochberg et al. "Model for Thermal Relic Dark Matter of Strongly Interacting Massive Particles". In: *Phys. Rev. Lett.* 115.2 (2015), p. 021301. DOI: 10.1103/PhysRevLett.115.021301. arXiv: 1411.3727 [hep-ph].

[64] Eric Kuflik et al. "Elastically Decoupling Dark Matter". In: *Phys. Rev. Lett.* 116.22 (2016), p. 221302. DOI: 10.1103/PhysRevLett.116.221302. arXiv: 1512.04545 [hep-ph].

[65] Nicolás Bernal and Óscar Zapata. "Self-interacting Dark Matter from Primordial Black Holes". In: *JCAP* 03 (2021), p. 007. DOI: 10.1088/1475-7516/2021/03/007. arXiv: 2010.09725 [hep-ph].

[66] Nashwan Sabti et al. "Refined Bounds on MeV-scale Thermal Dark Sectors from BBN and the CMB". In: *JCAP* 01 (2020), p. 004. DOI: 10.1088/1475-7516/2020/01/004. arXiv: 1910.01649 [hep-ph].

[67] Paul Frederik Depta et al. "BBN constraints on the annihilation of MeV-scale dark matter". In: *JCAP* 04 (2019), p. 029. DOI: 10.1088/1475-7516/2019/04/029. arXiv: 1901.06944 [hep-ph].

[68] Janina J. Renk et al. "CosmoBit: A GAMBIT module for computing cosmological observables and likelihoods". In: *JCAP* 02 (2021), p. 022. DOI: 10.1088/1475-7516/2021/02/022. arXiv: 2009.03286 [astro-ph.CO].

[69] Tracy R. Slatyer. "Indirect dark matter signatures in the cosmic dark ages. I. Generalizing the bound ons-wave dark matter annihilation from Planck results". In: *Physical Review D* 93.2 (2016). ISSN: 2470-0029. DOI: 10.1103/physrevd.93.023527. URL: http://dx.doi.org/10.1103/PhysRevD.93.023527.

[70] Marco Cirelli et al. "PPPC 4 DM ID: a poor particle physicist cookbook for dark matter indirect detection". In: *Journal of Cosmology and Astroparticle Physics* 2011.03 (2011), 051–051. ISSN: 1475-7516. DOI: 10.1088/1475-7516/2011/03/051. URL: http://dx.doi.org/10.1088/1475-7516/2011/03/051.

[71] Peter Reimitz. "MeV astronomy with Herwig?" In: *PoS* TOOLS2020 (2021), p. 008. DOI: 10.22323/1.392.0008. arXiv: 2102.00041 [hep-ph].

[72] Tilman Plehn, Peter Reimitz, and Peter Richardson. "Hadronic Footprint of GeV-Mass Dark Matter". In: *SciPost Phys.* 8 (2020), p. 092. DOI: 10.21468/SciPostPhys.8.6.092. arXiv: 1911.11147 [hep-ph].

[73] Adam Coogan, Logan Morrison, and Stefano Profumo. "Hazma: a python toolkit for studying indirect detection of sub-GeV dark matter". In: *Journal of Cosmology and Astroparticle Physics* 2020.01 (2020), 056–056. ISSN: 1475-7516. DOI: 10.1088/1475-7516/2020/01/056. URL: http://dx.doi.org/10.1088/1475-7516/2020/01/056.

[74] Cora Dvorkin, Tongyan Lin, and Katelin Schutz. *The cosmology of sub-MeV dark matter freeze-in*. 2020. arXiv: 2011.08186 [astro-ph.CO].

[75] Jonathan L. Feng. "Dark Matter Candidates from Particle Physics and Methods of Detection". In: *Ann. Rev. Astron. Astrophys.* 48 (2010), pp. 495–545. DOI: 10.1146/annurev-astro-082708-101659. arXiv: 1003.0904 [astro-ph.CO].

[76] Gerard Jungman, Marc Kamionkowski, and Kim Griest. "Supersymmetric dark matter". In: *Phys. Rept.* 267 (1996), pp. 195–373. DOI: 10.1016/0370-1573(95)00058-5. arXiv: hep-ph/9506380.

[77] Alexey Boyarsky, Oleg Ruchayskiy, and Mikhail Shaposhnikov. "The Role of sterile neutrinos in cosmology and astrophysics". In: *Ann. Rev. Nucl. Part. Sci.* 59 (2009), pp. 191–214. DOI: 10.1146/annurev.nucl.010909.083654. arXiv: 0901.0011 [hep-ph].

[78] David J. E. Marsh. "Axion Cosmology". In: *Phys. Rept.* 643 (2016), pp. 1–79. DOI: 10.1016/j.physrep.2016.06.005. arXiv: 1510.07633 [astro-ph.CO].

[79] Bob Holdom. "Two U(1)'s and Epsilon Charge Shifts". In: *Phys. Lett. B* 166 (1986), pp. 196–198. DOI: 10.1016/0370-2693(86)91377-8.

[80] Jared A. Evans, Stefania Gori, and Jessie Shelton. "Looking for the WIMP next door". In: *Journal of High Energy Physics* 2018.2 (2018). ISSN: 1029-8479. DOI: 10.1007/jhep02(2018)100. URL: http://dx.doi.org/10.1007/JHEP02(2018)100.

[81] Giorgio Arcadi, Abdelhak Djouadi, and Martti Raidal. "Dark Matter through the Higgs portal". In: *Phys. Rept.* 842 (2020), pp. 1–180. DOI: 10.1016/j.physrep.2019.11.003. arXiv: 1903.03616 [hep-ph].

[82] Joshua Berger, Karsten Jedamzik, and Devin G.E. Walker. "Cosmological constraints on decoupled dark photons and dark Higgs". In: *Journal of Cosmology and Astroparticle Physics* 2016.11 (2016), 032–032. ISSN: 1475-7516. DOI: 10.1088/1475-7516/2016/11/032. URL: http://dx.doi.org/10.1088/1475-7516/2016/11/032.

[83] Brian Patt and Frank Wilczek. "Higgs-field portal into hidden sectors". In: (May 2006). arXiv: hep-ph/0605188.

[84] Martin Bauer, Patrick Foldenauer, and Joerg Jaeckel. "Hunting All the Hidden Photons". In: *JHEP* 07 (2018), p. 094. DOI: 10.1007/JHEP07(2018)094. arXiv: 1803.05466 [hep-ph].

[85] J. Beacham et al. "Physics Beyond Colliders at CERN: Beyond the Standard Model Working Group Report". In: *J. Phys. G* 47.1 (2020), p. 010501. DOI: 10.1088/1361-6471/ab4cd2. arXiv: 1901.09966 [hep-ex].

[86] Francesco D'Eramo, Bradley J. Kavanagh, and Paolo Panci. "Probing Leptophilic Dark Sectors with Hadronic Processes". In: *Phys. Lett. B* 771 (2017), pp. 339–348. DOI: 10.1016/j.physletb.2017.05.063. arXiv: 1702.00016 [hep-ph].

[87] Philip Ilten et al. "Serendipity in dark photon searches". In: *JHEP* 06 (2018), p. 004. DOI: 10.1007/JHEP06(2018)004. arXiv: 1801.04847 [hep-ph].

[88] Peter Athron et al. "Status of the scalar singlet dark matter model". In: *Eur. Phys. J. C* 77.8 (2017), p. 568. DOI: 10.1140/epjc/s10052-017-5113-1. arXiv: 1705.07931 [hep-ph].

[89] Sergey Alekhin et al. "A facility to Search for Hidden Particles at the CERN SPS: the SHiP physics case". In: *Rept. Prog. Phys.* 79.12 (2016), p. 124201. DOI: 10.1088/0034-4885/79/12/124201. arXiv: 1504.04855 [hep-ph].

[90] Y. Mambrini. "Higgs searches and singlet scalar dark matter: Combined constraints from XENON 100 and the LHC". In: *Phys. Rev. D* 84 (2011), p. 115017. DOI: 10.1103/PhysRevD.84.115017. arXiv: 1108.0671 [hep-ph].

[91] Xiao-Gang He and Jusak Tandean. "Hidden Higgs Boson at the LHC and Light Dark Matter Searches". In: *Phys. Rev. D* 84 (2011), p. 075018. DOI: 10.1103/PhysRevD.84.075018. arXiv: 1109.1277 [hep-ph].

[92] Abdelhak Djouadi et al. "Implications of LHC searches for Higgs–portal dark matter". In: *Phys. Lett. B* 709 (2012), pp. 65–69. DOI: 10.1016/j.physletb.2012.01.062. arXiv: 1112.3299 [hep-ph].

[93] Sean Tulin and Hai-Bo Yu. "Dark Matter Self-interactions and Small Scale Structure". In: *Phys. Rept.* 730 (2018), pp. 1–57. DOI: 10.1016/j.physrep.2017.11.004. arXiv: 1705.02358 [hep-ph].

[94] Carlos E. Yaguna. "The Singlet Scalar as FIMP Dark Matter". In: *JHEP* 08 (2011), p. 060. DOI: 10.1007/JHEP08(2011)060. arXiv: 1105.1654 [hep-ph].

[95] James M. Cline et al. "Update on scalar singlet dark matter". In: *Physical Review D* 88.5 (2013). ISSN: 1550-2368. DOI: 10.1103/physrevd.88.055025. URL: http://dx.doi.org/10.1103/PhysRevD.88.055025.

[96] Michael Klasen and Carlos E Yaguna. "Warm and cold fermionic dark matter via freeze-in". In: *Journal of Cosmology and Astroparticle Physics* 2013.11 (2013), 039–039. ISSN: 1475-7516. DOI: 10.1088/1475-7516/2013/11/039. URL: http://dx.doi.org/10.1088/1475-7516/2013/11/039.

[97] Taeil Hur and P. Ko. "Scale Invariant Extension of the Standard Model with a Strongly Interacting Hidden Sector". In: *Physical Review Letters* 106.14 (2011). ISSN: 1079-7114. DOI: 10.1103/physrevlett.106.141802. URL: http://dx.doi.org/10.1103/PhysRevLett.106.141802.

[98] Matti Heikinheimo et al. "Erratum: Observational constraints on decoupled hidden sectors [Phys. Rev. D 94, 063506 (2016)]". In: *Physical Review D* 96.10 (2017). ISSN: 2470-0029. DOI: 10.1103/physrevd.96.109902. URL: http://dx.doi.org/10.1103/PhysRevD.96.109902.

[99] Peter Athron et al. "Global analyses of Higgs portal singlet dark matter models using GAMBIT". In: *Eur. Phys. J. C* 79.1 (2019), p. 38. DOI: 10.1140/epjc/s10052-018-6513-6. arXiv: 1808.10465 [hep-ph].

[100] Lawrence Lee et al. "Collider Searches for Long-Lived Particles Beyond the Standard Model". In: *Prog. Part. Nucl. Phys.* 106 (2019), pp. 210–255. DOI: 10.1016/j.ppnp.2019.02.006. arXiv: 1810.12602 [hep-ph].

[101] Anthony Fradette et al. "Cosmological beam dump: constraints on dark scalars mixed with the Higgs boson". In: *Phys. Rev. D* 99.7 (2019), p. 075004. DOI: 10.1103/PhysRevD.99.075004. arXiv: 1812.07585 [hep-ph].

[102] Vanda Silveira and A. Zee. "SCALAR PHANTOMS". In: *Phys. Lett. B* 161 (1985), pp. 136–140. DOI: 10.1016/0370-2693(85)90624-0.

[103] John McDonald. "Gauge singlet scalars as cold dark matter". In: *Phys. Rev. D* 50 (1994), pp. 3637–3649. DOI: 10.1103/PhysRevD.50.3637. arXiv: hep-ph/0702143.

[104] C. P. Burgess, Maxim Pospelov, and Tonnis ter Veldhuis. "The Minimal model of non-baryonic dark matter: A Singlet scalar". In: *Nucl. Phys. B* 619 (2001), pp. 709–728. DOI: 10.1016/S0550-3213(01)00513-2. arXiv: hep-ph/0011335.

[105] Abdelhak Djouadi. "The Anatomy of electro-weak symmetry breaking. I: The Higgs boson in the standard model". In: *Phys. Rept.* 457 (2008), pp. 1–216. DOI: 10.1016/j.physrep.2007.10.004. arXiv: hep-ph/0503172.

[106] K. G. Chetyrkin, Johann H. Kuhn, and A. K. Kwiatkowski. "Perturbative QCD corrections to the Z boson width and the Higgs decay rate". In: *29th Rencontres de Moriond: QCD and High-energy Hadronic Interactions*. July 1994. arXiv: hep-ph/9407271.

[107] A. Djouadi, J. Kalinowski, and M. Spira. "HDECAY: A Program for Higgs boson decays in the standard model and its supersymmetric extension". In: *Comput. Phys. Commun.* 108 (1998), pp. 56–74. DOI: 10.1016/S0010-4655(97)00123-9. arXiv: hep-ph/9704448.

[108] Abdelhak Djouadi et al. "HDECAY: Twenty$_{++}$ years after". In: *Comput. Phys. Commun.* 238 (2019), pp. 214–231. DOI: 10.1016/j.cpc.2018.12.010. arXiv: 1801.09506 [hep-ph].

[109] Valentin V. Khoze and Michael Spannowsky. "Higgsplosion: Solving the hierarchy problem via rapid decays of heavy states into multiple Higgs bosons". In: *Nucl. Phys. B* 926 (2018), pp. 95–111. DOI: 10.1016/j.nuclphysb.2017.11.002. arXiv: 1704.03447 [hep-ph].

[110] Kim Griest and Marc Kamionkowski. "Unitarity limits on the mass and radius of dark-matter particles". In: *Phys. Rev. Lett.* 64 (6 1990), pp. 615–618. DOI: 10.1103/PhysRevLett.64.615. URL: https://link.aps.org/doi/10.1103/PhysRevLett.64.615.

[111] G. Cynolter, E. Lendvai, and G. Pocsik. "Note on unitarity constraints in a model for a singlet scalar dark matter candidate". In: *Acta Phys. Polon. B* 36 (2005), pp. 827–832. arXiv: hep-ph/0410102.

[112] Martin Wolfgang Winkler. "Decay and detection of a light scalar boson mixing with the Higgs boson". In: *Phys. Rev. D* 99.1 (2019), p. 015018. DOI: 10.1103/PhysRevD.99.015018. arXiv: 1809.01876 [hep-ph].

[113] Oleg Lebedev. "The Higgs Portal to Cosmology". In: (Apr. 2021). arXiv: 2104.03342 [hep-ph].

[114] "Combination of searches for invisible Higgs boson decays with the ATLAS experiment". In: (Oct. 2020).

[115] Peter Galison and Aneesh Manohar. "Two Z's or not two Z's?" In: *Physics Letters B* 136.4 (1984), pp. 279–283. ISSN: 0370-2693. DOI: https://doi.org/10.1016/0370-2693(84)91161-4. URL: https://www.sciencedirect.com/science/article/pii/0370269384911614.

[116] Robert Foot. "New Physics From Electric Charge Quantization?" In: *Mod. Phys. Lett. A* 6 (1991), pp. 527–530. DOI: 10.1142/S0217732391000543.

[117] Julian Heeck and Werner Rodejohann. "Gauged $L_\mu - L_\tau$ symmetry at the electroweak scale". In: *Physical Review D* 84.7 (2011). ISSN: 1550-2368. DOI: 10.1103/physrevd.84.075007. URL: http://dx.doi.org/10.1103/PhysRevD.84.075007.

[118] Julian Heeck. "Unbroken B – L symmetry". In: *Physics Letters B* 739 (2014), 256–262. ISSN: 0370-2693. DOI: 10.1016/j.physletb.2014.10.067. URL: http://dx.doi.org/10.1016/j.physletb.2014.10.067.

[119] Xiao-Gang He et al. "Simplest $Z^{'}$ model". In: *Phys. Rev. D* 44 (7 1991), pp. 2118–2132. DOI: 10.1103/PhysRevD.44.2118. URL: https://link.aps.org/doi/10.1103/PhysRevD.44.2118.

[120] Michael Duerr and Pavel Fileviez Perez. "Baryonic Dark Matter". In: *Phys. Lett. B* 732 (2014), pp. 101–104. DOI: 10.1016/j.physletb.2014.03.011. arXiv: 1309.3970 [hep-ph].

[121] Haipeng An, Maxim Pospelov, and Josef Pradler. "Dark Matter Detectors as Dark Photon Helioscopes". In: *Phys. Rev. Lett.* 111 (2013), p. 041302. DOI: 10.1103/PhysRevLett.111.041302. arXiv: 1304.3461 [hep-ph].

[122] Daniel Feldman, Zuowei Liu, and Pran Nath. "The Stueckelberg Z-prime Extension with Kinetic Mixing and Milli-Charged Dark Matter From the Hidden Sector". In: *Phys. Rev. D* 75 (2007), p. 115001. DOI: 10.1103/PhysRevD.75.115001. arXiv: hep-ph/0702123.

[123] E. C. G. Stueckelberg. "Interaction forces in electrodynamics and in the field theory of nuclear forces". In: *Helv. Phys. Acta* 11 (1938), pp. 299–328.

[124] Patrick Foldenauer. "Phenomenology of Extra Abelian Gauge Symmetries". PhD thesis. U. Heidelberg (main), July 2019. DOI: 10.11588/heidok.00026777.

[125] Simon Knapen, Tongyan Lin, and Kathryn M. Zurek. "Light Dark Matter: Models and Constraints". In: *Phys. Rev. D* 96.11 (2017), p. 115021. DOI: 10.1103/PhysRevD.96.115021. arXiv: 1709.07882 [hep-ph].

[126] D. Comelli and J. R. Espinosa. "Bosonic thermal masses in supersymmetry". In: *Phys. Rev. D* 55 (1997), pp. 6253–6263. DOI: 10.1103/PhysRevD.55.6253. arXiv: hep-ph/9606438.

[127] Kunio Kaneta, Zhaofeng Kang, and Hye-Sung Lee. "Right-handed neutrino dark matter under the B-L gauge interaction". In: *JHEP* 02 (2017), p. 031. DOI: 10.1007/JHEP02(2017)031. arXiv: 1606.09317 [hep-ph].

[128] Arindam Das et al. "Freeze-in sterile neutrino dark matter in a class of U(1)′ models with inverse seesaw". In: (Apr. 2021). arXiv: 2104.13986 [hep-ph].

[129] Cora Dvorkin, Tongyan Lin, and Katelin Schutz. "Making dark matter out of light: freeze-in from plasma effects". In: *Phys. Rev. D* 99.11 (2019), p. 115009. DOI: 10.1103/PhysRevD.99.115009. arXiv: 1902.08623 [hep-ph].

[130] Paul Frederik Depta, Marco Hufnagel, and Kai Schmidt-Hoberg. "ACROPOLIS: A generiC fRamework fOr Photodisintegration Of LIght elementS". In: *JCAP* 03 (2021), p. 061. DOI: 10.1088/1475-7516/2021/03/061. arXiv: 2011.06518 [hep-ph].

[131] Joel R. Primack and David B. Cline. "Cosmology: Small Scale Issues". In: *AIP Conference Proceedings* (2009). DOI: 10.1063/1.3232194. URL: http://dx.doi.org/10.1063/1.3232194.

[132] James S. Bullock and Michael Boylan-Kolchin. "Small-Scale Challenges to the ΛCDM Paradigm". In: *Ann. Rev. Astron. Astrophys.* 55 (2017), pp. 343–387. DOI: 10.1146/annurev-astro-091916-055313. arXiv: 1707.04256 [astro-ph.CO].

[133] Manoj Kaplinghat, Sean Tulin, and Hai-Bo Yu. "Dark Matter Halos as Particle Colliders: Unified Solution to Small-Scale Structure Puzzles from Dwarfs to Clusters". In: *Phys. Rev. Lett.* 116.4 (2016), p. 041302. DOI: 10.1103/PhysRevLett.116.041302. arXiv: 1508.03339 [astro-ph.CO].

[134] Alyson M. Brooks et al. "A Baryonic Solution to the Missing Satellites Problem". In: *Astrophys. J.* 765 (2013), p. 22. DOI: 10.1088/0004-637X/765/1/22. arXiv: 1209.5394 [astro-ph.CO].

[135] Fabio Governato et al. "At the heart of the matter: the origin of bulgeless dwarf galaxies and Dark Matter cores". In: *Nature* 463 (2010), pp. 203–206. DOI: 10.1038/nature08640. arXiv: 0911.2237 [astro-ph.CO].

[136] Carlos A. Vera-Ciro et al. "Not too big, not too small: the dark halos of the dwarf spheroidals in the Milky Way". In: *Mon. Not. Roy. Astron. Soc.* 428 (2013), p. 1696. DOI: 10.1093/mnras/sts148. arXiv: 1202.6061 [astro-ph.CO].

[137] Ricardo A. Flores and Joel R. Primack. "Observational and theoretical constraints on singular dark matter halos". In: *Astrophys. J. Lett.* 427 (1994), pp. L1–4. DOI: 10.1086/187350. arXiv: astro-ph/9402004.

[138] Julio F. Navarro, Carlos S. Frenk, and Simon D. M. White. "A Universal density profile from hierarchical clustering". In: *Astrophys. J.* 490 (1997), pp. 493–508. DOI: 10.1086/304888. arXiv: astro-ph/9611107.

[139] W. J. G. de Blok. "The Core-Cusp Problem". In: *Adv. Astron.* 2010 (2010), p. 789293. DOI: 10.1155/2010/789293. arXiv: 0910.3538 [astro-ph.CO].

[140] Kyle A. Oman et al. "The unexpected diversity of dwarf galaxy rotation curves". In: *Mon. Not. Roy. Astron. Soc.* 452.4 (2015), pp. 3650–3665. DOI: 10.1093/mnras/stv1504. arXiv: 1504.01437 [astro-ph.GA].

[141] Rachel Kuzio de Naray et al. "The Case Against Warm or Self-Interacting Dark Matter as Explanations for Cores in Low Surface Brightness Galaxies". In: *Astrophys. J. Lett.* 710 (2010), p. L161. DOI: 10.1088/2041-8205/710/2/L161. arXiv: 0912.3518 [astro-ph.CO].

[142] Stacy Y. Kim, Annika H. G. Peter, and Jonathan R. Hargis. "Missing Satellites Problem: Completeness Corrections to the Number of Satellite Galaxies in the Milky Way are Consistent with Cold Dark Matter Predictions". In: *Phys. Rev. Lett.* 121.21 (2018), p. 211302. DOI: 10.1103/PhysRevLett.121.211302. arXiv: 1711.06267 [astro-ph.CO].

[143] Erik J. Tollerud et al. "Hundreds of Milky Way Satellites? Luminosity Bias in the Satellite Luminosity Function". In: *Astrophys. J.* 688 (2008), pp. 277–289. DOI: 10.1086/592102. arXiv: 0806.4381 [astro-ph].

[144] Michael Boylan-Kolchin, James S. Bullock, and Manoj Kaplinghat. "Too big to fail? The puzzling darkness of massive Milky Way subhaloes". In: *Mon. Not. Roy. Astron. Soc.* 415 (2011), p. L40. DOI: 10.1111/j.1745-3933.2011.01074.x. arXiv: 1103.0007 [astro-ph.CO].

[145] Shea Garrison-Kimmel et al. "Too Big to Fail in the Local Group". In: *Mon. Not. Roy. Astron. Soc.* 444.1 (2014), pp. 222–236. DOI: 10.1093/mnras/stu1477. arXiv: 1404.5313 [astro-ph.GA].

[146] Paul Bode, Jeremiah P. Ostriker, and Neil Turok. "Halo formation in warm dark matter models". In: *Astrophys. J.* 556 (2001), pp. 93–107. DOI: 10.1086/321541. arXiv: astro-ph/0010389.

[147] Jesper Sommer-Larsen and Alexandre Dolgov. "Formation of disk galaxies: warm dark matter and the angular momentum problem". In: *Astrophys. J.* 551 (2001), pp. 608–623. DOI: 10.1086/320211. arXiv: astro-ph/9912166.

[148] Mei-Yu Wang et al. "Cosmological simulations of decaying dark matter: implications for small-scale structure of dark matter haloes". In: *Mon. Not. Roy. Astron. Soc.* 445.1 (2014), pp. 614–629. DOI: 10.1093/mnras/stu1747. arXiv: 1406.0527 [astro-ph.CO].

[149] Sean Tulin, Hai-Bo Yu, and Kathryn M. Zurek. "Beyond Collisionless Dark Matter: Particle Physics Dynamics for Dark Matter Halo Structure". In: *Phys. Rev. D* 87.11 (2013), p. 115007. DOI: 10.1103/PhysRevD.87.115007. arXiv: 1302.3898 [hep-ph].

[150] Matthew R. Buckley and Patrick J. Fox. "Dark Matter Self-Interactions and Light Force Carriers". In: *Phys. Rev. D* 81 (2010), p. 083522. DOI: 10.1103/PhysRevD.81.083522. arXiv: 0911.3898 [hep-ph].

[151] Jonathan L. Feng, Manoj Kaplinghat, and Hai-Bo Yu. "Halo Shape and Relic Density Exclusions of Sommerfeld-Enhanced Dark Matter Explanations of Cosmic Ray Excesses". In: *Phys. Rev. Lett.* 104 (2010), p. 151301. DOI: 10.1103/PhysRevLett.104.151301. arXiv: 0911.0422 [hep-ph].

[152] Oleg Y. Gnedin and Jeremiah P. Ostriker. "Limits on collisional dark matter from elliptical galaxies in clusters". In: *Astrophys. J.* 561 (2001), p. 61. DOI: 10.1086/323211. arXiv: astro-ph/0010436.

[153] Shmuel Balberg, Stuart L. Shapiro, and Shogo Inagaki. "Selfinteracting dark matter halos and the gravothermal catastrophe". In: *Astrophys. J.* 568 (2002), pp. 475–487. DOI: 10.1086/339038. arXiv: astro-ph/0110561.

[154] Felix Kahlhoefer et al. "Colliding clusters and dark matter self-interactions". In: *Mon. Not. Roy. Astron. Soc.* 437.3 (2014), pp. 2865–2881. DOI: 10.1093/mnras/stt2097. arXiv: 1308.3419 [astro-ph.CO].

[155] Maxim Markevitch et al. "Direct constraints on the dark matter self-interaction cross-section from the merging galaxy cluster 1E0657-56". In: *Astrophys. J.* 606 (2004), pp. 819–824. DOI: 10.1086/383178. arXiv: astro-ph/0309303.

[156] C. V. Heer. *Statistical mechanics, kinetic theory, and stochastic processes*. Academic Press Inc, 1972.

[157] L. D. Landau and E. M. Lifshitz. *Quantum Mechanics: Non Relativistic Theory*. Butterworth-Heinemann, 1981. ISBN: 978-0750635394.

[158] Jonathan L. Feng, Manoj Kaplinghat, and Hai-Bo Yu. "Sommerfeld Enhancements for Thermal Relic Dark Matter". In: *Phys. Rev. D* 82 (2010), p. 083525. DOI: 10.1103/PhysRevD.82.083525. arXiv: 1005.4678 [hep-ph].

[159] Michael V. Berry and K. E. Mount. "Semiclassical approximations in wave mechanics". In: *Rept. Prog. Phys.* 35 (1972), p. 315. DOI: 10.1088/0034-4885/35/1/306.

[160] Xiaoyong Chu, Camilo Garcia-Cely, and Hitoshi Murayama. "A Practical and Consistent Parametrization of Dark Matter Self-Interactions". In: *JCAP* 06 (2020), p. 043. DOI: 10.1088/1475-7516/2020/06/043. arXiv: 1908.06067 [hep-ph].

[161] Sean Tulin, Hai-Bo Yu, and Kathryn M. Zurek. "Resonant Dark Forces and Small Scale Structure". In: *Phys. Rev. Lett.* 110.11 (2013), p. 111301. DOI: 10.1103/PhysRevLett.110.111301. arXiv: 1210.0900 [hep-ph].

[162] Rudolph E. Langer. "On the Connection Formulas and the Solutions of the Wave Equation". In: *Phys. Rev.* 51 (1937), pp. 669–676. DOI: 10.1103/PhysRev.51.669.

[163] Francis-Yan Cyr-Racine et al. "ETHOS-an effective theory of structure formation: From dark particle physics to the matter distribution of the Universe". In: *Phys. Rev. D* 93.12 (2016), p. 123527. DOI: 10.1103/PhysRevD.93.123527. arXiv: 1512.05344 [astro-ph.CO].

[164] Laura Sagunski et al. "Velocity-dependent Self-interacting Dark Matter from Groups and Clusters of Galaxies". In: *JCAP* 01 (2021), p. 024. DOI: 10.1088/1475-7516/2021/01/024. arXiv: 2006.12515 [astro-ph.CO].

[165] Tracy R. Slatyer. "Indirect Detection of Dark Matter". In: *Theoretical Advanced Study Institute in Elementary Particle Physics: Anticipating the Next Discoveries in Particle Physics*. Oct. 2017. DOI: 10.1142/9789813233348_0005. arXiv: 1710.05137 [hep-ph].

[166] Kevork N. Abazajian and Manoj Kaplinghat. "Detection of a Gamma-Ray Source in the Galactic Center Consistent with Extended Emission from Dark Matter Annihilation and Concentrated Astrophysical Emission". In: *Phys. Rev. D* 86 (2012). [Erratum:

Phys.Rev.D 87, 129902 (2013)], p. 083511. DOI: 10.1103/PhysRevD.86.083511. arXiv: 1207.6047 [astro-ph.HE].

[167] Lisa Goodenough and Dan Hooper. "Possible Evidence For Dark Matter Annihilation In The Inner Milky Way From The Fermi Gamma Ray Space Telescope". In: (Oct. 2009). arXiv: 0910.2998 [hep-ph].

[168] Jennifer M. Gaskins. "A review of indirect searches for particle dark matter". In: *Contemp. Phys.* 57.4 (2016), pp. 496–525. DOI: 10.1080/00107514.2016.1175160. arXiv: 1604.00014 [astro-ph.HE].

[169] Teresa Marrodán Undagoitia and Ludwig Rauch. "Dark matter direct-detection experiments". In: *J. Phys. G* 43.1 (2016), p. 013001. DOI: 10.1088/0954-3899/43/1/013001. arXiv: 1509.08767 [physics.ins-det].

[170] Felix Kahlhoefer. "Review of LHC Dark Matter Searches". In: *Int. J. Mod. Phys. A* 32.13 (2017), p. 1730006. DOI: 10.1142/S0217751X1730006X. arXiv: 1702.02430 [hep-ph].

[171] David G. Cerdeno and Anne M. Green. "Direct detection of WIMPs". In: (Feb. 2010). arXiv: 1002.1912 [astro-ph.CO].

[172] A. Liam Fitzpatrick et al. "The Effective Field Theory of Dark Matter Direct Detection". In: *JCAP* 02 (2013), p. 004. DOI: 10.1088/1475-7516/2013/02/004. arXiv: 1203.3542 [hep-ph].

[173] JiJi Fan, Matthew Reece, and Lian-Tao Wang. "Non-relativistic effective theory of dark matter direct detection". In: *JCAP* 11 (2010), p. 042. DOI: 10.1088/1475-7516/2010/11/042. arXiv: 1008.1591 [hep-ph].

[174] Felix Kahlhoefer and Sebastian Wild. "Studying generalised dark matter interactions with extended halo-independent methods". In: *JCAP* 10 (2016), p. 032. DOI: 10.1088/1475-7516/2016/10/032. arXiv: 1607.04418 [hep-ph].

[175] Marco Battaglieri et al. "US Cosmic Visions: New Ideas in Dark Matter 2017: Community Report". In: *U.S. Cosmic Visions: New Ideas in Dark Matter*. July 2017. arXiv: 1707.04591 [hep-ph].

[176] Marat Freytsis and Zoltan Ligeti. "On dark matter models with uniquely spin-dependent detection possibilities". In: *Phys. Rev. D* 83 (2011), p. 115009. DOI: 10.1103/PhysRevD.83.115009. arXiv: 1012.5317 [hep-ph].

[177] N. Fornengo, P. Panci, and M. Regis. "Long-range forces in direct dark matter searches". In: *Physical Review D* 84.11 (2011). ISSN: 1550-2368. DOI: 10.1103/physrevd.84.115002. URL: http://dx.doi.org/10.1103/PhysRevD.84.115002.

[178] N. Fornengo, P. Panci, and M. Regis. "Long-Range Forces in Direct Dark Matter Searches". In: *Phys. Rev. D* 84 (2011), p. 115002. DOI: 10.1103/PhysRevD.84.115002. arXiv: 1108.4661 [hep-ph].

[179] Annika H. G. Peter et al. "WIMP physics with ensembles of direct-detection experiments". In: *Phys. Dark Univ.* 5-6 (2014), pp. 45–74. DOI: 10.1016/j.dark.2014.10.006. arXiv: 1310.7039 [astro-ph.CO].

[180] E. Aprile et al. "Dark Matter Search Results from a One Ton-Year Exposure of XENON1T". In: *Phys. Rev. Lett.* 121.11 (2018), p. 111302. DOI: 10.1103/PhysRevLett.121.111302. arXiv: 1805.12562 [astro-ph.CO].

[181] R. Agnese et al. "Search for low-mass dark matter with CDMSlite using a profile likelihood fit". In: *Physical Review D* 99.6 (2019). ISSN: 2470-0029. DOI: 10.1103/physrevd.99.062001. URL: http://dx.doi.org/10.1103/PhysRevD.99.062001.

[182] E. Aprile et al. "Light Dark Matter Search with Ionization Signals in XENON1T". In: *Physical Review Letters* 123.25 (2019). ISSN: 1079-7114. DOI: 10.1103/physrevlett.123.251801. URL: http://dx.doi.org/10.1103/PhysRevLett.123.251801.

[183] A. Aguilar-Arevalo et al. "Results on low-mass weakly interacting massive particles from a 11 kg-day target exposure of DAMIC at SNOLAB". In: *Phys. Rev. Lett.* 125 (2020), p. 241803. DOI: 10.1103/PhysRevLett.125.241803. arXiv: 2007.15622 [astro-ph.CO].

[184] A.H. Abdelhameed et al. "First results from the CRESST-III low-mass dark matter program". In: *Physical Review D* 100.10 (2019). ISSN: 2470-0029. DOI: 10.1103/physrevd.100.102002. URL: http://dx.doi.org/10.1103/PhysRevD.100.102002.

[185] F. Ruppin et al. "Complementarity of dark matter detectors in light of the neutrino background". In: *Phys. Rev. D* 90 (8 2014), p. 083510. DOI: 10.1103/PhysRevD.90.083510. URL: http://link.aps.org/doi/10.1103/PhysRevD.90.083510.

[186] *Dark Matter Limit Plotter*. https://supercdms.slac.stanford.edu/dark-matter-limit-plotter.

[187] Thomas Hambye et al. "Dark matter direct detection is testing freeze-in". In: *Phys. Rev. D* 98.7 (2018), p. 075017. DOI: 10.1103/PhysRevD.98.075017. arXiv: 1807.05022 [hep-ph].

[188] Rouven Essig, Jeremy Mardon, and Tomer Volansky. "Direct Detection of Sub-GeV Dark Matter". In: *Phys. Rev. D* 85 (2012), p. 076007. DOI: 10.1103/PhysRevD.85.076007. arXiv: 1108.5383 [hep-ph].

[189] Rouven Essig, Tomer Volansky, and Tien-Tien Yu. "New Constraints and Prospects for sub-GeV Dark Matter Scattering off Electrons in Xenon". In: *Phys. Rev. D* 96.4 (2017), p. 043017. DOI: 10.1103/PhysRevD.96.043017. arXiv: 1703.00910 [hep-ph].

[190] Rouven Essig et al. "First Direct Detection Limits on sub-GeV Dark Matter from XENON10". In: *Phys. Rev. Lett.* 109 (2012), p. 021301. DOI: 10.1103/PhysRevLett.109.021301. arXiv: 1206.2644 [astro-ph.CO].

[191] Daniel Baxter, Yonatan Kahn, and Gordan Krnjaic. "Electron Ionization via Dark Matter-Electron Scattering and the Migdal Effect". In: (2019). arXiv: 1908.00012 [hep-ph].

[192] Itay M. Bloch et al. "Exploring new physics with O(keV) electron recoils in direct detection experiments". In: *JHEP* 01 (2021), p. 178. DOI: 10.1007/JHEP01(2021)178. arXiv: 2006.14521 [hep-ph].

[193] Rouven Essig et al. "Direct Detection of sub-GeV Dark Matter with Semiconductor Targets". In: *JHEP* 05 (2016), p. 046. DOI: 10.1007/JHEP05(2016)046. arXiv: 1509.01598 [hep-ph].

[194] E. Aprile et al. "Excess electronic recoil events in XENON1T". In: *Phys. Rev. D* 102.7 (2020), p. 072004. DOI: 10.1103/PhysRevD.102.072004. arXiv: 2006.09721 [hep-ex].

[195] Liron Barak et al. "SENSEI: Direct-Detection Results on sub-GeV Dark Matter from a New Skipper-CCD". In: *Phys. Rev. Lett.* 125.17 (2020), p. 171802. DOI: 10.1103/PhysRevLett.125.171802. arXiv: 2004.11378 [astro-ph.CO].

[196] E. Aprile et al. "Light Dark Matter Search with Ionization Signals in XENON1T". In: *Phys. Rev. Lett.* 123.25 (2019), p. 251801. DOI: 10.1103/PhysRevLett.123.251801. arXiv: 1907.11485 [hep-ex].

[197] Rouven Essig et al. "On the relation between Migdal effect and dark matter-electron scattering in atoms and semiconductors". In: (2019). arXiv: 1908.10881 [hep-ph].

[198] Masahiro Ibe et al. "Migdal Effect in Dark Matter Direct Detection Experiments". In: *JHEP* 03 (2018), p. 194. DOI: 10.1007/JHEP03(2018)194. arXiv: 1707.07258 [hep-ph].

[199] Matthew J. Dolan, Felix Kahlhoefer, and Christopher McCabe. "Directly detecting sub-GeV dark matter with electrons from nuclear scattering". In: *Phys. Rev. Lett.* 121.10 (2018), p. 101801. DOI: 10.1103/PhysRevLett.121.101801. arXiv: 1711.09906 [hep-ph].

[200] E. Aprile et al. "Search for Light Dark Matter Interactions Enhanced by the Migdal Effect or Bremsstrahlung in XENON1T". In: *Phys. Rev. Lett.* 123.24 (2019), p. 241803. DOI: 10.1103/PhysRevLett.123.241803. arXiv: 1907.12771 [hep-ex].

[201] Marco Fabbrichesi, Emidio Gabrielli, and Gaia Lanfranchi. "The Dark Photon". In: (May 2020). DOI: 10.1007/978-3-030-62519-1. arXiv: 2005.01515 [hep-ph].

[202] Philip Ilten et al. "Serendipity in dark photon searches". In: *Journal of High Energy Physics* 2018.6 (2018). ISSN: 1029-8479. DOI: 10.1007/jhep06(2018)004. URL: http://dx.doi.org/10.1007/JHEP06(2018)004.

[203] Patrick J. Fox et al. "LEP Shines Light on Dark Matter". In: *Phys. Rev. D* 84 (2011), p. 014028. DOI: 10.1103/PhysRevD.84.014028. arXiv: 1103.0240 [hep-ph].

[204] A. Anastasi et al. "Limit on the production of a low-mass vector boson in $e^+e^- \to U\gamma$, $U \to e^+e^-$ with the KLOE experiment". In: *Phys. Lett. B* 750 (2015), pp. 633–637. DOI: 10.1016/j.physletb.2015.10.003. arXiv: 1509.00740 [hep-ex].

[205] Roel Aaij et al. "Search for Dark Photons Produced in 13 TeV *pp* Collisions". In: *Phys. Rev. Lett.* 120.6 (2018), p. 061801. DOI: 10.1103/PhysRevLett.120.061801. arXiv: 1710.02867 [hep-ex].

[206] D. Banerjee et al. "Search for a Hypothetical 16.7 MeV Gauge Boson and Dark Photons in the NA64 Experiment at CERN". In: *Phys. Rev. Lett.* 120.23 (2018), p. 231802. DOI: 10.1103/PhysRevLett.120.231802. arXiv: 1803.07748 [hep-ex].

[207] A.H. Abdelhameed et al. "First results from the CRESST-III low-mass dark matter program". In: *Phys. Rev. D* 100.10 (2019), p. 102002. DOI: 10.1103/PhysRevD.100.102002. arXiv: 1904.00498 [astro-ph.CO].

[208] R. Agnese et al. "Search for Low-Mass Dark Matter with CDMSlite Using a Profile Likelihood Fit". In: *Phys. Rev. D* 99.6 (2019), p. 062001. DOI: 10.1103/PhysRevD.99.062001. arXiv: 1808.09098 [astro-ph.CO].

[209] W. Altmannshofer et al. "The Belle II Physics Book". In: *PTEP* 2019.12 (2019). Ed. by E. Kou and P. Urquijo. [Erratum: PTEP 2020, 029201 (2020)], p. 123C01. DOI: 10.1093/ptep/ptz106. arXiv: 1808.10567 [hep-ex].

[210] Akitaka Ariga et al. "FASER's Physics Reach for Long-Lived Particles". In: (2018). arXiv: 1811.12522 [hep-ph].

[211] N. Baltzell et al. "The Heavy Photon Search beamline and its performance". In: *Nucl. Instrum. Meth.* A859 (2017), pp. 69–75. DOI: 10.1016/j.nima.2017.03.061. arXiv: 1612.07821 [physics.ins-det].

[212] Philip Ilten et al. "Dark photons from charm mesons at LHCb". In: *Phys. Rev.* D92.11 (2015), p. 115017. DOI: 10.1103/PhysRevD.92.115017. arXiv: 1509.06765 [hep-ph].

[213] Philip Ilten et al. "Proposed Inclusive Dark Photon Search at LHCb". In: *Phys. Rev. Lett.* 116.25 (2016), p. 251803. DOI: 10.1103/PhysRevLett.116.251803. arXiv: 1603.08926 [hep-ph].

[214] S. Gardner, R. J. Holt, and A. S. Tadepalli. "New Prospects in Fixed Target Searches for Dark Forces with the SeaQuest Experiment at Fermilab". In: *Phys. Rev.* D93.11 (2016), p. 115015. DOI: 10.1103/PhysRevD.93.115015. arXiv: 1509.00050 [hep-ph].

[215] Torsten Åkesson et al. "Light Dark Matter eXperiment (LDMX)". In: (Aug. 2018). arXiv: 1808.05219 [hep-ex].

[216] A. Aguilar-Arevalo et al. "Constraints on Light Dark Matter Particles Interacting with Electrons from DAMIC at SNOLAB". In: *Phys. Rev. Lett.* 123.18 (2019), p. 181802. DOI: 10.1103/PhysRevLett.123.181802. arXiv: 1907.12628 [astro-ph.CO].

[217] D.W. Amaral et al. "Constraints on low-mass, relic dark matter candidates from a surface-operated SuperCDMS single-charge sensitive detector". In: (May 2020). arXiv: 2005.14067 [hep-ex].

[218] Q. Arnaud et al. "First results from the NEWS-G direct dark matter search experiment at the LSM". In: *Astropart. Phys.* 97 (2018), pp. 54–62. DOI: 10.1016/j.astropartphys.2017.10.009. arXiv: 1706.04934 [astro-ph.IM].

[219] Florian Reindl. private communication.

[220] M. Deniz et al. "Measurement of Nu(e)-bar -Electron Scattering Cross-Section with a CsI(Tl) Scintillating Crystal Array at the Kuo-Sheng Nuclear Power Reactor". In: *Phys. Rev. D* 81 (2010), p. 072001. DOI: 10.1103/PhysRevD.81.072001. arXiv: 0911.1597 [hep-ex].

[221] S. Bilmis et al. "Constraints on Dark Photon from Neutrino-Electron Scattering Experiments". In: *Phys. Rev. D* 92.3 (2015), p. 033009. DOI: 10.1103/PhysRevD.92.033009. arXiv: 1502.07763 [hep-ph].

[222] Torsten Bringmann et al. "DarkBit: A GAMBIT module for computing dark matter observables and likelihoods". In: *Eur. Phys. J. C* 77.12 (2017), p. 831. DOI: 10.1140/epjc/s10052-017-5155-4. arXiv: 1705.07920 [hep-ph].

[223] Felix Kahlhoefer. "An introduction to DDCalc". In: *PoS* TOOLS2020 (2021), p. 002. DOI: 10.22323/1.392.0002.

[224] D. S. Akerib et al. "Projected WIMP sensitivity of the LUX-ZEPLIN dark matter experiment". In: *Phys. Rev. D* 101.5 (2020), p. 052002. DOI: 10.1103/PhysRevD.101.052002. arXiv: 1802.06039 [astro-ph.IM].

[225] Tobias Binder et al. "Early kinetic decoupling of dark matter: when the standard way of calculating the thermal relic density fails". In: *Phys. Rev. D* 96.11 (2017). [Erratum: Phys.Rev.D 101, 099901 (2020)], p. 115010. DOI: 10.1103/PhysRevD.96.115010. arXiv: 1706.07433 [astro-ph.CO].

[226] Mateusz Duch and Bohdan Grzadkowski. "Resonance enhancement of dark matter interactions: the case for early kinetic decoupling and velocity dependent resonance width". In: *JHEP* 09 (2017), p. 159. DOI: 10.1007/JHEP09(2017)159. arXiv: 1705.10777 [hep-ph].

[227] Allan Sung, Gang Guo, and Meng-Ru Wu. "Supernova Constraint on Self-Interacting Dark Sector Particles". In: *Phys. Rev. D* 103.10 (2021), p. 103005. DOI: 10.1103/PhysRevD.103.103005. arXiv: 2102.04601 [hep-ph].

[228] B. Abi et al. "Measurement of the Positive Muon Anomalous Magnetic Moment to 0.46 ppm". In: *Phys. Rev. Lett.* 126.14 (2021), p. 141801. DOI: 10.1103/PhysRevLett.126.141801. arXiv: 2104.03281 [hep-ex].